METALS. SUPERCONDUCTORS

The possibility of introducing additional states in the conduction band of $YBa_2Cu_3O_y$ by Ca doping

V. É. Gasumyants, E. V. Vladimirskaya, M. V. Elizarova, and N. V. Ageev

St. Petersburg State Technical University, 195251 St. Petersburg, Russia
(Submitted March 13, 1998; resubmitted June 4, 1998)
Fiz. Tverd. Tela (St. Petersburg) **40**, 2145–2152 (December 1998)

Measurements of the temperature dependences of the resistivity and Seebeck coefficient S, as well as of the Hall coefficient R_H at $T=300$ K are reported for two series of ceramic $Y_{1-x}Ca_xBa_2Cu_3O_y$ samples with oxygen contents in the initial sample close to stoichiometric and then lowered by annealing. It has been found that an increase in calcium content in the first series results in a drop of the critical temperature T_c, a weak variation of S (300 K), and an increase of R_H (300 K), whereas in the second series T_c increases, S (300 K) decreases, and R_H (300 K) remains practically constant. The $S(T)$ relations acquire additional features with increasing doping level, which are not typical of the $YBa_2Cu_3O_y$ system for other types of substitution. An analysis of the data obtained made in terms of the phenomenological band model permits a conclusion that calcium is capable of introducing additional states in the conduction band. Based on this assumption, we have succeeded in providing a qualitative explanation for the unusual features in the behavior of the transport coefficients and critical temperature in $Y_{1-x}Ca_xBa_2Cu_3O_y$. © *1998 American Institute of Physics.*
[S1063-7834(98)00112-9]

The effect of nonisovalent substitutions on the various properties of $YBa_2Cu_3O_y$ is widely discussed presently in the literature. These substitutions have a common feature of affecting the content of oxygen and its distribution among various positions in the unit cell, whose character is primarily determined by the valence states of the substituting and replaced element. In most cases (partial replacement of chain copper by iron or cobalt, as well as of barium by various rare-earth metals), an increase in doping level results in an increase of the oxygen index because of the larger valency of the impurity, which is accompanied by disordering of the oxygen sublattice.[1–5] Calcium, whose valence is smaller than that of the yttrium it substitutes for, occupies a particular place among the various impurities. An increase of x in the $Y_{1-x}Ca_xBa_2Cu_3O_y$ system entails an increase in the number of oxygen vacancies, which not only inhibits growth of the formal carrier concentration but can even cause its drop, if the increasing oxygen deficiency overcompensates the effect of calcium.[6–8] At the same time the critical temperature in $Y_{1-x}Ca_xBa_2Cu_3O_y$ decreases weakly but monotonically with increasing x.[6,7]

There are reports that calcium impurity affects in a specific way the superconducting properties of the HTSC system Y-123. It was found[9–11] that after replacement of 20–25%Y by calcium, $YBa_2Cu_3O_y$, which is nonsuperconducting at $y=6.0-6.2$, becomes a superconductor with $T_c=20-44$ K, and that for $y\approx 6.7$ the value of T_c in $Y_{1-x}Ca_xBa_2Cu_3O_y$ increases with x,[12] while in $Pr_{0.5}Ca_{0.5}Ba_2Cu_3O_y$ $T_c=35$ K (Ref. 13). Finally, calcium restores superconductivity in Y-123 if it was previously suppressed by nonisovalent substitutions at the chain copper[14,15] or barium[16] sites.

Studies of the transport properties revealed that a decrease of y at a fixed calcium content in $Y_{1-x}Ca_xBa_2Cu_3O_y$ results, as in the case of $YBa_2Cu_3O_y$, in an increase of the Seebeck and Hall coefficients,[17–19] and that S decreases with increasing x for a fixed y (Ref. 20). Note that, as shown in Refs. 19 and 21, the empirical relation connecting T_c with the Hall concentration of carriers, which holds for many HTSC systems,[22] fails for $Y_{0.8}Ca_{0.2}Ba_2Cu_3O_y$ at large oxygen deficiencies.

All the above observations indicate a specific influence of calcium on the properties of the carrier system in $Y_{1-x}Ca_xBa_2Cu_3O_y$. At the same time the nature, the reasons and various aspects of this influence are practically ignored while the quoted publications, the conclusions drawn are often contradictory. Thus the problems associated with the mechanism of calcium's influence on the properties of Y-123 certainly deserve further investigation.

An analysis of the transport coefficients in a normal phase based on the electron-transport model used by us (the narrow-band model[23]) permits one to reveal the specific features of what effect various impurities have on band structure parameters and, by comparing these data with the variation of superconducting properties, to draw conclusions on the mechanism of this effect. This method was employed by us to advantage in studying the influence of such substitutions

as Fe, Co, Ni, Mn → Cu,[24,25] La → Ba,[26] and Pr → Y (Ref. 27).

The objective of this work was to study the behavior of the transport coefficients in Ca-doped $YBa_2Cu_3O_y$ in two series of samples with different oxygen contents, to analyze the results obtained within the narrow-band model, and to determine the character and mechanism of calcium effect on the parameters of the band spectrum and of the carrier system in $Y_{1-x}Ca_xBa_2Cu_3O_y$.

1. SAMPLES

Two series of $Y_{1-x}Ca_xBa_2Cu_3O_y$ ceramic samples ($x=0-0.2$) with different oxygen content were studied. The samples were prepared at the Institute of Silicate Chemistry, Russian Academy of Sciences, by standard solid-state technology. The pellets were annealed in air at $T=920-950\,^\circ$C with intermediate grindings. Next the samples were cooled and, in the final stage, maintained for 2 h in an oxygen flow at $T=450\,^\circ$C. The oxygen content in the second series was reduced by additional annealing of all samples for 2 h in air at $T=450\,^\circ$C, with subsequent quenching to room temperature. The oxygen content was determined by iodometric titration to within $\pm 0.01-0.02$. All the samples were homogeneous, which was confirmed by local Seebeck coefficient measurements made at room temperature at various points on their surface, and single phase to within 1–2%, as follows from x-ray diffraction analysis. The lattice parameters determined for the samples of the first series to within ± 0.001 from x-ray diffraction data, and the oxygen index both before and after the additional annealing are listed in Table I. The trend in their variation for the samples of the first series is similar to that quoted in the literature.[6,13,28] Note that while in both cases the oxygen content decreases with increasing doping level, in oxygen-deficient samples the value of y decreases considerably faster.

We performed measurements of the temperature dependences of resistivity and Seebeck coefficient within the range $T=T_c-300$ K, as well as of the Hall coefficient at $T=300$ K, with both series of samples. The method of measurement is described elsewhere.[24]

2. EFFECT OF CALCIUM ON THE TRANSPORT AND SUPERCONDUCTING PROPERTIES OF $Y_{1-x}Ca_xBa_2Cu_3O_y$

The temperature dependence of the resistivity reveals features typical of HTSC materials. The slope of the $\rho(T)$ graphs decreases gradually with increasing x; in samples of the first series an increase in Ca content results, starting with $x=0.15$, in a crossover of these relations to the semiconducting pattern at low temperatures. The parameters of the superconducting transition determined from resistance measurements are presented in Table II. Here T_c^m and T_c^0 are the temperatures corresponding to the midpoint of the transition and the drop of the resistivity by 1000 times from its value in the normal phase, and ΔT is the width of the resistive transition. Table II lists also the room-temperature values of the Seebeck coefficient.

Figure 1 plots the critical temperature T_c^0 as a function of Ca content. Doping with calcium is seen to exert opposite effects on the critical temperature in the two series of samples differing in oxygen content. While in the starting series T_c decreases monotonically with increasing x, in oxygen-deficient samples an increase in Ca content brings about a noticeable growth in critical temperature within the $x=0-0.1$ range (which supports the data quoted in Ref. 13) and a weak dependence $T_c(x)$ with further increase of the doping level. This behavior of the critical temperature appears fairly unusual, particularly if one takes into account the fact that, in the second series, the oxygen content decreases with increasing x more than it does in samples of the first series (see Table I), which, based on general considerations, should result in a steeper decrease of T_c. This implies the existence of some specific features in the effect that Ca has on the superconducting properties of $YBa_2Cu_3O_y$. We note also that the width of the superconducting transition ΔT, while growing monotonically in the first series, varies only weakly in samples of the second series (Table II).

Shown in Figs. 2 and 3 are the temperature dependences of the Seebeck coefficient. Note the following specific features. The Seebeck coefficient is negative for all samples of the high-oxygen series, a feature typical of close-to-stoichiometric $YBa_2Cu_3O_y$ compositions. As x increases, the magnitude of $S_{300\,\mathrm{K}}$ varies very little (see Fig. 2 and Table

TABLE I. Unit cell parameters for starting $Y_{1-x}Ca_xBa_2Cu_3O_y$ samples and oxygen index for both series of samples.

x	a, Å	b, Å	c, Å	Oxygen content	
				Series 1	Series 2
0.000	3.822	3.879	11.694	6.96	6.73
0.025	3.822	3.882	11.691	6.95	6.72
0.050	3.822	3.879	11.689	6.94	6.70
0.075	3.824	3.878	11.690	6.93	6.68
0.100	3.825	3.879	11.690	6.93	6.66
0.150	3.828	3.871	11.693	6.90	6.58
0.200	3.832	3.875	11.697	6.89	6.53

TABLE II. Electrophysical parameters obtained with $Y_{1-x}Ca_xBa_2Cu_3O_y$ samples.

x	T_c^m, K	ΔT, K	T_c^0, K	$S_{300\,\mathrm{K}}$, μV/K
1	2	3	4	5
		First Series		
0.000	92.3	4.7	90.7	−0.63
0.025	91.5	5.4	86.8	−1.48
0.050	88.2	6.0	83.3	−1.18
0.075	86.3	9.0	80.7	−1.20
0.100	83.3	10.0	71.9	−1.14
0.150	79.0	10.3	71.5	−1.29
0.200	78.2	10.9	66.6	−1.24
		Second Series		
0.000	63.7	5.3	61.1	17.8
0.025	70.8	7.5	67.9	14.0
0.050	72.0	4.0	69.7	12.4
0.075	75.1	6.0	73.1	13.3
0.100	80.0	5.6	77.3	9.4
0.150	80.6	8.0	74.2	9.3
0.200	80.9	7.6	76.6	8.0

II), while the $S(T)$ relations exhibit a feature characteristic of off-stoichiometric compositions, namely, a shift of the maximum in the $S(T)$ curve toward higher temperatures.

Note that, as follows from an analysis of the charge balance in the lattice with increasing Ca content, the decrease of positive charge resulting from the $Ca^{2+} \rightarrow Y^{3+}$ substitution is not fully compensated by the decrease in oxygen content (see Table I), which should give rise to a decrease in the number of free electrons [i.e., an increase in carrier (hole) concentration]. But, as already mentioned, one does not observe the expected decrease in the Seebeck coefficient. Consider in this connection the data obtained for the second series of samples. As this should be expected, an increase in oxygen deficiency resulted in an overall growth of the Seebeck coefficient. The stronger decrease of oxygen content with increasing x in the second series (see Table I) gives rise, however, to overcompensation of the charge effect of calcium, which should produce in this case an increase in the number of electrons and, accordingly, growth of the Seebeck coefficient. At the same time, our data show that an increase of Ca content in samples of the first series results in a noticeable decrease of the magnitude of $S_{300\,K}$ (see Fig. 3 and Table II). This discrepancy between the variation of charge balance in the lattice and the magnitude of the Seebeck coefficient observed in both series of samples is one more argument for the existence of another and very substantial influence of Ca impurity on the properties of $YBa_2Cu_3O_y$.

Note also the way in which the temperature dependence of the Seebeck coefficient changes with increasing Ca content in the second series. As x increases, a region of linear decrease of the Seebeck coefficient appears in the $S(T)$ relations above the temperature of the maximum in $S(T)$, and the slope of this relation becomes gradually steeper. To make this feature clearer, Fig. 4 presents two $S(T)$ graphs, namely, for a Ca-doped sample ($x=0.2$) and an undoped $YBa_2Cu_3O_{6.88}$ sample, which was chosen as having the same value of the Seebeck coefficient $S_{300\,K}$. We readily see that as the temperature increases, the slope of the $S(T)$ relation for $YBa_2Cu_3O_{6.88}$ decreases slowly, and that at $T \approx 300$ K the Seebeck coefficient becomes practically temperature independent, a feature characteristic of the yttrium system for small deviations from stoichiometry. At the same time for $Y_{0.8}Ca_{0.2}Ba_2Cu_3O_{6.53}$ one observes with increasing temperature, besides the persistence of the maximum in $S(T)$ at $T \approx 125$ K, a linear decrease of the Seebeck coefficient and a substantial increase of the slope of $S(T)$ compared to $YBa_2Cu_3O_{6.88}$, with no crossover to the temperature-independent region occurring up to $T=300$ K.

Thus Ca doping of $YBa_2Cu_3O_y$ reveals a number of features in the behavior of the critical temperature and Seebeck coefficient, such as an increase in T_c in oxygen-deficient samples, lack of agreement the changes in lattice charge balance and the absolute values of the Seebeck coefficient in both series studied, and an unusual pattern of transformation of the $S(T)$ relations with increasing doping level in the second series. We also carried out measurements of the Hall coefficient R_H at $T=300$ K, whose results are displayed graphically in Fig. 5. One immediately sees that R_H (300 K) in the first series increases rapidly with x while remaining practically constant in the second series. This observation likewise appears fairly unusual because, in other cases of deviation from stoichiometry in $YBa_2Cu_3O_y$, the absolute values of the Seebeck coefficient are found to correlate with the Hall coefficient (Refs. 29 and 30). Besides, the data obtained for the second series lack any correlation between the Hall carrier concentration and the critical temperature, whereas its presence is invoked by some authors[22,29,31] to account for the change in T_c when doping $YBa_2Cu_3O_y$ with various impurities.

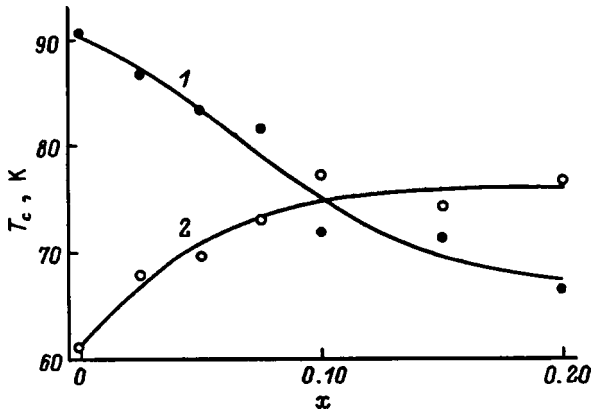

FIG. 1. Critical temperature *vs* calcium content in $Y_{1-x}Ca_xBa_2Cu_3O_y$. *1* — before annealing, *2* — after annealing.

Summing up the above observations, one can confidently maintain that calcium exerts a definite influence on the properties of the normal phase and superconducting parameters of $Y_{1-x}Ca_xBa_2Cu_3O_y$, which sets it off from a number of other dopants, because none of the other nonisovalent substitutions in the various cation sublattices of Y–Ba–Cu–O, along with deviations from oxygen stoichiometry, produces such results. It is reasonable to assume that incorporation of calcium in the lattice gives rise to additional features in the band spectrum of $YBa_2Cu_3O_y$, and this is what accounts for the observed unusual behavior of the transport coefficients. The nature of these features and a possible reason for their appearance will be discussed below.

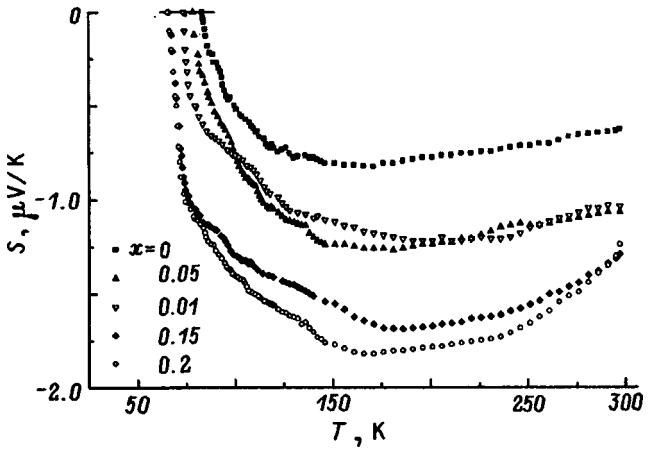

FIG. 2. Temperature dependences of the Seebeck coefficient for the first series of $Y_{1-x}Ca_xBa_2Cu_3O_y$ samples.

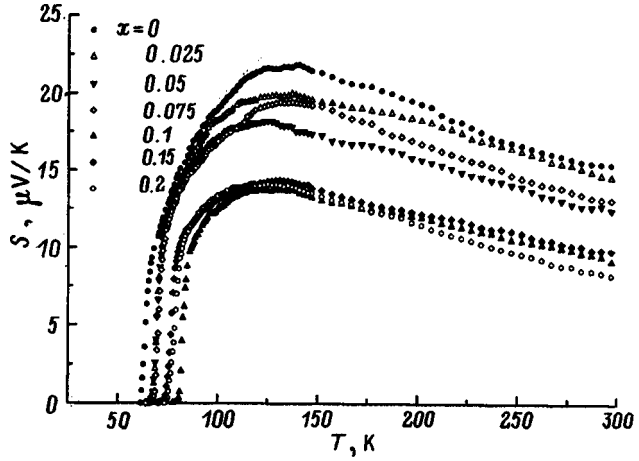

FIG. 3. Temperature dependences of the Seebeck coefficient for the second series of $Y_{1-x}Ca_xBa_2Cu_3O_y$ samples.

3. ANALYSIS OF THE EXPERIMENTAL DATA OBTAINED

We analyzed the experimental data within a phenomenological band model assuming in the band structure of HTSC materials the presence of a narrow density-of-states peak near the Fermi level. This model, described in detail in Ref. 23, was used by us to advantage in analyzing the effect of cation substitutions in various sublattices on the transport properties in normal phase, the band-spectrum parameters, and superconducting characteristics of the $YBa_2Cu_3O_y$ HTSC system.[16,24–27]

The model contains three main parameters, the band filling by electrons F, which is equal to the ratio of the number of electrons to the total number of states in the band, the total effective conduction-band width W_D, and the effective width of the interval of delocalized states W_σ. Using the simplest possible approximation for the density-of-states functions $D(E)$, as well as for the differential and Hall conductivities, one can obtain analytic expressions for the temperature dependences of the chemical potential μ, resistivity ρ, and the Seebeck, and Hall coefficients. Determination of

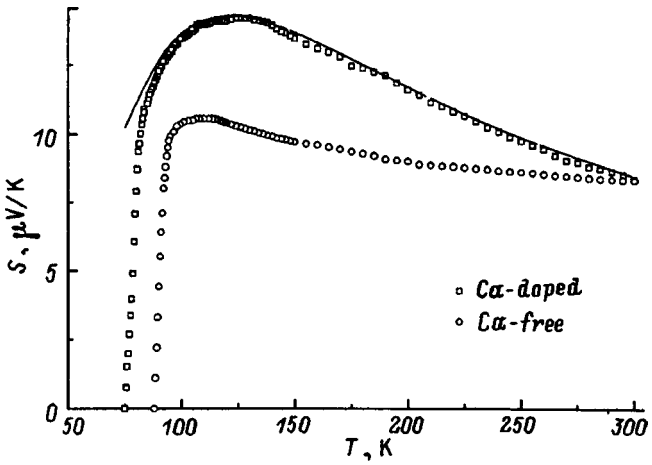

FIG. 4. Temperature dependence of the Seebeck coefficient for a $Y_{0.8}Ca_{0.2}Ba_2Cu_3O_{6.53}$ sample compared with a typical dependence for an undoped $YBa_2Cu_3O_{6.88}$ sample[23]. Solid line is a calculation using Eqs. (2) and (3).

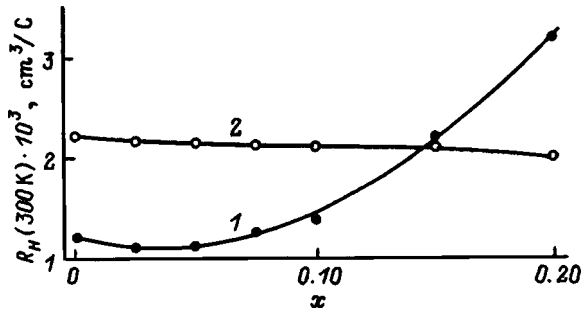

FIG. 5. Hall coefficient at $T=300$ K *vs* calcium content in $Y_{1-x}Ca_xBa_2Cu_3O_y$. *1* — before annealing, *2* — after annealing.

the model parameters requires an analysis of the experimental Seebeck-coefficient relations. The curves for the Seebeck coefficient can be obtained to within its sign, whereas those for the resistivity and the Hall coefficient, only to within a constant factor, which offers a possibility of performing a qualitative analysis of the $\rho(T)$ and $R_H(T)$ relations. Thus by fitting the calculated to experimental $S(T)$ curve one can determine the band spectral parameters for each given sample. The expressions derived for this purpose are as follows[25]

$$\mu^* \equiv \mu/k_BT = \ln \frac{\sinh(FW_D^*)}{\sinh[(1-F)W_D^*]}, \tag{1}$$

$$S = -\frac{k_B}{e}\left\{\frac{W_\sigma^*}{\sinh W_\sigma^*}\left[\exp(-\mu^*)+\cosh W_\sigma^*\right.\right.$$
$$-\frac{1}{W_\sigma^*}(\cosh\mu^*+\cosh W_\sigma^*)\ln$$
$$\left.\left.\times\frac{\exp(\mu^*)+\exp(W_\sigma^*)}{\exp(\mu^*)+\exp(-W_\sigma^*)}\right]-\mu^*\right\}, \tag{2}$$

where μ is the chemical potential, k_B is the Boltzmann constant, e is the electronic charge, $W_D^* \equiv W_D/2k_BT$, and $W_\sigma^* \equiv W_\sigma/2k_BT$.

Equations (1) and (2) previously permitted us to achieve a good agreement between experimental and calculated $S(T)$ relations for Y–Ba–Cu–O samples with various substitutions.[16,24–27] As already pointed out, however, the $S(T)$ relations for the system under study here exhibit additional features. Although our previous studies showed the conduction band in $YBa_2Cu_3O_y$ to be nearly symmetrical, one does not succeed in reaching a good quantitative agreement of calculated $S(T)$ relations with experimental data for $Y_{1-x}Ca_xBa_2Cu_3O_y$ within a symmetric model. On the other hand, the obtained $S(T)$ relations are qualitatively similar to those observed in the bismuth-based HTSC system characterized by a linear growth of the Seebeck coefficient with decreasing temperature.[30,32] Our earlier quantitative analysis of the dependence of $S(T)$ in bismuth-based samples showed that they can also be described in terms of the above model provided one introduces an additional assumption of a weak asymmetry of the conduction band.[32,33] Thus the experimental $S(T)$ relations for $Y_{1-x}Ca_xBa_2Cu_3O_y$ give one

grounds to assume that Ca doping creates in the band of $YBa_2Cu_3O_y$ features inherent in a bismuth-based HTSC system, to wit, makes the conduction band asymmetric. For this reason we carried out calculations of $S(T)$ within an asymmetric model.

The simplest way to take into account the asymmetry, described in detail in Ref. 25, consists in introducing a distance (bW_D, where b is the asymmetry parameter) between the centers of the rectangles approximating the density-of-states and differential conductivity functions. In this case Eq. (3) remains valid if one replaces in it μ^* calculated from Eq. (1) with

$$(\mu^*)' = \mu^* - bW_D/k_0T. \tag{3}$$

Our quantitative analysis of the calcium-induced changes in the band spectrum of $Y_{1-x}Ca_xBa_2Cu_3O_y$ made use of data obtained only for the second series of samples, because the absolute values of the Seebeck coefficient for all samples of the first series were found to be very small. In this case the pattern of the $S(T)$ relation is affected strongly by small features in the conduction-band structure, which are difficult to take into account within the approximation used here. This may result in a larger error of calculated band parameters. For this reason the data obtained for the first series were employed only in a qualitative analysis. On the other hand, the Seebeck coefficient of second-series samples increased in absolute magnitude due to the higher oxygen deficiency, which should weaken the effect of small features in the band structure on the overall pattern of the $S(T)$ relations. This permits one to derive reliable information on band-structure parameters from a quantitative analysis of the experimental data and to use subsequently these results, combined with the qualitative conclusions drawn from the data obtained from samples of the first series, in considering the effect of calcium on the properties of $Y_{1-x}Ca_xBa_2Cu_3O_y$.

We have succeeded in reaching within this approach a good quantitative agreement between the experimental and calculated $S(T)$ relations for all samples of the second series. For illustration, the solid line in Fig. 4 shows a relation calculated for a $Y_{0.8}Ca_{0.2}Ba_2Cu_3O_{6.53}$ sample. By using Eqs. (1)–(3) and comparing the calculations with experiment, we derived the parameters of the carrier system for all samples of the second series. Figure 6 plots concentration dependences of the electron band filling and of the degree of conduction-band asymmetry. We readily see that F decreases linearly with increasing Ca content, and that the behavior of the asymmetry parameter b is likewise linear and can be described by the expression $b \approx -0.1x$. The values of parameter b are small, i.e. the conduction band is only slightly asymmetric. Besides, calculations showed that the total effective band width W_D for the second series of $Y_{1-x}Ca_xBa_2Cu_3O_y$ samples varies only insignificantly with increasing Ca content (the value of W_D lies from 160 to 190 meV). Note that W_σ likewise varies little with increasing x, so that our data do not support the assumption[7,20] that doping with calcium causes strong carrier localization.

The linear increase in the conduction-band asymmetry with increasing x clearly implies that it is the increase in Ca content that accounts for the appearance of additional features in the band structure of $YBa_2Cu_3O_y$. We believe that the most probable cause for the observed changes in the band structure is the Ca-induced additional states in the conduction band. This gives rise to an additional Ca peak in the density-of-states function, and this is what accounts for the onset of conduction-band asymmetry and its subsequent growth with increasing doping level.

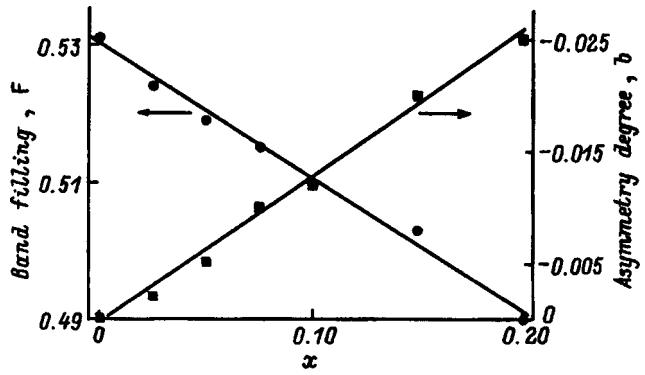

FIG. 6. Band filling by electrons and band asymmetry *vs* calcium content for $Y_{1-x}Ca_xBa_2Cu_3O_y$ samples of the second series.

The assumption of the onset of asymmetry in the conduction band provides an explanation for the concentration dependences of the filling and effective width of the conduction band.

As already mentioned, a comparison of the changes in the oxygen index with Ca content (Table I) makes it clear that, while in the first series the calcium-induced distortion of the charge balance is not fully compensated by decreasing oxygen content, in samples of the second series, by contrast, the effect of calcium is overcompensated by the increasing oxygen deficiency, and this should result in a decrease of carrier (hole) concentration, i.e. an increase of the number of electrons. This means that the Seebeck coefficient should increase and the band filling by electrons, calculated within our model, grow with x. Our experimental data (the decrease of $S_{300\,K}$) and calculations (the decrease of the F parameter) may be considered as a further argument for the appearance of additional states in the band due to calcium. Indeed, the band filling by electrons is determined by the ratio $F = n/N$, where n and N are the numbers of electrons and states in the band, respectively. Only the creation of additional band states by calcium (i.e., an increase of N with increasing x) can account for the decrease in the filling and, accordingly, the decrease of the value of $S_{300\,K}$ obtained in the experiment.

The observed weak change in the conduction-band width also finds an explanation. In principle, a substantial decrease of oxygen content, which brings about disordering of the oxygen sublattice, should tend to broaden the conduction band.[23,25] It should, however, be borne in mind that calculations yield the effective band width, i.e., the width of the rectangle approximating the $D(E)$ function and, in this case, the weak variation of W_D with increasing calcium content may actually result from a combination of two effects, namely, a broadening of the band due to disordering of the

oxygen sublattice, and its affective narrowing due to the formation of an additional peak created by the Ca-induced states.

As for the Hall coefficient, calculations made in terms of our model for the $R_H(T)$ relations showed that for large band fillings (the case of samples of the second series) the decrease of F and the increase of band asymmetry practically counterbalance their effects on the Hall coefficient. At the same time, at close to half band filling (samples of the first series), the effect of asymmetry becomes more essential and gives rise to an increase of $R_H(300\ \mathrm{K})$. Note that, even a qualitative analysis of the Hall coefficient data obtained on the first series of samples supports the conclusion of a gradual increase in conduction-band asymmetry with increasing doping level. Because for the starting sample of the first series $F<0.5$, and data obtained for the second series suggest that the band filling decreases with increasing x, it becomes obvious that the $F<0.5$ condition is upheld for all samples in the first series, and that, most probably, the value of F in this series likewise decreases with increasing x. Nevertheless, the Hall coefficient remains positive for all first-series samples, an observation that can be explained only by assuming the conduction band to become asymmetric.

The results obtained also provide a qualitative explanation for the opposite trends in the variation of critical temperature with increasing doping level in the two sample series, namely, its decrease in the first series and growth in the second. In the first series, the composition of the starting sample is close to stoichiometric and, hence, the band is nearly half full, i.e., the Fermi level lies close to the midband position and, judging from the negative Seebeck coefficient, in the lower half of the band. The calcium impurity creates additional states in the band, the filling decreases, and the Fermi level shifts from the maximum of the $D(E)$ function toward lower energies. Thus the density of states at Fermi level decreases, and this is what causes the decrease of T_c observed in this series. By producing oxygen deficiency in the starting sample of the second series, we shift the Fermi level toward higher energies. Doping with calcium, as in the first case, reduces the band filling, and the Fermi level also shifts toward lower energies but, in this case, this corresponds to approaching the maximum in the $D(E)$ function. As a result, the critical temperature in this series increases with increasing impurity content. In both cases, therefore, one observes a correlation between the variation of $D(E_F)$ and the critical temperature.

Thus the assumption that Ca doping of $YBa_2Cu_3O_y$ introduces additional states in the conduction band explains all the results obtained, both the critical temperature and the specific features in the behavior of the transport coefficients. These results and their analysis made within a phenomenological band-structure model permits the following conclusions.

1) As the Ca content in $Y_{1-x}Ca_xBa_2Cu_3O_y$ increases, the critical temperature decreases in samples with close-to-stoichiometric oxygen content, and increases in oxygen-deficient samples;

2) The absolute values of the Seebeck coefficient vary weakly with increasing doping level in oxygen-rich samples and decrease monotonically in oxygen-deficient samples, whereas the Hall coefficient at $T=300$ K increases markedly in the first case and remains practically constant in the second;

3) Ca doping changes the pattern of the $S(T)$ relations for oxygen-deficient samples, namely, it results in the appearance of an extended region of linear growth of the Seebeck coefficient with decreasing temperature, which is due to a specific calcium-induced modification of the band structure;

4) An analysis of the $S(T)$ relations and of the $R_H(300\ \mathrm{K})$ data made for the $Y_{1-x}Ca_xBa_2Cu_3O_y$ compound within the narrow-band model shows that Ca doping gives rise to a conduction band asymmetry, which increases monotonically with doping level. The most probable reason for the onset of asymmetry is Ca-induced formation of additional states in the conduction band;

5) The assumption of the formation of additional conduction-band states by calcium provides an explanation for the observed transformation of transport properties in normal phase and for the pattern of critical temperature variation in $Y_{1-x}Ca_xBa_2Cu_3O_y$ for different oxygen contents. One observes also a correlation between the density-of-states function at Fermi level and the critical temperature.

The authors owe their warm thanks to I. B. Patrina and N. P. Baranskaya of the Institute of Silicate Chemistry for preparation of samples for the investigation, x-ray diffraction measurements, and oxygen content determination.

[1] J. M. Tarascon, P. Barboux, P. F. Miceli, L. H. Greene, G. W. Hull, M. Eibschutz, and S. A. Sunshine, Phys. Rev. B **37**, 7458 (1988).
[2] K. Westerholt, H. J. Wüller, H. Bach, and P. Stauche, Phys. Rev. B **39**, 11680 (1989).
[3] Y. Xu, R. Sabatini, A. R. Moodenbaugh, Y. Zhu, S.-G. Shyu, M. Suenaga, K. W. Dennis, and R. W. McCallum, Physica C **169**, 205 (1990).
[4] R. Liang, M. Itoh, T. Nakamura, and R. Aoki, Physica C **157**, 83 (1989).
[5] A. Manthiram and J. B. Goodenough, Physica C **159**, 760 (1989).
[6] A. Tokiwa, Y. Syono, M. Kikuchi, R. Suzuki, T. Kajitani, N. Kobayashi, T. Sasaki, O. Nakatsu, and Y. Muto, Jpn. J. Appl. Phys. **27**, L1009 (1988).
[7] Z. Jirak, J. Hejtmanek, E. Pollert, A. Triska, and P. Vasek, Physica C **156**, 750 (1988).
[8] M. R. Chandrachood, I. S. Mulla, S. M. Gorwadkar, and A. P. B. Sinha, Appl. Phys. Lett. **56**, 183 (1990).
[9] E. M. McCarron III, M. K. Crawford, and J. B. Parise, J. Solid State Chem. **78**, 192 (1989).
[10] J. B. Parise and E. M. McCarron III, J. Solid State Chem. **83**, 188 (1989).
[11] R. S. Liu, J. R. Cooper, J. W. Loram, W. Zhou, W. Lo, P. P. Edwards, W. Y. Liang, and L. S. Chen, Solid State Commun. **76**, 679 (1990).
[12] V. P. S. Awana, S. K. Malik, and W. B. Yelon, Physica C **262**, 272 (1996).
[13] D. P. Norton, D. H. Lowndes, B. C. Sales, J. D. Budai, B. C. Chakoumakos, and H. R. Kerchner, Phys. Rev. Lett. **66**, 1537 (1991).
[14] E. Suard, A. Maignan, V. Caignaert, and B. Raveau, Physica C **200**, 43 (1992).
[15] R. Suryanarayanan, S. Leelaprute, L. Ouhammou, and A. Das, J. Supercond. **7**, 77 (1994).
[16] E. V. Vladimirskaya, V. É. Gasumyants, and I. B. Patrina, Fiz. Tverd. Tela (St. Petersburg) **37**, 1990 (1995) [Phys. Solid State **37**, 1084 (1995)].
[17] B. Fisher, J. Genossar, C. G. Kuper, L. Patlagan, G. M. Reisber, and A. Knizhnik, Phys. Rev. B **47**, 6054 (1993).
[18] T. Honma and K. Yamaya, Physica C **185–189**, 1245 (1991).
[19] G. Xiao and N. S. Rebello, Physica C **211**, 433 (1993).
[20] C. Legros-Gledel, J.-F. Marucco, E. Vincent, D. Favrot, B. Poumellec, B. Touzelin, M. Gupta, and H. Alloul, Physica C **175**, 279 (1991).
[21] Y. Sun, G. Strasser, E. Gornik, W. Seidenbusch, and W. Rauch, Physica C **206**, 291 (1993).

[22] M. H. Whangbo and C. C. Torardi, Science **249**, 1143 (1990).
[23] V. É. Gasumyants, S. A. Kaz'min, V. I. Kaĭdanov, V. I. Smirnov, Yu. M. Baĭkov, and Yu. P. Stepanov, Sverkhprovodimost' (KIAE) **4**, 1280 (1991) [Superconductivity **4**, 1184 (1991)].
[24] E. V. Vladimirskaya and V. É. Gasumyants, Fiz. Tverd. Tela (St. Petersburg) **36**, 1002 (1994) [Phys. Solid State **36**, 545 (1994)].
[25] V. E. Gasumyants, V. I. Kaidanov, and E. V. Vladimirskaya, Physica C **248**, 255 (1995).
[26] V. É. Gasumyants, E. V. Vladimirskaya, and I. B. Patrina, Fiz. Tverd. Tela (St. Petersburg) **40**, 17 (1998) [Phys. Solid State **40**, 14 (1998)].
[27] V. É. Gasumyants, E. V. Vladimirskaya, and I. B. Patrina, Fiz. Tverd. Tela (St. Petersburg) **39**, 1520 (1997) [Phys. Solid State **39**, 1352 (1997)].
[28] Y. Zhao, Y. He, H. Zhang, X. Zuge, and X. Tang, J. Phys.: Condens. Matter **4**, 2263 (1992).
[29] N. P. Ong, in *Physical Properties of High-Temperature Superconductors II*, edited by D. M. Ginsberg (World Scientific, Singapore, 1990), p. 459.
[30] A. B. Kaiser and C. Uher, in *Studies of High-Temperature Superconductors*, edited by A. V. Narlikar (Nova Science, New York, 1990), p. 353.
[31] Y. Iye, in *Physical Properties of High-Temperature Superconductors III*, edited by D. M. Ginsberg (World Scientific, Singapore, 1992), p. 285.
[32] N. V. Ageev, V. É. Gasumyants, and V. I. Kaĭdanov, Fiz. Tverd. Tela (St. Petersburg) **37**, 2152 (1995) [Phys. Solid State **37**, 1171 (1995)].
[33] V. E. Gasumyants, N. V. Ageev, E. V. Vladimirskaya, V. I. Smirnov, A. V. Kazanskiy, and V. I. Kaidanov, Phys. Rev. B **53**, 905 (1996).

Translated by G. Skrebtsov

Superconductivity in the Ti–D system under pressure

I. O. Bashkin,* M. V. Nefedova, V. G. Tissen, and E. G. Ponyatovskiĭ

Solid-State Physics Institute, Russian Academy of Sciences, 142432 Chernogolovka, Moscow Region, Russia
(Submitted April 7, 1998; resubmitted June 15, 1998)
Fiz. Tverd. Tela (St. Petersburg) **40**, 2153–2155 (December 1998)

The pressure dependence of the superconducting transition temperature in $TiD_{0.74}$ has been measured up to 30 GPa in a diamond high-pressure chamber. It is found that the deuteride $TiD_{0.74}$ becomes a superconductor at pressures corresponding to the transition to the high-pressure ζ phase, with a transition temperature that increases from 4.17 to 4.43 K in the interval $P=14-30$ GPa. The value extrapolated to atmospheric pressure $T_c(0)=4.0$ K is significantly lower than the superconducting transition temperature ($T_c=5.0$ K) measured earlier in the metastable state obtained by quenching $TiD_{0.74}$ under pressure. It is assumed that the significant difference of the extrapolated value from the superconducting transition temperature in the metastable state after quenching under pressure is caused by a phase transition on the path from the stability region of the ζ phase under pressure to the region of the metastable state at atmospheric pressure. © *1998 American Institute of Physics.* [S1063-7834(98)00212-3]

The $T-c$ diagram of the Ti–H (Fig. 1) and Ti–D systems at atmospheric pressure includes the eutectoid equilibrium of the α, β, and δ phases, based on the hexagonal close-packed (hcp), body-centered cubic (bcc), and face-centered cubic (fcc) titanium sublattices, respectively.[1–3] A new phase, ζ,[2,3] appears at a pressure of 2.05 GPa (3.4 GPa in the deuterides) and a temperature of ~560 K in the alloy of eutectoid composition ($x=$ H(D)/Ti≈ 0.74). The structure of the ζ phase directly under pressure has been determined only by an x-ray method: It was found that, at $P\approx 5$ GPa, in the temperature interval $T=520-720$ K, the metal atoms in the ζ phase are packed into a face-centered tetragonal (fct) sublattice with a parameter ratio of $c/a=0.89$.[2] In order to study the properties of the new phase in more detail, it was quenched to 80 K after heat treating the samples at $T\geqslant 560$ K under a pressure above 5 GPa. After quenching under pressure, the single-phase state remained metastable at temperatures below 95 (100) K all the way to atmospheric pressure.[4] The structural characteristics of the metastable quenched state have been studied in detail at $T\leqslant 90$ K by inelastic neutron scattering and diffraction.[3,5–7] In this state, the hydrogen statistically occupies octahedral interstitial sites of the fct titanium sublattice,[7] unlike phases that are stable at $P=1$ atm, where the hydrogen is always located at tetrapores.[1,6] Since the specific volumes of the ζ phase and the metastable quenched state were extremely close to each other and much less (~10%) than in the other hydride phases of this system, it was assumed that, in the ζ phase, the hydrogen also was distributed over the octopores.[2,7] However, the ratio of the lattice parameters in the state after quenching was appreciably closer to unity than in the ζ phase, $c/a=0.95$.[7] It was therefore assumed[2,7] that the hydrogen distribution over the octopores can be different in the ζ phase than in the state after quenching, and the metastable quenched state was given an independent designation—the χ phase.

The difference in crystal structure must be reflected in the structure-sensitive physical properties. One of the clearest features of the χ phase is superconductivity with a transition temperature that is high for the Ti–H(D) system [$T_c=4.3$ (5.0) K],[8,9] which is a result of the transition of the hydrogen into the octopores. The superconductive properties of the χ phase have not previously been studied *in situ*. For this paper, we measured the pressure dependence of the superconducting transition temperature in ζ-$TiD_{0.74}$ up to 30 GPa and found that extrapolating the $T_c(P)$ dependence for the ζ phase to atmospheric pressure gives a value lower than was determined earlier for the χ phase. The measurements were made on the deuteride, since it has a higher superconducting transition temperature than does the hydride.

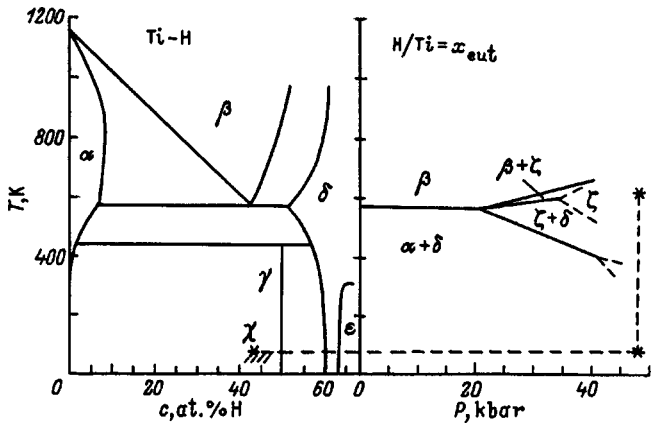

FIG. 1. Phase diagram of Ti–H. On the left is the $T-c$ projection for atmospheric pressure, and on the right is the $T-P$ projection for the hydrides of the near-eutectoid state.[3] The dashed lines denote the thermobaric treatment of the ζ phase and the unloading that results in the synthesis of the χ phase (its region of metastability at $P=1$ atm is hatched). On the $T-P$ projection, the low-temperature boundary of the region of the ζ phase ends with a dashed bifurcation, representing the region where the existence of a second high-pressure phase is probable.

1. TECHNIQUE

The initial two-phase deuteride of chemical composition $D/Ti=0.74\pm0.01$ was synthesized by the reaction of high-purity ($\sim$99.98 at.%) titanium with deuterium gas, given off by heating TiD_2 (see Ref. 10, for example, for more details). The deuterium content was determined by weighing. In order for the small fabricated samples $\sim0.1\times0.1\times0.03$ mm to maintain the average chemical composition, it was required that the microstructure of the two-phase deuteride be homogeneous and fine-grained. The limiting comminution of a crystalline grain (the characteristic size of the Ti precipitates in the matrix of the γ phase was[11] $\leqslant100$ Å) was accomplished by heat-treating and quenching to 80 K a pellet of $TiD_{0.74}$ under a pressure of 6.5 GPa, followed by decay of the quenched χ phase when the sample was quickly returned to normal conditions.

An apparatus with diamond anvils fabricated from nonmagnetic materials was used to create high pressures.[12] The sample and crystals of a ruby standard were placed in the aperture of a metallic gasket 0.15 mm in diameter. A 4:1 methanol–ethanol mixture served as a pressure-transmission medium. The pressure was varied and measured at room temperature. The pressure was determined to within ±0.05 GPa from the shift of the R line of ruby. The superconducting transition was determined from ac measurements of the magnetic susceptibility $\chi(T)$.[13] The amplitude of the variable 5.2-kHz magnetic field was 0.3 Oe. The high-pressure apparatus was cooled as a whole to 1.5 K in a cryostat, and the measurements of $\chi(T)$ were made while heating, using a (Cu–Fe)–Cu thermocouple to measure the temperature to within ±0.2 K. Because of the necessity of repeatedly heating the apparatus to vary and determine the pressure, a measurement cycle at each pressure took days.

2. RESULTS AND DISCUSSION

In the range $P\leqslant7$ GPa in which the $T-P$ diagram of the Ti–D system was studied earlier,[2] the line of the transformation into the ζ phase was located at temperatures above 450 K. Extrapolating this line makes it possible to estimate the transition pressure into the ζ phase when the sample is loaded at room temperature as approximately 10 GPa. The first measurement cycle of $\chi(T)$ was therefore carried out at a pressure of 9.5 GPa. No superconducting transition was observed in this cycle. In the next cycle, under a pressure of $P=11.8$ GPa, an anomalous superconducting transition on the $\chi(T)$ isobar was clearly evident, although the jump is rather smeared out and has a low-temperature tail (Fig. 2). A further increase of the pressure to 30 GPa results in an increase of the superconducting transition temperature, while the jump becomes sharper and increases somewhat in magnitude. As the pressure is decreased, the superconducting transition becomes still more distinct than in the process of loading the chamber. However, after the pressure is reduced from 11.2 to 8.2 GPa, the superconductivity in the sample completely disappears, which is obviously associated with the decay of the ζ phase at room temperature to the low-pressure phase.

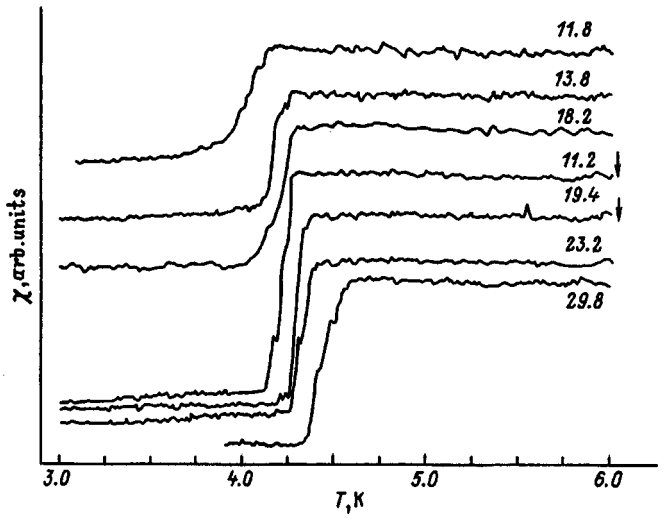

FIG. 2. Experimental curves of the temperature dependence of the magnetic susceptibility of $TiD_{0.74}$ under conditions of heating at fixed pressures (indicated in GPa near the curves). The arrows show curves recorded during unloading of the high-pressure chamber.

The temperature at which the jump in $\chi(T)$ reaches one half was taken as the superconducting transition point. The superconducting transition temperatures determined in this way are shown in Fig. 3 as a function of the pressure. It can be seen from this figure that the $T_c(P)$ dependence is close to linear in the region $P>12$ GPa. On one hand, the deviation of the initial load point $P=11.8$ GPa from a linear dependence, as well as the smearing of the jump of $\chi(T)$, can be regarded as evidence that the transition into a phase with superconducting properties was incomplete. On the other hand, when the $T-P$ diagram of the Ti–H system above 4 GPa was studied, bifurcation of the anomalies of the electrical resistance and the thermal effects of the transition into the ζ phase was observed, and, based on this, the possibility that a second high-pressure phase exists was indicated.[2] The

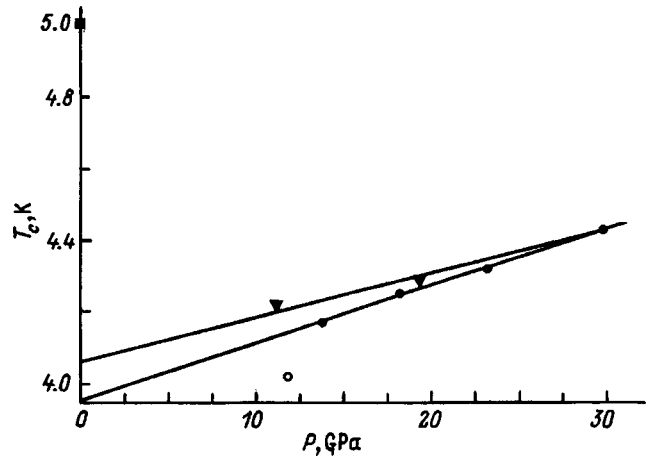

FIG. 3. Pressure dependence of the superconducting transition temperature in ζ-$TiD_{0.74}$. Transitions during loading are denoted by circles, and transitions during unloading are denoted by triangles. The initial load point probably reflects a property of an intermediate phase, and therefore is not filled in. For comparison, the superconducting transition temperature in χ-$TiD_{0.74}$ is shown by a square.[8]

formation of some intermediate phase in a relatively narrow region of the $T-P$ diagram can be another explanation of the observed deviation.

The slope of the dependence for the load curve in the region $P>12$ GPa is $dT_c/dP=0.016$ K/GPa, and the slope of the unloading curve is close to this value. Linear extrapolation of the $T_c(P)$ dependence to atmospheric pressure gives a value of $T_c^0=4.0\pm0.05$ K (Fig. 3), which is significantly lower than the superconducting transition temperature in the χ phase obtained after thermobaric treatment ($T_c=5.0$ K). The entire $T_c(P)$ curve in the interval to 30 GPa lies below 4.5 K. The strong noncorrespondence of one of the main superconductivity characteristics of the χ and ζ phases agrees with the assumption expressed earlier[2,7] that it is possible that the hydrogen sublattice is reconstructed during the transition from the stability region of the ζ phase ($P\approx5$ GPa, $T\approx650$ K) into the region of the metastable existence of the χ phase. The set of experimental facts shown above makes it possible to discuss two mechanisms for such a reconstruction.

The chemical composition of the ζ phase corresponds to the composition of a number of possible tetragonally distorted ordered inclusion superstructures.[14] It is therefore extremely probable that the hydrogen in the high-pressure phase is ordered below a certain temperature. This transition cannot be recorded by differential thermal analysis because of kinetic or thermodynamic causes. If the hydrogen sublattice of the ζ phase is ordered under the conditions from which its quenching is carried out, reconstruction of the octahydrogen sublattice during thermobaric treatment and the return to atmospheric pressure can be the initial stage of the decay of the ζ phase as it becomes unstable; i.e., the disordering of the hydrogen can decrease the tetragonal distortion and increase the superconducting temperature in the χ phase. If, on the contrary, the hydrogen sublattice of the ζ phase is disordered for the initial parameters of the quenching, an ordered superstructure could arise during the rather slow cooling in the experiments to measure the superconductivity. The question of the possibility of ordering in the high-pressure phase can be definitively solved by a more detailed structural investigation under pressure.

Measurements of the $T_c(P)$ dependence have thus shown that the high-pressure phase in the Ti–D system is a superconductor with a transition temperature that increases from 4.17 to 4.43 K in the interval 14–30 GPa. The value of $T_c(P)$ extrapolated to atmospheric pressure is significantly below the superconducting transition temperature in the χ phase. This noncorrespondence serves as a basis for a question concerning a structural transition in the high-pressure phase, associated with the ordering of hydrogen.

The authors are grateful to V. G. Glebovskiĭ for preparing the ingot of high-purity titanium.

This work was carried out with the support of the Russian Fund for Fundamental Research in the framework of Projects No. 97-02-17614 and No. 96-15-96806.

*E-mail: bashkin@issp.ac.ru

[1] A. San-Martin and F. D. Manchester, Bull. Alloy Phase Diagrams **8**, 1, 30 (1987).
[2] I. O. Bashkin, T. I. Dyuzheva, L. M. Lityagina, and V. Yu. Malyshev, Fiz. Tverd. Tela (St. Petersburg) **35**, 3104 (1993) [Phys. Solid State **35**, 1528 (1993)].
[3] I. O. Bashkin, A. I. Kolesnikov, and E. G. Ponyatovsky, High Press. Res. **14**, 91 (1995).
[4] I. O. Bashkin, I. M. Barkalov, A. I. Bashkin, V. Yu. Malyshev, and E. G. Ponyatovskiĭ, Fiz. Tverd. Tela (Leningrad) **32**, 2684 (1990) [Sov. Phys. Solid State **32**, 1556 (1990)].
[5] A. M. Balagurov, I. O. Bashkin, A. I. Kolesnikov, V. Yu. Malyshev, G. M. Mironova, E. G. Ponyatovskiĭ, and V. K. Fedotov, Fiz. Tverd. Tela (Leningrad) **33**, 1256 (1991) [Sov. Phys. Solid State **33**, 711 (1991)].
[6] A. I. Kolesnikov, A. M. Balagurov, I. O. Bashkin, V. K. Fedotov, V. Yu. Malyshev, G. M. Mironova, and E. G. Ponyatovsky, J. Phys.: Condens. Matter **5**, 5043 (1993).
[7] I. O. Bashkin, A. I. Kolesnikov, E. G. Ponyatovskiĭ, A. M. Balagurov, and G. M. Mironova, Fiz. Tverd. Tela (St. Petersburg) **37**, 3744 (1995) [Phys. Solid State **37**, 2065 (1995)].
[8] I. O. Bashkin, V. Yu. Malyshev, V. I. Rashchupkin, and E. G. Ponyatovskiĭ, Fiz. Tverd. Tela (Leningrad) **30**, 2003 (1988) [Sov. Phys. Solid State **30**, 1155 (1988)].
[9] V. M. Teplinskiĭ, I. O. Bashkin, V. Yu. Malyshev, and E. G. Ponyatovskiĭ, Fiz. Tverd. Tela (Leningrad) **31**, No. 2, 91 (1989) [Sov. Phys. Solid State **31**, 225 (1989)].
[10] I. O. Bashkin, A. F. Gurov, V. Yu. Malyshev, and E. G. Ponyatovskiĭ, Fiz. Tverd. Tela (Leningrad) **34**, 1276 (1992) [Sov. Phys. Solid State **34**, 674 (1992)].
[11] I. O. Bashkin, A. I. Kolesnikov, V. Yu. Malyshev, E. G. Ponyatovsky, S. Borbély, L. Rosta, and G. Pépy, J. Phys. IV (Colloque C8, Suppl. J. de Phys. I, 12), **3**, 287 (1993).
[12] N. N. Kolesnikov, M. P. Kulakov, M. V. Nefedova, and V. G. Tissen, Sverkhprovodnost' (KIAE) **6**, 281 (1993).
[13] V. G. Tissen, E. G. Ponyatovskii, M. V. Nefedova, L. A. Klinkova, and N. V. Barkovskii, J. Phys.: Condens. Matter **8**, 3069 (1996).
[14] A. G. Khachaturyan, *Theory of Phase Transitions and Structure of Solid Solutions* (Nauka, Moscow, 1974), 384 pp.

Translated by W. J. Manthey

SEMICONDUCTORS AND INSULATORS

Luminescence spectra produced by exciton relaxation at local magnetization fluctuations in semimagnetic semiconductors

A. V. Kudinov and Yu. G. Kusraev

A. F. Ioffe Physicotechnical Institute, Russian Academy of Sciences, 194021 St. Petersburg, Russia
(Submitted June 4, 1998)
Fiz. Tverd. Tela (St. Petersburg) **40**, 2156–2160 (December 1998)

An analysis is made of the exciton angular-momentum alignment along a fluctuation in local magnetization, which is the first stage in evolution of the localized-exciton spin state in a semimagnetic semiconductor. It is shown that spin relaxation of localized excitons subjected to resonant optical excitation is accompanied by their relaxation in energy. When excited by polarized light, this process gives rise to an anisotropic angular-momentum distribution in the spectrum of final exciton states and, hence, to polarization of the secondary luminescence. Luminescence spectra of a cubic crystal are calculated, and the possibility of their experimental observation discussed. [S1063-7834(98)00312-8]

1. In CdMnTe-type semimagnetic semiconductors, exchange interaction of excitons with $3d$ electrons localized at manganese ions results in a substantial dependence of exciton energy on the average manganese-ion spin. If excitons are delocalized, this is observed in an external magnetic field as giant Zeeman splitting of spin sublevels,[1] but in zero magnetic field the exciton state is degenerate, because the exciton interacts with numerous randomly oriented spins of magnetic ions. Localized excitons feel only the magnetic-ion spin averaged over the exciton localization region. The spin projection averaged over the localization region (local magnetization) is nonzero due to fluctuations even with no external field present. The energy of exciton interaction with local magnetization depends on the relative fluctuation of the latter, and therefore the fluctuation effect is the stronger, the smaller is the exciton localization region.

Magnetization fluctuations give rise to exciton-line broadening,[2] and are seen in Raman spin-flip processes[3–5] and in polarized luminescence[6–8]. As the temperature is lowered, the relaxation times in the disordered and strongly interacting spin system of magnetic ions become long, and this results eventually in freezing in of the random state (a spin-glass transition).[9] The existence of persistent fluctuations in magnetization is evidenced by optical field-cooling experiments.[10]

It is possibly because of the long relaxation times that magnetization fluctuations are seen in the polarization of stationary magnetic-polaron luminescence in semimagnetic systems, although the magnetic moment created in polaron formation exceeds by far the fluctuation moment. A fluctuation-based approach was proposed to account for the high degree of circular polarization of the luminescence observed under resonant excitation of localized states in semimagnetic semiconductors.[6] The spectral response of the luminescence polarization arising in such an experiment was analyzed for bulk CdMnTe crystals[7] and CdMnTe quantum-well structures[8]. These experiments revealed a fluctuation-induced shift between the maxima in the spectra of circularly-polarized luminescence components, which is the most revealing argument for the fluctuation mechanism. At the same time the polaron-induced broadening of the luminescence line in stationary conditions (which occurs even under resonant excitation[11]) washes out considerably the spectral features in polarization, a phenomenon relating particularly to bulk cubic crystals.

The idea of inelastic spin-flip transition in zero magnetic field is in no way new. Light scattering involving spin flip of a neutral-donor-bound electron was reported, for instance, in Ref. 5, where the Raman line shift was assigned to the magnetic polaron effect. In the present work we calculate polarized spin-flip spectra of localized excitons, which are resonantly excited in the exchange fields of magnetic fluctuations. We shall use the results of Ref. 7 and complement them by taking into account the distribution of magnetic fluctuations in magnitude but, by contrast, shall abandon phenomenological inclusion of the polaron shift and broadening. The latter corresponds to the initial stage in the evolution of the spin state of a localized exciton, which is the alignment of its angular momentum with a magnetization fluctuation. While major focus will be placed on the cubic crystal, we are going to discuss also the simpler case of hexagonal crystals or quantum wells.

2. Let light with a narrow spectral width excite resonantly localized excitons in the Urbach region of the density-of-states tail. The excited excitons do not migrate, i.e. recombination takes place in the same microregions of the crystal as excitation. A fluctuation in the total manganese-ion spin present in the vicinity of each localized exciton splits the exciton state. Following Ref. 6, we shall assume an isotropic normal distribution of local magnetization, so that the probability for the magnetization in a given region to be of magnitude m will be proportional to $m^2\exp(-m^2)$. Also, if the

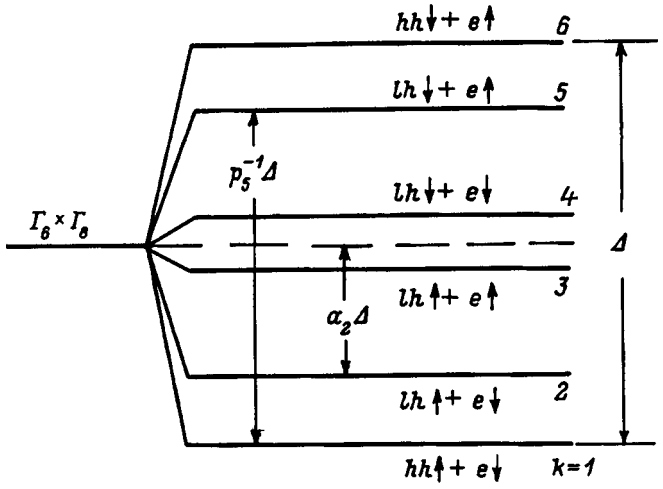

FIG. 1. Diagram of optically active exciton spin sublevels in a cubic CdMnTe-type semimagnetic semiconductor. The levels are split by the exchange field of a magnetic fluctuation. The figure explains the meaning of coefficients a_k and p_k (in this case, a_2 and p_5): they relate the position of the kth sublevel to multiplet center and to the lowest sublevel, respectively. The coefficients are connected through the obvious relation $p_k^{-1}=a_k+1/2$.

characteristic fluctuation magnetization is not large, and the exciton splitting is linear in m (a condition always upheld in real systems), the magnetization can be described conveniently in terms of the splitting Δ induced by it:

$$W(\Delta)\propto\Delta^2\exp(-\Delta^2), \tag{1}$$

where $W(\Delta)$ characterizes the probability to observe in a randomly chosen state an exciton splitting Δ, and Δ is a dimensionless splitting in units of $\langle\Delta\rangle=\Delta(\langle m^2\rangle^{1/2})$. We shall understand here by the exciton splitting the splitting of the extreme sublevels of the exciton spin multiplet (Fig. 1).

The exponential decay of the density of states close to the pump photon energy is characterized by the Urbach parameter U, which we shall likewise measure in units of $\langle\Delta\rangle$. It should be stressed that this bare density of states is assumed to be unperturbed by the exchange fields of fluctuations, and that their effect will be taken into account in our calculations.

The principle underlying the calculations is explained in detail in Ref. 7. Because the local fields are randomly oriented, light of any polarization will excite excitons at each spin sublevel (Fig. 1), but the efficiency of excitation is different and is determined by the pump-light polarization, the actual selection rules, the position of the given sublevel in the multiplet, and the density-of-states function. Excitons excited in upper sublevels will thereafter undergo spin relaxation to the lowest sublevels, with the energy released in the process depending on the number of the excited sublevel and the local splitting, and recombine already from the lowest spin sublevel (we assume the temperature to be small compared to $\langle\Delta\rangle$, i.e., neglect thermal activation of the excitons). Accordingly, the recombining excitons will emit photons with energies lower than that of the pump photon. By contrast, excitons excited at the lowest spin sublevel will emit at the pump frequency, irrespective of the local splitting.

TABLE I. Coefficients a_k, p_k and polarization factors Λ_k^π for the cases of exciton orientation and alignment according to Ref. 6 in cubic semimagnetic semiconductors.

k	a_k	p_k	Λ_k^+	Λ_k^-	$\Lambda_k^\parallel$	$\Lambda_k^\perp$
1	1/2	∞	18	3	12	9
2	7/30	15/4	6	6	4	8
3	1/30	15/7	6	1	4	3
4	−1/30	15/8	1	6	4	3
5	−7/30	15/11	6	6	4	8
6	−1/2	1	3	18	12	9

Note: a_k and p_k were calculated under the assumption that the electronic and hole exchange constants relate as 1:4, and that they have opposite signs. This is valid with good accuracy for the widespread cubic semimagnetic semiconductors.[1] The factors Λ_k^π are relative luminescence intensities in the π polarization geometry with only the kth spin sublevel excited; they take into account the selection rules in angular momentum and the random local-field orientation. Index π takes on the values $(+,-,\parallel,\perp)$, which corresponds to circular polarization (the first pair of symbols) or linear polarization (the second pair) of pump light, with measurement performed in the same polarization (the first and third symbols) or orthogonal polarization (the second and fourth symbols).

Taking into account Eq. (1), the recombination-emission intensity distribution of excitons excited at the kth spin sublevel in local splitting can be written

$$\frac{dI_k^\pi}{d\Delta}\propto\Lambda_k^\pi\Delta^2\exp(-\Delta^2)\exp(a_k\Delta/U). \tag{2}$$

Here Λ_k^π are the polarization factors corresponding to the π polarization geometry of experiment which were calculated in Ref. 7 (see caption to Table I), and the meaning of coefficients a_k is clear from Fig. 1. To obtain the luminescence intensity spectrum, we have to take into account that the energy deficit ε of the emitted photon originating from the transition to the lowest spin sublevel (the spin-flip transition), rather than being equal to the total spin splitting Δ, is only a fraction of Δ which depends on k. By applying the corresponding transformation to compress the distributions (2), $\Delta=p_k\varepsilon$ (the meaning of coefficients p_k is clear from Fig. 1), one can now obtain already the distribution of intensity in ε, i.e., actually the luminescence spectrum itself

$$\frac{dI_k^\pi}{d\varepsilon}\propto\Lambda_k^\pi p_k(p_k\varepsilon)^2\exp[-(p_k\varepsilon)^2]\exp(a_kp_k\varepsilon/U). \tag{3}$$

For the lowest sublevel, p_k goes to infinity (but the intensity remains naturally finite), and the spectrum becomes δ shaped:

$$\frac{dI_1^\pi}{d\varepsilon}\propto\delta(\varepsilon)\Lambda_1^\pi\left\{\frac{1}{8U}+\frac{\sqrt{\pi}}{4}\exp\left(\frac{1}{16U^2}\right)\times\left[1+\Phi\left(\frac{1}{4U}\right)\right]\left(1+\frac{1}{8U^2}\right)\right\}. \tag{4}$$

Here $\delta(x)$ is the delta function, and $\Phi(y)$ is the error integral. As seen from Eqs. (3) and (4), the only parameter of the model is the Urbach parameter U (expressed in units of $\langle\Delta\rangle$). As we shall see later, some of the results obtained in this way depend fairly weakly on this parameter as well.

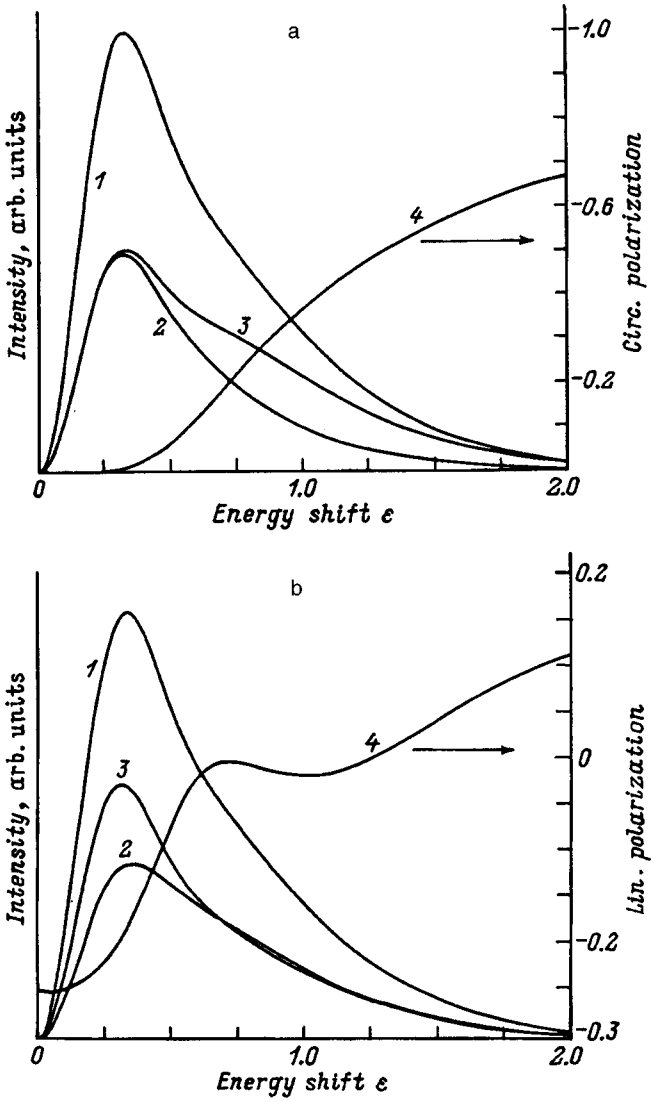

FIG. 2. Exciton-luminescence spin-flip spectra calculated using Eqs. (3) for (a) optical orientation geometry and (b) optical alignment geometry. *1* — total intensity spectrum, *2* and *3* — intensity spectra of the luminescence components polarized (*2*) in the pump-light direction and (3) orthogonal to it, *4* — polarization spectra (difference between spectra *2* and *3* normalized to their sum).

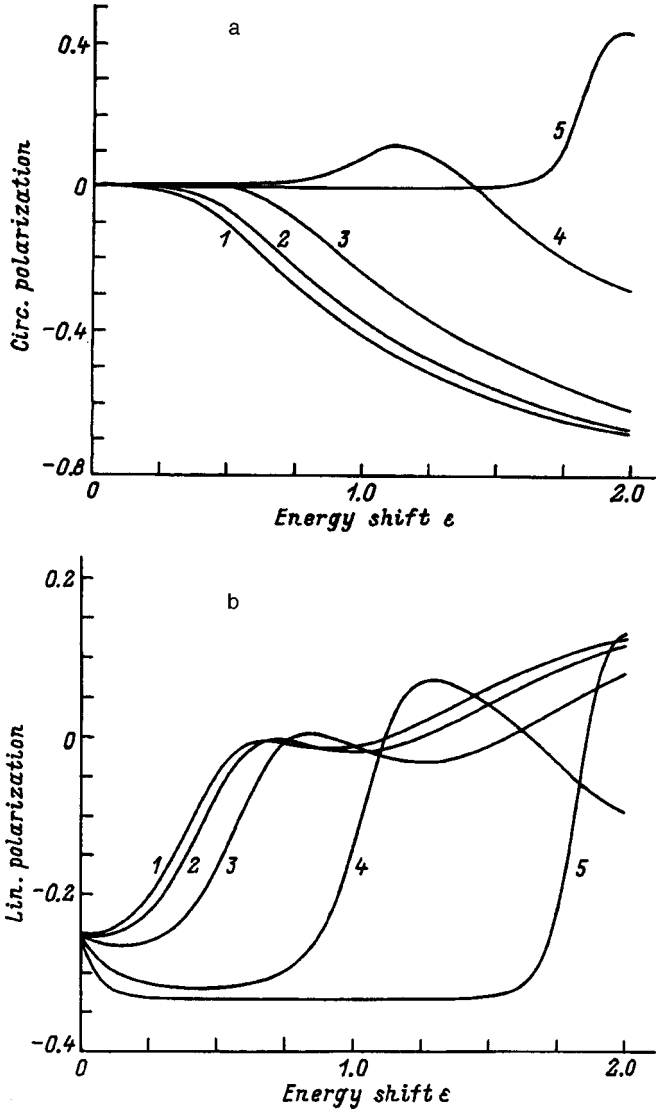

FIG. 3. Luminescence polarization spectra (same as curves *4* in Fig. 2) for different values of the Urbach parameter: (*1*) $U=\infty$, (*2*) 1, (*3*) 0.3, (*4*) 0.1, (*5*) 0.05.

The total emission spectrum is a sum of the δ-shaped burst at $\varepsilon=0$ associated with the excitation of excitons in the lowest spin sublevels (''the resonant line'') and of the flip spectrum itself, which is produced by the other spin sublevels. For zero ε, only the resonant line has a finite intensity, and its polarization depends only on the polarization geometry of the experiment (it is 5/7 for the optical orientation, and 1/7 for the alignment). Now the flip-spectrum polarization depends on U, and it is mostly opposite in sign to that of the pump light and of the resonant line. The polarization integrated over the spectrum depends on U and is confined between zero (for constant density of states, $U\to\infty$) and the resonant-line polarization (for a steep density-of-states function, $U\to 0$).

Figure 2a and 2b presents spin-flip spectra calculated using Eq. (3) for the optical-orientation and alignment geometries for $U=1$, which estimates[6–8] suggest to be a reasonable value. One readily sees that the polarization in the optical-orientation geometry (Fig. 2a) is larger in absolute magnitude than that observed in the conditions of alignment (Fig. 2b), and exhibits a larger asymmetry over the spectrum (recall that for $\varepsilon=0$ the resonant line polarization is positive). Therefore the conditions for observation of orientation in a broadened spectrum of stationary magnetic-polaron luminescence are considerably more favorable than those in the alignment geometry.[7] At the same time it is the alignment flip spectra that exhibit, in contrast to the orientation spectra, an interesting nonmonotonic polarization behavior, which is seen (Fig. 3) to have a nearly universal pattern down to very small values of U (curves *1–3*).

In concluding the discussion of Figs. 2 and 3, consider two points. First, one readily sees that the steeper the spectral course of the density-of-states function, the larger the fraction of luminescence intensity confined to the resonant line, and the weaker the flip-spectrum intensity. Therefore the calculated dependences of type *4* and *5*, corresponding to the

cases where the flip spectra are dominated by the contribution of the second spin sublevel, can hardly be of practical interest. Second, one has to bear in mind that thermal activation of excitons at a finite temperature results in a modification of the flip spectra, which primarily involves states with small local splittings. This should contribute to the spectral region within a few k_BT from the resonant line, and for real fluctuation-induced splittings can bring about a wash-out of the gap between the resonant line and the flip spectrum.

Consider finally the case of uniaxial crystals, superlattices, or quantum wells excited by polarized light along the Z axis. In the presence of strong enough fluctuations, the exciton-state spin structure is here substantially simpler than that in cubic crystals because of the strong anisotropy of the hole g factor in zero external field. The fluctuation-induced exchange fields will split the doublets of optically active heavy-hole excitons. Because all final states here correspond to Z-oriented circular dipoles, no alignment can be expected to occur in this model, although unpolarized flip spectra can be observed under linearly polarized pump light. As for the orientation effect, it should manifest itself in the appearance of a fully polarized resonant line and of a flip spectrum, likewise fully polarized but of the opposite sign. Note that because of the g factor anisotropy only the Z components of the fluctuation magnetization will be significant, and, therefore, for a Gaussian distribution of fluctuations there should be no gap between the resonant line and the flip spectrum, the latter forming a monotonically declining wing of the resonant line. For a constant density of states, this wing will directly reproduce the distribution of the Z component of fluctuation magnetization while, for a decaying density-of-states function, the wing should also decay down to complete disappearance for $U \rightarrow 0$.

3. Let us discuss now the qualitative results of this work as applied to possible experimental observation of exciton spin-flip spectra. The emission spectrum forming under resonant excitation of a localized exciton in the exchange field of a magnetization fluctuation consists of a nonshifted resonant line, partially polarized in the direction of the pump light, and an energy-shifted spin-flip spectrum, polarized predominantly in the opposite direction. Therefore, in appropriate experimental conditions, one should observe the exciton recombination-radiation polarization to reverse its sign in the vicinity of the pump line. In a general case, the degree of polarization of the resonant line is not one; it is particularly small in the alignment geometry, and this can be used to detect penetration of the exciting light into the measurement channel. The shape and polarization of the flip spectra bear information on the distribution of local magnetization fluctuations.

Magnetic polaron formation and processes involving acoustic phonon emission can prevent observation of spin-flip spectra. One can try to suppress the magnetic-polaron shift by choosing properly the system so that the polaron state forms slowly on the exciton-lifetime scale.[12] Another way consists in making time-resolved measurements of the luminescence. Because the spin-relaxation time in semimagnetic semiconductors is typically ~ 1 ps,[13,14] and the polaron formation time ~ 100 ps,[12] the gated time interval should be from 1–2 to 10–20 ps. This makes sense, however, only if the pump pulses are sufficiently short. The characteristic fluctuation-induced splitting (i.e., the unit on the ε scale) was estimated[6–8] as 1–3 meV, so that for a 1-ps pulse its spectral width will be of the order of the spin-flip spectrum width. This would require replacement of the δ function in Eq. (4) with the real pulse shape and convolution with the pulse spectrum in Eq. (3). While the spectrum of a pulse a few tens of ps long may be considered δ shaped, its duration approaches already the polaron formation time. Thus the optimum pulse duration is 5–10 ps.

Processes involving acoustic phonon emission in II–VI solid solutions, both in quasi-resonant excitation and in recombination of localized excitons, are quite frequently capable of competing in efficiency with the corresponding zero-phonon processes.[15] Because such transitions shift the emission spectrum by the same amount (a few meV) from the exciting line as the spin-flip transitions, these processes may become spectrally superimposed. We have no reliable information on comparative efficiency of zero-phonon transitions and transitions involving phonons in semimagnetic solid solutions, and it would be difficult to arrive a priori at a correct conclusion, because the answer to this problem depends on more than one factor. Based on general considerations, one can suggest that in order to suppress nonresonant processes involving acoustic phonons one should choose a material with as weak electron-phonon coupling as possible, and excite states localized within not too small a volume (see Ref. 15). Should a need arise to separate the spin-flip from nonresonant phonon processes, it may be advisable to apply to the sample a weak magnetic field to shift the flip spectrum toward longer wavelengths.

The authors owe sincere thanks to A. N. Reznitskiĭ, V. F. Sapega, A. A. Bugaev, K. V. Kavokin, and I. A. Merkulov for fruitful discussions.

Support of the Russian Fund for Fundamental Research (Grant 96-02-16887) is gratefully acknowledged.

[1] J. A. Gaj, in *Diluted Magnetic Semiconductors*; Eds., J. Furdyna, and J. Kossut (Academic, New York, 1988), p. 275.
[2] Yu. G. Semenov, S. M. Ryabchenko, Fiz. Tekh. Poluprovodn. **17**, 2040 (1983) [Sov. Phys. Semicond. **17**, 1301 (1983)]; S. M. Ryabchenko, Yu. G. Semenov, and O. V. Terletskiĭ, Fiz. Tverd. Tela (Leningrad) **27**, 2901 (1985) [Sov. Phys. Solid State **27**, 1746 (1985)].
[3] D. L. Alov, S. I. Gubarev, and V. B. Timofeev, Zh. Éksp. Teor. Fiz. **84**, 1806 (1983) [Sov. Phys. JETP **57**, 1052 (1983)].
[4] D. Heiman, P. A. Wolff, and J. Warnock, Phys. Rev. B **27**, 4848 (1983).
[5] D. L. Peterson, D. W. Bartholomew, U. Debska, A. K. Ramdas, and S. Rodrigues, Phys. Rev. B **32**, 323 (1985).
[6] J. Warnock, R. N. Kershaw, D. Ridgely, K. Dwight, A. Wold, and R. R. Galazka, J. Lumin. **34**, 25 (1985).
[7] B. P. Zakharchenya, A. V. Kudinov, and Yu. G. Kusraev, Zh. Éksp. Teor. Fiz. **110**, 177 (1996) [JETP **83**, 95 (1996)].
[8] D. R. Yakovlev and K. V. Kavokin, Comments Condens. Matter Phys. **18**, 51 (1996).
[9] S. Oseroff and P. H. Keesom, in *Diluted Magnetic Semiconductors*, Eds. J. Furdyna and J. Kossut (Academic, New York, 1988), p. 73.
[10] B. P. Zakharchenya and Yu. G. Kusraev, JETP Lett. **50**, 225 (1989).
[11] Yu. G. Kusraev and A. V. Kudinov, Fiz. Tverd. Tela (St. Petersburg) **36**, 2088 (1994) [Phys. Solid State **36**, 1140 (1994)].

[12] G. Mackh, W. Ossau, D. R. Yakovlev, A. Waag, G. Landwehr, R. Hellmann, and E. O. Göbel, Phys. Rev. B **49**, 10248 (1994).
[13] H. Krenn, K. Kaltenegger, T. Dietl, J. Spalek, and G. Bauer, Phys. Rev. B **39**, 10918 (1989).
[14] M. R. Freeman, D. D. Awschalom, J. M. Hong, and L. L. Chang, Phys. Rev. Lett. **64**, 2430 (1990).
[15] S. Permogorov and A. Reznitsky, J. Lumin. **52**, 201 (1992).

Translated by G. Skrebtsov

Electric-field and interface effects on the orientation of Jahn–Teller vacancy distortions in semiconductors

N. S. Averkiev, A. A. Gutkin, and S. Yu. Il'inskiĭ

A. F. Ioffe Physicotechnical Institute, Russian Academy of Sciences, 194021 St. Petersburg, Russia
(Submitted June 4, 1998)
Fiz. Tverd. Tela (St. Petersburg) **40**, 2161–2164 (December 1998)

Energy variation of various Jahn–Teller vacancy configurations in thin near-surface layers of a semiconductor is considered. The calculations are made within a model in which each dangling bond near a vacancy is described by the wave function of an electron localized at a defect with a zero-range potential. The Jahn-Teller stabilization energy was assumed to be much smaller than the crystal-field splitting but substantially larger than the energy variations introduced by other perturbations. It is shown that vacancy alignment in semiconductor layers with thickness $\geqslant 100$ Å at liquid-nitrogen temperatures and lower can be most effectively caused by the electric field which can exist in such layers due to a surface-state charge. The direct effect of the interface on both the electronic and nuclear energies of various configurations is weak and can become manifest only in layers less than 10 Å thick at liquid-helium temperature. © *1998 American Institute of Physics.* [S1063-7834(98)00412-2]

Single vacancies and complexes containing them are common defects in semiconductors. These defects may create a number of deep levels in the gap, whose position depends on the actual number of localized carriers. In cubic semiconductors, the initial state of such a deep center can be orbitally degenerate and have a lower symmetry because of the Jahn–Teller effect. Such symmetry distortions were indeed observed in the case of vacancies and vacancy-containing complexes in Si,[1,2] GaAs,[3,4], and some II–VI semiconductors (Ref. 5). Defect distortions were observed to change direction spontaneously even at relatively low temperatures and to become aligned under uniaxial crystal strains,[1,2,6] which destroy the initial equivalence of Jahn-Teller configurations of defects with different distortion orientations. Electric field also disrupts the original crystal symmetry and can give rise to energy differences between the various Jahn–Teller defect configurations caused by interaction of the electric field with the defect dipole moment. Vacancies in diamond and zinc blende semiconductors can have a dipole moment for two reasons. First, a vacancy in state t_2 possesses an initial dipole moment because of the original T_d symmetry of the local environment, and this moment will be affected by the Jahn–Teller effect. Second, even in the case where the initial dipole moment is zero, spatial distortions of the defect induced by the Jahn–Teller effect may create a dipole moment. Because in the first case the magnitude of the dipole moment is determined by the lattice atom separation, and in the second, by the Jahn–Teller vacancy shift, the major contribution to the dipole moment will come from the component associated with the original T_d symmetry of the vacancy, and it is this component that should be considered when analyzing the electric-field effect. This is why the model to be used in calculations should take into account the initial T_d symmetry of the vacancy.

A strong electric field, which appears quite frequently in near-surface space-charge layers in a semiconductor, is generated by electric charges localized in interface states. Vacancies located in these layers are acted upon, besides the electric field, by the interface, which destroys the equivalence of the Jahn–Teller configurations; in particular, the existence of an interface gives rise to mechanical and electrical image forces, whose influence on the nuclear subsystem of Jahn–Teller defects was considered in Ref. 7. An interface, however, acts not only on nuclei but on the carriers trapped by a defect as well. This action is associated with the boundary conditions imposed on the bound-carrier wave function. The purpose of this work is to study the influence of the above phenomena on the energy of vacancy configurations in cubic semiconductors and to estimate the role played by various mechanisms in disrupting their equivalence near the surface.

1. MODEL OF THE VACANCY

For definiteness, we are going to consider a cation vacancy in a III–V semiconductor, and a hole localized at it which interacts with the F_2 mode of local vibrations of an originally tetrahedral quasi-molecule $V_A 4B$ (Fig. 1).

The electronic structure of the defect will be presented in terms of a model[8] in which each dangling bond of a vacancy is described by a wave function φ_i of a zero-radius center[9] located at the atom B_i adjacent to V_A. This means that we can write

$$\varphi_i = \sqrt{\frac{\alpha}{2\pi}}\,\frac{e^{-\alpha r_i}}{r_i} \equiv \sqrt{\frac{\alpha}{2\pi}}\,q(\alpha, r_i). \tag{1}$$

Here r_i is the distance from the electron to atom B_i

$$\alpha = \frac{\sqrt{2m^*/E_0}}{\hbar},$$

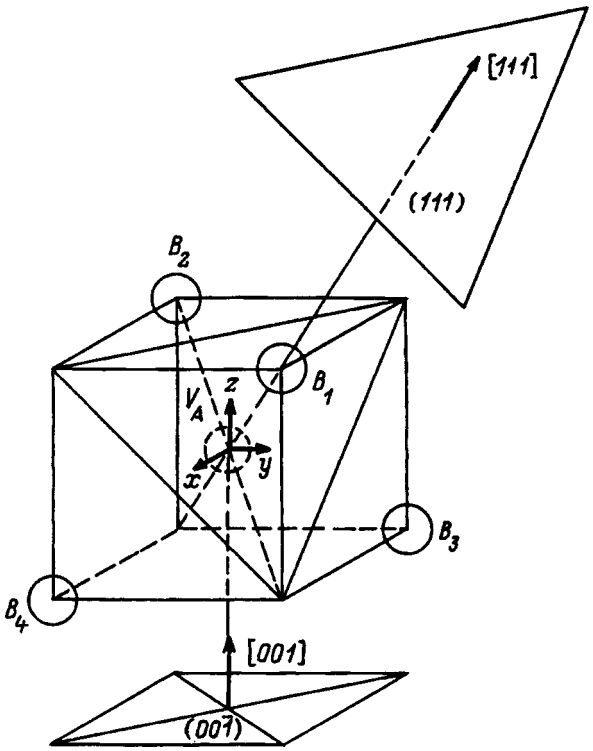

FIG. 1. Position of a V_A4B quasi-molecule relative to the semiconductor-vacuum interfaces.

where E_0 is the energy needed to detach an electron from an isolated dangling bond, and m^* is the effective electron mass. In accordance with the zero-range potential method,[9] the wave function $\psi(\mathbf{r})$ of an electron localized at a vacancy (four dangling bonds) is a linear combination of four functions $q(\kappa,r_i)$ subject to the following boundary conditions

$$\frac{\partial}{\partial r}\ln(r\psi(\mathbf{r}))\big|_{\mathbf{r}\to\mathbf{R}_i}=-\alpha, \quad i=1,2,3,4, \tag{2}$$

where $\mathbf{r}$ and $\mathbf{R}_i$ are the position vectors of the electron and of the ith B_i atom. Because B_i atoms occupy the vertices of a tetrahedron, the wave functions $\psi(\mathbf{r})$ will correspond to the original local tetrahedral symmetry of the vacancy and account for the existence of an electric dipole moment appropriate for a defect of tetrahedral symmetry. On the other hand, using a linear combination of wave functions of type (1) permits an analytical description of the effect on a vacancy of both an electric field and a semiconductor interface.

As follows from Eqs. (1) and (2), the one-electron energy level of the quasi-molecule V_A4B, which is originally fourfold degenerate (according to the number of the B atoms), splits into a singlet, which has the lowest energy, and a triplet. Because localization of one hole at a vacancy means that the dangling bonds accommodate seven electrons, the hole ground state is a triplet (t_2 state). As already mentioned, the hole interacts in this state with F_2 vibrations of the quasi-molecule, and this gives rise to four quasi-molecule configurations with C_{3v} symmetry. In the absence of anisotropic factors, these configurations in the bulk of the crystal are equivalent, i.e. their energies W_j $(j=1,2,3,4)$ are the same. For the sake of simplicity, we shall assume the Jahn-Teller stabilization energy E_{JT} to be much less than the splitting between the singlet and the triplet

$$E_{JT}\ll|E_{t_2}-E_{a_1}|=\Delta. \tag{3}$$

In this case the wave functions of the hole ϕ_j in each of the equivalent configurations j $(j=1,2,3,4)$ are derived only from the t_2-state wave functions

$$\begin{aligned}
\phi_1&=\frac{1}{\sqrt{3}}(\psi_{1t}+\psi_{2t}+\psi_{3t}),\\
\phi_2&=\frac{1}{\sqrt{3}}(-\psi_{1t}-\psi_{2t}+\psi_{3t}),\\
\phi_3&=\frac{1}{\sqrt{3}}(-\psi_{1t}+\psi_{2t}-\psi_{3t}),\\
\phi_4&=\frac{1}{\sqrt{3}}(\psi_{1t}-\psi_{2t}-\psi_{3t}),
\end{aligned} \tag{4}$$

where $\psi_{1t},\psi_{2t},\psi_{3t}$ are the wave functions of the hole t_2 state, which satisfy conditions (2). As follows from Eqs. (2), these functions can be written

$$\begin{aligned}
\phi_{3t}&=C[q(\kappa,r_1)+q(\kappa,r_2)-q(\kappa,r_3)-q(\kappa,r_4)] &&\sim Z,\\
\phi_{2t}&=C[q(\kappa,r_1)-q(\kappa,r_2)+q(\kappa,r_3)-q(\kappa,r_4)] &&\sim Y,\\
\phi_{1t}&=C[q(\kappa,r_1)-q(\kappa,r_2)-q(\kappa,r_3)+q(\kappa,r_4)] &&\sim X.
\end{aligned} \tag{5}$$

Here C is a normalization constant, and the positive parameter κ is found from the relation

$$\kappa=\alpha-\frac{e^{\kappa R_0}}{R_0}, \tag{6}$$

where R_0 is the distance between the B atoms.

2. EFFECT OF ELECTRIC FIELD

Because for real electric fields, the splitting of the original vacancy t_2 state is substantially smaller than Δ, the matrix elements of the dipole moment should be calculated using functions (5). In this way one obtains the following expressions for the Hamiltonian describing the interaction of the system under study (a vacancy binding a hole with a charge q) with electric field $\mathbf{E}$:

$$H^{\mathbf{E}}_{[111]}=-\frac{q}{2\sqrt{6}}ER_0\begin{pmatrix}0&1&1\\1&0&1\\1&1&0\end{pmatrix} \tag{7}$$

in the case where $\mathbf{E}$ is oriented along [111], and

$$H^{\mathbf{E}}_{[001]}=-\frac{q}{4\sqrt{2}}ER_0\begin{pmatrix}0&1&0\\1&0&0\\0&0&0\end{pmatrix}, \tag{8}$$

for the orientation of $\mathbf{E}$ along the [001] direction. If the vacancy is subjected to a strong Jahn–Teller effect exceeding

the action of the electric field, the change in the total energies ΔW_i of the equivalent configurations of the V_B4A molecule can be calculated similar to the way this was done[8] to take into account the effect of a donor on this quasimolecule. In an electric field directed along [111], the energy of configuration 1 with a three-fold axis aligned in this direction will change by

$$\Delta W_1 = -\frac{qER_0}{\sqrt{6}}. \tag{9}$$

The energies of the other three configurations will change by the same amount

$$\Delta W_{2,3,4} = \frac{qER_0}{3\sqrt{6}}. \tag{10}$$

For an electric field aligned with [001]

$$\Delta W_1 = \Delta W_2 = -\Delta W_3 = -\Delta W_4 = -\frac{qER_0}{6\sqrt{2}}. \tag{11}$$

3. EFFECT OF THE INTERFACE

We shall assume the potential barrier at the interface to be infinitely high, so that the carrier wave function will vanish there. The resulting lowering of the wave function symmetry brings about a splitting of the original t_2 state of the vacancy-bound hole even without the Jahn–Teller effect. The magnitude of this splitting depends both on the distance from the vacancy to the surface and on the orientation of this surface relative to the crystallographic axes.

Using symmetry considerations one can show that the Hamiltonians describing this splitting in the basis functions (5), in the cases where the interfaces are parallel to the {111} or {001} planes, can be written, respectively,

$$H^s_{\{111\}} = -\frac{\delta_0}{3}\begin{pmatrix} 0 & 1 & 1 \\ 1 & 0 & 1 \\ 1 & 1 & 0 \end{pmatrix}, \tag{12}$$

$$H^s_{\{001\}} = -\frac{1}{6}\begin{pmatrix} \delta_1+2\delta_2 & 3\delta_1 & 0 \\ 3\delta_1 & \delta_1+2\delta_2 & 0 \\ 0 & 0 & -2(\delta_1+2\delta_2) \end{pmatrix}. \tag{13}$$

The quantities δ_k can be calculated in terms of the zero-range potential model, within which the vanishing of a wave function at the interface is satisfied if this function is chosen in the form of a linear combination of functions $q(\kappa,r_i) - q'(\kappa,r_i)$, where $q'(\kappa,r_i)$ $(i=1,2,3,4)$ corresponds to a dangling bond of the mirror reflection of atom B_i in the interface plane [see Eq. (1)]. Using the basis (5) here means that the interface-induced change in the level positions is substantially smaller than Δ, i.e., that the distance from the vacancy to the interface (R) exceeds by far the smallest separation between atoms B:

$$R \gg R_0. \tag{14}$$

It can be shown (see, e.g., Refs. 8 and 9) that the zero-range potential model allows the existence of a bound t_2 state provided

$$\alpha R_0 > 1. \tag{15}$$

On the other hand, the model under study assumes for the sake of simplicity that the crystal-field splitting Δ exceeds all splittings of the t_2 state. Because Δ decreases exponentially with increasing αR_0 (Refs. 8,9), inequality (3) requires that αR_0 is not too large. If conditions (14) and (15) are upheld, the expressions for δ_k for the interfaces shown in Fig. 1 can be written

$$\delta_0 = -\frac{E_0}{8}e^{-2\alpha R}\frac{R_0}{R}\left[6\sqrt{3}(\sqrt{2}-1) \times\left(1-\frac{e^{-\alpha R_0}}{\alpha R_0}\right)-7e^{-\alpha R_0}\right], \tag{16}$$

$$\delta_1 = -\frac{E_0}{2}e^{-2\alpha R}\left(\frac{R_0}{R}\right)^2\left(1-\frac{e^{-\alpha R_0}}{\alpha R_0}\right)\sinh\frac{\alpha R_0}{\sqrt{2}}, \tag{17}$$

$$\delta_2 = -2E_0\frac{e^{-2\alpha R}}{\alpha R}\left(1-\frac{e^{-\alpha R_0}}{\alpha R_0}\right)\left(\cosh\frac{\alpha R_0}{\sqrt{2}}-1\right). \tag{18}$$

We readily see that matrices (12) and (13) are similar to matrices (7) and (8). Therefore the energy splitting of Jahn-Teller configurations described by Hamiltonians (12) and (13) in first order of perturbation theory in $H^s_{\{111\}}$ and $H^s_{\{001\}}$ will be proportional to δ_0 for $H^s_{\{111\}}$ and to δ_1 for $H^s_{\{001\}}$. The corresponding expressions for ΔW_j for the (111) interface are obtained from Eqs. (9) and (10) by replacing $-9ER_0/\sqrt{6}$ with $2\delta_0/3$, and for the (001) interface, from Eq. (11) by substituting $-\delta_1$ for $qER_0/2\sqrt{2}$.

Let us estimate and compare the differences in energy between various vacancy configurations associated with the presence of an electric field and an interface in some real cases. We shall assume for definiteness that $\alpha R_0 = 2$, which means, for instance, for GaAs that the energy required to detach an electron from one of the vacancy bonds $\sim$1 eV ($R_0 = 2.45$ Å). According to Eqs. (9)–(11), the energy difference between the originally equivalent configurations induced by an electric field $E = 10^5$ V/cm is 3–1 meV. This means that such a field can produce noticeable alignment of vacancy distortions at temperatures of 77 K and lower. The field strength $\sim 10^5$ V/cm appears realistic enough for *n*-type gallium arsenide, where surface-band warping due to interface states $\sim$1 eV. For an electron concentration in this material $\sim 10^{18}$ cm^{-3} the width of the space-charge region $\sim$400 Å and the mean field $\sim 2\times 10^5$ V/cm, so that fields above 10^5 V/cm can exist in layers $\sim$300 Å wide.

On the other hand, according to Eqs. (16) and (17), for $\alpha R_0 = 2$ the quantities δ and δ_1 do not exceed 0.1 meV even at distances from the surface $R = 2R_0$, and they decrease exponentially with increasing R. Therefore the interface-induced change in the wave functions of a localized carrier should not affect noticeably the energy of different configurations in near-surface layers above 5 Å in thickness.

Besides, as already mentioned, the interface influences also the nuclear subsystem of a Jahn–Teller quasi-molecule changing the configuration energy thereby. This change is connected primarily with a change in the elastic constants of the defect. Estimation of the energy difference between various defect configurations based on the results of Ref. 7 shows that at a distance of 10 Å it does not exceed 0.1 meV.

The above permits a conclusion that an alignment of Jahn–Teller–induced vacancy distortions in near-surface layers of a semiconductor with thickness of the order of 100 Å and larger can become noticeable only in sufficiently strong electric fields. In the absence of such a field, the interface can affect directly the orientation of distortions only in layers not thicker than 10 Å and at temperatures ~1 K or lower.

Partial support of the Russian Fund for Fundamental Research (Grants 96-15-96955 and 98-02-18327) is gratefully acknowledged.

[1] G. D. Watkins, in *Deep Centers in Semiconductors*, edited by S. T. Pantelides (Gordon and Breach, New York, 1986), p. 147.
[2] E. L. Elkin and G. D. Watkins, Phys. Rev. **174**, 881 (1968).
[3] Y. Q. Jia, H. J. von Bardeleben, D. Stievenard, and C. Delerue, Phys. Rev. B **45**, 1645 (1992).
[4] N. S. Averkiev, A. A. Gutkin, M. A. Reshchikov, and V. E. Sedov, Fiz. Tekh. Poluprovodn. **30**, 1123 (1996) [Semiconductors **30**, 595 (1996)].
[5] D. Y. Jeon, H. P. Gislason, and G. D. Watkins, Phys. Rev. B **48**, 7872 (1993).
[6] N. S. Averkiev, A. A. Gutkin, E. B. Osipov, M. A. Reshchikov, and V. R. Sosnovskiĭ, Fiz. Tekh. Poluprovodn. **26**, 1269 (1992) [Sov. Phys. Semicond. **26**, 708 (1992)].
[7] V. S. Vikhnin and N. S. Averkiev, Fiz. Tverd. Tela (St. Petersburg) **36**, 1480 (1994) [Phys. Solid State **36**, 810 (1994)].
[8] N. S. Averkiev, A. A. Gutkin, S. Yu. Il'inskii, M. A. Reshchikov, and V. E. Sedov, Z. Phys. Chem. (Munich) **200**, 209 (1997).
[9] Yu. N. Demkov and V. N. Ostrovskiĭ, *Zero-Range Potential Method in Atomic Physics* [in Russian] (LGU, Leningrad, 1975), 240 pp.

Translated by G. Skrebtsov

Effect of intercalation by silver on the charge-density-wave state in $TiSe_2$

L. S. Krasavin, A. N. Titov, and V. M. Antropov

Ural State University, 620083 Ekaterinburg, Russia
(Submitted April 23, 1998; resubmitted June 23, 1998)
Fiz. Tverd. Tela (St. Petersburg) **40**, 2165–2167 (December 1998)

The temperature dependence of electrical conductivity σ (77–300 K) and magnetic susceptibility χ (2–300 K) of Ag_xTiSe_2 in the $Ag_{1/4}TiSe_2$ phase has been studied in order to determine the possibility of preserving the charge-density-wave state in silver-intercalated $TiSe_2$. The behavior of χ and σ in this phase is compared with that of the starting compound $TiSe_2$.
 [S1063-7834(98)00512-7]

Titanium diselenide is the only Group-IV transition-metal dichalcogenide exhibiting a commensurate charge-density-wave (CDW) state.[1] This state sets in when cooled to 202 K and manifests itself as a $2a_0\times 2a_0\times 2c_0$ superstructure produced by periodic in-plane titanium-atom displacements in the Se–Ti–Se sandwich. The transition is accompanied by a diffuse resistive anomaly in the temperature dependence of conductivity[1,2] and a drop of the Pauli contribution[3] to magnetic susceptibility. The CDW in $TiSe_2$ is associated with electron-hole pairing,[4,5] which requires balance of free electrons in the conduction band with holes in the valence band. Extensive studies of the effect of doping on the CDW state showed that any change in composition affecting the balance of free electrons and holes in this semimetallic material (intercalation, substitution) destroys the CDW state at impurity concentrations of a few percent.[1,2,6,7] This observation is traditionally assigned to the extremely high sensitivity of the transition to the Fermi surface shape.

On the other hand, it has been established recently that many metals intercalated in $TiSe_2$ donate their electrons not to the conduction band but rather to a band of localized states, which apparently appear in hybridization of the titanium d_2^2 orbital with valence states of the intercalant. Among such compounds are Ag_xTiSe_2,[8] Fe_xTiSe_2,[9] Co_xTiSe_2,[10] and probably Ni_xTiSe_2 (Ref. 11). Obviously enough, such localized electrons may leave the band carrier balance unchanged, but random impurity distribution can suppress regular lattice distortions (Ref. 12). At the same time all the above compounds exhibit ordering of impurity atoms at $x=0.25$ (x is the stoichiometric index in the formula M_xTiSe_2) into the $2a_0\times 2a_0\times 2c_0$ superstructure for M=Fe, Co, Ni (Ref. 11) and into the $2a_0\times 2a_0\times c_0$ superstructure for M=Ag (Ref. 13), which practically coincide with the superstructure produced by periodic displacements of titanium atoms in the presence of a CDW. It appeared of interest to study the possibility of preserving the CDW state in such materials.

The coincidence of the superstructure formed in impurity atom ordering with the one produced by periodic titanium atom displacements makes detection of the CDW state by diffraction methods difficult. Therefore the most suitable experimental method for this purpose appears to be measurement of the temperature dependences of the transport properties and of magnetic susceptibility. Such measurements were previously made in the Co_xTiSe_2 system,[10] where a

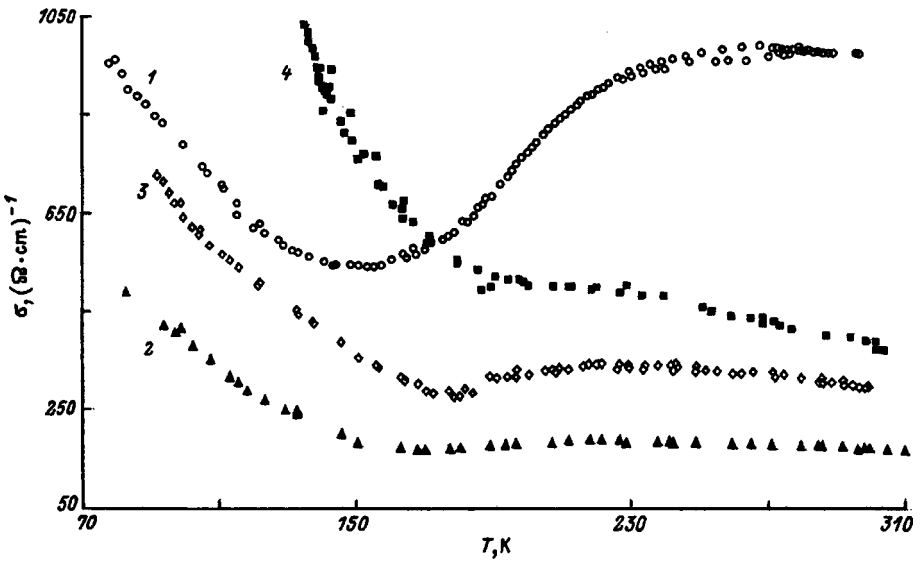

FIG. 1. Temperature dependence of the electrical conductivity of (*1*) starting compound $TiSe_2$ and (*2–4*) Ag_xTiSe_2. x and T_c(K): *1* — 0 and 202, *2* — 0.244 and ≈196, *3* — 0.256 and ≈201, and *4* — 0.265 and ≈208.

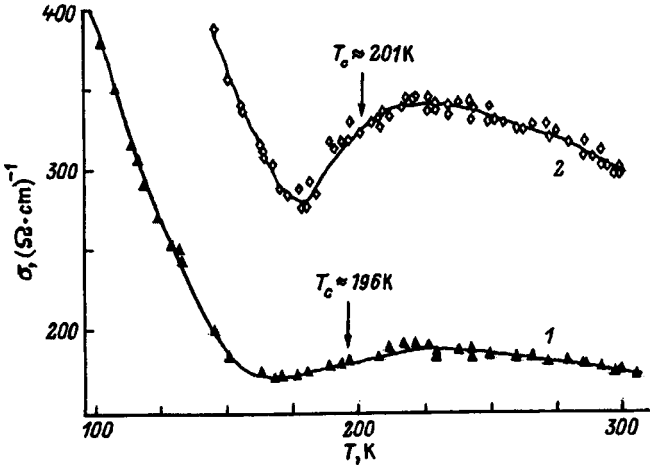

FIG. 2. Temperature dependence of the electrical conductivity of Ag_xTiSe_2. (*1*) $x=0.244$ and (*2*) $x=0.256$. One can see on this scale a shift of the CDW transition temperature T_c.

broad maximum in the temperature dependence of electrical conductivity was found at a temperature of about 300 K. The nature of the temperature dependence of conductivity depended only weakly on intercalant content, which was interpreted as an argument for the formation of polarons bound to Ti–Co–Ti centers. Magnetic susceptibility measurements do not reveal any decrease in the density of states at Fermi level at the temperature corresponding to the conductivity minimum, which should be observed in the case of onset of a CDW state. A similar situation was found to exist for the Fe_xTiSe_2 system.[14,15] Note, however, that intercalation gives rise to a substantial distortion of the host lattice in these materials, namely, parameter c_0 decreases, and parameter a_0 increases with increasing x, which obviously causes deformation of the Brillouin zone and of the Fermi surface.

In contrast to these materials, Ag_xTiSe_2 exhibits within the $Ag_{1/4}TiSe_2$ phase (the closest to the starting $TiSe_2$ compound) an extremely weak dependence of lattice parameters on the intercalant content.[13] In connection with this, we measured the electrical conductivity (within the 77–300 K range) and magnetic susceptibility (2–300 K) of Ag_xTiSe_2 in the

TABLE I. Dependence of $TiSe_2$ lattice parameters on silver content.

	Ag_xTiSe_2		Fe_xTiSe_2 (Ref. 11)		Co_xTiSe_2 (Ref. 11)	
x	a_0, Å	c_0, Å	a_0, Å	c_0, Å	a_0, Å	c_0, Å
0	3.5419	6.0095				
0.250	3.5352	6.0041	3.574	5.985	3.545	5.880
0.252	3.5397	6.0098				
0.260	3.5387	6.0091				
0.267	3.5373	6.0087				

$Ag_{1/4}TiSe_2$ phase in order to study the possibility of preserving the CDW state under the above conditions.

The starting material $Ag_{0.244}TiSe_2$ intended for sample preparation was obtained in the usual way from elements in an ampoule. The silver content was varied and checked by amperometric titration. Sample characterization and measurement of the crystal-lattice parameters were carried out on a DRON-3M diffractometer (Cu $K\alpha$ radiation, a graphite monochromator). The electrical conductivity was measured by the four-probe technique. The sample to be studied was maintained at each temperature until the equilibrium obtained. The methods used for sample preparation and characterization and for conductivity measurements are described in detail elsewhere.[8,13] Table I summarizes the results obtained in the study of the concentration dependence of the $Ag_{1/4}TiSe_2$-phase lattice parameters, together with the parameters of the compounds obtained by cobalt and iron intercalation. One readily sees that the parameters of the $TiSe_2$ host lattice do not depend on silver content within experimental error, whereas intercalation of cobalt and iron substantially deforms the lattice. Typical temperature dependences of the electrical conductivity are presented in Figs. 1 and 2. At T_c of about 200 K one can see a resistive anomaly similar to the one accompanying CDW formation in $TiSe_2$. The fact that the Pauli magnetic susceptibility measured in the high-temperature region is the same in the starting and intercalated $TiSe_2$ (Fig. 3) indicates preservation of the free-carrier concentration in accordance with the above conjecture that the electrons introduced in intercalation become localized. The feature in the $\chi(T)$ relation assigned to the

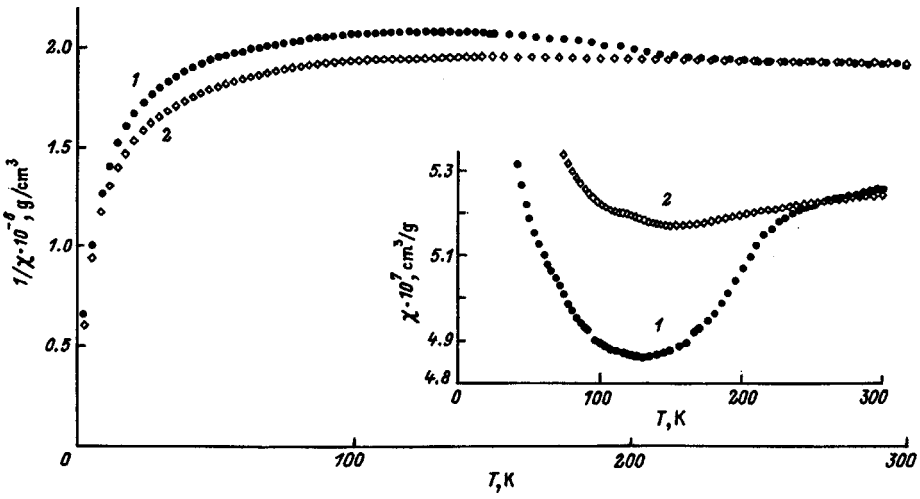

FIG. 3. Temperature dependence of inverse magnetic susceptibility (after subtraction of the diamagnetic contribution $\chi_d \approx -4.86\times10^{-7}$ cm^3/g) of (*1*) starting compound $TiSe_2$ and (*2*) $Ag_{0.256}TiSe_2$. The inset shows on an enlarged scale the feature in the temperature dependences of magnetic susceptibility for the same compounds.

decrease in the density of states at Fermi level because of the opening of a pseudogap is retained (see inset to Fig. 3). Thus the closeness of the transition temperatures and the coincidence of the electrical conductivity and susceptibility in temperature dependence with those observed in $TiSe_2$ suggest that the transition occurring in Ag_xTiSe_2 is associated with formation of a CDW state.

The resistive anomaly in Ag_xTiSe_2 is most clearly pronounced in the $x=0.256$ composition (Fig. 2). According to Ref. 13, this composition is stoichiometric in the $Ag_{1/4}TiSe_2$ phase and exhibits the strongest ordering of silver atoms inside the van der Waals gaps, thus corresponding to a minimum in the concentration dependence of entropy for the intercalant subsystem. This gives us grounds to relate the weakening of the resistive anomaly observed to occur with deviation from stoichiometry to suppression of the commensurate CDW by the random defect potential on the silver sublattice. The general weakening of the amplitude of the feature in the conductivity and susceptibility of Ag_xTiSe_2 compared with the starting $TiSe_2$ can also be attributed to the effect of the relatively large amount of defects on the intercalant sublattice. The ratio of the density of states at the Fermi level, derived from the Pauli contribution to magnetic susceptibility in normal state, to that of the CDW state is 1.014 for $Ag_{0.256}TiSe_2$ against 1.082 for $TiSe_2$.

The Seebeck coefficient in the $Ag_{1/4}TiSe_2$ phase demonstrates the change in the dominant type of carriers from *n* to *p* under heating.[8] The compensation temperature depends on silver content and increases with increasing x. A similar dependence on x of the minimum in the $\sigma(T)$ relation can be seen in Fig. 1, which we believe to argue for electron-hole pairing being the reason for formation of charge-density waves.

The authors express their sincere thanks to A. V. Korolev (Institute of Metal Physics, UB RAS) for assistance in magnetic experiments.

Support of the Russian Fund for Fundamental Research (Grant 97-03-33615a) and of the Ministry of Education of the Russian Federation (Grant 97-0-7.1-169) is gratefully acknowledged.

[1] R. H. Friend and A. D. Yoffe, Adv. Phys. **36**, 1 (1987).
[2] F. J. DiSalvo, D. E. Moncton, and J. W. Waszczak, Phys. Rev. B **14**, 4321 (1976).
[3] D. R. P. Guy, R. H. Friend, M. R. Harrison, D. C. Johnson, and M. J. Sienko, J. Phys. C **15**, L1245, L1231 (1982).
[4] J. A. Wilson, Solid State Commun. **22**, 551 (1977).
[5] J. A. Wilson and S. Mahajan, Commun. Phys. **2**, 23 (1977).
[6] F. Levy, H. P. Vaterlaus, and H. Berger, Physica B **105**, 151 (1981).
[7] F. J. DiSalvo and J. V. Waszczak, Phys. Rev. B **17**, 3801 (1978).
[8] V. M. Antropov, A. N. Titov, and L. S. Krasavin, Fiz. Tverd. Tela (St. Petersburg) **38**, 1288 (1996) [Phys. Solid State **38**, 713 (1996)].
[9] A. N. Titov, Fiz. Met. Metalloved. **81**, 75 (1996).
[10] V. G. Pleshchyov, A. N. Titov, and A. V. Kuranov, Fiz. Tverd. Tela (St. Petersburg) **39**, 1618 (1997) [Phys. Solid State **39**, 1442 (1997)].
[11] Y. Arnaud, M. Chevreton, A. Ahouandjinou, M. Danot, and J. Rouxel, J. Solid State Chem. **18**, 9 (1976).
[12] F. J. DiSalvo and T. M. Rice, Phys. Today **32**, 32 (1979).
[13] A. N. Titov and S. G. Titova, Fiz. Tverd. Tela (St. Petersburg) **37**, 567 (1995) [Phys. Solid State **37**, 310 (1995)].
[14] M. A. Buhannic, P. Colombet, M. Danot, and G. Calvarin, J. Solid State Chem. **69**, 280 (1987).
[15] D. R. Huntley, M. J. Sienko, and K. Hiebel, J. Solid State Chem. **52**, 233 (1974).

Translated by G. Skrebtsov

Determining the lattice parameter and the single-electron model potential of the compound CdS by means of the soft x-ray absorption spectra

Yu. F. Migal', A. A. Lavrent'ev, B. V. Gabrel'yan, and I. Ya. Nikiforov

Don State Technical University, 344010 Rostov-on-Don, Russia
(Submitted February 18, 1998)
Fiz. Tverd. Tela (St. Petersburg) **40**, 2168–2171 (December 1998)

The method of determining the structure parameters of multiatomic systems, using the spectra of soft x rays (XANES) proposed earlier, is extended to the case of nonmetallic crystal bodies. This method is used to determine the lattice parameter and the empirical muffin-tin potential from the positions of maxima of single-electron origin in the sulfur *K* spectrum in the compound CdS. © *1998 American Institute of Physics.* [S1063-7834(98)00612-1]

Pronounced maxima in soft x-ray absorption spectra (XANES) usually correspond to a transition of a photoelectron from the ground state, localized inside the absorbing atom, to unfilled discrete or quasi-discrete single-electron states belonging to the entire multiatomic system. The main characteristics of these maxima (the energies and widths) strongly depend on the relative location of the atoms, the presence and nature of the defects, etc. For this reason, an analysis of the features in XANES can be used to obtain information on the structure and physical properties of molecules and solids. This method could be especially useful in studying disordered systems (glasses, alloys, molecules adsorbed on the surface of solids, etc.), since conventional diffraction-based methods of structural analysis are not very convenient for such systems.

Systems began to be developed in Refs. 1–3 to make it possible to extract from XANES information on the geometrical parameters and single-electron potential of multiatomic objects. One is actually dealing with a method of solving the inverse problem in the theory of the multicenter resonance states that manifest themselves in XANES. The resulting system was used to analyze the spectra of the N_2, SO_2, NO_2, and CH_3NO_2 molecules and the NO_2 complex in the compound $NaNO_2$. The internuclear distances were determined in this case to within 1%, while the valence angles were determined to within 3%. The method was also used to investigate the adsorption of the O_2 molecule on a Cu (100) surface.[4]

The goal of this paper is to extend the method to the case of crystalline nonmetallic structures. The compound CdS, whose geometrical parameters are known, was chosen as a test object. The general formalism is first briefly explained, and it is then used to obtain the crystal lattice parameter and the model single-electron potential.

1. SOLVING THE INVERSE PROBLEM OF XANES THEORY

To simulate the single-electron quasi-stationary states (shape resonances) in a multiatomic system, we shall use the muffin-tin (MT) potential, whose applicability for this kind of problem has long since been proven. It is convenient to define the main characteristics of the resonance states (the energies and lifetimes) by means of the poles of the *S* matrix in the complex energy plane. It is well known that the real coordinate of the pole corresponds to the energy E of the state, while the imaginary part determines its lifetime τ (see, for example, Ref. 5). These values can be found from experiment with a comparatively small error (this mainly refers to the energies and to a lesser extent to the lifetime), and their most important use is to interpret the information contained in the spectra.

The equation for the poles of the *S* matrix in the MT approximation was obtained in Ref. 6 and has the form

$$\det\Big\|[1+i\cot\delta_l^{(j)}]\delta_{jj'}\delta_{LL'} + \sum_{L''} H_{LL'L''}^{j,j'} h_{l''}^{+}(k|\mathbf{r}_j-\mathbf{r}_{j'}|)\Big\| = 0, \tag{1}$$

where $k=(E)^{1/2}$, $\mathbf{r}_j$ is the radius vector of the jth nucleus, $\delta_l^{(j)}$ is the phase shift at the jth atomic sphere, and $H_{LL'L''}^{j,j'}$ are the real structural constants. In terms of the method, the poles S_i obtained by means of Eq. (1) for the model with some chosen set of parameters are compared with the experimental values of $E_i - i\Gamma_i/2$, where E_i is the energy of the ith maximum and Γ_i is its half-width, and the set of parameters is then varied until the functional $\Phi=\Sigma_i\{S_i-(E_i-i\Gamma_i/2)\}^2$ is minimized.

The geometrical parameters (the internuclear distance and the bond angles) are chosen as variable parameters in the method, along with the parameters of the MT potential. We assume that this potential inside the atomic spheres has the form

$$V(r)=V_0(r)+\sum_n b_n r^n \quad (n=0,1,\ldots), \tag{2}$$

with a given initial potential $V_0(r)$ of the atomic or MT type. The coefficients b_n are variable parameters.

The total number of the variable quantities must not exceed the number of experimental characteristics E_i and Γ_i. Otherwise the problem becomes ill-conditioned and can only be solved by resorting to additional information (see, for example, Refs. 3 and 7). It follows from this that, for a small number of experimental quantities, the number of variable

coefficients b_n must also be small. It was shown in previous papers that, to reproduce the main characteristics of shape resonances, it is sufficient to have a model in which the energy and the mean radii of the valence states of the individual atoms of the system are correctly reproduced. In particular, for an atom with m valence states, it is necessary in general to have $2m$ parameters of the potential available. However, if the shape of the initial intra-atomic potential V_0 is chosen approximately correctly, the number of parameters can be substantially reduced (the smaller the size of the atom, the fewer coefficients are required). In such a situation, it can be expected that the available volume of experimental information will be sufficient to solve the problems that need to be solved.

2. RESULTS OF THE CALCULATIONS AND DISCUSSION

Let us consider the K absorption spectrum of sulfur in CdS (Fig. 1a).[8] The origin of the energy readings on the figure is chosen where the absorption coefficient rises sharply. In the 0–1 Ry region close to the absorption threshold, there is a group of maxima, some of which presumably correspond to transitions to states with a single-electron origin. Our problem is to choose these states and, by using the characteristics of these states, to determine the crystal lattice parameter and the model MT potential of the compound.

At the first stage, the density of p states inside the MT sphere of the absorbing sulfur atom is calculated for clusters of various sizes, containing as many as eight coordination spheres (Figs. 1b–1d show the data for small clusters). The MT potential from program FEFF7 was used in this case[9] and was taken as the starting potential in what follows. This potential contains three different atomic potentials: that of the absorbing sulfur atom (V_0^{S+}), that of the remaining (nonabsorbing) sulfur atoms (V_0^{S}), and that of the cadmium atoms (V_0^{Cd}). The internuclear distance in the initial calculation is taken to be equal to the value known for CdS, $R_{S\text{-}Cs}=2.53$ Å.[10] As can be seen from Fig. 1, all clusters except the smallest are characterized by the presence of three groups of states, the positions of whose centers of gravity are virtually unchanged as the cluster size increases. Based on this observation, one can restrict oneself in the subsequent computations to a comparatively small cluster, containing three coordination spheres with a total of 29 atoms; one can then determine the poles of the S matrix for this cluster and use them to optimize the parameters of the model system.

The filling of the states of the system by electrons was analyzed at the same stage. It turned out that the boundary between filled and unfilled states lies close to $E=0$, and thus all the states shown in Fig. 1 are free and must show up in the K absorption spectrum of sulfur.

A comparison of the experimental curve with the distributions of p states in the model makes it possible to assume that the four maxima in the spectrum that appear in the 0–1-Ry region correspond to transitions to single-electron states. The energies of these states equal 0.15, 0.39, 0.63, and 0.92 Ry. The main contribution to the first three states comes from the s and p states of cadmium, and the fourth is caused by the presence of a weakly expressed d resonance in the MT

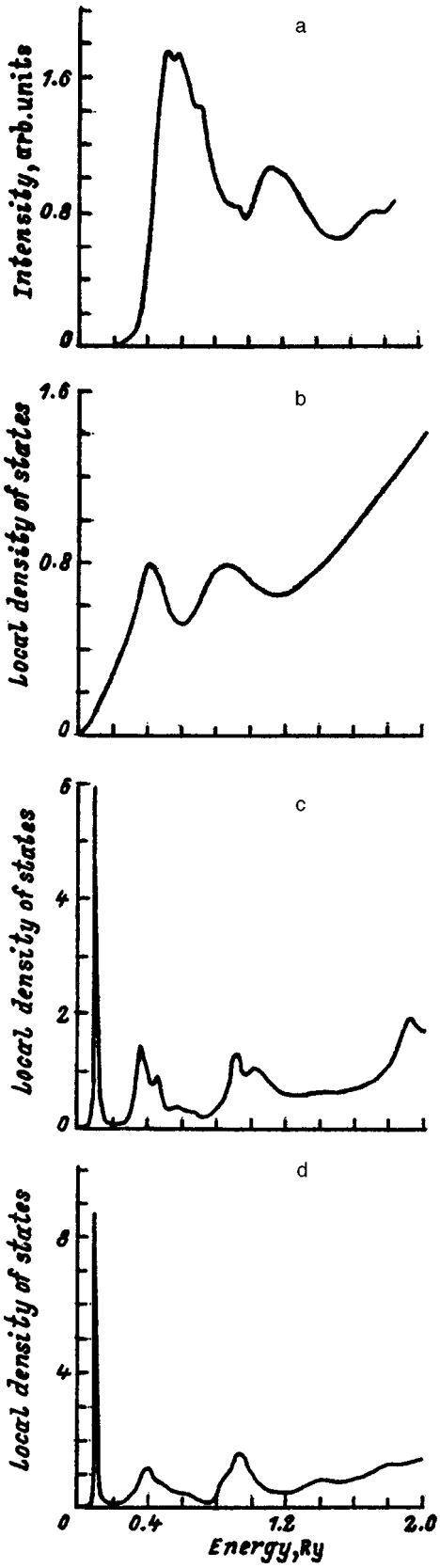

FIG. 1. The K absorption spectrum of sulfur in CdS (a) and local densities of p states inside the MT sphere of an absorbing atom in the case of a model cluster with one (b), two (c), and three (d) coordination spheres.

potential of the sulfur atom. The peak with energy 0.23 Ry cannot be identified in such an approach and evidently is not associated with single-electron transitions.

The following poles of the S matrix correspond to the maxima of single-electron origin in the case of a 29-atom cluster: $0.100-i0.0036$, $0.384-i0.047$, $0.627-i0.111$, and $0.911-i0.060$. The real parts of these poles are obviously rather close to the energies of the experimental peaks. The energy of the first peak, for which the difference between the experimental and calculated values is 0.05 Ry, is an exception.

For the best agreement of calculation with experiment, the parameters of the model must be optimized. To do this, it is first necessary to choose a set of experimental quantities to which the results of the calculation will be adjusted and then to choose a set of variable parameters by means of which this adjustment will be carried out. The set of experimental quantities definitely should include the energies E_i of the four peaks of single-electron origin. The half-widths Γ_i of these peaks, however, cannot be determined with sufficient precision in this experiment. The problem arises mainly because there is a contribution to the experimental values of Γ_i not only from the decay process of the state when an electron escapes to infinity, which is taken into account in the model, but also from many factors that are neglected in the model (the vibrational structure of the spectrum, instrumental distortions, the decay of the resonance state due to the return of the photoelectron to the initial $1s$ state of the sulfur atom, etc.). If there were peaks in the spectrum corresponding to transitions to states of the discrete spectrum, the effect of these factors could be approximately estimated (see Ref. 1). However, there are no such peaks in the given spectrum, and we are compelled to refrain from using the Γ_i as adjustment characteristics and must restrict ourselves to a set made up only of the four E_i values, determined fairly reliably.

When the variable parameters of the model were chosen, it turned out that variations of the potential of the absorbing sulfur atom have an extremely small effect on the characteristics of the resonances under discussion. For this reason, it is impossible to make potential V_0^{S+} more accurate in this system; the corresponding coefficients b_n were taken to be equal to zero and in what follows were not varied. Since the total number of variable parameters must not be greater than the number of experimental characteristics, the following four quantities were taken as these parameters: the internuclear distance $R_{\text{S-Cd}}$, the coefficients b_0 and b_1 for the cadmium atom, and the coefficient b_0 for the nonabsorbing sulfur atoms (in accordance with what was said in Sec. 1, a larger number of variable parameters is introduced for the larger cadmium atom).

The results of the optimization are as follows: $R_{\text{S-Cd}} = 2.548$ Å, $b_0 = 1.7476$ and $b_1 = -0.8615$ (for the cadmium atoms), and $b_0 = 0.0277$ (for the nonabsorbing sulfur atoms). The crystal lattice parameter in this case equals 5.884 Å. The difference between the resulting value of $R_{\text{S-Cd}}$ and the value from Ref. 10 is 0.018 Å (0.8%), which does not exceed the errors of this method when determining internuclear distances (see above). However, it should be emphasized that complete agreement is not in general possible for structure parameters obtained by means of different experiments (Ref. 10 gives data obtained by means of x-ray structural analysis). In particular, according to the estimate of Ref. 11, the disagreement for internuclear distances can be of the order of 0.01 Å, which is indeed observed in our case.

The values of the poles of the S matrix in the optimized potential are as follows: $0.150-i0.0076$, $0.393-i0.051$, $0.629-i125$, and $0.918-i0.065$. The real parts of these poles virtually coincide with the experimental energies E_i. Figure 2 shows the distribution of p states in the optimized potential. The energies of the peaks in this distribution obviously coincide with the energies of the spectral maxima, and

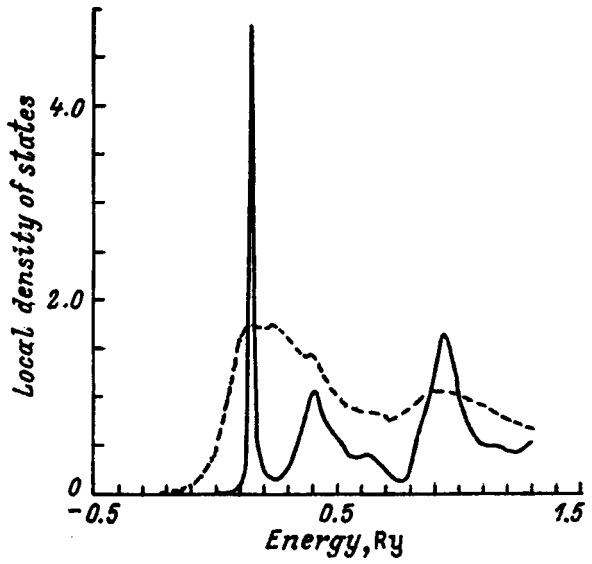

FIG. 2. Local density of p states inside the MT sphere of an absorbing atom, calculated for the optimized potential. For comparison, the dashed curve shows the experimental spectrum.

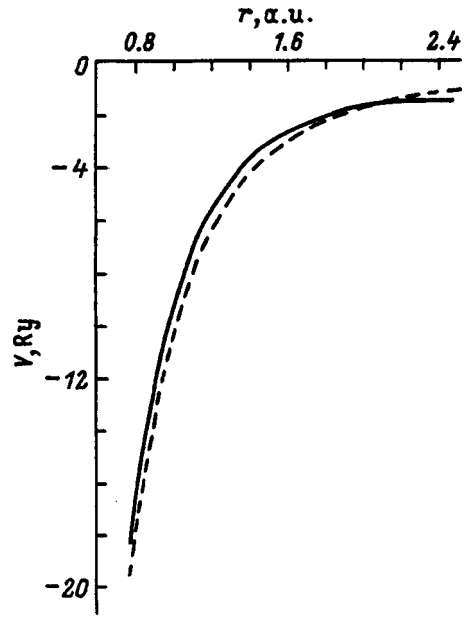

FIG. 3. The MT potential of cadmium in the compound CdS. The dashed curve corresponds to the potential obtained by means of program FEFF7, and the solid curve corresponds to the optimized potential.

consequently the adjustment has been successful.

Judging from the values of coefficients b_n, the optimized potential of the sulfur atoms differs little from the original value. More substantial changes occurred in the potential of the cadmium atoms. This is associated with the fact that the optimization was mainly to shift the first peak, corresponding to the transition of a photoelectron into a state whose main contribution comes from the *s* state of cadmium. Figure 3 shows the optimized MT potential of the cadmium atoms. It can be seen from this picture that, by comparison with the initial potential, its shape was somewhat changed: it became weaker at the internal points of the atom and stronger close to the sulfur atom.

It is important to emphasize that the empirical potential obtained here is the best possible potential of the given type when describing single-electron quasi-stationary states of the compound under investigation. By comparison with any MT potential constructed from first principles, this potential also automatically allows for multielectron effects, deviations of the actual potential from the MT approximation, etc. The geometrical parameters of the crystal are determined more accurately by using this potential. For example, if only the internuclear distance is varied for CdS, while the initial potential V_0 is used as the potential, optimization gives the value $R_{\text{S-Cd}}=2.489$ Å, which differs by 0.04 Å from the known value and is substantially worse than the result obtained by jointly varying the geometrical parameters and the parameters of the potential.

These results thus confirm that the proposed scheme for analyzing XANES data is capable of giving information concerning the geometrical parameters of nonmetallic crystalline bodies and makes it possible to construct an empirical model single-electron potential for them. It has been shown that more accurate values of the geometrical parameters are obtained if, along with the variation of these parameters, the parameters of the potential are varied.

This work was carried out with the support of the Russian Fund for Fundamental Research (Project No. 96-03-32204a).

[1] Yu. F. Migal, J. Phys. B **27**, 1515 (1994).
[2] Yu. F. Migal, Physica B **208–209**, 77 (1995).
[3] Yu. F. Migal', Zh. Strukt. Khim. **39**, 1, 18 (1998).
[4] Yu. F. Migal, J. Phys. IV **7**, C2–169 (1997).
[5] J. R. Taylor, *Scattering Theory: The Quantum Theory of Nonrelativistic Collisions* (Wiley, New York, 1972; Mir, Moscow, 1975, 565 pp.).
[6] Yu. F. Migal, J. Phys. B **26**, 2755 (1993).
[7] V. P. Baltakhinov, in *Modern Vibrational Spectroscopy of Inorganic Compounds* (Nauka, Novosibirsk, 1990) p. 243.
[8] A. A. Lavrent'ev, I. Ya. Nikiforov, A. B. Kolpachev, and B. V. Gabrel'yan, Fiz. Tverd. Tela (St. Petersburg) **38**, 2347 (1996) [Phys. Solid State **38**, 1291 (1996)].
[9] A. L. Ankudinov and J. J. Rehr, J. Phys. IV **7**, C2–121 (1997).
[10] A. V. Novoselova and V. B. Lazarev, Eds., *Physicochemical Properties of Semiconductor Substances. A Handbook* (Nauka, Moscow, 1979), 340 pp.
[11] L. A. Gribov, Zh. Strukt. Khim. **35**, 4, 123 (1994).

Translated by W. J. Manthey

Local lattice distortions and ligand hyperfine interactions in Eu^{2+}- and Gd^{3+}-doped fluorites

A. D. Gorlov, V. B. Guseva, A. Yu. Zakharov, A. E. Nikiforov, A. I. Rokeakh, V. A. Chernyshev, and S. Yu. Shashkin

Ural State University, 620083 Ekaterinburg, Russia
(Submitted February 16, 1998; resubmitted May 11, 1998)
Fiz. Tverd. Tela (St. Petersburg) **40**, 2172–2177 (December 1998)

A computer simulation of lattice distortions around an impurity ion Eu^{2+} in MeF_2 fluorites (Me=Ca, Sr, Ba) is reported. ENDOR data on displacements of F^- ions distant from an impurity center were used to determine the parameters of the $Eu^{2+}-F^-$ short-range interaction potential. A theoretical study of the effect of hydrostatic pressure on the impurity-center local structure has been made. A comparison with experimental data permits a conclusion that the calculated ligand displacements are reliable. An experimental ENDOR investigation of the ligand hyperfine interaction (LHFI) in $MeF_2:Gd^{3+}$ crystals (Me=Ca, Sr, Pb, Ba) has been performed. The results obtained in the simulation are used to describe the LHFI of impurity ions with the nearest-neighbor fluorine environment. The contributions to LHFI associated with ligand polarization are shown to constitute 10–50% of the experimental LHFI constants. The inclusion of such contributions results in practically linear dependences of the remaining short-range part of the LHFI on distance. © *1998 American Institute of Physics.* [S1063-7834(98)00712-6]

Many important physical properties of doped crystals, e.g. the mechanisms responsible for impurity-ion luminescence and the interaction of impurity ions with lattice vibrations, are intimately related to the local lattice distortions created by introducing an impurity into the crystal. Experimental determination of ion positions in the nearest-neighbor environment of an impurity center presents, however, considerable difficulties. On the other hand, ENDOR data offer a possibility to measure the ligand hyperfine interaction (LHFI) for both nearest-neighbor and distant ions. In the latter case LHFI originates from the dipole-dipole magnetic interaction of the impurity electronic moment with the nuclear moments of host-lattice ions, thus making it possible to determine the distance to these ions. LHFI for nearest-neighbor ions is dominated by the overlap and covalency effects, which precludes isolation of the dipole-dipole contribution to LHFI and determination of the metal-ligand distance. This paper reports determination of the nearest-neighbor environment of the Eu^{2+} impurity ion in fluorites within a pair-potential model made using experimental LHFI data for distant fluorine ions. Because published experimental data on the parameters of Gd^{3+}-center LHFI with nearest-neighbor fluorines in fluorite crystals disagree to some extent, these parameters were redetermined in our work. The calculated distances and dipole moments induced at the ligands permit construction of a phenomenological model of LHFI in Gd^{3+}- and Eu^{2+}-doped fluorites which takes into account the important contribution to LHFI of polarization of the ligand electronic shells.

1. CALCULATION OF THE LATTICE RELAXATION AROUND AN IMPURITY ION

The equilibrium positions of the nearest-neighbor ions around an impurity center can be found by energy minimization of a lattice with an impurity. The crystal is divided into two parts, the defect region and the remainder of the crystal. The defect region consists of the impurity ion and the nearest-neighbor ions, which are allowed to displace from their positions in the pure crystal. To reduce the calculational difficulties, the minimization procedure allows only the ion displacements which do not change the impurity-center local symmetry. In the case of a Eu^{2+} center in fluorites, one should take into account only the displacements that transform according to the A_{1g} representation of the O_h group. The defect region breaks up into sets of ions, subsequently called orbits,[1] such that all ions in a given orbit can be obtained by applying to any initial ion in the orbit all point-group symmetry operations of the doped crystal. All orbits are numbered, subsequently, in the order of increasing distance from the impurity ion. The ions in the remainder of the crystal are considered fixed. Accordingly, the size of the defect region should be chosen such that its further increase does not produce substantial changes in ion positions in this region. Our calculations included 247 ions into the defect region, which, judging from the results obtained, is large enough.

The lattice energy was described in terms of the pairwise-interaction approximation and the shell model, which considers each ion to consist of a positively charged core and a negatively charged shell. Then the lattice energy can be written

$$U_{\mathrm{lat}}=\frac{1}{2}\sum_i \sum_{k(\neq i)} V_{ik}+\frac{1}{2}\sum_i k_i\delta_i^2 . \qquad (1)$$

Here $k_i\delta_i^2$ is the energy of core interaction with the ith ion shell, and V_{ik} the interaction energy between the ith and kth ions, which can be presented in the form

$$V_{ik}=\frac{X_iX_k}{r_{ik}}+\frac{Y_iX_k}{|r_{ik}-\delta_i|}+\frac{X_iY_k}{|r_{ik}+\delta_k|}+\frac{Y_iY_k}{|r_{ik}-\delta_i+\delta_k|}+f_{ik}(r_{ik})+g_{ik}(|r_{ik}-\delta_i+\delta_k|), \quad (2)$$

where the function

$$f_{ik}(r)=-A_{ik}\exp(-B_{ik}r)/r \quad (3)$$

describes the short-range screening of the electrostatic ion-core interaction, and the function

$$g_{ik}(r)=C_{ik}\exp(-D_{ik}r)-\lambda_{ik}/r^6 \quad (4)$$

relates to the short-range repulsion between ionic shells written in the form of the Born–Meier potential and the van der Waals interaction, X_i, Y_i are the core and shell charges of the ith ion, δ_i is the shell shift of the ith ion relative to its core, and r_{ik} is the core distance between the ith and kth ions. We used the following core charges: $X_F=+5$, $X_{Ca,Sr,Ba,Eu}=+8$. The F^-–F^- interaction parameters were obtained semiempirically by the Hartree–Fock and configurational interaction formalisms[2]. The parameters of the Me^{2+}–F^- short-range repulsion potential (Me = Ca, Sr, Ba) were derived by fitting the calculated properties of pure MeF_2 crystals to available experimental data (lattice constants, dielectric permittivities ε_0 and ε_∞, elastic constants C_{11}, C_{12}, and C_{44}, and the fundamental vibrational frequencies ω_{TO} and ω_R), and the electrostatic screening parameters were obtained by numerical integration of the free-ion electronic-density interaction. The short-range interaction between metal ions was neglected because of their being far apart. The F^-–F^- and Me^{2+}–F^- interaction potential parameters calculated in this way can be found in Ref. 3. The energy of Coulomb interaction of ions in the defected region with those in the remainder of the crystal was calculated by the Ewald method.

To check the reliability of the Me^{2+}–F^- potentials thus obtained, we calculated dispersion curves for the CaF_2, SrF_2, and BaF_2 crystals along certain high-symmetry directions in the Brillouin zone. A comparison of the calculated dispersion curves with slow-neutron diffraction measurements[4–6] showed that our model is capable of fitting adequately the experimental data.

The main feature of our work consists in using experimental data on radial ion displacements in the second to fifth anion orbits in the doped crystals under study, which were derived from ENDOR data,[7] to find the Eu^{2+}–F^- short-range repulsion potential parameters. Parameters C and D were determined from the condition of an optimum fit of the calculated to experimental radial ion displacements in the second to fifth anion orbits, with experimental errors of ion displacement measurement taken into account. Although the angular displacements of F^- ions in the second orbit were measured experimentally, they were not used in fitting of the C and D parameters because of a poor agreement between the experimental and calculated values (see below). The fitting yielded the following values: $C=268.3$ at. un. and $D=1.921$ at. un.

Figure 1 compares the radial displacements of host lattice ions around a Eu^{2+} impurity ion calculated for CaF_2, SrF_2, and BaF_2 crystals with ENDOR data. Because the experimental lattice constants differ from the constants calculated by our model, the ion displacements are given in units of lattice constants [experimental and calculated, respectively (Ref. 3)]. ENDOR data permit high-accuracy determination of distances only to the second anion orbit. The experimental error increases by more than an order of magnitude for more distant anion orbits, and for BaF_2 one could not derive distances to the fourth and fifth orbits at all. It is also evident that the agreement between calculated and experimental displacements for the second anion orbit is good enough, whereas while the ion displacements calculated for more distant orbits still lie within experimental error the agreement with experiment is substantially worse. We believe, however, that experimental data on distant anion orbits, particularly the experimentally predicted behavior of displacements with increasing distance from an impurity center, should be considered with caution. For instance, in SrF_2 the ionic displacements in the third–fifth orbits are sub-

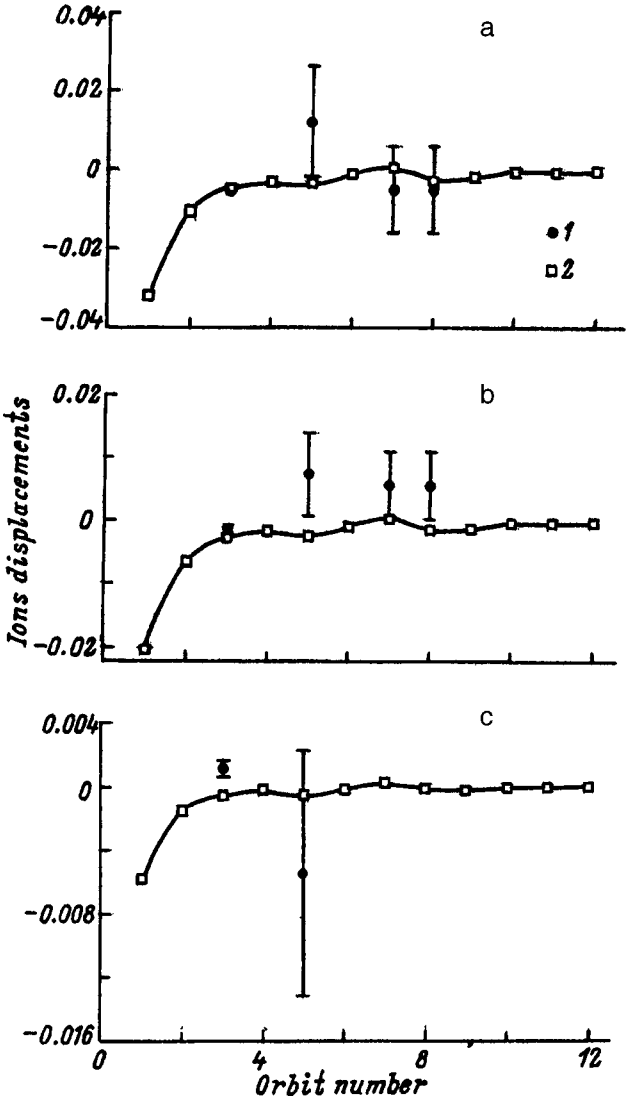

FIG. 1. (*1*) Experimental and (*2*) calculated radial displacements of ions around a Eu^{2+} impurity center (in units of the lattice constant). (a) CaF_2, (b) SrF_2, (c) BaF_2.

TABLE I. F^- ion displacements in the first anion orbit in $MeF_2:Eu^{2+}$ crystals (in units of the lattice constant).

Crystal	Calc.	FP-LMTO	By Kanzaki (Ref. 8)
CaF_2	−0.0318	−0.0288	−0.0176
SrF_2	−0.0204	−0.0232	−0.0009
BaF_2	−0.0058	0.0	0.0209

Note: Negative sign means displacement away from the impurity ion.

stantially larger than those in the second orbit. Interestingly, experimental data suggest that the ionic displacements in the second anion orbit in SrF_2 and BaF_2 crystals are equally small and opposite in sign, whereas model considerations based on the concept of ionic radii, as well as calculations made by the modified Kanzaki method,[8] predicted that only in the case of $SrF_2:Eu^{2+}$ could one expect very small lattice distortions.

By our calculations, radial displacements in all the crystals studied are, on the whole, monotonic (except for the seventh orbit) and decrease away from the crystal surface. The ionic displacements are the largest in CaF_2, and the smallest, in BaF_2, and in BaF_2 the displacement does not exceed about 0.006 in units of the lattice constant. The monotonic character of ion displacement, as well as the practically zero displacements starting with the tenth orbit, appear to be a consequence of isovalent substitution. Table I presents the ligand positions in $MeF_2:Eu^{2+}$ crystals calculated by us, as well as the results obtained by full-potential linear muffin-tin orbital method (FP LMTO) with a real form of the crystal-field potential and charge density[9] and by a modified Kanzaki method[8]. One readily sees that our calculations agree fairly well with the FP-LMTO results while disagreeing markedly with the predictions of Ref. 8. It is essential that both our calculations and the FP-LMTO data expect the effect of Eu^{2+} introduction to be the smallest in BaF_2.

Table II presents calculated and experimental[7] data for angular displacements of F^- ions in the second anion orbit. As already mentioned, the calculated angular displacements do not show good agreement with experiment, which, in our opinion, could be caused by our models lattice energy disregard of many-particle interactions. On the other hand, our data on angular ionic displacements fit well into the overall pattern of lattice distortions around a Eu^{2+} impurity center in fluorites, where one observes a monotonic decrease of both radial and angular ion displacements in going from crystal with a smaller lattice constant to another with a larger one for all fluorites. The experimental values of angular displacements do not exhibit such a monotonic behavior. Calculations made for more distant orbits predict only insignificant angular displacements, and therefore the absence of experimental data on the angular positions of these orbits is connected, most probably, with the impossibility of their experimental determination.

TABLE II. Angular displacements of F^- ions in the second anion orbit in $MeF_2:Eu^{2+}$ crystals (in deg.).

Crystal	Calc.	Exp. (Ref. 7)
CaF_2	−0.16	0.07 (Ref. 9)
SrF_2	−0.08	0.12 (Ref. 15)
BaF_2	−0.01	0.07 (Ref. 6)

Note: Negative sign means decrease of angle between the direction to the ion and C_4 axis.

We studied also the effect of hydrostatic pressure (up to 3 GPa) on the local structure of the Eu^{2+} impurity center in fluorites. An analysis of the results obtained can be conveniently done by introducing the concept of local compressibility of a crystal determined for any ionic orbit. All ions in an orbit can be imagined to lie on a sphere with a radius equal to the distance to ions in the given orbit. Hydrostatic compression of the crystal will change the distance to ions in an arbitrary orbit while leaving the orbit symmetry unchanged. This will entail a change in the volume of the imaginary sphere, on the surface of which all ions of the orbit lie. Then the local compressibility coefficient for the nth orbit, which we denote by k_n, can be introduced through the change in the sphere volume $V_n(p)$ induced by application of hydrostatic pressure p in the following way:

$$k_n = -\frac{1}{V_n(0)} \frac{V_n(p) - V_n(0)}{p}. \tag{5}$$

Expressing the sphere volume $V_n(p)$ through the distance to the orbit ions $r_n(p)$ yields

$$k_n = -\frac{1}{r_n^3(0)} \frac{r_n^3(p) - r_n^3(0)}{p}. \tag{6}$$

Obviously enough, in the case of pure crystals, coefficient k_n is the same for any orbit and equal to the volume compressibility coefficient for a pure crystal. Introduction of an impurity permits one to probe selectively the elastic properties of individual orbits. After calculation of the lattice distortion around an impurity ion for various hydrostatic pressures, the local compressibility coefficients were determined for each orbit by using Eq. (6) for fitting. The results of the simulation are shown graphically in Fig. 2. Note that impurity introduction results only in insignificant changes of the local compressibility coefficient compared to the volume compressibility coefficient for pure crystals (particularly compared to the case of the Gd^{3+} impurity center in the same materials[3]). For a more comprehensive analysis of the data obtained, one has to separate the local compressibility coefficients for cation and anion orbits. As seen from Fig. 2, the elastic properties of cation and anion orbits in fluorite crystals are affected in essentially different manner by introduction of an impurity ion. The local compressibility coefficients for cation orbits remain practically unaffected. Anion orbits turn out to be much more sensitive to the presence of an impurity ion. The results obtained are in accord with the preexisting opinion regarding the MeF_2 lattice, according to which the cation sublattice is rigid, whereas the anion sublattice is flexible, a feature used, in particular, to account for the phenomenon of superionic conduction[10] in these materials. The local compressibility coefficients obtained by us can be employed in ENDOR experiments performed on these crystals under hydrostatic pressure.[11]

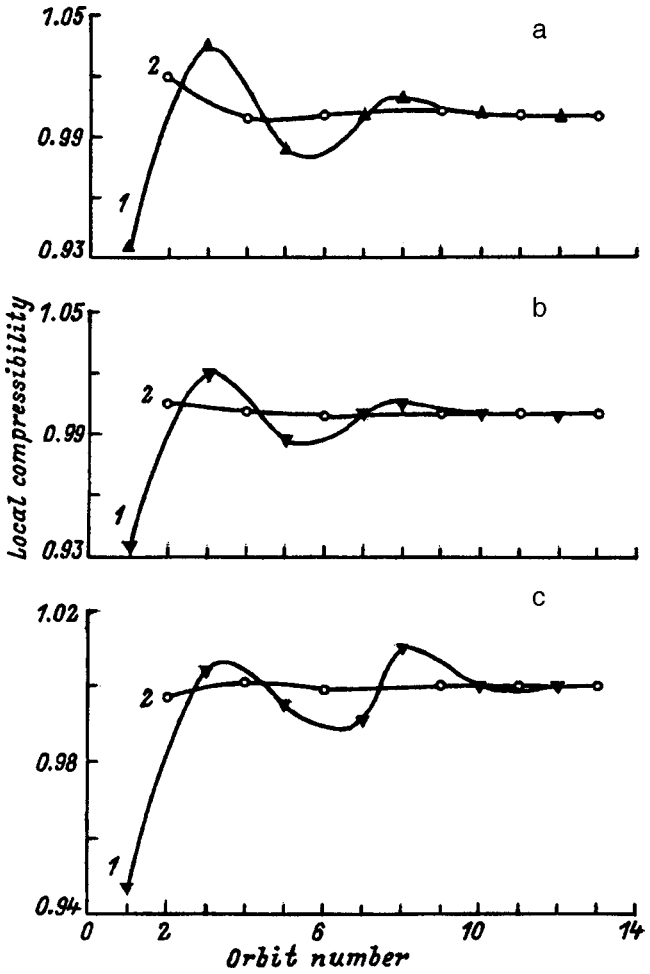

FIG. 2. Local compressibility coefficients for (*1*) anion and (*2*) cation orbits (in units of pure-crystal volume compressibility coefficients). (a) CaF_2, (b) SrF_2, (c) BaF_2.

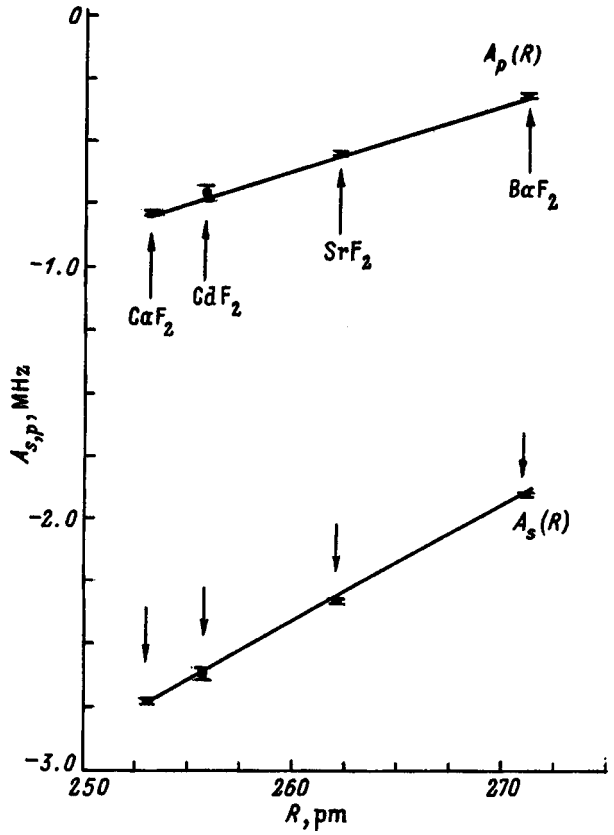

FIG. 3. $A_s(R)=A_s^{\exp}-K_sD(MeF_2)$ and $A_p(R)=A_p^{\exp}-A_d(R)-K_pD(MeF_2)$ as functions of distance for $MeF_2:Eu^{2+}$ crystals.

2. LIGAND HYPERFINE INTERACTION OF Eu^{2+} AND Gd^{3+} IN THE LOCAL-DISTORTION MODEL FOR FLUORITES

It is known[7,12–14] that the experimentally measured LHFI of Eu^{2+} and Gd^{3+} impurity centers in fluorites depends nonmonotonically on the lattice constants of pure crystals. On the other hand, calculations[13] suggest that LHFI should be a monotonic function of R_1 (distance between the impurity ion and the nearest-neighbor fluorine). We are going to describe now the LHFI based on the values of R_1 calculated by us[3] both for Eu^{2+} and for Gd^{3+}.

LHFI of the cubic Eu^{2+} and Gd^{3+} centers is described by an isotropic A_s and axially symmetric A_p contributions. All contributions to LHFI, except for the magnetic dipole interaction A_d, are determined by covalence and overlap of the $5s$ and $5p$ electrons of Eu^{2+} and Gd^{3+} with the $1s$, $2s$, and $2p$ shells of F^-, as well as by the induced spin density in the $3s$ and $3p$ orbitals of the F^- ion.[11–15] The spin density in the previously empty fluorine orbitals is due to the mixing of even and odd states by the low-symmetry crystal field, which gives rise also to an electric dipole moment D. This moment is induced both by the impurity center (in the case of nonisovalent substitution) and, what is more essential, by displacements of ions from their equilibrium positions; note that, as shown by our calculations, the lattice distortions around an impurity ion induce a dipole moment D at ligands amounting to 10–50% of that generated by the impurity itself.

We shall describe LHFI only with the fluorines nearest to the impurity center, because interaction with more distant anions involves only magnetic dipole interaction proportional to R^{-3}, and can be readily measured by ENDOR. In contrast to Refs. 7 and 12, we take into account the contributions to A_s and A_p due to ligand polarization without imposing on them the assumption of their being linearly dependent on the displacements of the nearest ligands.

The experimental parameters of LHFI can be described phenomenologically in the form used in Ref. 12

$$A_s^{\exp}=A_{s,p}(R)+A'_{s,p}(D), \tag{7}$$

where $A_{s,p}(R)$ is a contribution depending only on distance (it is determined by radial dependences of the covalence and overlap parameters in a cluster consisting of the impurity ion and the nearest-neighbor fluorines under the assumption that $D=0$), and $A'_{s,p}(D)=K_{s,p}D(MeF_2)$ is a contribution proportional to the induced dipole moment. Because both impurity centers have spherically symmetric electron distributions and the same ground state, we assume that the $K_{s,p}$ coefficients for Eu^{2+} and Gd^{3+} should be close in magnitude.

Figure 3 displays the $A_s(R)$ and $A_p(R)-A_d(R)$ relations for Eu^{2+} in MeF_2. One readily sees that $A_s(R)$ and $A_p(R)-A_d(R)$ are linear functions of R. Similar relations are obtained for all $MeF_2:Gd^{3+}$ crystals. Both for Eu^{2+} and

TABLE III. Experimental values of LHFI parameters for $MeF_2:Gd^{3+}$ at 4.2 K, calculated distances to nearest-neighbor fluorines, and dipole moments induced on them in MeF_2:Eu^{2+}, Gd^{3+} crystals.

Parameter	CdF_2	CaF_2	SrF_2	PbF_2	BaF_2
A_s, MHz	−1.78(3) (Ref. 12)	−1.876(6)	−1.871(5)	−1.656(4)	−1.808(6)
A_p, MHz	5.16(2) (Ref. 12)	5.104(4)	4.851(3)	4.771(2)	4.637(4)
R_1, pm	231.9(4)	230.5	237.2	242.9(4)	243.1
D, $e\cdot$pm	12.8(4)	11.9	11.0	11.7(4)	10.4
A, MHz(Gd^{157})	16.856(1) (Ref. 14)	16.8828(13)	16.7534(10)	16.644(2)	16.6398(15)
		Eu^{2+}			
R_1, pm	255.7(6)	253.1	262.1		271.1
D, $e\cdot$pm	5.65	4.00	2.94		1.83

for Gd^{3+}, the parameters $K_s=12.3(3)\times10^{-2}$ MHz/$(e\cdot\text{pm})$ and $K_p=7.1(3)\times10^{-2}$ MHz/$(e\cdot\text{pm})$ (e is the absolute value of the electronic charge). Note that the LHFI parameters calculated for doped CdF_2 and PbF_2 crystals likewise fit well onto these relations within experimental error and calculational inaccuracies, although, as evident from Table III, the experimental values of A_s and A_p for these materials fall out of the general trend of A_s and A_p variation with R.

Table III presents experimental values of A_s and A_p, both measured by us and taken from literature[12,14], as well as the values of R_1 and D calculated for all crystals. Note that our data for Gd^{3+} differ from those quoted in Ref. 7. The reason for this lies in that ENDOR experiments were treated in the above-mentioned works without taking into account the contribution of initial splitting to the position of the electronic and nuclear levels. Therefore, as pointed out in Refs. 7 and 12, the sets of the LHFI parameters found in different magnetic-field orientations were different. We used in the treatment of experimental data numerical diagonalization of the total energy matrix and obtained for each crystal a common set of A_s and A_p parameters describing all angular dependences.

The experimental LHFI parameters for $MeF_2:Eu^{2+}$ were taken from Refs. 12 and 14. The dipole moments at the ligands were calculated in terms of the above lattice relaxation model.

The electric dipole moments induced at the nearest-neighbor fluorines and R_1 for the CdF_2 and PbF_2 crystals were calculated based on the following considerations. The hyperfine interaction constant A for odd Eu^{2+} and Gd^{3+} isotopes were found to depend linearly on R_1 determined within our model. Assuming this to hold for CdF_2 and PbF_2 as well, the values of R_1 were derived from the known values of A (see Table III). Such relations were discussed in the literature[12] and are well known. Note that $D(MeF_2)$ depends substantially both on displacements of the nearest-neighbor ions and on the dipole moments induced at the neighboring ions. As a result, dipole moments D and, hence, the contributions to A_s and A_p due to fluorine polarization can in no way be proportional to $\Delta R=R_1-R_0$, as this was postulated in Ref. 12. Moreover, the moments D at the nearest-neighbor fluorines in the doped crystals CdF_2 and PbF_2 fall out of a possible monotonic dependence for other crystals altogether. As a result, in contrast to Ref. 12, the value of R_1 calculated for $CdF_2:Eu^{2+}$ and $CdF_2:Gd^{3+}$ is larger than that for CaF_2 having the same impurities, and R_1 derived for $PbF_2:Gd^{3+}$ is approximately equal to that for $BaF_2:Gd^{3+}$. Thus the final expressions for $A_s(R)$ and $A_p(R)$ can be written as follows

$$A_s(R)=A_s^{\text{exp}}-A_s'(D)=A_s(0)(1+B_sR), \tag{8}$$

where

$$A_s(0)=-14.39(9)\ \text{MHz}, \quad B_s=-3.200(7)\times10^{-3}\ 1/\text{pm}$$

for

$$Eu^{2+}\ \text{and}\ A_s(0)=-7.88(7)\ \text{MHz},$$

$$B_s=-2.485(10)\times10^{-3}\ 1/\text{pm for}\ Gd^{3+};$$

$$A_p(R)=A_p^{\text{exp}}-A_d(R)-A_p'(D)=A_p(0)(1+B_pR), \tag{9}$$

where

$$A_p(0)=-7.42(10)\ \text{MHz}, \quad B_p=-3.53(5)\times10^{-3}\ 1/\text{pm}$$

for

$$Eu^{2+}\ \text{and}\ A_p(0)=-11.75(20)\ \text{MHz},$$

$$B_p=-3.668(12)\times10^{-3}\ 1/\text{pm for}\ Gd^{3+}.$$

In our opinion, we obtained a fairly good phenomenological description for the variation of LHFI parameters for the whole set of crystals in terms of the simplest model using calculated distances and, what appears most essential, the dipole moments induced at the nearest-neighbor fluorines. Note that such a model of a radial variation of A_s and A_p is not connected in any way to one of the basic assumptions[7,8,12] that R_1 cannot be less than the sum of ionic radii of the impurity and fluorine ions. It describes quite well also our ENDOR data on Gd^{3+} and Eu^{2+} in CdF_2 and PbF_2, which also supports our assumption of the closeness of the parameters connected with the polarization contributions to LHFI in magnitude.

We can compare the derivatives obtained from $CaF_2:Gd^{3+}$ ENDOR experiments on the effect of electric field and hydrostatic pressure. The values quoted in Ref. 15 are $dA_s/dR=1.0(12)\times10^{-3}$ MHz/pm and $dA_p/dR=7.69(2.5)\times10^{-2}$ MHz/pm, and our data are $1.96(70)\times10^{-2}$ MHz/pm and $4.4(25)\times10^{-2}$ MHz/pm, respectively. The values of the derivatives depending on dipole moments

are likewise close to the data of Ref. 15. The value[11] $dA_p/dP = 5.5(2.5)$ kHz/kbar is to be compared with ours of 2.4(1.5) kHz/kbar.

To conclude, the displacements of the fluorines closest to an impurity center and the corresponding induced dipole moments calculated within the crystal-lattice relaxation model permit description of experimental LHFI data on both Eu^{2+} and Gd^{3+} for all isostructural crystals without invoking any additional assumptions connected with ionic radii and with a linear dependence of the induced dipoles on the displacements of the nearest-neighbor ligands only. Note that the linear dependences obtained by us are most likely a part of more complex relations, which allow linear approximation only within small portions of R_1 variation.

[1] Yu. A. Izyumov and V. N. Syromyatnikov, *Phase Transitions and Crystal Symmetry* [in Russian] (Nauka, Moscow, 1984), p. 9.
[2] A. E. Nikiforov and S. Yu. Shashkin, *Crystal Spectroscopy* [in Russian] (Nauka, Leningrad, 1989), p. 44.
[3] V. A. Chernyshev, A. D. Gorlov, A. A. Mekhonoshin, A. E. Nikiforov, A. I. Rokeakh, S. Yu. Shashkin, and A. Yu. Zaharov, Appl. Magn. Reson. **14**, 37 (1998).
[4] M. M. Elcombe and A. W. Pryor, J. Phys. C **3**, 492 (1970).
[5] M. M. Elcombe, J. Phys. C **5**, 2702 (1972).
[6] J. P. Hurrell and V. J. Minkiewicz, Solid State Commun. **8**, 463 (1970).
[7] J. M. Baker and L. J. C. Bluck, J. Phys.: Condens. Matter **2**, 7537 (1990).
[8] Y. Y. Yeung, J. Phys. C **21**, L549 (1988).
[9] A. Yu. Zakharov, Yu. E. Medvedeva, A. E. Nikiforov, and S. Yu. Shashkin, *Problems in Spectroscopy and Spectrometry* [in Russian] (UGTU, Ekaterinburg, 1998) (in press).
[10] *Physics of Superionic Conductors* [in Russian], edited by M. B. Salamon (Zinatne, Riga, 1982), p. 315.
[11] S. V. Kasatochkin and E. N. Yakovlev, Fiz. Tverd. Tela (Leningrad) **17**, 520 (1975) [Sov. Phys. Solid State **17**, 324 (1975)].
[12] J. M. Baker, J. Phys. C **12**, 4039 (1979).
[13] J. Casas-González, P. Studzinski, J. Andriessen, J. K. Buzaré, J. C. Fayet, and J.-M. Spaeth, J. Phys. C **19**, 6767 (1986).
[14] R. H. Borcherts, T. Cole, and T. Horn, J. Chem. Phys. **49**, 4880 (1968).
[15] S. M. Arkhipov, N. V. Legkikh, B. Z. Malkin, and Yu. A. Sherstkov, Zh. Éksp. Teor. Fiz. **74**, 1717 (1978) [Sov. Phys. JETP **47**, 896 (1978)].

Translated by G. Skrebtsov

Monopolarity of extrinsic photoconduction in sillenite-type crystals

A. I. Grachev

A. F. Ioffe Physicotechnical Institute, Russian Academy of Sciences, 194021 St. Petersburg, Russia
(Submitted May 19, 1998)
Fiz. Tverd. Tela (St. Petersburg) **40**, 2178–2179 (December 1998)

An analysis of available data on the electronic structure of nominally undoped sillenite crystals and on their surface-barrier photoemf provides a basis for an unambiguous conclusion of a monopolar (electronic) character of photoconduction in these materials in the blue-green region of the spectrum. © *1998 American Institute of Physics.* [S1063-7834(98)00812-0]

The present communication discusses the idea of bipolarity of photoconduction in nominally undoped crystals with sillenite structure $Bi_{12}MO_{20}$ (M=Si, Ge, Ti) used by some authors (see, e.g., Refs. 1–4) to interpret the observed features of holographic recording in these materials. An analysis based on available data on the electronic structure of sillenites and on studies of the photovoltaic effect in these crystals suggests that the contribution of minority carriers (holes) to extrinsic photoconduction in the blue-green spectral region is of a minor significance. It should be stressed that we are speaking about the photoconduction observed under quasi-steady-state illumination. The problem of the extent to which holes participate in the photoconduction generated by high-power laser pulses of nano- and subnanosecond duration requires a separate consideration.

It is known[5] that nonequilibrium conduction becomes bipolar under extrinsic excitation as a result of either thermo-optical or two-step optical transitions. Let us estimate the contribution of both mechanisms to hole generation in sillenites using a simplified diagram of energy levels and corresponding electronic transitions (Fig. 1). Photogeneration of electrons in the blue-green spectral region ($h\nu \sim 2.5$ eV) involves primarily optical transitions from close-to-midgap M levels with concentration $M \sim 10^{19}$ cm^{-3}. The criterion of monopolarity of photoconduction in the case of thermo-optical hole ejection from M levels is the condition[5] $\xi_M = m_0^2/MP_{vM} \gg 1$ (here m_0 is the M-level filling in the dark, $P_{vM} = P_v \exp[(E_M - E_g)/kT] \sim P_v \exp(-E_g/2kT)$, P_v is the effective density of states in the v band, k is the Boltzmann constant, and T is the temperature). At room temperature and for $P_v \sim 10^{20}$ cm^{-3}, P_{vM} is negligible ($\sim 10^{-7}$ cm^{-3}), and therefore $\xi_M \gg 1$. In principle, at $h\nu \sim 2.5$ eV, optical transitions of electrons to the c band can take place from the lower-lying A levels as well ($A \sim D \sim 10^{16} - 10^{17}$ cm^{-3}). However, even assuming the optical and thermal electron ionization energies from the A levels being equal, i.e., that $E_A \sim E_g - h\nu \sim 0.8$ eV, the corresponding value $P_{vA} \sim 10^6$ cm^{-3} likewise is not large enough for the condition $\xi_A \sim 1$ to be met.

For $h\nu \geqslant 1.65$ eV, M levels can take part in two-step optical transitions. The criterion of monopolarity is determined in this case by the following relation[5] between the electronic ($n_{\rm ph}$) and hole ($p_{\rm ph}$) contributions to photoconduction: $n_{\rm ph}/p_{\rm ph} = q_e \gamma_e m_0^2/q_h \gamma_h (M - m_0)^2$, where q_e and q_h are the photon capture cross sections for optical transitions to the c and v bands, respectively, and γ_e and γ_h are the recombination coefficients for the corresponding reverse transitions. One cannot give a priori the values of the above quantities for sillenites. Therefore in order to estimate the efficiency of two-step optical transitions, we shall invoke the results of a study of steady-state photovoltaic effect in sillenites.[6,7]

A photovoltaic effect in undoped sillenite crystals, associated with the existence of a surface barrier for electrons, is observed both in the intrinsic and extrinsic excitation regions. In the latter case the required minority carriers (i.e., holes) are generated primarily in two-step optical transitions, with the holes excited in the space-charge region (SCR) providing the predominant contribution.[7] As it is known,[8] an alternative situation occurs when the photovoltaic current is dominated by minority carriers generated at a distance of the order of their diffusion length (L_h) from the SCR. Hence, if the first of the two mechanisms is operative in the sillenites, this means that either the SCR width w exceeds by far L_h or the hole generation rate in the SCR is substantially higher than that in the bulk of the crystal.

In the first case, the upper limit of L_h is determined by

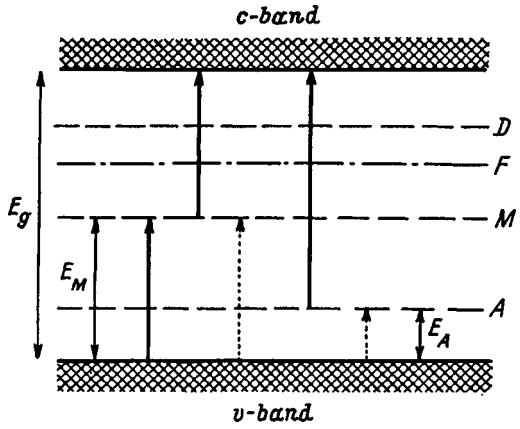

FIG. 1. Diagram of local levels and assumed thermo-optical and two-step optical transitions producing holes in nominally undoped sillenite crystals ($E_g \sim 3.3 - 3.4$ eV) under blue-green excitation. The optical transitions of electrons are denoted by solid arrows, their thermal ejection from the v band, by dashed arrows, and the dot-and-dash line identifies the approximate position of the Fermi level.

w, which permits one to obtain an upper estimate of the product $\mu_h\tau_h$ (where μ_h and τ_h are the hole mobility and lifetime, respectively) using the expression following from Einstein's relation: $L_h^2=\mu_h\tau_h(kT/e)$. In BSO crystals $w\sim10^{-5}$ cm,[7] which for $kT/e=2.5\times10^{-2}$ V yields the following estimate: $\mu_h\tau_h=4\times10^{-9}$ cm^2 V^{-1}. This value is about two orders of magnitude lower than the estimate made[9] for electrons.

If the second mechanism is operative, we can obtain an upper estimate for the ratio $n_{\rm ph}/p_{\rm ph}=G_e\mu_e\tau_e/G_h\mu_h\tau_h$ [where G_e and G_h are equal, respectively, to q_em_0 and $q_h(M-m_0)$] using the following relations[7]: 1) the electron (g_e) and hole (g_h) generation rates in the SCR are equal, 2) G_e is at least not smaller (in real fact it is larger) than g_e, and 3) $G_hL_h\leqslant g_hw$. In this case the relation we are looking for can be written as $n_{\rm ph}/p_{\rm ph}=\mu_e\tau_e/w(\mu_h\tau_he/kT)^{1/2}$. Assuming $\mu_h\tau_h=\mu_e\tau_e\sim10^{-6}$ cm^2 V^{-1} s^{-1}, we obtain $n_{\rm ph}/p_{\rm ph}\sim10^3$. Clearly enough, if the true value of $\mu_h\tau_h$ exceeds the above estimate by about, say, a factor 100, which is extremely unlikely, the hole contribution to extrinsic photoconduction of BSO cannot be anything but insignificant.

Thus in none of the above scenarios does the existence of two-step optical transitions in bulk BSO result in destruction of monopolarity of extrinsic photoconduction. The closeness of all undoped sillenites in electronic structure suggests that this conclusion is valid for BGO and BTO as well. On the whole, taking into account estimates of the efficiency of thermo-optical transitions, the above results show that the model of bipolar extrinsic photoconduction is inapplicable to the crystals under study. Moreover, our analysis (its results will be published separately) shows that the features observed[1–4] in holographic recording can be explained by considering the drift and diffusion processes under conditions of nonsteady-state and nonlinear photoconduction.

[1] A. A. Kamshilin and M. P. Petrov, Fiz. Tverd. Tela (Leningrad) **23**, 3110 (1981) [Sov. Phys. Solid State **23**, 1811 (1981)].
[2] F. P. Strohkendl and R. W. Hellwarth, J. Appl. Phys. **62**, 2450 (1987).
[3] M. Miteva and L. Nikolova, Opt. Commun. **67**, 192 (1988).
[4] S. G. Odulov, K. V. Shcherbin, and A. N. Shumelyuk, J. Opt. Soc. Am. B **11**, 1780 (1994).
[5] S. M. Ryvkin, *Photoelectric Effects in Photoconductors* (Consultants Bureau, New York, 1964; Fizmatgiz, Moscow, 1963, 494 pp.).
[6] A. I. Grachev and M. V. Krasin'kova, Zh. Tekh. Fiz. **53**, 2293 (1983) [Sov. Phys. Tech. Phys. **28**, 1410 (1983)].
[7] A. I. Grachev, Fiz. Tverd. Tela (Leningrad) **26**, 227 (1984) [Sov. Phys. Solid State **26**, 132 (1984)].
[8] T. S. Moss, G. J. Burrell, and B. Ellis, *Semiconductor Opto-Electronics* (Butterworths, London, 1973), 441 pp.
[9] M. P. Petrov, S. I. Stepanov, and A. V. Khomenko, *Photorefractive Crystals in Coherent Optics* [in Russian] (Nauka, St. Petersburg, 1992), 317 pp.

Translated by G. Skrebtsov

DEFECTS. DISLOCATIONS. PHYSICS OF STRENGTH

Dynamics of nanodefects on a loaded gold surface

V. I. Vettegren', S. Sh. Rakhimov, and V. N. Svetlov

A. F. Ioffe Physicotechnical Institute, Russian Academy of Sciences, 194021 St. Petersburg, Russia
(Submitted April 17, 1998)
Fiz. Tverd. Tela (St. Petersburg) **40**, 2180–2183 (December 1998)

The dynamics of defects with linear dimensions from ≈ 1 to ≈ 100 nm on a Au surface under load have been studied by means of tunnelling microscopy. It is found that the origin, growth, and resorption of the defects is caused by displacements of bands of material from 5 to 50 nm wide, parallel to the {111} slip planes. The defects can be separated into two groups: nonsteady-state defects, whose lifetime does not exceed 15 min, while the depth is $\leqslant 20$ nm, and quasi-steady-state defects, with a lifetime three orders of magnitude greater than the first. It is assumed that the nonsteady-state defects are formed when the ensemble of dislocations is being reconstructed, while the quasi-steady-state defects are formed at the instant of formation of dislocation substructures during the creep of the loaded metal. © *1998 American Institute of Physics.* [S1063-7834(98)00912-5]

In earlier papers,[1–3] tunnel microscopy was used to begin systematic studies of submicroscopic defects formed on the surfaces of loaded metals. It was found that the main defects that appear have the form of an impression of a prism with a definite size and vertex angle for each metal. For example, Fig. 1 shows a ''primary'' defect on a Au surface, formed 2 h after a tensile stress of 350 MPa was applied. The depth of the defect is ≈ 20 nm, while the dimensions in the plane of the surface are $\approx 60 \times 100$ nm. Three walls of the defect are approximately perpendicular to the plane of the sample surface, while the fourth makes an angle of $\approx 30°$ with it. The angle at the vertex of the defect is $\approx 70°$.

The size of the defects increased with time. This process has a discontinuous character: The size remained unchanged during some interval Δt, then increased or decreased by several tens of nanometers in a time of $\approx 0.1\Delta t$, again stabilized, once again changed, etc. This character of the evolution of the defects made it possible to separate them into two groups: One group included quasi-stationary defects with a lifetime of Δt, while the other included non-steady-state defects that lived for an order of magnitude less than the first ones. It turned out[1,2] that the depth H_s of the quasi-steady-state defects is approximately a multiple of the depth H_0 of the primary defects: $H_s \approx nH_0$, where n is a whole number. It was then found[3] that the angles at the vertices of the defects are close to the angles between the slip planes, while the walls are oriented parallel to such planes. Based on this, the formation of the defects was explained by the emergence of dislocations at the surface of the loaded metal along intersecting slip planes. The discontinuous character of the defect growth was explained on the basis of a model proposed by Cottrell,[4] who assumed that the defects result from the merging of dislocations blocked by a sessile dislocation on the intersection line of the slip planes.[5]

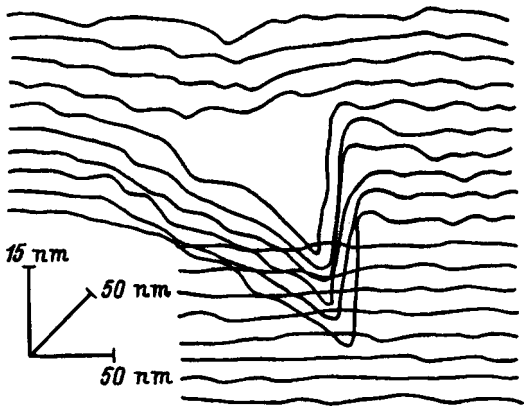

FIG. 1. Segment of a topogram of a Au surface with a primary defect.

This paper continues this series of studies. If Cottrell's model actually describes the formation of the defects, they must appear with the velocity of sound and have linear dimensions no less than those of a primary defect. This paper has the goal of checking these assumptions.

The surface profile of rolled foils of Au with a purity of 99.99%, from 30 to 60 μm thick, was studied by means of an RTP-1 scanning tunnelling profilometer, developed at the Physics Institute of the St. Petersburg State University[6] and fabricated by the Éra Production Cooperative. Samples in the form of shovels were cut out along the direction of rolling, were polished using chromium-oxide buffing compound, were rinsed in acetone, and were loaded by means of a spring apparatus.[1] The chemical composition of the samples before and after loading was studied by Auger spectroscopy. Within the sensitivity limits of this method, it was impossible to detect the presence of foreign atoms on the Au surfaces.

The time to record one topogram by means of the profilometer is ≈ 40 min. Therefore, earlier, only defects whose lifetime was greater than the indicated time interval were

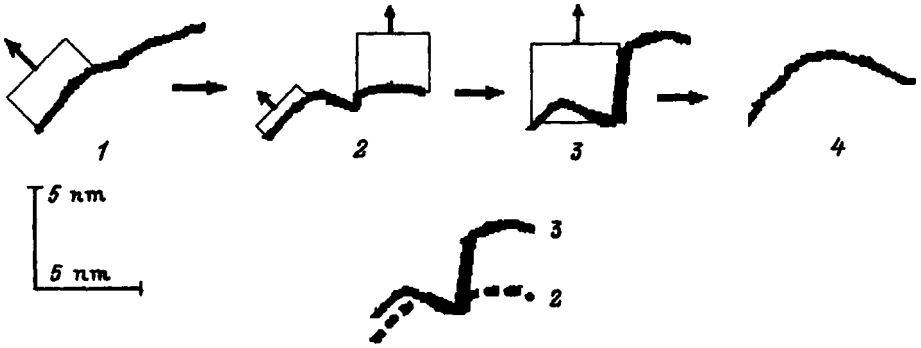

FIG. 2. Evolution of a fine defect on a Au surface under a load of 350 MPa with time t (sec): *1*—0; *2*—38; *3*—76; *4*—114. The rectangles show the bands during whose displacement a defect is formed and is resorbed, while the arrows show the direction and the displacement. The lower part shows cross sections of the surface 38 (*2*) and 76 sec (*3*) after loading, superimposed on each other.

detected and studied.[1–3] In order to elucidate whether defects with a smaller lifetime exist, the surface profile of a loaded sample was recorded in one of the chosen cross sections. The time to record a profile in one cross section is 38 sec, i.e., ≈ 2 orders of magnitude less than the time to record a complete topogram. The scale perpendicular to the surface was simultaneously increased by a factor of from 3 to 10, and this made it possible to reliably record defects with a depth of ≈ 1 nm.

The studies showed that the formation of a quasi-steady-state primary defect precedes the appearance of the finer defects. For example, Figs. 2 and 3 show the evolution of such defects, while Fig. 4 shows the dependences of their depth on time. It can be seen that the defects grow with time and are then resorbed, with their shape constantly pulsating. These results contradict Cottrell's model.

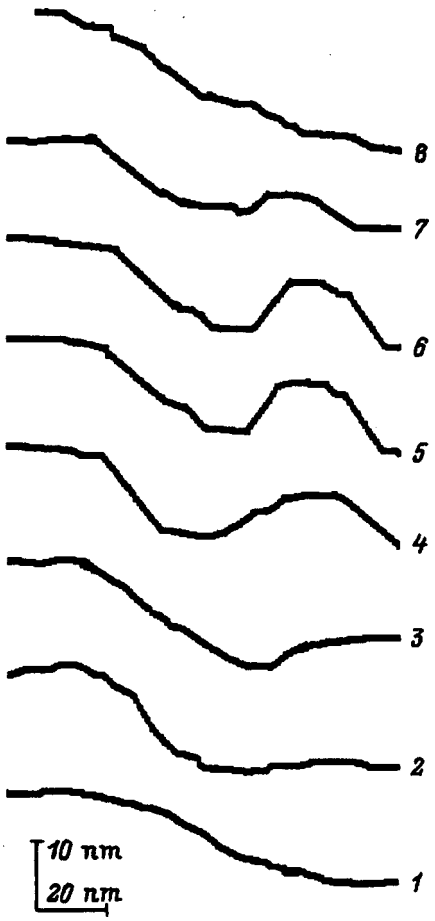

FIG. 3. Evolution of the shape of a fine defect on a Au surface under a load of 350 MPa with time t (sec); *1*—0, *2*—38, *3*—76, *4*—114, *5*—152, *6*—190, *7*—228, *8*—266.

To explain the defect-formation mechanism, we compared successive recordings of the surface cross section, superimposing them on each other (for example, see the lower part of Fig. 2). It turned out that the defects are formed and resorbed when bands of the material from 5 to 50 nm wide move at angles of ≈ 90 and $\approx 30°$ to the surface. Figure 2 schematically shows the bands and the directions in which they move during the evolution of one of the defects. It can be seen that the band of material in the right part of the picture first moves by ≈ 2 nm at an angle of $\approx 30°$ to the plane of the surface. As a result, a defect with a depth of ≈ 1 nm is formed. At ≈ 38 sec, a band of material to the right of the defect begins to move perpendicular to the plane of the surface. In the next 38 sec, it moves by ≈ 3 nm, and the depth of the defect reaches ≈ 4 nm. Afterwards, a band of material in the left part of the figure moves in the same direction. As a result, the defect disappears.

The directions of motion of the bands of material were ≈ 90 and $\approx 30°$ to the plane of the sample surface and were consequently parallel to the (111) slip planes. Actually, as already mentioned, pre-rolled Au foils were used for the studies. It is well known[7] that the (111) slip planes in rolled samples of metals with a fcc lattice lie at angles of ≈ 90 and $\approx 30°$ to the surface. The movements of the bands of material are apparently caused by the displacement of trains of edge dislocations. In this case, the number of dislocations whose emergence at the surface forms a defect can be estimated by dividing the depth of the defect by the Burgers vector. Thus, a defect with a depth of ≈ 1 nm is formed when two or three dislocations emerge at the surface.

Figure 5 shows the dependence of the lifetime τ of the defects on the maximum depth H_m that they reach during their evolution. It can be seen that the lifetime is approximately directly proportional to the maximum depth of the defect. By extrapolating the straight line to the depth of a primary defect with $H_0 = 20$ nm, we find that its lifetime must be ≈ 15 min. In actuality, it is significantly greater. In order to estimate it, let us consider the time dependence of the concentration of such defects (Fig. 6). It can be seen that it has a bell shape: The concentration of primary defects increases, reaches a maximum, and then decreases. By measuring the width of the bell at half of the maximum value, we found that the mean lifetime τ_{or} of the primary defects is

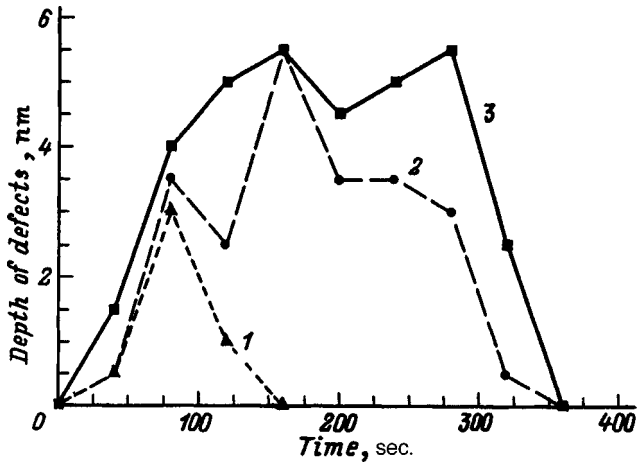

FIG. 4. Evolution of the depth of three arbitrarily chosen defects on a Au surface under a load of 320 MPa.

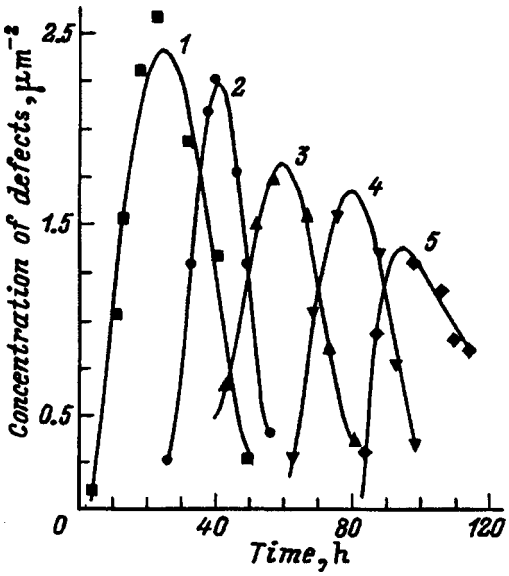

FIG. 6. Time dependence of the concentration of quasi-steady-state defects with various depths on a Au surface. *H* (nm): *1*—20, *2*—40, *3*—60, *4*—120, *5*—240. The loading on the sample is 350 MPa.

≈30 h. This value is three orders of magnitude greater than that found by extrapolating the straight line in Fig. 4 to 20 nm.

Let us now consider the evolution of defects whose depth is greater than 20 nm. For example, Fig. 7 shows a segment of the dependence of the depth of a defect, whose value at one instant exceeded 20 nm and began to grow. It can be seen that the depth stops increasing with time and then decreases to its earlier value (≈20 nm). Measurements showed that, for all defects whose depth exceeds ≈20 nm, in the course of 15–20 min, the depth either decreases to the indicated value or increases in the same time to ≈40 nm. However, if the depth of the defect reaches 40 nm, its lifetime again increases to ≈20 h. It is possible to convince oneself of this if the width of the time dependence of the concentration of such defects shown in Fig. 6 is measured. For defects with a depth between 40 and 60 nm, the lifetime again decreases to 10–15 min, and, for defects with a depth of ≈60 nm, it increases to ≈30 h, etc. It turned out that the lifetime of all defects whose depth is a multiple of that of a primary defect is 20–40 h, while, for other defects, it is three orders of magnitude less. Thus, defects whose depth is a multiple of 20 nm behave like attractive trajectories in a nonlinear nonequilibrium system.

Analysis shows that the formation, growth, and resorption mechanism of all defects with a depth of from ≈1 to ≈700 nm is identical. It consists of disordered movements of bands of material with a depth of from ≈5 to ≈100 nm parallel to the {111} slip planes. Consequently, the difference of the lifetimes of the defects is not caused by any change in the defect-formation mechanism.

It is well known[8,9] that, during creep, an ensemble of dislocations is reconstructed and forms a series of stable, long-lived substructures. Apparently, mainly nonsteady-state defects are formed on the surface during the reconstruction of the ensembles. Conversely, when a stable substructure is formed, mainly quasi-steady-state defects are formed on the surface. In terms of the proposed explanation, the fact that the depth of the quasi-steady-state defects is a multiple of the depth of the primary defect can mean that the stable dislocation substructures consist of aggregates that are multiples of

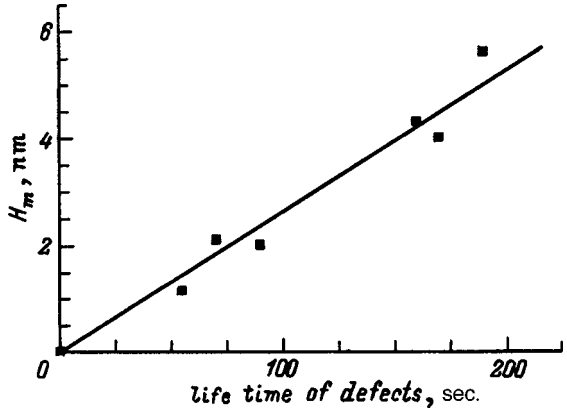

FIG. 5. Connection between the maximum depth H_m of a defect and its lifetime.

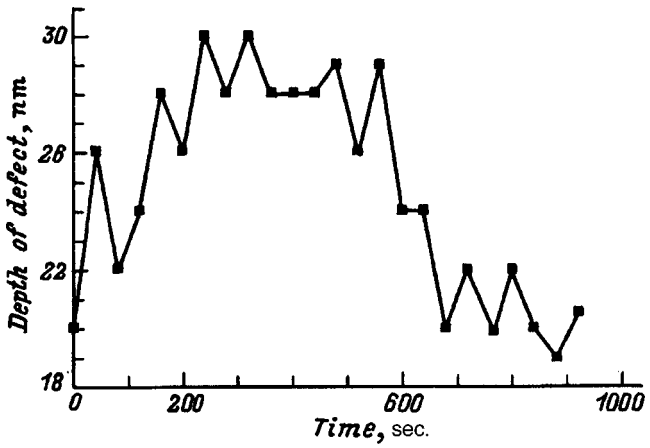

FIG. 7. Part of the time dependence of the depth of a primary defect.

the same number. For example, an aggregate of ≈ 50 dislocations emerges on the Au surface during the formation of the vertical wall of a quasi-steady-state primary defect.

Thus, all the defects on the Au surface are formed when bands of material move parallel to a {111} slip direction. They can be arbitrarily separated into two groups. One group includes quasi-steady-state defects, whose depth is a multiple of that of a primary defect—the smallest of them (≈ 20 nm)—and the lifetime is 20–40 h when the load is 350 MPa. The other group includes nonsteady-state defects, which live for ≈ 3 orders of magnitude less than the former group and have depths that are not multiples of the depth of a primary defect. The nonsteady-state defects apparently form during the reconstruction of dislocation ensembles, whereas the quasi-steady-state defects form at the instant of formation of stable dislocation substructures.

This work was carried out with the financial support of the Russian Fund for Fundamental Research (Project code 96-02-16874-a).

[1] V. I. Vettegren', S. Sh. Rakhimov, and V. N. Svetlov, Fiz. Tverd. Tela (St. Petersburg) **37**, 913 (1995) [Phys. Solid State **37**, 495 (1995)]; **37**, 3635 (1995) [Phys. Solid State **37**, 2001 (1995)]; **38**, 590 (1996) [Phys. Solid State **38**, 323 (1996)]; **38**, 1142 (1996) [Phys. Solid State **38**, 632 (1996)]; **39**, 1560 (1997) [Phys. Solid State **39**, 1383 (1997)].
[2] V. I. Vettegren', S. Sh. Rakhimov, and E. A. Bakulin, Fiz. Tverd. Tela (St. Petersburg) **37**, 3630 (1995) [Phys. Solid State **37**, 1998 (1995)].
[3] V. I. Vettegren', V. L. Gilyarov, S. Sh. Rakhimov, and V. N. Svetlov, Fiz. Tverd. Tela (St. Petersburg) **40**, 668 (1998) [Phys. Solid State **40**, 614 (1998)].
[4] A. H. Cottrell, *The Mechanical Properties of Matter* (Wiley, New York, 1958), 350 pp.
[5] J. W. Christian, *The Theory of Transformation in Metals and Alloys* (Pergamon Press, Oxford, 1965), 428 pp.
[6] V. K. Adamchuk, Prib. Tekh. Eksp. **5**, 4, 182 (1989).
[7] M. C. Smith, *Principles of Metallurgy* (Harper Brothers, New York, 1956), 450 pp.
[8] V. E. Panin, V. A. Likhachev, and Yu. V. Grinyaev, *Structural Deformation Levels of Solids* (Nauka, Novosibirsk, 1985), 163 pp.
[9] N. A. Koneva and I. V. Kozlov, Izv. Vyssh. Uchebn. Zaved. Fiz. **2**, 89 (1990).

Translated by W. J. Manthey

The effect of magnetic and electric fields on the state of point defects in single-crystal NaCl

Yu. I. Golovin, R. B. Morgunov, A. V. Tyutyunnik, S. E. Zhulikov, and N. M. Afonina

Tambov State University, 392622 Tambov, Russia
(Submitted May 5, 1998)
Fiz. Tverd. Tela (St. Petersburg) **40**, 2184–2188 (December 1998)

It is established that exposing crystals to a pulsed electric field with an amplitude of $\sim 10^3$ kV/m creates metastable states of the point defects, while a magnetic field with an induction of 7 T causes them to relax. © *1998 American Institute of Physics.* [S1063-7834(98)01012-0]

It was established in Refs. 1 and 2 that one cause for the plastification of ionic crystals in a weak magnetic field (MF) with an induction of $B \sim 1$ T can be a change of state of the point defects in the absence of freshly introduced dislocations. The nature of these magnetosensitive centers (MCs) is currently unknown. However, the experimental data of Refs. 3 and 4 make it possible to assume that they are metastable long-lived complexes whose Gibbs free energy can be reduced under the action of an MF, which in turn affects the mobility of the dislocations. This hypothesis concerning the irreversibility of changes of point defects in an MF needs to be experimentally checked.

Moreover, it is not clear what factors cause these metastable complexes to be formed. Since the MCs and the individual defects of which they consist can possess a charge, an electric dipole moment, or a higher-order multipole moment, like many other types of structural defects in ionic crystals, it seems very likely that the internal nonsteady-state electric fields that arise when ionic crystals are plastically deformed[5] can ''pump'' point defects into metastable states. This assumption can be checked and the charge state of the MCs can be established in experiments in which the crystals undergo the action of not only an MF but also external electric fields (EFs). The first experiments of this kind were reported in Refs. 6 and 7, where it was found that the combined action of magnetic and electric fields results in a greater plastification of the crystals than when they are exposed to only an EF or an MF. As proposed by Al'shits *et al.*,[6,7] the role of the EF in their experiments consisted of a strong influence on charged dislocation segments, as a result of which the conditions improve for unpinning the dislocations from local stoppers. At the same time, in these crystals, where the point defects are sensitive to MFs, it can be essential that the pinning centers can themselves alter their state in an EF by reorientation,[8] change of the degree of aggregation,[9,10] ionization,[11] and other methods.

The goal of this work was to study the question of the possible influence of an EF on the state of magnetosensitive point defects in the absence of freshly introduced dislocations, as well as to establish the degree of reversibility of the changes introduced by a weak MF into the point-defect subsystem.

The effect of an EF and an MF on the state of the point defects was studied in nominally pure single crystals held for five days at 700 K and cooled at a mean rate of 1–2 K/min, called NaCl(I), as well as in crystals of NaCl(II), which differed from NaCl(I) by the fact that, after heat treatment, they were held for a year at $T = 293$ K. Fresh edge dislocations were introduced by applying scratches to the sample after it was exposed in these fields. This eliminated the influence of the EF and MF on the dislocations themselves and the process by which they interact with point defects in this phase of the experiment. After the dislocations were introduced, their movement was initiated by a MF pulse, identical in all the experiments and having the shape of one half period of a sinusoid of amplitude 7 T and a width of 10^{-2} sec. The change of state of the point defects was measured by the difference $\Delta L = L_0 - L$ between the path length L_0 of the dislocations in control samples not subjected to the introduction of dislocations by external action and the path length L in crystals subjected to preliminary exposure to an EF and an MF, switched on in various sequences. The values of L_0 and L were determined by double chemical etching and by averaging the displacement of 100–150 dislocations for each point on the graphs. To elucidate the character of the influence of MFs and EFs on the evolution of the point defects, three series of experiments were carried out, differing in the nature and sequence of the procedures.

In the first series of experiments, a NaCl(I) crystal was processed with an MF pulse; edge dislocations were then introduced into it and their motion was initiated at time t_p by a second (the same as the first) MF pulse. The path length L of the dislocations in this case was less than the path length L_0 in experiments in which the crystal was not processed in an MF before dislocations were introduced. As the pause t_p between the first and second MF pulses was increased, the value of $\Delta L = L_0 - L$ decreased (Fig. 1). The inclusion of additional MF pulses immediately before introducing the dislocations had no effect on the behavior of the $\Delta L(t_p)$ dependence (Fig. 1).

In the NaCl(II) crystals, ΔL equalled zero for any t_p; i.e., aging the crystals caused the sensitivity of the defects to an MF to be lost (Fig. 1). In the second series of experiments, the NaCl(II) crystals were subjected to processing in a strong EF pulse (amplitude $\sim 3 \times 10^6$ V/m, pulsewidth $\sim 10\,\mu$s, mean repetition rate ~ 1 kHz) for 15 min. It was

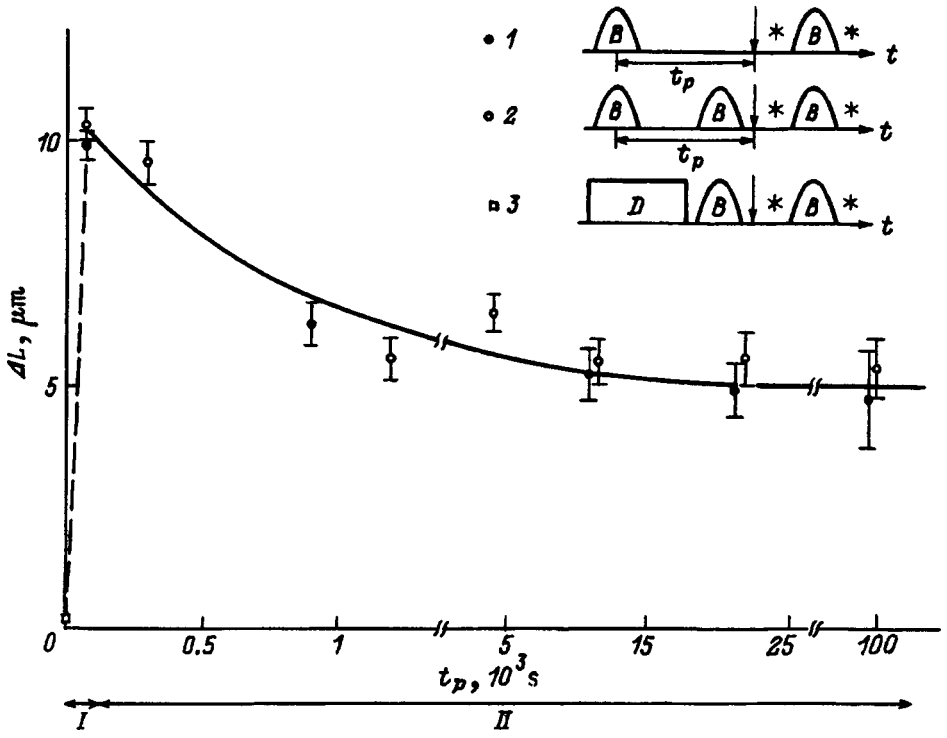

FIG. 1. Difference $\Delta L = L_0 - L$ between the mean path lengths of dislocations initiated by MF pulses in NaCl(I) crystals not subjected (L_0) and subjected (L) to processing in an MF before the introduction of dislocations vs the duration of the pause t_p between the first processing of the crystals in an MF and the introduction of dislocations (*1*); the same when the NaCl(I) sample was subjected to the action of an additional intermediate MF pulse before the dislocations were introduced (*2*); and $\Delta L = L_0 - L$ in NaCl(II) crystals (*3*). I is the first stage, and II is the second stage. The inset schematically shows the sequences of the procedures in each type of experiment in which the deviation of the path lengths of the dislocations from L_0 was studied. On the diagrams, *B* is an MF pulse, an arrow is the introduction of dislocations, an asterisk is etching, and *D* is aging.

found that, after the crystals were exposed to an EF, the value of ΔL, measured by the same method as in the previous series of experiments, differs from zero (Fig. 2); i.e., under the action of an EF, the point defects become sensitized to the action of an MF. Increasing the pause between holding the crystals in an EF and beginning the procedure of measuring ΔL to 15 min causes the EF-induced sensitivity of the crystals to an MF to disappear; i..e, ΔL again becomes zero (Fig. 2). Processing the NaCl(II) crystals in a weak sinusoidal EF with an amplitude of $\sim 10^5$ V/m does not cause them to be sensitized to an MF.

In the third series of experiments, the sequence of the procedures and the samples that were used were the same as in the first series, except that, in the pause between the first MF pulse and the introduction of dislocations, the crystals were exposed to a weak sinusoidal EF (amplitude $\sim 10^5$ V/m and frequency 100 Hz) for time t_e. It is found that exposing the NaCl(I) crystals to such a field in the pause between the two MF pulses accelerates (by a factor of $\sim 10-100$) the reconstruction of L (Fig. 3).

The $\Delta L(t_p)$ dependence obtained in the first series of experiments (Fig. 1) reflected the kinetics of the magnetically stimulated transformations of the point defects, which can be characterized by two successive stages. The first stage occurs during the first MF pulse, and its result is to reduce the path lengths of the dislocations stimulated by the second MF pulse (Fig. 1). As a result of the occurrence of the second stage, which starts immediately after the first MF pulse ends, the path lengths of the dislocations caused by the action of the second MF pulse increase as the pause between the MF pulses increases. An analysis of the kinetics of the MF-stimulated process in the point-defect subsystem shows that

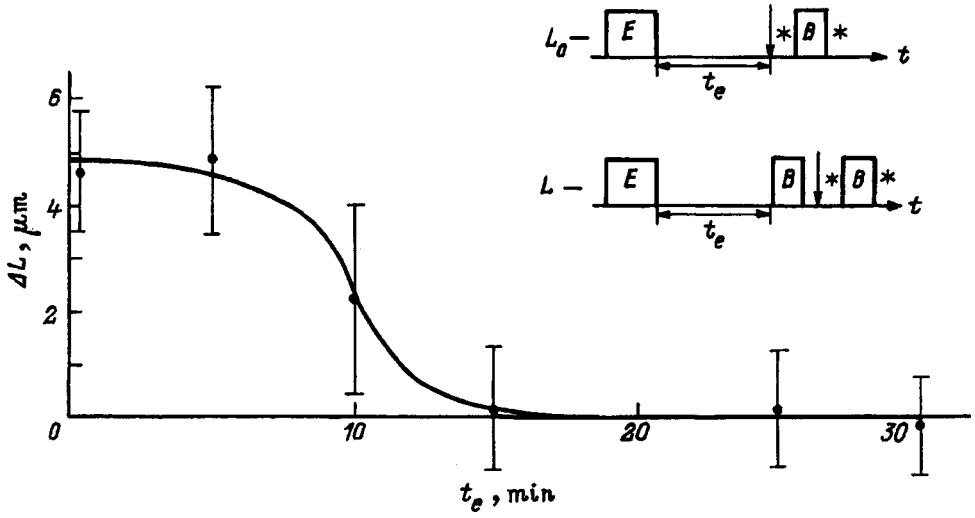

FIG. 2. Difference $\Delta L = L_0 - L$ between the mean path lengths of the dislocations initiated by MF pulses in NaCl(II) crystals not subjected (L_0) and subjected (L) to processing in an MF before the introduction of dislocations vs the duration t_e of the pause between the preliminary exposure of the samples in an EF pulse and the procedure of measuring ΔL. The inset schematically shows the sequences of the procedures in the experiments in which the values of L and L_0 were determined in crystals preprocessed in a strong pulsed EF for 15 min. The notation is the same as in Fig. 1; *E* is exposure in an EF.

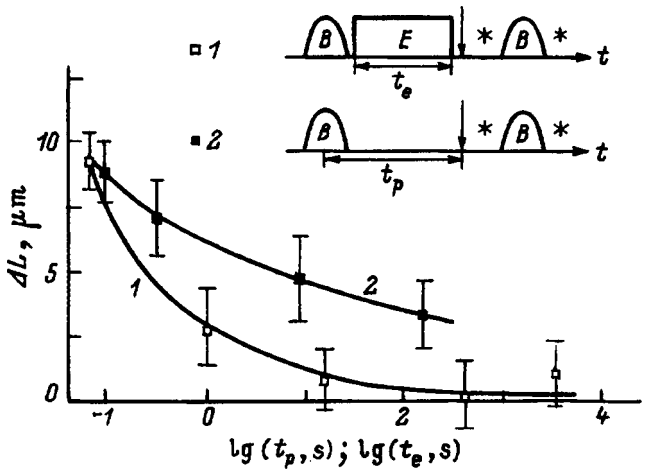

FIG. 3. Difference $\Delta L = L_0 - L$ between the mean path lengths of the dislocations initiated by MF pulses in NaCl(I) crystals not subjected (L_0) and subjected (L) to processing in an MF before the introduction of dislocations vs the duration t_e of the exposure of the samples in a weak sinusoidal EF in the pause between the first processing in an MF and the introduction of dislocations (*1*); ΔL vs the duration t_p of the pause between the first processing in an MF and the introduction of dislocations when there was no EF in the pause (*2*). The notation in the inset is the same as in Fig. 1.

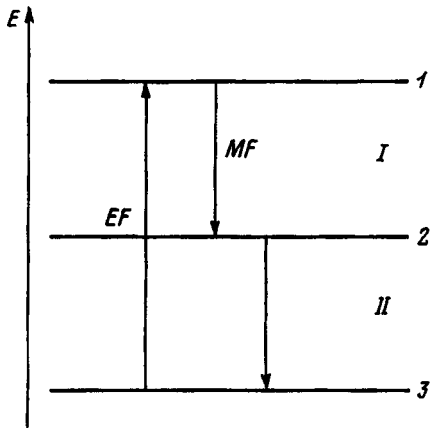

FIG. 4. Schematic energy-level diagram of the subsystem of magnetically sensitive point defects and the transitions between them caused by the action of an EF or an MF. The numbers denote the level numbers, and the arrows show the transitions. I — is the first stage, and II — is the second stage.

monomolecular reactions occur at the first stage, and bimolecular reactions occur at the second stage.[12] This can mean that the defect complexes decay at the first stage, and that the decay products recombine with each other or with other point defects at the second stage.

The insensitivity of the $\Delta L(t_p)$ dependence to switching on additional MF pulses at the second stage means that 1) the first MF pulse changes the state of the point defects irreversibly, and 2) the MF pulse that initiated the movement of the dislocations results in no additional changes of the states of the point defects by comparison with those that were achieved at the time of the first pulse. Consequently, one cause for the change of the plastic properties of the NaCl(I) crystals in an MF is that it affects the relaxation rate of metastable point defects. Since the path length of the dislocations in an MF does not equal zero even after the relaxation of the MCs, the effect of the field on the process of unpinning the dislocations from the stoppers, which was first detected in Ref. 13, should probably be regarded as another cause. In the NaCl(II) crystals, this cause of the plastification is probably the only one, as in Ref. 12. The superposition of two channels of the effect of the MF on the mobility of the dislocations in the NaCl(I) crystals apparently explains its complex multistage character.

At first glance, the spontaneous reconstruction of the path lengths of the dislocations as the pause between the MF pulses increases (Fig. 1) seems to contradict the assumption that the change of the states of the MCs is irreversible. However, in the process of introducing the dislocations, they acquire charge and can create electric fields that sensitize the point defects to the action of an MF; i.e., the sensitization of the crystal to an MF can occur not spontaneously but under the action of an external perturbation. This assumption is confirmed by the results of the second series of experiments (Fig. 2), which are evidence that an EF is capable of pumping the point defects into metastable states sensitive to an MF. This suggests that the EFs that arise during the introduction of the dislocations play a substantial role in forming the sensitivity of the plastic properties of the crystals to MFs.

Generalizing these results, the following thermodynamic scheme can be proposed to describe the transitions between the energy levels of the point-defect subsystem, whose change of state during the transitions can consist of dissociation, recombination, or intracenter transformations. As a result of the occurrence of two stages, the MCs make a transition from the initial magnetosensitive state *1* (Fig. 4) to a lower-energy state: first into state *2*, in which the mobility of the dislocations in an MF decreases, and then into a still lower-energy state *3*, in which the mobility of the dislocations again increases to a level somewhat less than in state *1*. The procedure of introducing dislocations (or of exposing the crystals to a strong EF) apparently promotes a transition of type $3 \rightarrow 1$, partially returning the defects to the magnetically sensitive state. If it is assumed that the procedure of introducing dislocations does not affect the point defects residing in state *2*, the necessity of pause t_p for reconstructing the sensitivity of the path lengths of the dislocations to an MF (Fig. 1) can be explained by the expectation of the transition of the defects into state *3*. The fact that the point defects cannot be sensitized to an MF by introducing dislocations if they are not in a definite state similar to *3* is also indirectly evidenced by the experiments reported in Ref. 4, where it was established that the softening of crystals in an MF when they are macroplastically deformed shows up most clearly in quenched crystals.

In this paper, the sensitivity of the point defects to an MF is detected after the crystals are heat-treated at 700 K, and subsequent aging at 293 K causes the influence of an MF on the point defects to disappear, and this also confirms the considerations expressed above. We should point out that the excitation mechanism and the type of MCs formed during heat treatment and exposure to an EF can be different, since the relaxation times of the induced metastable states in these cases (1 year and 15 min, respectively) differ by many orders of magnitude.

The thermodynamic scheme developed above makes it possible to assume that the third series of experiments detected the influence of a weak EF on the kinetics of the occurrence of the second (recombination) stage of the relaxation process stimulated by an MF in the point-defect subsystem. The increase of the sensitization rate of the crystal to an MF in a weak EF (Fig. 3) can be explained in principle in two ways: by the acceleration of a transition of type $2 \rightarrow 3$, or by pumping of the point defects from state *2* to state *1* (Fig. 4). The latter seems unlikely, since, for the EF used in the third series of experiments, $E \sim 10^5$ V/m, the energy communicated by the field to the point defects when they are reoriented, dissociated, ionized, and when they undergo other known excitation methods is several orders of magnitude lower than the mean thermal-fluctuation energy. At the same time, it is known that a weak EF is capable of stimulating relaxation processes in a point-defect subsystem: the aggregation of impurity–vacancy dipoles into complexes[9,10] assisted diffusion,[14] reorientation and dissociation of impurity–vacancy components when the frequency of the external field coincides with the frequency of intrinsic thermally activated jumps of the complexes to positions equivalent in energy,[8] etc.

The specific mechanism of the effect of weak and strong EFs on the point defects is still unclear, but the results obtained here make it possible to propose a simple phenomenological scheme for the processes that occur in the crystals when they are macroplastically deformed in an MF.[15,16] During the motion of charged edge dislocations, a variable EF is created around them, which keeps the point defects around a dislocation in a metastable state. It is known that the efficiency with which a dislocation overcomes point stoppers depends on the state in which they are found.[17] Switching on an MF causes the metastable states induced by the EF of the moving dislocations to relax and consequently changes the efficiency with which the dislocations are pinned by the point defects. The correlation between the charge of the dislocations and the value of the softening effect of the crystals in a constant MF, detected in Ref. 15, confirms this viewpoint.

It has thus been established that an MF promotes the relaxation of metastable point defects. Such defects can result from heat treatment or under the action of a pulsed EF. This elucidates the mechanism by which the nonequilibrium necessary for the point defects to be sensitive to an MF is created and indicates that the MCs studied here and the products of their relaxation possess uncompensated charge or dipole moment.

This work was carried out with the financial support of the Russian Fund for Fundamental Research (Grant No. 97-02-16074).

[1] Yu. I. Golovin and R. B. Morgunov, JETP Lett. **58**, 191 (1993).
[2] Yu. I. Golovin, R. B. Morgunov, S. E. Zhulikov, and D. Yu. Golovin, Fiz. Tverd. Tela (St. Petersburg) **38**, 3047 (1996) [Phys. Solid State **38**, 1666 (1996)].
[3] Yu. I. Golovin, R. B. Morgunov, and V. E. Ivanov, Fiz. Tverd. Tela (St. Petersburg) **39**, 2016 (1997) [Phys. Solid State **39**, 1803 (1997)].
[4] Yu. I. Golovin, R. B. Morgunov, and V. E. Ivanov, Izv. Vyssh. Uchebn. Zaved. Fiz. No. 4, 117 (1998).
[5] R. W. Whitworth, Adv. Phys. **24**, 203 (1975).
[6] V. I. Al'shits, E. V. Darinskaya, E. Yu. Mikhina, and E. A. Petrzhik, Fiz. Tverd. Tela (St. Petersburg) **38**, 2426 (1996) [Phys. Solid State **38**, 1333 (1996)].
[7] V. I. Al'shits, E. V. Darinskaya, O. L. Kazakova, E. Yu. Mikhina, and E. A. Petrzhik, J. Alloys Compd. **211/212**, 548 (1994).
[8] D. W. Dreyfus and R. B. Laibowitz, Phys. Rev. A **115A**, 1413 (1964).
[9] O. K. Tsarev, A. N. Narozhnyĭ, L. B. Zuev, and S. A. Datsuk, Probl. Prochnosti **32**, 1, 111 (1977).
[10] L. B. Zuev, *The Physics of the Electroplasticity of Alkali Halide Crystals* (Nauka, Novosibirsk, 1990), 120 pp.
[11] J. Frenkel, Phys. Rev. **54**, 647 (1938).
[12] Yu. I. Golovin, R. B. Morgunov, S. E. Zhulikov, V. A. Kiperman, and D. V. Lopatin, Fiz. Tverd. Tela (St. Petersburg) **39**, 634 (1997) [Phys. Solid State **39**, 554 (1997)].
[13] V. I. Al'shits, E. V. Darinskaya, T. M. Perekalina, and A. A. Urusovskaya, Fiz. Tverd. Tela (Leningrad) **29**, 467 (1987) [Sov. Phys. Solid State **29**, 265 (1987)].
[14] B. A. Zon, Izv. Vyssh. Uchebn. Zaved. Fiz. **33**, No. 11, 131 (1974).
[15] Yu. I. Golovin and R. B. Morgunov, JETP Lett. **61**, 596 (1995).
[16] A. A. Urusovskaya, V. I. Al'shits, A. E. Smirnov, and N. N. Bekkauer, JETP Lett. **65**, 497 (1997).
[17] C. Zaldo, J. Garcia Sole, and F. Agullo-Lopez, J. Mater. Sci. **17**, 1465 (1982).

Translated by W. J. Manthey

Distribution of the isotopes produced in the $YBa_2Cu_3O_{7-x}$ superconductor and $PbZr_{0.54}Ti_{0.46}O_3$ ferroelectric by energetic charged particles

V. A. Didik, R. Sh. Malkovich, and E. A. Skoryatina

A. F. Ioffe Physicotechnical Institute, Russian Academy of Sciences, 194021 St. Petersburg, Russia

V. V. Kozlovskiĭ

St. Petersburg State Technical University, 195251 St. Petersburg, Russia

(Submitted May 26, 1998)
Fiz. Tverd. Tela (St. Petersburg) **40**, 2189–2192 (December 1998)

A study has been made of the concentration profiles of radioactive isotopes produced by transmutation in the $YBa_2Cu_3O_{7-x}$ superconductor and $PbZr_{0.54}Ti_{0.46}O_3$ ferroelectric by energetic protons (10 and 15 MeV), deuterons (4 MeV), and ^{3}He and ^{4}He nuclei (20 MeV). Profiles of two types have been observed: monotonic and with a maximum. It is shown that the type of isotope concentration profile is determined by the nature of the cross-section energy dependence of the nuclear reaction producing a given isotope. © *1998 American Institute of Physics.* [S1063-7834(98)01112-5]

Nuclear transmutation is widely used in the production of radioactive isotopes and analysis of residual impurities in solids. Considerable interest has been expressed recently in transmutation doping of solids by thermal neutrons. In contrast to neutrons, which possess a high penetrating ability, charged particles penetrate into a solid to a very small depth. As a result, transmutation-produced isotopes occur only within a local near-surface layer, and it is here that the isotope profiles are formed.

Our earlier studies dealt with the profiles of the isotopes produced in III–V compounds[1,2] and chalcopyrite $CuInSe_2$ (Ref. 3 and 4) by energetic charged particles, namely, protons, deuterons, and ^{3}He and ^{4}He nuclei. This work reports preparation and profile analysis of the isotopes created by such irradiation in the $YBa_2Cu_3O_{7-x}$ superconductor (YBCO) and $PbZr_{0.54}Ti_{0.46}O_3$ ferroelectric (PZT).

1. EXPERIMENTAL TECHNIQUE

Plane-parallel samples 1–2 mm thick and 0.1–1 cm^2 in area were clamped to a water-cooled brass plate and irradiated through a 1-cm^2 diaphragm in a cyclotron.[5] The YBCO superconductor was irradiated by 10-MeV protons, 4-MeV deuterons, 20-MeV ^{3}He nuclei, and 20-MeV ^{4}He nuclei. The PZT ferroelectric was subjected to 15-MeV protons and 20-MeV ^{4}He nuclei. The beam was monochromatic to within 5%. The particle flux was varied from 6×10^{11} to 3×10^{12} cm$^{-2}\cdot$s^{-1}, and the irradiation time, from 15 min to 4 h. Accordingly, the dose accumulated varied from 10^{15} to 10^{16} cm^{-2}.

The profiles of transmutation-produced radioactive isotopes were determined by successive removal of thin plane-parallel layers and by measuring their activity. The layers were ground off, and their activity was measured with a calibrated Ge(Li) gamma spectrometer. The uniformity of isotope distribution over the sample cross section was monitored by autoradiography.

2. RESULTS AND THEIR DISCUSSION

We measured in the YBCO superconductor the profiles of the radioactive isotopes ^{65}Zn, ^{89}Zr, ^{64}Cu, ^{90}Nb, ^{66}Ga, ^{92m}Nb, ^{139}Ce, and ^{141}Ce produced by reactions[6] ^{65}Cu$(p,n)^{65}$Zn, ^{89}Y$(p,n)^{89}$Zr, ^{63}Cu$(d,p)^{64}$Cu, ^{89}Y$(^3$He$,2n)^{90}$Nb, ^{63}Cu$(^4$He$,n)^{66}$Ga, ^{89}Y$(^4$He$,n)^{92m}$Nb, ^{136}Ba$(^4$He$,n)^{139}$Ce, and ^{138}Ba$(^4$He$,n)^{141}$Ce. As seen from Fig. 1a–1d, the concentration of various isotopes reaches $10^{13}-10^{14}$ cm^{-3} in irradiation by protons, deuterons, and ^{4}He nuclei, and is slightly in excess of 10^{12} cm^{-3} in the case of ^{3}He nuclei (the quoted concentrations relate to the end of the irradiation). The profile depth varies from 60 to 170 μm. When irradiated by ^{4}He nuclei, the profile depth is the largest for the ^{66}Ga isotope, and the smallest for ^{139}Ce. All profiles fall off monotonically away from the surface, with the exception of the ^{92m}Nb isotope profile, which exhibits a fairly flat maximum. Note that irradiation by protons was carried out under oblique incidence (18° beam angle to the surface).

In the PZT ferroelectric, we measured the profiles of the radioactive isotopes ^{48}V, ^{90}Nb, ^{92m}Nb, ^{206}Bi, ^{51}Cr, ^{93m}Mo, and ^{99}Mo produced by the reactions (Ref. 6) ^{48}Ti$(p,n)^{48}$V, ^{90}Zr$(p,n)^{90}$Nb, ^{92}Zr$(p,n)^{92m}$Nb, ^{206}Pb$(p,n)^{206}$Bi, ^{48}Ti$(^4$He$,n)^{51}$Cr, ^{90}Zr$(^4$He$,n)^{93m}$Mo, and ^{96}Zr$(^4$He$,n)^{99}$Mo. The concentration of various isotopes reaches $4\times10^{12}-10^{13}$ cm^{-3} in irradiation by protons, and $10^{13}-10^{14}$ cm^{-3} when irradiated by ^{4}He nuclei (Fig. 2a and 2b). The profile depth is 70–150 μm for ^{4}He nuclei, and 420–650 μm for protons. The profiles of the ^{90}Nb, ^{206}Bi, and ^{93m}Mo isotopes are monotonic, whereas those of ^{48}V, ^{92m}Nb, ^{51}Cr, and ^{99}Mo pass through a maximum. The PZT was irradiated by protons under continuous variation of the beam incidence angle.

As follows from the measurements, the concentration profiles obtained in the above experimental conditions are of two types, namely, monotonic and with a maximum. Profiles with a maximum are observed for the ^{92m}Nb, ^{99}Mo, and ^{51}Cr

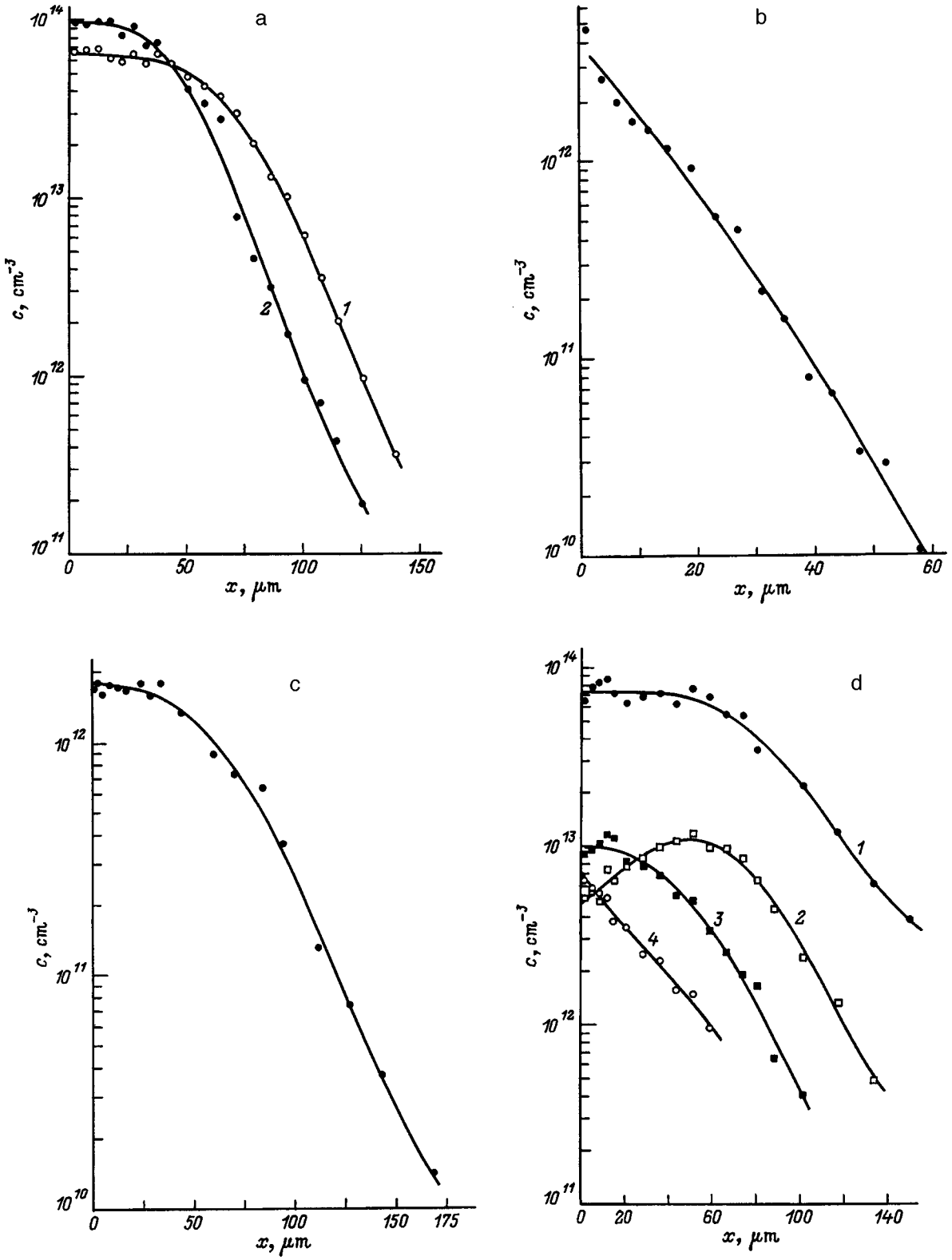

FIG. 1. Depth profiles of radioactive transmutation isotopes produced in irradiation of $YBa_2Cu_3O_{7-x}$ by (a) protons, (b) deuterons, (c) ^{3}He, and (d) ^{4}He. (a) *1* — ^{65}Zn, *2* — ^{89}Zr; (b) ^{64}Cu; (c) ^{90}Nb; (d) *1* — ^{66}Ga, *2* — ^{92m}Nb, *3* — ^{141}Ce, *4* — ^{139}Ce.

isotopes produced by ^{4}He nuclei in the $(^4\mathrm{He},n)$ reaction, as well as for ^{92m}Nb and ^{48}V obtained by the (p,n) reaction.

To find an interpretation for the isotope profile pattern, consider the expression relating the concentration of the transmutation-produced radioactive isotope $c(x)$ to the parameters of the material and irradiation[2,7]

$$c(x)=N\Phi\sigma(x)\lambda^{-1}[1-\exp(-\lambda t)], \qquad (1)$$

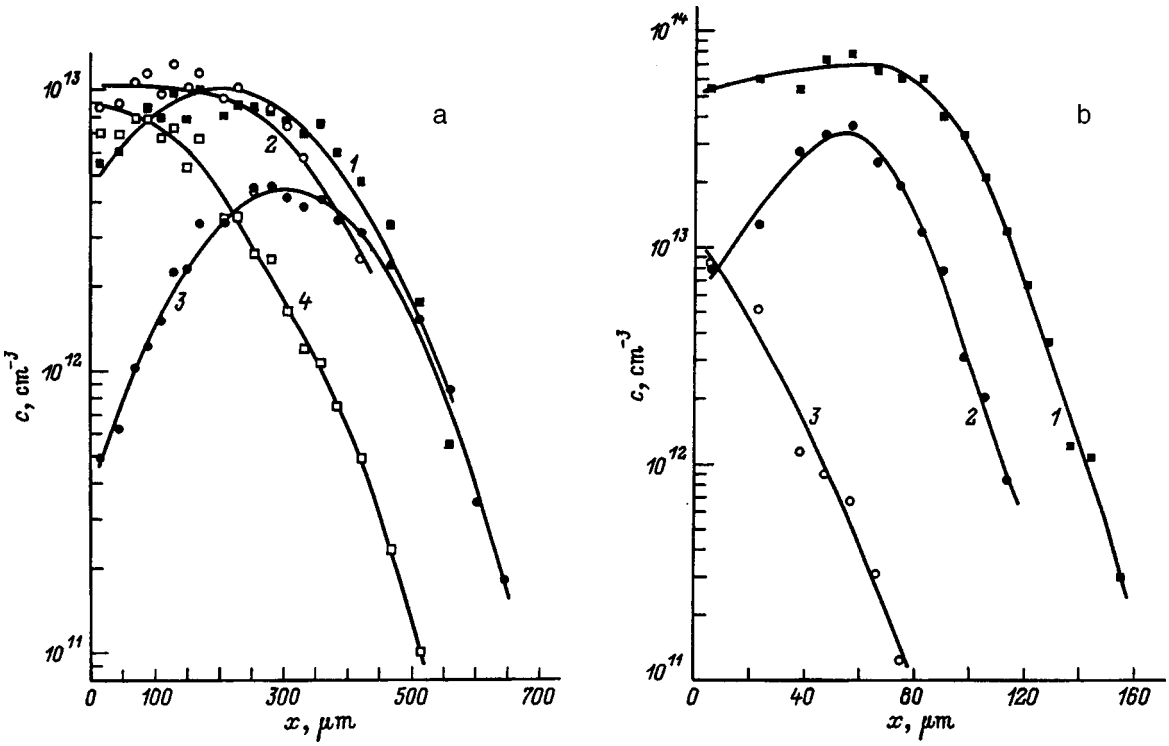

FIG. 2. Depth profiles of radioactive transmutation isotopes produced in irradiation of $PbZr_{0.54}Ti_{0.46}O_3$ by (a) protons and (b) ^{4}He nuclei. (a) *1* — ^{48}V, *2* — ^{90}Nb, *3* — ^{92m}Nb, *4* — ^{206}Bi; (b) *1* — ^{51}Cr, *2* — ^{99}Mo, *3* — ^{93m}Mo.

where N is the concentration of the stable isotope of the material, Φ is particle flux, σ is the cross section of the nuclear reaction, λ is the isotope decay constant, t is the irradiation time, and x is the coordinate (the distance from the sample surface). $c(x)$ is the concentration at the end of irradiation.

Assuming the particle flux to be coordinate independent, $\Phi = \text{const}$, and taking into account that $N = \text{const}$, one readily sees that the isotope profile pattern is determined by the variation of the reaction cross section with coordinate, i.e., by the behavior of function $\sigma(x)$, namely, $c(x) \propto \sigma(x)$. The reaction cross section is an indirect function of coordinate, because it depends on the local energy of the particles, $\sigma = \sigma(E)$, and the latter, in its turn, varies with coordinate, $E = E(x)$. Thus we have $\sigma = \sigma[E(x)]$. The particle energy decreases monotonically with depth, whereas the $\sigma(E)$ dependence may follow a more complex course. In particular, the $\sigma(E)$ function for $(^4\text{He},n)$ reactions is a curve with a maximum.[8] In this case the pattern of the $c(x)$ dependence will be determined by the relative magnitude of E_m, which is the position of the maximum in the $\sigma(E)$ curve, and by E_0, the initial energy of ^{4}He nuclei. If $E_0 < E_m$, the reaction cross section will decrease monotonically with decreasing particle energy, i.e., with depth $(d\sigma/dE > 0)$, which implies a monotonic decrease of the transmutation isotope concentration $c(x)$. And conversely, if $E_0 > E_m$, the reaction cross section will initially increase with decreasing particle energy $(d\sigma/dE < 0)$, to begin a monotonic fall-off after the local energy of particles has dropped to E_m. The concentration $c(x)$ of the transmutation-produced isotope will behave in the same way, namely, it

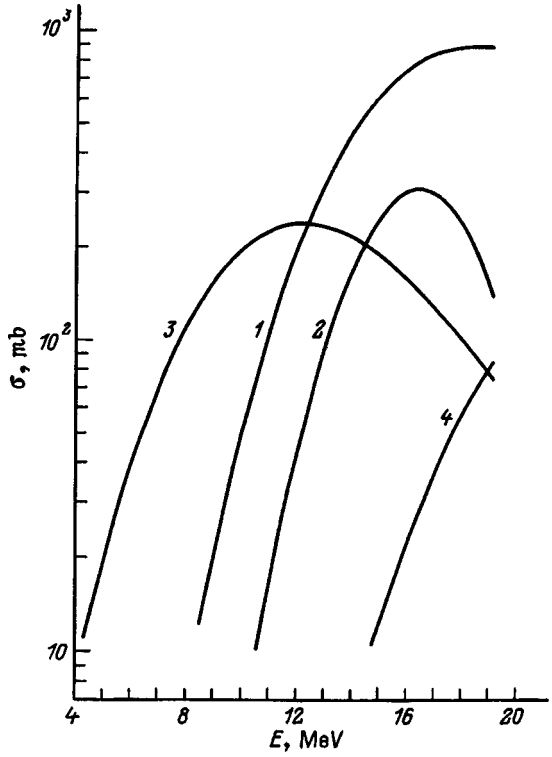

FIG. 3. Energy dependence of nuclear reaction cross sections. *1* — ^{63}Cu $(^4\text{He},n)$ ^{66}Ga, *2* — ^{89}Y $(^4\text{He},n)$ ^{92m}Nb, *3* — ^{96}Zr $(^4\text{He},n)$ ^{99}Mo, *4* — ^{90}Zr $(^4\text{He},n)$ ^{93m}Mo.

will increase with distance from the surface, reach a maximum at a certain depth, and decrease subsequently. The maximum for the $(^4\mathrm{He},n)$ reactions lies usually at energies exceeding the reaction threshold E_{th} by about the same amount ΔE, $E_{\mathrm{m}}=E_{\mathrm{th}}+\Delta E$, where $\Delta E\simeq 11$ MeV.[8] Hence for the isotopes forming in the $(^4\mathrm{He},n)$ reaction with a low threshold E_{th} the inequality $E_0>E_{\mathrm{m}}$ will hold, and the profiles for such isotopes should have maxima. By contrast, for isotopes with a high threshold E_{th} the inequality $E_0<E_{\mathrm{m}}$ will be upheld, thus making their depth profiles monotonic. Indeed, the profiles obtained in our experiments for isotopes with a low reaction threshold, namely, ^{92}Nb ($E_{\mathrm{th}}=7.2$ MeV, $E_{\mathrm{m}}=18.2$ MeV), ^{99}Mo ($E_{\mathrm{th}}=5.1$ MeV, $E_{\mathrm{m}}=16.1$ MeV), and ^{51}Cr ($E_{\mathrm{th}}=2.9$ MeV, $E_{\mathrm{m}}=13.9$ MeV) pass through a maximum (at $E_0=20$ MeV), see Figs. 1d and 2b), whereas the other isotopes exhibit monotonic profiles. Similar considerations can apparently be used for interpretation of the depth profiles of isotopes forming in other nuclear reactions.

As for the concentration profile depth, it correlates with the particle range and increases with decreasing threshold of the nuclear reaction involved. Indeed, as evident from Fig. 1d, the profile depth is the largest for the ^{66}Ga isotope, which is characterized by the lowest threshold ($E_{\mathrm{th}}=6.9$ MeV), and the smallest, for ^{139}Ce with $E_{\mathrm{th}}=7.9$ MeV.

We used the transmutation isotope profiles to determine the cross-section energy dependence $\sigma(E)$ for the nuclear reactions producing the given isotopes. The procedure employed to find $\sigma(E)$ was as follows.[9] First the experimental dependence $c(x)$ was used to derive the function $\sigma(x)$, after which $\sigma(E)$ was determined by means of $E(x)$. The $E(x)$ dependence $E(x)$ was calculated from data[10] on the retardation power of elements, taking due account of the principle of additivity. The results obtained are illustrated for a few reactions in Fig. 3.

[1] V. A. Didik, V. V. Kozlovskiĭ, R. Sh. Malkovich, E. A. Skoryatina, and B. A. Shustrov, Pis'ma Zh. Tekh. Fiz. **15**, 12, 19 (1989) [Sov. Tech. Phys. Lett. **15**, 920 (1989)].
[2] V. A. Didik, V. V. Kozlovskiĭ, R. Sh. Malkovich, and E. A. Skoryatina, Fiz. Tekh. Poluprovodn. **27**, 265 (1993); *ibid.* **29**, 2078 (1995) [Semiconductors **27**, 148 (1993); **29**, 1085 (1995)].
[3] V. A. Didik, V. V. Kozlovskiĭ, R. Sh. Malkovich, and E. A. Skoryatina, Pis'ma Zh. Tekh. Fiz. **20**, 16, 59 (1994) [Tech. Phys. Lett. **20**, 920 (1994)].
[4] K. Gartsman, L. Chernyak, V. Lyahovitskaya, D. Cahen, V. Didik, V. Kozlovsky, R. Malkovich, E. Skoryatina, and V. Usacheva, J. Appl. Phys. **82**, 4282 (1997).
[5] B. N. Zabrodin, L. F. Zakharenkov, and V. V. Kozlovskiĭ, Vopr. At. Nauki Tekhn., Ser. Fiz. Rad. Povr. Rad. Mat. 3(57), 87 (1991).
[6] G. Maples, G. Goth, and J. Cerny, Nucl. Data, Sect. A **2**, 429 (1967).
[7] C. Vandecasteele, *Activation Analysis with charged particles* [Ellis Horwood Ltd, Chichester, 1988; Mir, Moscow, 1991, 208 pp.].
[8] H. Münzel and J. Lange, in *Uses of Cyclotrons in Chemistry, Metallurgy, and Biology*, edited by C. B. Amphlett (Butterworths, London, 1969), p. 373.
[9] V. A. Didik, R. Sh. Malkovich, E. A. Skoryatina, and V. V. Kozlovskiĭ, At. Energ. **77**, 81 (1994).
[10] O. F. Nemets and Yu. F. Gofman, *Handbook on Nuclear Physics* (Naukova Dumka, Kiev, 1975).

Translated by G. Skrebtsov

MAGNETISM AND FERROELECTRICITY

Local structure of the rhombic Fe^{3+} center in $KTaO_3$

V. V. Laguta

Institute for Problems in Materials Sciences, National Academy of Sciences of Ukraine, 252180 Kiev, Ukraine

(Submitted April 30, 1998)
Fiz. Tverd. Tela (St. Petersburg) **40**, 2193–2197 (December 1998)

A study is reported of the effect of high-temperature annealing in oxygen, an inert gas, and water vapor on EPR spectra of the Fe^{3+} center of different local symmetries in the incipient ferroelectric $KTaO_3$. An analysis of the relations obtained permits one to propose and substantiate a model of the rhombic Fe^{3+} center, by which Fe^{3+} substitutes for Ta^{5+} near two oxygen vacancies (Fe^{3+}-$2V_O$). Calculations of the crystal-field parameters performed within the Newman superposition model showed in the rhombic center the Fe^{3+} ion is displaced along [011] from the Ta^{5+} position it occupies within the tetrahedron formed by four oxygens, to a distance of about 0.25 Å. Some of the recent results obtained in second-harmonic light scattering in iron-doped $KTaO_3$ samples are interpreted. It is shown that, within the temperature range of 4.2–300 K, rhombic Fe^{3+} centers are static electric dipoles, and that they cannot therefore be a source of dielectric losses in $KTaO_3$ at $T \approx 40$ K, as suggested earlier in some publications. © *1998 American Institute of Physics.* [S1063-7834(98)01212-X]

Recent years have been witnessing increasing interest in the investigation of Fe^{3+} paramagnetic centers in $KTaO_3$ in connection with observation in this crystal at low temperatures ($T<40$ K) of second-harmonic light scattering,[1] weak first-order Raman scattering,[2] and dielectric losses,[3] phenomena atypical of its cubic centrosymmetric structure. Because all these phenomena turned out to be dependent on the actual sample type, they were assumed to be due to defects. Iron impurity centers were most frequently discussed as possible candidates among some residual impurities and intrinsic defects occurring in $KTaO_3$. The Fe^{3+} ion substitutes for both K^+ and Ta^{5+} cations to form a number of low-symmetry paramagnetic centers, which may serve as sources of polar regions at low temperatures, where the polarization correlation length becomes large.

The least studied among all known Fe^{3+} centers in $KTaO_3$ is a center of rhombic symmetry first described in Ref. 4. This observation was followed by a comprehensive study of EPR spectra of these paramagnetic impurities.[5,6] In particular, there were even found two different Fe^{3+} EPR spectra of rhombic symmetry, one of which was assumed to be associated with Fe^{3+} occupying a Ta^{5+} site, and the other, a K^+ site. Quite recently, however, it has been shown that in actual fact there is only one rhombic Fe^{3+} center, but it exhibits strongly temperature-dependent parameters of the spin Hamiltonian.[7] Despite such comprehensive studies of EPR spectra of this center, its local structure remained, nevertheless, unclear. The model proposed earlier,[5] namely, Fe^{3+} occupying a Ta^{5+} site with a charge-compensating interstitial ion nearby, did not find experimental confirmation, as this will be shown below.

The present work studies the effect of high-temperature annealing in He, O_2, and water vapor ambients on the EPR spectrum of the rhombic Fe^{3+} center. An analysis of the relations obtained, as well as the crystal-field parameters calculated within the superposition model of Newman permitted us to propose and substantiate the model by which Fe^{3+} substitutes for Ta^{5+} with formation of two oxygen vacancies (V_O) on the adjacent faces of the $KTaO_3$ cubic lattice. A discussion is given of the role of iron rhombic centers in such low-temperature phenomena occurring in the centrosymmetric cubic $KTaO_3$ as second-harmonic light scattering, first-order Raman scattering, and dielectric losses.

1. EXPERIMENTAL

Most of the EPR measurements were made in the 9 GHz range on $KTaO_3$ samples exhibiting the strongest rhombic Fe^{3+} spectrum (Fig. 1a). The analysis of rhombic Fe^{3+} spectra was based on the spin Hamiltonian of the type

$$\hat{H} = g\beta \mathbf{B}\hat{S} + b_2^0\hat{O}_2^0 + b_2^2\hat{O}_2^2, \tag{1}$$

where for $T=300$ K, $g=2.00$, $b_2^0=0.440(2)$ cm^{-1}, $b_2^2=0.196(2)$ cm^{-1} coincide with the values quoted[5] earlier. The principal axes Z and X of the centers are always oriented along the $\langle 011\rangle$ directions, and the Y axis coincides with one of the $\langle 001\rangle$ cubic directions of the crystal. There are six magnetically nonequivalent rhombic Fe^{3+} centers altogether, which differ in the direction of their principal axes. As the temperature is lowered, b_2^0 and b_2^2 decrease substantially to reach 0.485 cm^{-1} and 0.277 cm^{-1}, respectively, at $T=4.2$ K. The temperature dependences $b_2^0(T)$ and $b_2^2(T)$ obtained by us (Fig. 2) are similar to those reported[7] earlier.

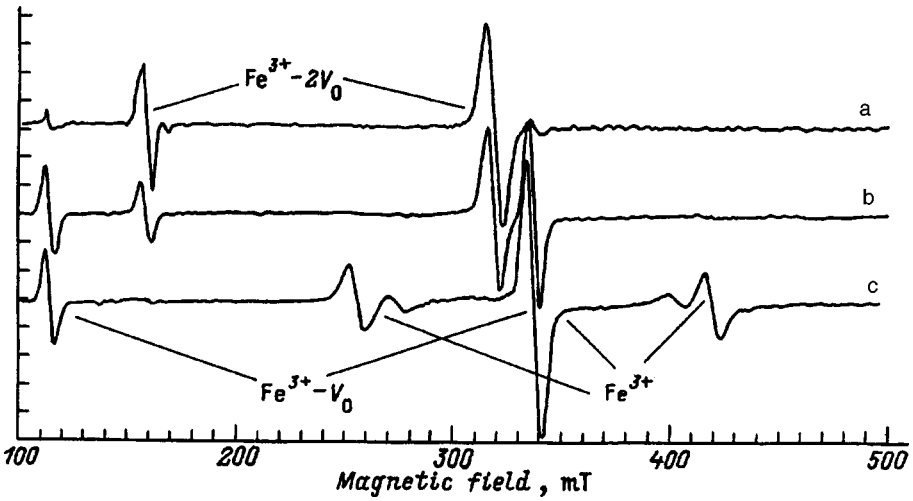

FIG. 1. EPR spectra of Fe^{3+} in $KTaO_3$: (a) as-grown, (b) after annealing in O_2 ambient, (c) after annealing in water vapor. $\nu = 9.4$ GHz, $T = 300$ K.

To establish the type of the defects lowering the local symmetry of the Fe^{3+} ion in $KTaO_3$ and acting at the same time as compensators of its deficient positive charge, we carried out a number of high-temperature anneals in O_2, He, and H_2O ambients. As demonstrated earlier (see, e.g., Ref. 8), such treatment of crystals has a very strong influence on impurity charge compensation and permits one therefore to test reliably various models of the local structure of paramagnetic centers. The high-temperature annealing of the crystals was carried out at 950–1000 °C for three to six h, with a slow (~10 °C/min) cooling and heating of samples. EPR spectra were recorded at 295–300 K.

Annealing a crystal in the O_2 ambient for five to six h reduced the EPR signal intensity of rhombic Fe^{3+} by about two times and brought about the appearance of a strong $Fe^{3+}-V_O$ spectrum, which was practically absent before the anneal, and of a weak spectrum of cubic Fe^{3+} in the Ta^{5+} site (Fig. 1b). Repeated anneal of the crystal in an inert environment (Ar or He) restored the original rhombic spectrum. Annealing the crystals with a rhombic Fe^{3+} in water vapor produced still stronger changes in EPR spectra. Already after a 2–3-h anneal, the rhombic Fe^{3+} spectrum disappeared completely, to be replaced by strong signals of $Fe^{3+}-V_O$ and cubic Fe^{3+} in the Ta^{5+} site (Fig. 1c). Subsequent annealing in an inert atmosphere likewise restored the original rhombic spectrum. The above changes in Fe^{3+} EPR spectra are displayed schematically in Fig. 3. One can see, in particular, that the total concentration of all Fe^{3+} centers remained practically constant in all crystal treatments, which implies that the only factor that did change was the mechanism of iron charge compensation in the lattice. It may be of interest to note in this connection that treatment of a crystal in a hydrogen ambient results in disappearance of all Fe^{3+} spectra. This behavior of spectra under annealing in hydro-

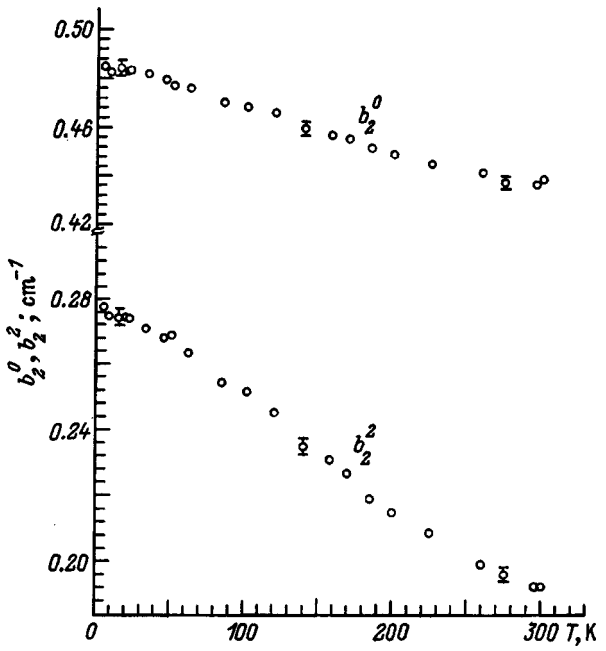

FIG. 2. Temperature dependence of spin-Hamiltonian parameters b_2^0 and b_2^2 of rhombic Fe^{3+} center in $KTaO_3$.

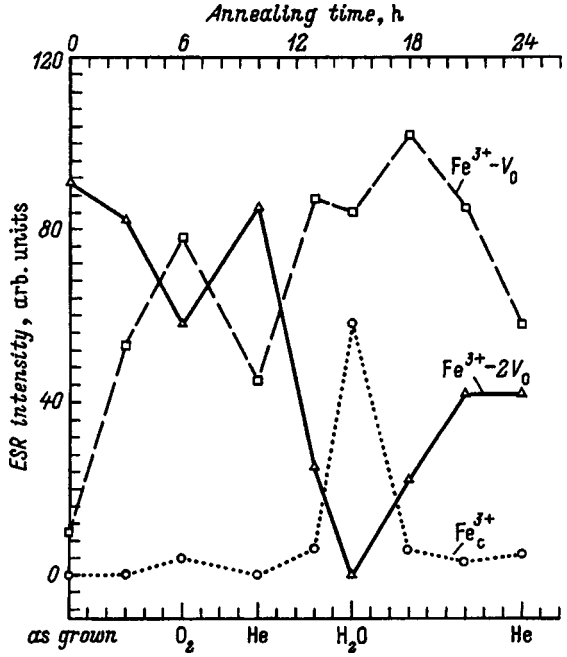

FIG. 3. Dependence of EPR spectral intensity of Fe^{3+} in $KTaO_3$ on annealing in O_2, He, and H_2O ambients. $T = 300$ K.

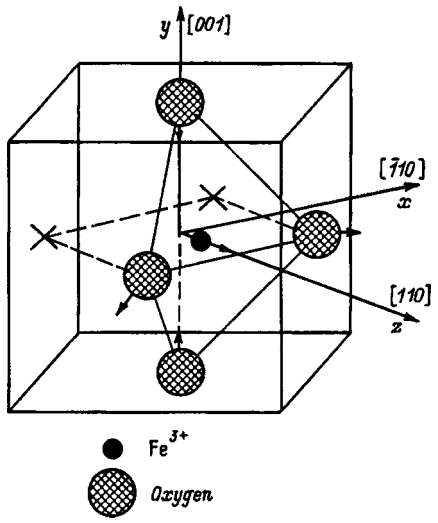

FIG. 4. Model of rhombic $Fe^{3+}-2V_O$ center in $KTaO_3$.

gen attests to a change of the charge state of the iron impurity itself, rather than of its local environment.

Let us consider to what extent the model of a rhombic Fe^{3+} center with a positively charged interstitial compensating ion proposed earlier can be reconciled with the above experimental data. Obviously enough, in order to account for the spectral changes observed under annealing in oxygen and H_2O vapor with this mechanism of compensation of the deficient Fe^{3+} charge one has to assume removal of the charge-compensating ion from the paramagnetic ion and its subsequent return under annealing in an inert atmosphere. The probability of such a process can be very low, because the $KTaO_3$ lattice does not have free channels for transport of interstitials. It would be difficult also to explain the rise in $Fe^{3+}-V_O$ concentration under annealing in H_2O, which usually drops noticeably in the absence of rhombic Fe^{3+} centers[8].

In our opinion, the consecutive transformation of the rhombic to axial $Fe^{3+}-V_O$ to cubic $Fe^{3+}(Ta^{5+})$ center under annealing in oxygen clearly implies its connection with oxygen vacancies. It is obvious also that the rhombic symmetry of the center may be due to the two oxygen vacancies in the vicinity of Fe^{3+}, as this is shown schematically in Fig. 4. The charge of the $Fe^{3+}-2V_O$ center is not compensated in the crystal lattice, and therefore formation of this defect requires the presence of impurities with smaller valence than Ta^{5+}, for instance, of Al^{3+} or Sn^{4+}, and, possibly, of a K vacancy.

Annealing in water vapor also changes the compensation mechanism of the deficient Fe^{3+} charge. Such annealing is known[9] to entail saturation of the crystal by protons bound to oxygen in OH^- molecular groups, which compensate efficiently the positive charge deficiency in the lattice due to their high mobility. As a result, the oxygen vacancies are no longer operative and become filled by the oxygen forming in water decomposition on the crystal surface, which leads to the transformation of the rhombic $Fe^{3+}-2V_O$ center first to the trigonal $Fe^{3+}-V_O$, and, finally, to the cubic Fe^{3+} center.

Formation of two oxygen vacancies near Fe^{3+} shift the remaining four oxygens and the Fe^{3+} ion itself from their sites toward new equilibrium positions. Further calculations made within the Newman superposition model show that it is this rearrangement in the environment of Fe^{3+} and its displacement that govern the symmetry and magnitude of the crystal field. The model of Newman was chosen by us because it is simple and was used extensively in studies of the behavior of Fe^{3+} in octahedral structures. It was applied to advantage before in the investigation of the local structure of iron centers in $SrTiO_3$,[10] $BaTiO_3$,[11] $PbTiO_3$,[12] and other crystals.

It is known that the Newman superposition model is based on a linear summation of contributions due to each ligand to the quantities b_n^m:

$$b_n^m=\sum_i \bar{b}_n(R_i)K_n^m(\theta_i,\varphi_i), \tag{2}$$

where $K_n^m(\theta_i,\varphi_i)$ are spherical functions of polar angles θ and φ. For instance, for $n=2$

$$K_2^0=\frac{1}{2}(3\cos^2\theta-1) \quad \text{and} \quad K_2^2=\frac{3}{2}\sin^2\theta\cos 2\varphi. \tag{3}$$

The model function of distance R between the paramagnetic ion and a ligand, $\bar{b}_n(R_i)$, is usually assumed to be a power-law function of the interatomic distance

$$\bar{b}_2(R_i)=\bar{b}_2(R_0)(R_0/R_i)^{t_2}, \tag{4}$$

where exponent t_2 is of the order of eight, R_0 is the origin for distance reckoning, and is usually chosen equal to $c/2$ (c is the lattice constant), and $\bar{b}_2(R_0)$ is a model parameter. The values of t_2 and $\bar{b}_2(R_0)$ can be obtained for each type of ligand and lattice structure from an experimental study of the effect of axial pressure on EPR spectra. Because these data are not available for $KTaO_3$, parameter $\bar{b}_2(R_0)$ was calculated by us in the same way this was done[11] for $BaTiO_3$, namely, by assuming $\bar{b}_2(R_0)$ to behave with distance as in Eq. (4), and using the parameters obtained[10] for MgO:

$$\bar{b}_2(R_0)=\bar{b}_2(2.101\,\text{Å})\left[\frac{2.101(\text{Å})}{R_0}\right]^8, \tag{5}$$

where

$$\bar{b}_2(2.101\,\text{Å})=-0.412(25)\ \text{cm}^{-1},$$

and

$$R_0=c/2=1.994\ \text{Å}.$$

Applying Eqs. (2)–(5) to the rhombic $Fe^{3+}-2V_O$ center with due account of its geometry shown in Fig. 4, we obtained dependences of the spin-Hamiltonian parameters b_2^0 and b_2^2 on the magnitude and direction of displacement of the oxygen ions and of the Fe^{3+} itself. Some of these relations, which approach closest the experimental values of b_2^0 and b_2^2, are presented graphically in Fig. 5. As seen from the figure, in order to reconcile the latter with calculations, the Fe^{3+} ion should be displaced from the Ta^{5+} position at the center of the oxygen octahedron into the quasi-tetrahedron made up by four oxygens, as shown in Fig. 4. For $T=300$ K, the displacement $\Delta=0.25$ Å. The oxygens near

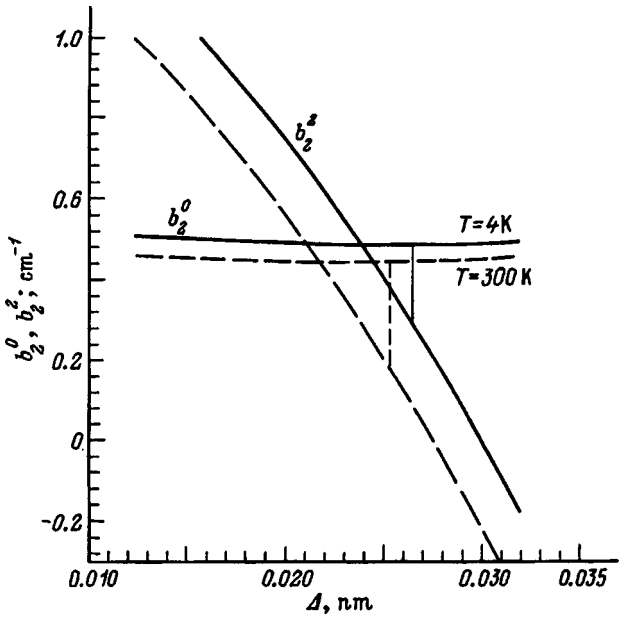

FIG. 5. Calculated crystal-field parameters b_2^0 and b_2^2 of rhombic Fe^{3+} center in $KTaO_3$ *vs* off-center Fe^{3+} displacement. Solid lines correspond to $T=4.2$ K, and dashed lines, to $T=300$ K. Vertical sections identify Fe^{3+} displacement for $T=4.2$ and 300 K.

the Fe^{3+} ion likewise undergo positional changes. The two of them lying on the Y axis shift toward one another to a distance $d\approx 0.044$ Å, whereas the other, by contrast, move away through about the same distance.

The presence of two oxygen vacancies near Fe^{3+} makes the position of this ion unstable, which becomes manifest in a strong variation of the crystal-field parameters with temperature (Fig. 2). These temperature-induced variations $b_2^0(T)$ and $b_2^2(T)$ can be readily derived by making the Fe^{3+} and oxygen displacements temperature dependent. As shown by calculations, b_2^0 depends primarily on the displacement of the oxygens lying on the [001] axis, whereas b_2^2 is determined by movements of both the oxygens and of the Fe^{3+} itself (Fig. 5). As the temperature decreases, both b_2^0 and b_2^2 increase, as does their ratio b_2^2/b_2^0, which corresponds to increasing Δ and d.

This pattern of ionic displacements in the $Fe^{3+}-2V_O$ rhombic center is not in full accord with purely ionic Coulomb interactions, because a Fe^{3+} ion occupying the Ta^{5+} position carries an effective negative charge and, hence, should be attracted toward the positive vacancy V_O. Such a center can apparently be configurationally stable only in the presence of strong covalent interactions, and an analysis of its electronic structure should preferably be done in terms of a more rigorous shell model.

2. DISCUSSION OF RESULTS

A rhombic Fe^{3+} center, similar in symmetry, exists in $SrTiO_3$ as well,[13] where it was supposed to be associated with an interstitial ion (possibly Na^+) located in the [011] direction. This model of the center has a number of inconsistencies, the most significant of them being that the distortions introduced by the interstitial ion into the cubic lattice near Fe^{3+} should be axially symmetric relative to the [011] axis. Obviously enough, the lower rhombic symmetry of a paramagnetic center in a cubic lattice requires the presence of two rather than one additional defect. Therefore the model of a rhombic Fe^{3+} center in $SrTiO_3$ requires refinement.

The rhombic $Fe^{3+}-2V_O$ center in $KTaO_3$ is an extended defect which has an electric dipole moment in addition to disrupting locally the inversion symmetry. At low temperatures ($T<40$ K), the local distortions induced by this defect in $KTaO_3$ is characterized by a high polarizability and may be as large as a few lattice constants, thus giving rise to weak first-order Raman and second-harmonic light scattering. Consider in this connection some results on second-harmonic scattering obtained[4] recently on Fe-doped $KTaO_3$.

It was established[14] that Fe doping of $KTaO_3$ in amounts up to 5,000 ppm does not bring about a noticeable increase in second-harmonic light scattering, as could be expected, and does not bear out, therefore, the contribution of Fe centers to the low-temperature anomalies. In our opinion, this result could be due to the low concentration of low-symmetry (non-cubic) Fe^{3+} centers in the samples under study, because a Fe impurity produces in $KTaO_3$ a variety of paramagnetic centers of different symmetries. The concentration ratios among these centers depend very strongly on the doping level and crystal growth technology. As a rule, the concentration of low-symmetry iron centers ($Fe^{3+}-V_O$, $Fe^{3+}-O^{2-}$, $Fe^{3+}-2V_O$) is small and constitutes 100–200 at. ppm only. Their number is determined by the amount of defects compensating the deficient (extra) Fe^{3+} charge, such as oxygen vacancies and interstitial oxygen. The number of such defects in crystals grown under proper conditions should be small. As a result, the total number of centers capable of locally distorting the cubic symmetry in the presence of an iron impurity may not change compared to their number in an undoped crystal. Annealing iron-doped $KTaO_3$ in a hydrogen environment, as already mentioned, reduces the valence of Fe^{3+}, and therefore, all other conditions being equal, one should expect in such crystals a smaller number of defects involving oxygen vacancies and, hence, a lower intensity of second-harmonic scattering, i.e., exactly what was observed in the experiment.

Rhombic Fe^{3+} centers were invoked also to explain the dielectric losses in $KTaO_3$ at $T\approx 40$ K ($\nu=1$ kHz).[3] The frequency dispersion of the losses was described by the Arrhenius law with an activation energy $E_a\approx 0.078$ eV and a prefactor $\tau_0\approx 10^{-13}$ s^{-1}. The dielectric loss peak in crystals containing rhombic Fe^{3+} centers was found to increase. As already pointed out, these centers have indeed an electric dipole moment, but they are static, non-orienting dipoles, at least within the 4.2–300 K temperature range, because neither the EPR line widths nor the spectrum symmetry vary at these temperatures. It is clear also that reorientation of a dipole impurity with $E_a=0.078$ eV and $\tau_0=10^{-13}$ s^{-1}, which has a magnetic spin moment, would produce a strong broadening of EPR spectra already at $T\approx 100$ K. In a general case, for such a dipole impurity one should expect the values of E_a and τ_0 derived from dielectric-loss dispersion and variation of EPR spectra with temperature or frequency to

coincide, as this occurs, for example, for Mn^{2+} in $KTaO_3$ (Ref. 15) and KCl (Ref. 16).

Thus rhombic Fe^{3+} centers cannot be responsible for dielectric losses in $KTaO_3$ at $T \approx 40$ K, as this was assumed earlier, and the origin of these losses remains unclear.

[1] W. Prusseit-Elffroth and F. Schwabl, Appl. Phys. A **51**, 361 (1990).
[2] H. Uwe, K. B. Lyons, H. L. Carter, and P. A. Fleury, Phys. Rev. B **33**, 6436 (1986).
[3] B. Salce, J. L. Gravil, and L. A. Boatner, J. Phys.: Condens. Matter **6**, 4077 (1994).
[4] G. Wessel and H. Goldick, J. Appl. Phys. **39**, 4855 (1968).
[5] A. P. Pechenyi, M. D. Glinchuk, T. V. Antimirova, and W. Kleemann, Phys. Status Solidi B **174**, 325 (1992).
[6] A. P. Pechenyi, M. D. Glinchuk, C. B. Azzoni, F. Scardina, and A. Paleari, Phys. Rev. B **51**, 12165 (1995).
[7] H.-J. Reyher, B. Faust, M. Maiwald, and H. Hesse, Appl. Phys. B: Lasers Opt. **63**, 331 (1996).
[8] V. V. Laguta, M. D. Glimchuk, A. A. Karmazin, I. P. Bykov, and P. P. Syrnikov, Fiz. Tverd. Tela (Leningrad) **27**, 2211 (1985) [Sov. Phys. Solid State **27**, 1328 (1985)].
[9] H. Engstrom, J. B. Bates, and L. A. Boatner, J. Chem. Phys. **73**, 1073 (1980).
[10] E. Siegel and K. A. Müller, Phys. Rev. B **19**, 109 (1979).
[11] E. Siegel and K. A. Müller, Phys. Rev. B **20**, 3587 (1979).
[12] V. V. Laguta, M. D. Glinchuk, I. P. Bykov, Yu. L. Maksimenko, J. Rosa, and L. Jastrabik, Phys. Rev. B **54**, 12353 (1996).
[13] R. L. Berney and D. L. Cowan, Phys. Rev. B **23**, 37 (1981).
[14] C. Auf Der Horst, S. Magnien, and S. Kapphan, Ferroelectrics **185**, 265 (1996).
[15] A. S. Nowick, S. Q. Fu, W. K. Lee, B. S. Lim, and T. Scherban, Mater. Sci. Eng., B **23**, 19 (1994).
[16] G. D. Watkins, Phys. Rev. **113**, 91 (1959).

Translated by G. Skrebtsov

Dielectric relaxation in the weak ferroelectric $Li_2Ge_7O_{15}$ near the ferroelectric phase transition

A. Yu. Kudzin, M. D. Volnyanskiĭ, M. P. Trubitsyn, and I. A. Busoul

Dnepropetrovsk State University, 320625 Dnepropetrovsk, Ukraine
(Submitted May 7, 1998)
Fiz. Tverd. Tela (St. Petersburg) **40**, 2198–2201 (December 1998)

The dielectric permittivity of Ni-doped $Li_2Ge_7O_{15}$ crystals was studied in the vicinity of the ferroelectric phase transition. Introduction of Ni has been shown to suppress the dielectric anomaly and to reduce substantially the transition temperature. A temperature hysteresis in $\varepsilon(T)$ has been observed in nominally pure and Ni-doped $Li_2Ge_7O_{15}$ crystals near the transition point. Measurements performed under cooling from the paraphase reveal dispersion of dielectric permittivity at Debye relaxation frequencies of the order of 10^4-10^5 Hz at T_c. It is proposed that the hysteresis phenomena and the low-frequency dispersion are caused by residual defects (of the type of random local fields), which become polarized in the ferroelectric phase and become disordered above T_c. © *1998 American Institute of Physics.* [S1063-7834(98)01312-4]

The $Li_2O–GeO_2$ system comprises a number of compounds with interesting physical properties. For instance, Li_2GeO_3 is a pyroelectric crystal, $Li_2Ge_4O_9$ is a ferroelectric exhibiting fairly high spontaneous polarization, and $Li_2Ge_7O_{15}$ is classed among weak ferroelectrics.

Lithium heptagermanate $Li_2Ge_7O_{15}$ (LGO) crystals undergo a second-order transition at $T_c=283.5$ K from a high-temperature paraelectric to a polar phase, which entails a change in symmetry $D_{2h}^{14}\rightarrow C_{2v}^{5}$.[1–3] A Raman and submillimeter-range spectroscopic study of lattice vibrations revealed a soft mode responsible for the phase transition.[4,5] On the other hand, the Curie-Weiss constant of LGO is very small, and the phase-transition temperature is observed to increase strongly with hydrostatic pressure ($\sim$14.2 K/kbar).[3,6] Thus the properties of LGO in the vicinity of T_c combine features characteristic of classical displacive and order-disorder transitions.

The dielectric permittivity ε_M at the transition point T_c exceeds by far the value accounted for by the soft-mode contribution,[5] due to the small effective charge of the mode. The dielectric dispersion revealed in the GHz frequency range showed ε to be dominated by relaxation-type dynamics.[7]

A number of studies have dealt with the LGO structure and its changes induced by the phase transition.[1,8,9] The framework of the LGO lattice is formed by GeO_6 octahedra and GeO_4 tetrahedra, which share corners. Neutron diffraction measurements[8,9] permitted one to assign the GeO_4 tetrahedron vibrations to an oscillator mode and to relate the major contribution to the anomaly in dielectric permittivity to Li^+ dynamics exhibiting an ordering pattern.

Essential information on the phase-transition mechanism can also be derived from studies of the effects of substituting an impurity for the host-lattice atoms. Such investigations were made on doped LGO crystals.[10–12] It was shown that isovalent substitution of Ge^{4+} ions shifts substantially the phase-transition temperature, while Li^+ substitution affects only weakly T_c. These data fit qualitatively into the above ideas about the role of Ge and Li ions in the LGO lattice rearrangement during the transition.

1. EXPERIMENTAL RESULTS AND THEIR DISCUSSION

This work reports on a study of dielectric permittivity of undoped and Ni-doped LGO crystals in the vicinity of T_c. LGO:Ni single-crystals were grown by pulling from the melt by the technique described elsewhere.[13] The crystals obtained with Ni concentrations up to 0.2% were of sufficient quality to permit measurements of their electrical and optical properties. The observed crystal coloring suggests that the impurity enters the LGO lattice are Ni^{2+} ions.

Plane-parallel samples with a large-area surface oriented normal to the [001] polar axis were prepared for dielectric studies. Platinum electrodes deposited in vacuum allowed dielectric permittivity measurements. Within the 273–293 K interval, ε was measured by the bridge and resonance methods at frequencies from 700 Hz to 1 MHz. The rate of temperature variation in the cooling and heating runs was $\sim$0.3 K/min. The temperature was stabilized to within 0.1 K.

The results obtained for nominally undoped and Ni-doped LGO crystals (0.1 and 0.2%) are presented graphically in Fig. 1a and 1b. We readily see that Ni doping (a) shifts strongly the phase-transition temperature (by $\sim$37 K per 1% addition), which exceeds substantially the concentration-induced T_c shifts observed to occur under isovalent substitution (Table I) and (b) reduces markedly and washes out the dielectric anomalies at the phase transition. For the 0.2% impurity content, several poorly resolved dielectric-permittivity peaks appear near the Curie temperature, which may be due to a nonuniform Ni distribution throughout the crystal.

The temperature dependence of spontaneous polarization P_s was extracted from dielectric hysteresis loops. Figure 2

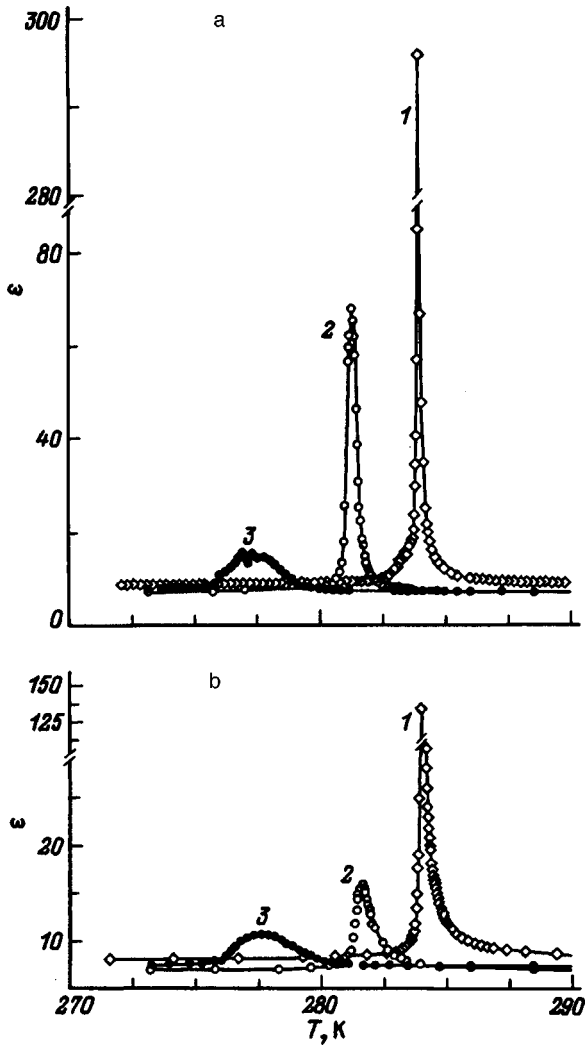

FIG. 1. Temperature dependences of the dielectric permittivity of LGO crystals: *1* — nominally pure, *2* — 0.1%Ni, *3* — 0.2%Ni; (a) cooling run, (b) heating run.

shows that the saturation polarization P_s decreases slightly with increasing impurity content, and its temperature dependence becomes smoother.

A comparison of the relations displayed in Figs. 1 and 2 shows that introduction of Ni suppresses noticeably the static dielectric response while affecting much weaker P_s, which is determined by displacements in the Ge-O framework of the LGO structure.

A characteristic feature in the relations is the temperature hysteresis of $\varepsilon(T)$ (Fig. 1b), which manifests itself in the difference between the maximum dielectric permittivities

TABLE I. Concentration-induced shift of T_c (in K) under isovalent substitution.

Impurity	T_c shift per 1%
Na	−0.24
Si	−10
Ti	−10
Ni	−37
Cr	−70

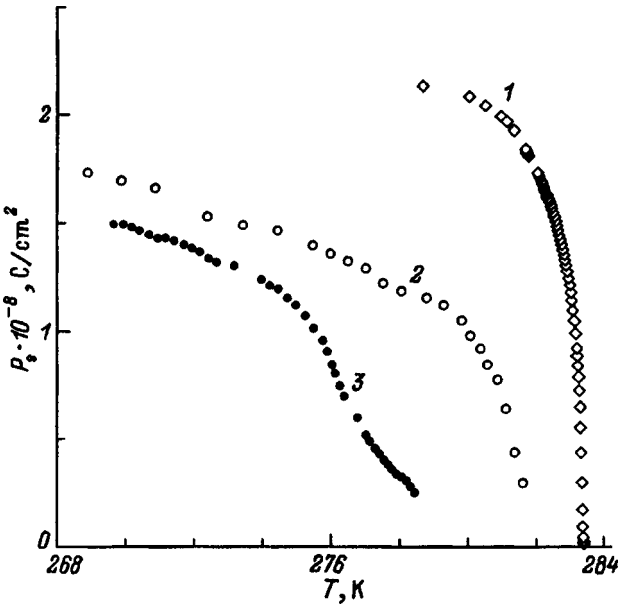

FIG. 2. Temperature dependences of the spontaneous polarization of LGO crystals: *1* — nominally pure, *2* — 0.1%Ni, *3* — 0.2%Ni.

measured under cooling (ε_M^C) and heating (ε_M^H) of a sample. It should be stressed that the temperature hysteresis is observed both in nominally pure and on Ni-doped samples. Therefore there are no grounds to associate the hysteresis phenomena with the presence of Ni in the LGO lattice. The dielectric permittivity measurements were carried out on samples differing in domain structure, its state being derived from studies of the pyroelectric effect. The results of these studies suggest that single- and polydomain samples do not differ in the hysteretic behavior of $\varepsilon(T)$.

Measurements of the dielectric permittivity made within the 700 Hz–1 MHz range revealed the existence of a considerable frequency dispersion. Note that this dispersion is connected directly to the hysteresis of $\varepsilon(T)$ and is observed only in the cooling runs. When measured under heating, the course of $\varepsilon(T)$ does not depend on measuring frequency within the range studied. Therefore we studied the frequency dependence of the dielectric peak under cooling ε_M^C. The measurements were performed in the following way. The sample was maintained at a temperature T_c+10 K for 1–2 h to reach equilibrium, and only after this ε_M^C was measured under cooling at the chosen frequency. The results plotted in Fig. 3 show ε_M^C to decrease with increasing frequency. For frequencies above 10^5 Hz, ε_M^C approaches in magnitude ε_M^H. Thus for both undoped and Ni-doped crystals frequency dispersion involves only the part of the dielectric permittivity $\Delta\varepsilon(T)=\varepsilon^C(T)-\varepsilon^H(T)$ which freezes in during the time the sample resides in the ferroelectric phase. The frequency dependence of ε_M^C has a pattern typical of relaxation mechanisms. Unfortunately, the small magnitude of dielectric losses in the samples did not permit measuring the imaginary part of the dielectric permittivity with sufficient accuracy to permit obtaining additional information on the observed relaxation. As follows from the relations displayed in Fig. 3, the relaxation times observed in undoped and doped samples are of about the same order of magnitude, $10^{-4}-10^{-5}$ s.

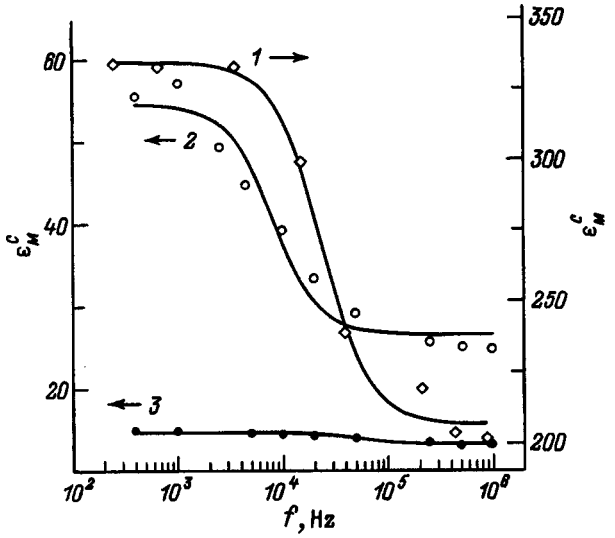

FIG. 3. Frequency dependences of the dielectric permittivity (ε_M^C) of LGO crystals: *1* — nominally pure, *2* — 0.1%Ni, *3* — 0.2%Ni.

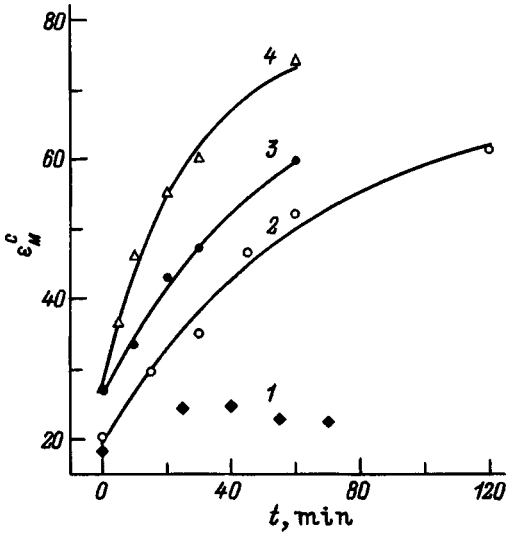

FIG. 4. Recovery of the frozen-in part of dielectric permittivity vs delay time at temperature T^*: (*1*) T_c, (*2*) T_c+1 K, (*3*) $T_c+2.5$ K, (*4*) T_c+5 K.

These data show also that the hysteresis phenomena and the low-frequency dispersion observed in all samples have the same nature, which is not associated directly with the Ni impurity.

As already mentioned, to return a sample to the initial state after it had been in the ferroelectric phase it had to be annealed above the Curie temperature. To determine the parameters of crystal recovery under annealing in the paraelectric phase, the kinetics of variation of dielectric permittivity with temperature and anneal time were studied. Unfortunately, it is difficult to perform these experiments in pure form, because the difference between the dielectric permittivities measured under heating and cooling is within experimental error already at T_c+1 K. Taking into account that the Ni impurity is not connected directly with the hysteresis and relaxation effects, we performed measurements on LGO:Ni (0.1%), a composition whose dielectric anomaly width permitted reducing the experimental errors connected with inaccuracies in maintaining the temperature regimes. The measurements were carried out in the following way. The sample was cooled from the equilibrium state through the transition and maintained in ferroelectric phase at T_c-10 K for 30 min, then was heated to $T^*=T_c+\Delta T$ and maintained at this temperature a certain time (which was increased in each cycle), after which it was cooled, and ε_M^C was measured in the process. Measurements were made with different anneal temperatures T^*. The results of these measurements are plotted in Fig. 4. Since reaching the transition point under cooling from T^* takes a certain time, the data presented in Fig. 4 should be considered only as qualitative. Nevertheless, the dependence of ε_M^C on anneal time can be fitted fairly well by an exponential, with the recovery time τ_R decreasing with increasing T^*-T_c. The case of annealing at $T^*=T_c$ (stabilization of the sample temperature at the transition point after a holdup in the ferroelectric phase) corresponds to an infinitely long time τ_R (curve *1* in Fig. 4).

Figure 5 plots the dielectric-permittivity recovery time τ_R *vs* (T^*-T_c). We readily see that τ_R depends essentially on how close the anneal temperature T^* is to the transition point. The experimental values obtained can be fitted by a power-law relation $1/\tau_R=(T^*-T_c)^p$ with the exponent $p=0.54\pm0.03$.

In considering the effect of Ni impurity on the phase transition in LGO, we note that the ionic radius of Ni^{2+} is 0.74 Å, which should make its substitution by Li^+, whose ionic radius is 0.7 Å, highly probable. In this case the concentration-induced decrease of ε at the peak for Ni-doped crystals can be associated with the influence of impurity ions on the Li^+ relaxation dynamics. The pronounced shift of the transition point is apparently connected with Ni being nonisovalent, which, in accordance with the charge-neutrality principle, produces complex defects of the type impurity-ion–excess-charge-compensator. Because Ni^{2+} has a spin moment, one should not overlook the possibility of identification by EPR of the defect states forming in the lattice.

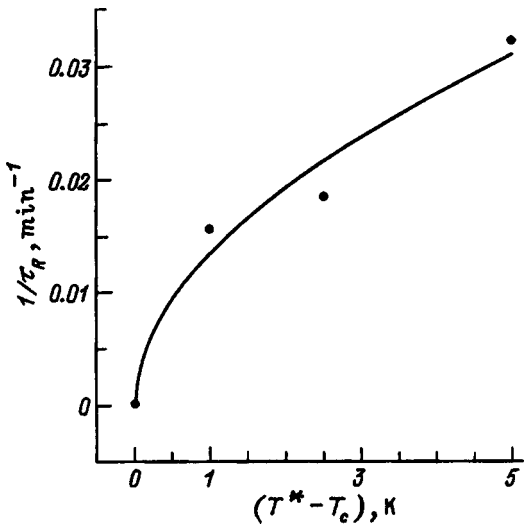

FIG. 5. Recovery time τ_R of the frozen-in state vs annealing temperature. Plotted along the vertical axis is the difference $\Delta T=T^*-T_c$.

It may be conjectured that the temperature hysteresis and the low-frequency dispersion of dielectric permittivity originate from residual defects, which distort locally the lattice symmetry and can be classed among perturbations of the type of local random fields[14]. The defect-induced local fields are randomly oriented in the paraphase and do not affect noticeably any anomalies in thermodynamic properties[14] detected under cooling. The delay in the ferroelectric phase of the appearance of a nonzero P_s orients the local fields of defects. Thus the phase transition induced by heating occurs in the presence of an internal bias field generated by a system of polarized defects. This results in a partial suppression of the dielectric anomaly. When it passes through T_c in the absence of orienting interaction by the local fields of structural distortions in the low-symmetry phase, the system with polarized defects becomes unstable. The recovery to the equilibrium (disordered) state depends exponentially on the delay time and occurs faster as one moves away from the transition point toward higher temperatures. If the above conjectures are correct, the low-frequency $(10^4-10^5$ Hz) dielectric-permittivity dispersion can be assigned to the relaxation dynamics of the defect regions of the crystal.

[1] H. Völlenkle, F. Wittmann, and H. Nowotny, Monatsch. Chem. **101**, 46 (1970).
[2] S. Haussühl, F. Wallrafen, K. Recker, and J. Eckstein, Z. Kristallogr. **153**, 329 (1980).
[3] M. Wada and Y. Ishibashi, J. Phys. Soc. Jpn. **52**, 1478 (1983).
[4] H. Orihara, M. Wada, and Y. Ishibashi, J. Phys. Soc. Jpn. **52**, 1478 (1983).
[5] A. A. Volkov, G. V. Kozlov, Yu. G. Goncharov, M. Wada, A. Sawada, and Y. Ishibashi, J. Phys. Soc. Jpn. **54**, 818 (1985).
[6] P. Preu and S. Haussühl, Solid State Commun. **41**, 627 (1982).
[7] M. Horioka, A. Sawada, and M. Wada, J. Phys. Soc. Jpn. **58**, 3793 (1989).
[8] Y. Iwata, I. Shibuya, M. Wada, A. Sawada, and Y. Ishibashi, Jpn. J. Appl. Phys. **24**, Supl. 24-2, 597 (1987).
[9] Y. Iwata, I. Shibuya, M. Wada, A. Sawada, and Y. Ishibashi, J. Phys. Soc. Jpn. **56**, 2420 (1987).
[10] M. D. Volnyanskiĭ and A. Yu. Kudzin, Fiz. Tverd. Tela (Leningrad) **30**, 1520 (1988) [Sov. Phys. Solid State **30**, 878 (1988)].
[11] M. D. Volnyanskiĭ, A. Yu. Kudzin, and T. V. Shwets, Fiz. Tverd. Tela (Leningrad) **32**, 3134 (1990) [Sov. Phys. Solid State **32**, 1818 (1990)].
[12] M. D. Volnyanskiĭ, A. Yu. Kudzin, and T. V. Shwets, Fiz. Tverd. Tela (Leningrad) **33**, 2228 (1991) [Sov. Phys. Solid State **33**, 1257 (1991)].
[13] M. D. Volnyanskiĭ, A. Yu. Kudzin, and D. M. Volnyanskiĭ, Fiz. Tverd. Tela (St. Petersburg) **36**, 2785 (1991) [Phys. Solid State **36**, 1522 (1991)].
[14] A. P. Levanyuk and S. A. Sigov, Izv. Akad. Nauk SSSR, Ser. Fiz. **49**, 219 (1985).

Translated by G. Skrebtsov

Anomalous behavior of the elastic and inelastic properties in the ferroelectric phase of single-crystal $(NH_4)_2SO_4$

S. A. Gridnev,* L. P. Safonova, and O. N. Ivanov

Voronezh State Technical University, 394026 Voronezh, Russia

T. N. Davydova

L. V. Kirenskiĭ Physics Institute, Siberian Division, Russian Academy of Sciences, 660036 Krasnoyarsk, Russia

(Submitted May 26, 1998)
Fiz. Tverd. Tela (St. Petersburg) **40**, 2202–2205 (December 1998)

The anomalous changes of the low-frequency elastic and inelastic properties of single-crystal $(NH_4)_2SO_4$ accompanying the phase transition from the paraelectric to the ferroelectric phase have been studied by the reverse torsion-pendulum method at 223 K and in the temperature region where the spontaneous polarization changes sign. © *1998 American Institute of Physics.* [S1063-7834(98)01412-9]

It is well known (see, for example, Refs. 1 and 2) that ammonium sulfate $(NH_4)_2SO_4$ at a temperature of $T_c = 223$ K undergoes a structural phase transition from a high-temperature rhombic (D_{2h}^{16}–$Pnam$) to a low-temperature rhombic (C_{2v}^{9}–$Pna2$) phase, accompanied by the appearance of spontaneous polarization along the c axis. In the ferroelectric phase, the spontaneous polarization P_s has an unusual temperature dependence: having abruptly appeared at T_c, upon further cooling, the spontaneous polarization, after a brief increase, begins to gradually decrease, passes through zero close to a temperature of ~ 85 K, and changes sign below this temperature.[3] The sign change of the spontaneous polarization implies a complex phase-transition mechanism, associated, for example, with the appearance of ferroelectricity in two different sublattices, so that the total polarization of the crystal depends both on the direction and on the temperature evolution of the spontaneous polarizations of the sublattices.[4]

The presence of an unusual ferroelectric phase transition and the appearance of spontaneous-polarization compensation phenomena associated with it at some temperature below T_c makes ammonium sulfate an interesting object of study among compounds of the family A_2BX_4.

This paper discusses the structure-sensitive low-frequency elastic and inelastic properties of single-crystal $(NH_4)_2SO_4$ in the temperature region that includes both T_c and the spontaneous-polarization compensation temperature.

A single crystal of $(NH_4)_2SO_4$ was grown for the study by evaporation at a temperature of 303 K from a saturated aqueous solution with $pH=4$. Twice-recrystallized material was used to prepare the ammonium sulfate solution.

The low-frequency elastic (shear modulus G) and inelastic (internal friction Q^{-1}) properties were measured by means of a reverse torsion pendulum at a frequency of ~ 10 Hz for a strain amplitude of the sample of $\sim 10^{-4}$. The measurements were made on samples in the form of rectangular $2\times 2\times 18$ mm bars oriented in such a way that their long side coincided with one of the crystallographic axes of the crystal: a, b or c (x, y and z orientation, respectively). The relative errors of measuring G and Q^{-1} did not exceed 2 and 10%, respectively. The temperature was measured by means of a chromel–alumel thermocouple with an error of ± 0.2 K.

Figure 1 shows the temperature dependences of the shear modulus and the internal friction of samples with x, y and z orientation in the neighborhood of the ferroelectric phase transition, recorded in a cooling regime with a rate of 0.2 K/min. It can be seen that samples of all three orientations demonstrate qualitatively identical behavior in the $G(T)$ and $Q^{-1}(T)$ dependences. In the paraelectric phase, the moduli of elasticity and internal friction are virtually independent of temperature. At the transition to the ferroelectric phase, moduli G_x, G_y, and G_z sharply decrease in magnitude and, as the temperature is reduced further, gradually increase, so that the temperature dependences of the moduli of elasticity have minima at T_c. Sharp peaks of Q^{-1} are observed on the temperature dependences of the internal friction, corresponding to the minima of the $G(T)$ dependences. When $T<T_c$, the values of the internal friction are significantly higher and the moduli of elasticity are significantly lower than their values when $T>T_c$; this is evidence of the appearance of an additional contribution to the low-frequency elastic and inelastic properties of $(NH_4)_2SO_4$ in the ferroelectric phase.

The existence of significant anomalies of the elastic and inelastic properties at the ferroelectric phase transition is rather unexpected in the compound $(NH_4)_2SO_4$. Such anomalies could be observed at a ferroelectric phase transition when a change of the point symmetry results in the appearance of a shear component or causes the breakdown of the equality of certain components in the elastic-compliance matrix. The ferroelectric phase transition in $(NH_4)_2SO_4$ is accompanied only by the appearance at T_c of spontaneous-polarization caused by the cooperative change of the orientations, positions, and magnitudes of the distortions of the

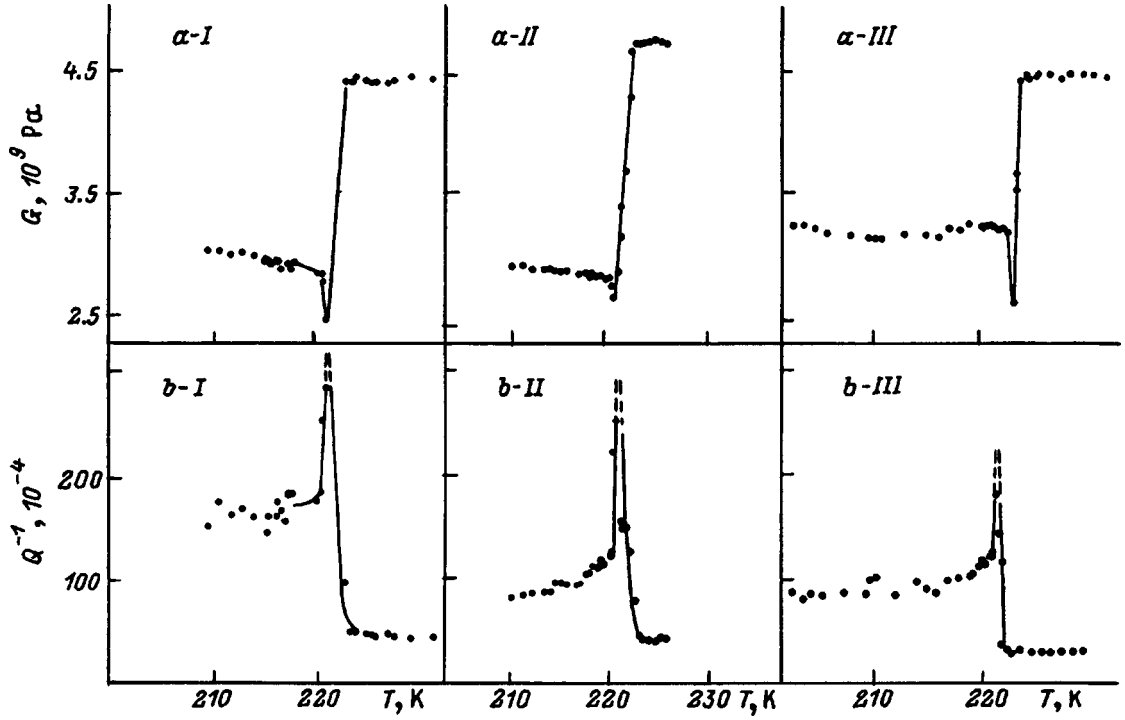

FIG. 1. Temperature dependences of the shear modulus (a) and the internal friction (b) of single-crystal ammonium sulfate for a sample with x (I), y (II), and z orientation (III) in the neighborhood of $T_c = 223$ K.

SO_4 groups. The elastic-compliance matrices S_{ij}, however, have identical form for both the paraelectric phase (symmetry point group mmm) and for the ferroelectric phase ($mm2$), and it consequently does not seem possible to describe the change of the elastic properties during the $mmm \rightarrow mm2$ phase transition on the basis of an analysis of the behavior of certain components of S_{ij} absent in one phase and appearing in the other.

It must be recalled that the spontaneous polarization accompanying the ferroelectric phase transition can cause strain in the crystal, with this strain having either an electrostrictive or a piezoelectric nature. However, the matrices of the electrostriction coefficients of crystals of rhombic structure are identical, and indeed the electrostrictive strain itself is usually significantly less than the strain caused by the piezoelectric effect. It is consequently necessary to analyze the change of the piezoelectric properties of $(NH_4)_2SO_4$ accompanying the ferroelectric phase transition. $(NH_4)_2SO_4$ possesses no piezoelectric effect in the paraelectric phase, whereas there is a piezoelectric effect in the ferroelectric phase, and the matrix of piezoelectric moduli d_{ij} for point symmetry group $mm2$ contains the components $d_{15}, d_{24}, d_{31}, d_{32}$ and d_{33}.[5] Here components d_{15} and d_{24} determine the appearance in the crystal of P_1 and P_2 polarization under the action of a mechanical shear stress, while components d_{31}, d_{32} and d_{33} establish the connection between polarization $P_3 = P_s$ and the mechanical stresses σ_1, σ_2 and σ_3 for the direct piezoelectric effect. As a consequence of the inverse piezoelectric effect, however, the existence of polarization P_3 must lead to strains X_1, X_2 and X_3 (along the a, b and c axes of the unit cell), associated with P_3 via the piezoelectric moduli g_{31}, g_{32}, g_{33}, and must result in the corresponding anomalous changes at T_c of the elastic compliances S_{11}, S_{22} and S_{33}. Both the strains X_1, X_2 and X_3 and the abrupt change of the S_{11}, S_{22} and S_{33} components were actually detected in $(NH_4)_2SO_4$ during a ferroelectric phase transition of the first type.[6,7]

We now take into account that torsional strain was produced in our experiments, resulting in a complex stressed state of the sample. In a torsion process, the elastic properties are characterized by the so-called shear modulus G_k of an anisotropic material under torsion, which is defined both by the corresponding shear components of the elastic compliance tensor and by a longitudinal component, which characterizes the strain of the sample along the torsional axis.[8] An analysis of the stressed state of the crystalline rod gives the following expression for the inverse value of modulus G_k^- :[8]

$$G_k^{-1}(q) = [q \cdot Z \cdot q - E^{-1}(q)], \tag{1}$$

where q is the unit vector along the axis around which the torsion of the sample is produced, $E^{-1}(q)$ is the inverse of Young's modulus, and Z is a symmetric material tensor of second rank, whose components are determined by the components of the elastic compliance tensor according to the rule $Z_{ji} = S_{kjkl}$, taking into account the symmetry of the crystal.

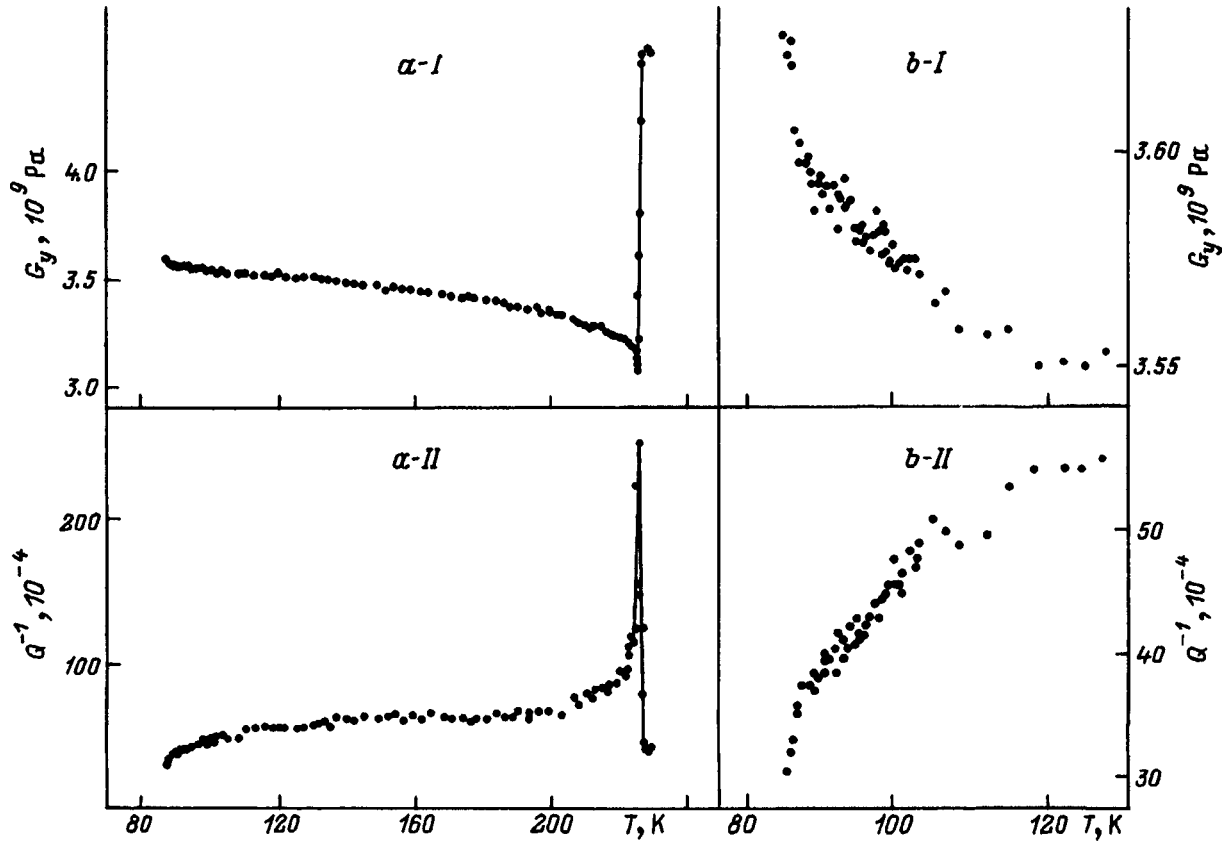

FIG. 2. Temperature dependences of the shear modulus (I) and the internal friction (II) of single-crystal ammonium sulfate for a sample with *y* orientation in a broad temperature interval (a) and in the temperature region where the spontaneous polarization changes sign (b).

For a rhombic system, tensor Z has the form

$$\begin{pmatrix} S_{11}+\frac{1}{4}S_{65}+\frac{1}{4}S_{66} & 0 & 0 \\ 0 & S_{22}+\frac{1}{4}S_{66}+\frac{1}{4}S_{44} & 0 \\ 0 & 0 & S_{33}+\frac{1}{4}S_{44}+\frac{1}{4}S_{55} \end{pmatrix}. \tag{2}$$

Here the diagonal components correspond to the torsion of the crystal around the x, y and z axes, respectively. The elastic properties of the crystal under torsion can consequently depend not only on the shear but also on the longitudinal components S_{ii} in Eq. (1) both in Young's modulus and in the components of the Z tensor.

It is obvious that the anomalous behavior of the moduli of elasticity G_x, G_y and G_z (which in this case are the shear moduli of an anisotropic material under torsion) can be determined for the $(NH_4)_2SO_4$ crystal by the corresponding strain of the sample along the x, y and z directions, caused by the presence of polarization P_3 via the piezoelectric moduli g_{31}, g_{32} and g_{33}. Since ammonium sulfate breaks up into ferroelectric domains below T_c, torsion of the samples can displace the domain boundaries. The internal friction must then be higher in the ferroelectric phase (since a new energy-scattering mechanism appears, associated with vibrations of the domain boundaries in varying mechanical fields), while the shear modulus is lower (since the sample can be put under strain by displacing the grain boundaries) relative to their values in the paraelectric phase. This pattern has indeed been observed in experiment.

If our assumption that the low-frequency elastic and inelastic properties of $(NH_4)_2SO_4$ in the ferroelectric phase are associated with spontaneous polarization is valid, it would be interesting to study the temperature dependences of G and Q^{-1} close to the temperature of the sign change of the spontaneous polarization (~ 85 K). The $G(T)$ and $Q^{-1}(T)$ dependences recorded for the sample with y orientation in a wide temperature region when it was cooled into the ferroelectric phase are shown in Fig. 2. It can be seen that, as the temperature decreases, the internal friction monotonically decreases, while the shear modulus increases. Upon cooling to the temperature of the spontaneous-polarization compensation region, the internal friction begins to sharply drop, while the shear modulus begins to rapidly increase (Fig. 2b), Such behavior can be explained by taking into account that the dynamics of the domain boundaries make a substantial contribution to the temperature dependences of G and Q^{-1}. At the polarization-compensation temperature, $P_s=0$. The sample will consequently not break up into domains, and the domain contribution, which provides high values of the internal friction and low values of the shear modulus in the ferroelectric phase, will be absent.

This work was carried out with the financial support of

the Russian Fund for Fundamental Research (Project No. 98-02-16055).

*E-mail: gridnev@nsl.vstu.ac.ru

[1] T. Yamaguchi, T. Tomita, and N. Ikarashi, Ferroelectrics **169**, 173 (1995).
[2] A. K. Tagantsev, I. G. Siniĭ, and S. D. Prokhorova, Izv. Akad. Nauk SSSR, Ser. Fiz. **1**, 12, 2082 (1985).
[3] H. G. Unruh, Solid State Commun. **8**, 1951 (1970).
[4] V. Dvorak and Y. Ishibashi, J. Phys. Soc. Jpn. **41**, 548 (1976).
[5] J. F. Nye, *Physical Properties of Crystals: Their Representation by Tensors and Matrices* (Clarendon Press, Oxford, 1957; Mir, Moscow, 1967, 385 pp.).
[6] N. A. Romanyuk, V. M. Gaba, and Z. M. Ursul, Ukr. Fiz. Zh. **33**, 9, 1381 (1988).
[7] T. Ikeda, K. Fujibayashi, T. Nagai, and J. Kobayashi, Phys. Status Solidi A **16**, 279 (1973).
[8] Yu. I. Sirotin and M. P. Shaskol'skaya, *Fundamentals of Crystal Physics* (Nauka, Moscow, 1975), 355 pp.

Translated by W. J. Manthey

Effective dielectric and piezoelectric constants of thin polycrystalline ferroelectric films

N. A. Pertsev*

A. F. Ioffe Physicotechnical Institute, Russian Academy of Sciences, 194021 St. Petersburg, Russia; Institut für Werkstoffe der Electrotechnik, RWTH Aachen, D-52056 Aachen, Germany

A. G. Zembil'gotov

St. Petersburg State Technical University, 195251 St. Petersburg, Russia; Institut für Werkstoffe der Electrotechnik, RWTH Aachen, D-52056 Aachen, Germany

R. Wazer

Institut für Werkstoffe der Elektrotechnik, RWTH Aachen, D-52056 Aachen, Germany
(Submitted June 3, 1998)
Fiz. Tverd. Tela (St. Petersburg) **40**, 2206–2212 (December 1998)

The averaged dielectric, piezoelectric, and elastic constants of thin polycrystalline barium titanate and lead titanate films are calculated within a modified effective-medium approximation, which takes fully into account piezoelectric interactions between crystallites. Films with *c*- or *a*-type crystal texture resulting from mechanical interaction with the substrate are considered when the film becomes ferroelectric under cooling of the heterostructure. The dependences of the effective material constants of textured films on the residual macroscopic polarization of a film are described. An analysis is made of the effect of two-dimensional clamping of a film on a thick substrate on measurements of dielectric and piezoelectric constants. © *1998 American Institute of Physics.* [S1063-7834(98)01512-3]

Material systems, which include thin ferroelectric films grown on metallized substrates, belong to heterostructures with considerable practical potential.[1] The interest in such systems stems from the high dielectric permittivity and large piezoelectric coefficients of ferroelectric films.[2,3] Experimental studies of the physical properties of films are mostly done on polycrystalline samples. This accounts for the renewed interest in theoretical calculations of the effective dielectric constants and piezoelectric coefficients of polycrystalline ferroelectrics.

Effective material constants of a polycrystal can be correctly calculated from data on the physical properties of the corresponding single crystal by means of the effective-medium approximation. This method was used previously to calculate the constants of bulk ferroelectric ceramics.[4–9] Physical properties of a ferroelectric film may differ substantially, however, from those of a bulk polycrystal even for grains of the same size. The reason for this lies in the mechanical interaction between the film and the substrate, which brings about 2D clamping of the ferroelectric layer.[10] As a first consequence, this clamping should result, in a general case, in texturing of the polycrystalline film in the course of preparation of a heterostructure. Second, the geometric parameters of the ferroelastic domain structure of grains should change, depending on the actual misfit strains between the film and the substrate,[11,12] up to complete suppression of ferroelectric polydomain formation[13] typical of bulk tetragonal ceramics. And finally, third, the observed dielectric and piezoelectric responses of a thin polarized film are modified by 2D clamping compared to a free polycrystal.

This has stimulated our present calculation of the effective dielectric, piezoelectric, and elastic constants of thin polycrystalline films of two classical ferroelectrics, namely, $BaTiO_3$ and $PbTiO_3$. The calculation is based on the most rigorous formulation of the effective-medium approximation, which takes full account of the piezoelectric interaction between crystallites. The calculations are carried out in linear approximation, which permits one to use for starting data the experimental constants of $BaTiO_3$ and $PbTiO_3$ single crystals (see Sec. 1).

We are going to consider two types of crystal structure characteristic of films, which are induced by external mechanical stresses, viz., 1) the *c* texture, where the four-fold axes of crystallites forming in the ferroelectric phase during cooling are oriented closest to the surface normal, and 2) the *a* texture, in which the four-fold grain axes deviate by the minimum possible amount from the plane parallel to the film-substrate interface. These two textures are typical of the compressive and tensile substrates, respectively (see Sec. 2). We shall study the dependence of the effective constants of textured films on the macroscopic residual polarization P_r of the film, under the assumption that a change in P_r is the result of 180° switching of polarization of individual crystallites, which were initially in single-domain state or had a 90° layered domain structure stabilized by mechanical clamping of the film to the substrate.

1. SELF-CONSISTENT APPROXIMATION OF EFFECTIVE PIEZOELECTRIC MEDIUM

We shall limit ourselves to considering polycrystalline films with fine-grained microstructure[1]. In this case the properties of a polycrystal can be calculated in the model of a

material system consisting of a single crystallite (an inclusion V) embedded in a homogeneous piezoelectric medium (matrix). Because we are interested only in the behavior of our system on the mesoscopic level, which is given by the grain size, and the macroscopic level, the material properties of the inclusion will be assumed uniform both for single-domain grains and in the typical case of a layered 90° structure with a period much smaller than the grain size. In linear theory, weak-signal response of crystallites to external factors are assumed to be independent of the internal mechanical and electric fields usually existing in ferroelectric polycrystals. Therefore the properties of a single crystallite can be prescribed through material constants measured or calculated in a single-crystal sample. We are going to use here as starting parameters for the single crystal (inclusions) elastic rigidities c^E_{ijkl} at a constant electric field $\mathbf{E}$, piezoelectric coefficients e_{ikl}, and dielectric permittivities ε^S_{ij} at a constant strain $\mathbf{S}$ $(i,j,k,l=1,2,3)$. The matrix constants c^{*E}_{ijkl}, e^*_{ijk}, and ε^{*S}_{ij} should be considered, in their turn, as effective macroscopic constants of the polycrystalline material, which are to be determined by calculation.

We now assume that the inhomogeneous system consisting of a matrix and an inclusion is subjected to an external electromechanical action which produces in the system strains S_{kl} and an electric field E_l, and that far from the inclusion V these fields are uniform and equal to S^a_{kl} and E^a_l, respectively. If V is ellipsoidal in shape, the strains S_{kl} and the field E_l inside it will retain their uniformity while differing from S^a_{kl} and E^a_l.[14,15] The uniform fields S_{kl} and E_l induced by the external action, as well as the mechanical stresses T_{ij} and electric induction D_i inside the inclusion, can be calculated by the equivalent-inclusion approach proposed by Eshelby[16] and generalized recently[15] to the piezoelectric case. As shown later, this will permit us to calculate the effective polycrystalline-film constants we are looking for.

To find the fields inside an ellipsoidal inhomogeneity V, we replace it with an equivalent ellipsoid V^* of the same initial shape and volume but having material constants c^{*E}_{ijkl}, e^*_{ijk}, and ε^{*S}_{ij} which coincide with those of the matrix. We also assume that the inclusion V^* undergoes an irreversible uniform strain S^{0*}_{kl} and acquires a constant uniform polarization P^0_i in the absence of mechanical stresses and of a depolarizing field. Because the material constants in the new system are everywhere the same, the total elastic and electric fields here will be equal to a sum of the uniform external fields and of additional fields, which are induced by the polarization charges $\rho=-\operatorname{div}\mathbf{P}^0$ on the surface of the inclusion, and by the change of its size and shape as a result of the inelastic strain S^{0*}_{kl}. Inside the ellipsoidal inclusion V^* these additional fields are uniform and can be readily calculated as functions of P^0_i and S^{0*}_{kl}.[15,17,18]

For the sake of convenience, we use the four-dimensional formulation accepted in the theory of piezoelectrics[17–19] and introduce the following notation

$$T_{iJ}=\begin{cases} T_{ij}, & J=1,2,3, \\ D_i, & J=4, \end{cases} \qquad S_{Kl}=\begin{cases} S_{kl}, & K=1,2,3, \\ -E_l, & K=4, \end{cases}$$

$$c_{iJKl}=\begin{cases} c^E_{ijkl}, & J,K=1,2,3, \\ e_{lij}, & J=1,2,3;\quad K=4, \\ e_{ikl}, & J=4;\quad K=1,2,3, \\ -\varepsilon^S_{il}, & J,K=4. \end{cases} \tag{1}$$

Then the piezoelectric equations can be recast in a compact form $T_{iJ}=c_{iJKl}S_{Kl}$, with the summation running over repeated indices (in K from 1 to 4). The equations relating stresses T^*_{ij} and induction D^*_i inside the equivalent inclusion V^* to strains and the electric field can be presented in a similar form

$$T^*_{iJ}=c^*_{iJKl}(S^{*t}_{Kl}-S^0_{Kl}), \tag{2}$$

where S^{*t}_{kl} is the total strain in the inclusion V^* which is equal to the sum of the elastic and inelastic components, $S^{*t}_{4l}=-E^*_l$ are the components of the total electric field $\mathbf{E}^*$ inside V^* taken with the opposite sign, $S^0_{kl}=S^{0*}_{kl}+\Delta S^0_{kl}$, and $S^0_{4l}=-E^0_l$. We have renormalized here the inelastic strain S^{0*}_{kl} and introduced a fictitious electric field $\mathbf{E}^0$ inside the ellipsoid so as to satisfy the coupled equations

$$\begin{aligned} &c^{*E}_{ijkl}\Delta S^0_{kl}-e^*_{lij}E^0_l=0, \\ &e^*_{ikl}\Delta S^0_{kl}+\varepsilon^{*S}_{il}E^0_l=-P^0_i. \end{aligned} \tag{3}$$

This transformation is valid because the quantities ΔS^0_{kl} and E^0_l are uniquely determined by Eqs. (3) as linear functions of components of the polarization vector $\mathbf{P}^0$. Accordingly, S^0_{kl} and E^0_l can be introduced in place of S^{0*}_{kl} and P^0_i as parameters ensuring the equivalence of V^* and V.

The fields S^{*t}_{Kl} entering Eq. (2) can be calculated from the expression

$$S^{*t}_{Kl}=S^a_{Kl}+\Sigma^*_{KlMn}S^0_{Mn}, \tag{4}$$

where Σ^*_{KlMn} are the electromechanical tensors of Eshelby[17,18] for an ellipsoidal piezoelectric inclusion embedded in a matrix with the same constants c^*_{iJKl}. The quantity Σ^*_{KlMn} is a set of four tensors (corresponding to $K=1,2,3,4$), which can be prescribed by the following integral relations

$$\Sigma^*_{KlMn}=\frac{a_1a_2a_3}{8\pi}c^*_{iJMn}\int_\Omega \frac{z_i[(zz)^{-1}_{Jk}z_l+(zz)^{-1}_{Jl}z_k]}{(a_1^2z_1^2+a_2^2z_2^2+a_3^2z_3^2)^{3/2}}d\Omega, \tag{5}$$

$$\Sigma^*_{4lMn}=\frac{a_1a_2a_3}{4\pi}c^*_{iJMn}\int_\Omega \frac{z_i(zz)^{-1}_{J4}z_l}{(a_1^2z_1^2+a_2^2z_2^2+a_3^2z_3^2)^{3/2}}d\Omega, \tag{6}$$

Here the integration is performed over the surface Ω of a unit sphere, z_i are components of a unit vector $\mathbf{z}$, $(zz)^{-1}_{JK}$ is a matrix inverse to a symmetrical fourth-rank square matrix $(zz)_{MJ}$ whose elements are $(zz)_{MJ}=z_ic^*_{iJMn}z_n$, and a_1,a_2,a_3 are the ellipsoid semi-axes. Equations (5) and (6) were constructed under the assumption that the constants of the medium c^*_{iJMn} are defined in the coordinate frame with axes parallel to the major axes of the ellipsoid.

The quantities S^0_{Mn} in Eq. (4) should be chosen so as to preserve the same total strains and electric fields for the equivalent inclusion V^* and piezoelectric inhomogeneity V:

$S_{Kl}^{*t}=S_{Kl}$. The condition of the strains and electric induction being also the same in the equivalent and initial inclusions ($T_{iJ}^{*}=T_{iJ}$) leads us to the relation

$$(c_{iJKl}-c_{iJKl}^{*})S_{Kl}^{*t}=-c_{iJKl}^{*}S_{Kl}^{0}. \tag{7}$$

Substituting Eq. (4) for S_{Kl}^{*t} into (7) yields nine coupled equations

$$[c_{iJMn}^{*}+(c_{iJKl}-c_{iJKl}^{*})\Sigma_{KlMn}^{*}]S_{Mn}^{0}=(c_{iJKl}^{*}-c_{iJKl})S_{Kl}^{a}, \tag{8}$$

permitting one to find the nine unknown parameters S_{Mn}^{0} of inclusion V^{*}, which make it equivalent to the inhomogeneity V embedded in an external field S_{Kl}^{a}.

We may recall that the self-consistent solution to the problem of effective constants of a polycrystal is sought by the method of successive approximations (see, e.g., Ref. 8). In doing this, the constants c_{iJKl}^{*} of the matrix are assigned definite values in each iteration. Accordingly, parameters S_{Mn}^{0} of an equivalent inclusion can be calculated for given external fields S_{Kl}^{a} numerically by means of the coupled equations (8). This permits one to find from Eq. (4) the quantities S_{Kl}^{*t}, which yield the strains S_{kl} and the electric field E_l inside the inhomogeneity V (crystallite) we have been looking for. Finally, using the piezoelectric equations one can readily calculate the stresses T_{ij} and the electric induction D_i induced within V by the external fields S_{kl}^{a} and E_l^{a} from the found values of S_{kl} and E_l^{a}.

We shall limit ourselves in what follows to a consideration of polycrystals having grains with equal axes, which can be simulated by spherical inclusions ($a_1=a_2=a_3$). In this case the stresses T_{ij} and the induction D_i inside a trial crystallite will be functions of only three Euler angles, which specify the grain lattice orientation relative to the matrix frame. By calculating T_{ij} and D_i in this system for various Euler angles and averaging them subsequently over all possible lattice orientations in the polycrystal (see Sect. 2), one can determine the average stresses $\langle T_{ij}\rangle$ and average induction $\langle D_i\rangle$ in a polycrystalline material. Having established further the dependence of these quantities on external fields S_{kl}^{a} and E_l^{a}, one comes finally to the effective constants of the polycrystal in the form

$$c_{iJKl}^{*}=\frac{\partial\langle T_{iJ}\rangle}{\partial S_{Kl}^{a}}=\langle c_{iJKl}\rangle+\frac{\partial\langle c_{iJMn}(S_{Mn}-S_{Mn}^{a})\rangle}{\partial S_{Kl}^{a}}. \tag{9}$$

The first term on the right-hand side of (9) is the result of direct averaging of the constants c_{iJKl}, which can obviously serve as a first approximation to constants c_{iJKl}^{*}. The other terms take into account the elastic, electric, and piezoelectric interactions between the crystallites and the surrounding polycrystalline medium. Their contribution is refined by iterative procedure. To do this, the effective constants (9) obtained in the preceding iteration are used as matrix constants c_{iJKl}^{*} in the subsequent iteration, which permits one to calculate the changes $S_{Mn}-S_{Mn}^{a}$ of the external fields in the trial crystallite.

2. EFFECTIVE MATERIAL CONSTANTS OF TEXTURED $BaTiO_3$ AND $PbTiO_3$

The effective piezoelectric-medium approximation has been used by us to calculate the dielectric, piezoelectric, and elastic constants of thin polycrystalline barium titanate (BT) and lead titanate (PT) films at room temperature. The starting data were taken from experimental measurements[20] of elastic compliances s_{ij}^{E} at constant electric field, piezoelectric coefficients d_{ij} and dielectric permittivities ε_{ij}^{S} at constant strain made on single-domain BT and PT single crystals. (We are going to use in this Section the matrix notation of Voigt[21] for the elastic and piezoelectric constants.) These data were used directly to calculate the properties of films with single-domain crystallites, and the elastic rigidities c_{ij}^{E} and piezoelectric coefficients e_{ij} entering Eqs. (1)–(9) were derived from s_{ij}^{E} and d_{ij} using the well-known relations[21] $c_{ij}^{E}s_{jk}^{E}=\delta_{ik}$ and $e_{ij}=d_{ik}c_{kj}^{E}$ (δ_{ik} is the Kronecker symbol).

The calculations were performed for a number of model distributions of grain-lattice orientations relative to the substrate. These distributions were described by means of $F(\theta,\varphi,\psi)$ functions of the three Euler angles specifying the orientation of the crystallographic axes in a crystallite with respect to the substrate frame. The distribution functions $F(\theta,\varphi,\psi)$ corresponding to the crystalline textures characteristic of ferroelectric films prepared usually at temperatures above the Curie point[1] were found based on the following considerations.

It was assumed that all grain-lattice orientations in a forming paraelectric film are equally probable. In this case the film becomes textured in the course of the ferroelectric transition and is induced by the internal stresses created in the film by the 2D clamping at the substrate. The stressed state existing in the film directly before the transition depends primarily on the difference between the thermal-expansion coefficients of the paraelectric film and of the substrate. (The stresses generated during the film growth on the substrate surface may provide an additional contribution, Ref. 22.) If the substrate is an amorphous solid or a crystal of cubic, tetragonal, or hexagonal symmetry with the surface perpendicular to the highest-order symmetry axis (x_3 axis), then only normal stresses T_{11} and T_{22}, which are equal in magnitude, will be, on the average, nonzero. In this typical situation the actual form of the texture will depend only on the sign of these stresses.

In a compressed film, spontaneous polarization in a single crystallite should arise along the pseudocubic axis which is the least misoriented with respect to the substrate surface normal (the *c* texture). This is energetically preferable, because it reduces the elastic energy built up in the film. (In BT and PT, the lattice is extended along the polar axis and compressed in transverse directions.[23]) If the effective misfit strain in a heterostructure has a large enough negative value, the resulting *c* texture will be stabilized under further cooling of the film.[10]

For the same reason, crystallite polarization in a film under tensile stress should align with the pseudocubic axis oriented closest to the substrate surface (the *a* texture). Because our analysis is made using linear theory, we assume

the crystallites in the *a* texture to transfer to the tetragonal state typical of free BT and PT crystals at room temperature.[23] Accordingly, we ignore the possibility of a transformation of the stable phase under two-dimensional extension of the film.[10]

We can thus assume that the polar-axis orientations of crystallites in an unpolarized *c*-textured film are distributed uniformly within two solid angles specified by the inequalities $0 \leqslant \theta < \theta^{**} = \arctan\sqrt{2}$ and $\pi - \theta^{**} < \theta \leqslant \pi$ (for any φ and ψ), where θ is the angle made by the polar axis of a single-domain crystallite with the surface normal of the substrate. In the case of the *a* texture, the grain polar axes will be distributed uniformly outside the above solid angles. To describe the changes in the corresponding distribution functions F_c and F_a in a film polarized by an external field **E**, we shall use the following simplest model of polarization switching. Since 90° turns of the spontaneous polarization vector $\mathbf{P}_s$ in crystallites are energetically unfavorable because of the 2D clamping of the film which stabilizes the initial orientations of the four-fold axes, we shall assume the switching to occur only in 180° turns of $\mathbf{P}_s$. Neglecting further the effects due to electrostatic interaction among the crystallites, we shall assume that the polarization in a crystallite switches simultaneously throughout the crystallite volume as soon as the external field $E\cos(\pi-\varphi)$ along its polar axis has reached a critical value E^*. Then, for a given field strength $E > E^*$, the $\mathbf{P}_s$ vectors will reorient in all crystallites where the initial deviation θ of the polar axis from the field direction **E** exceeds the threshold value $\theta^* = \pi - \arccos(E^*/E)$. This model yields the following relation for the distribution function F_c of crystallites in orientation in a poled film with *c* texture:

$$F_c(\theta^*) = \begin{cases} \dfrac{1}{4\pi^2(1-\cos\theta^{**})}, & 0 \leqslant \theta < \theta^*, \\ \dfrac{1}{8\pi^2(1-\cos\theta^{**})}, & \theta^* \leqslant \theta < \theta^{**} \\ & \pi - \theta^{**} \leqslant \theta < \pi - \theta^*, \\ 0, & \theta^{**} \leqslant \theta < \pi - \theta^{**}, \\ & \pi - \theta^* \leqslant \theta \leqslant \pi, \end{cases} \tag{10}$$

where the threshold angle θ^* increases from zero to $\theta^{**} = \arctan\sqrt{2}$ in the course of the film polarization. For poled films with *a* texture, the distribution function F_a has the form

$$F_a(\theta^*) = \begin{cases} 0, & 0 \leqslant \theta < \theta^{**}, \quad \pi - \theta^* \leqslant \theta \leqslant \pi, \\ \dfrac{1}{4\pi^2\cos\theta^{**}}, & \theta^{**} \leqslant \theta < \theta^*, \\ \dfrac{1}{8\pi^2\cos\theta^{**}}, & \theta^* \leqslant \theta < \pi - \theta^*, \end{cases} \tag{11}$$

where the threshold angle varies from θ^{**} to $\pi/2$.

Equations (10) and (11) were used to calculate the effective material constants of textured BT and PT films with various degrees of polarization. The latter was characterized by the residual macroscopic polarization P_r determined as $P_r = (1-\cos 2\theta^*)/4(1-\cos\theta^{**})$ for the *c* texture, and as $P_r = (\cos 2\theta^{**} - \cos 2\theta^*)/4\cos\theta^{**}$ for the *a* texture. The results of the calculations are presented in Figs. 1–4 and Tables I and II only for the dielectric permittivities ε_{ij}^{*T} at constant stresses, piezoelectric coefficients d_{ij}^*, and elastic compliances s_{ij}^{*E}, which are usually measured experimentally. These constants were determined by means of the relations[21] $s_{ij}^{*E} c_{jk}^{*E} = \delta_{ik}$, $d_{ij}^* = e_{ik}^* s_{kj}^{*E}$, and $\varepsilon_{ij}^{*T} = \varepsilon_{ij}^{*S} + d_{ik}^* d_{jl}^* c_{kl}^{*E}$ using the theoretical values of $c_{ij}^{*E}(P_r)$, $e_{ij}^*(P_r)$, and $\varepsilon_{ij}^{*S}(P_r)$ calculated from Eq. (9). (Numerical

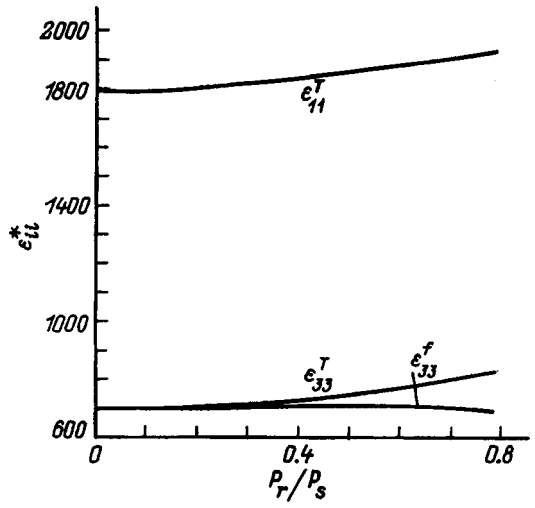

FIG. 1. Theoretical dielectric constants ε_{ii}^{*T} of a *c*-textured BT film *vs* normalized residual polarization P_r/P_s. The curve labeled $\varepsilon_{33}^{*f}(P_r/P_s)$ describes the effective film permittivity measured in a standard experiment.

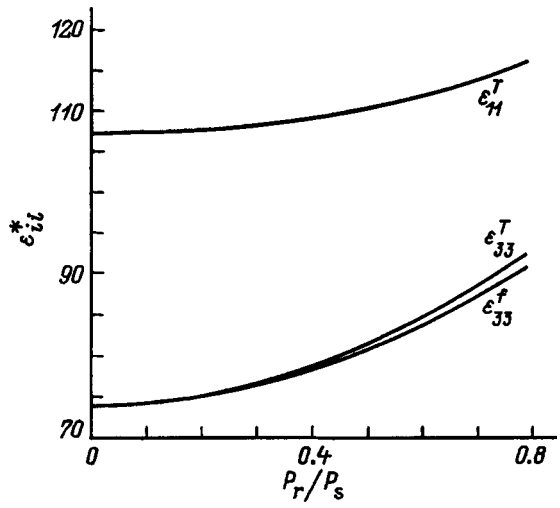

FIG. 2. Theoretical permittivities ε_{ii}^{*T} of a *c*-textured PT film *vs* residual film polarization. The curve labeled ε_{33}^{*f} illustrates the observed dielectric response of the film.

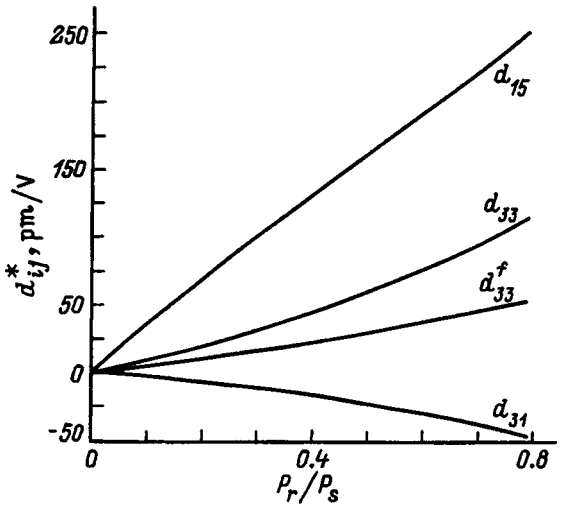

FIG. 3. Theoretical piezoelectric coefficients d^*_{ij} of a *c*-textured BT film vs normalized residual polarization. The curve labeled $d^{*f}_{33}(P_r/P_s)$ describes the effective piezoresponse of the film observed in a standard measurement procedure.

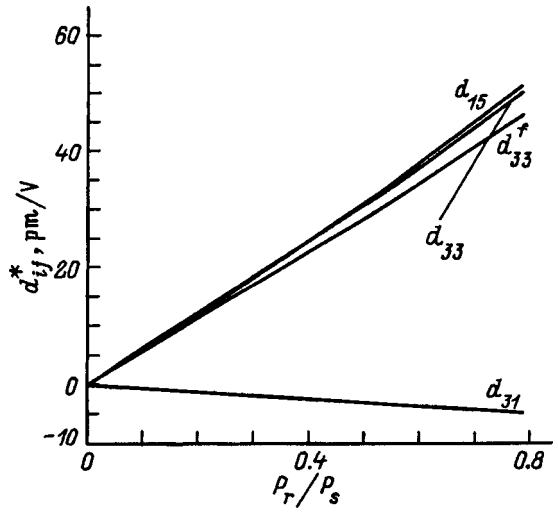

FIG. 4. Theoretical piezoelectric coefficients d^*_{ij} of a *c*-textured PT film vs residual film polarization. The curve labeled d^{*f}_{33} describes the observed piezoresponse of the film.

calculations made by successive approximations require up to 15–20 iterations to reach a self-consistent result.)

Turning now to a discussion of the results obtained, we note first of all that the material properties of textured films are naturally anisotropic. The degree of anisotropy is particularly large for the dielectric properties of BT films because of single-crystal BT having a large ratio $\varepsilon_{11}/\varepsilon_{33} \approx 16$.[20] The anisotropy depends on the type of crystalline texture and manifests itself stronger in *c*-textured films. In contrast to BT films, PT films exhibit a considerable anisotropy in elastic properties, because for this single crystal $s^E_{33}/s^E_{11} \approx 5$.[20]

As seen from Tables I and II, the dielectric permittivity ε^{*T}_{33} of *c*-textured films grows substantially with polarization, whereas in *a*-type films all dielectric constants remain practically unchanged. Note also that the $\varepsilon^{*T}_{33}(P_r)$ relation exhibits a certain nonlinearity (Figs. 1 and 2). The piezoelectric coefficients d^*_{ij} of *c*-textured films increase in absolute magnitude practically linearly with residual polarization P_r (see Figs. 3 and 4), and the maximum polarization-induced values of d^*_{ij} reached in these films turn out to be substantially larger than those in films with the *a* texture (Tables I and II). The weaker effect of polarization on the dielectric and piezoelectric constants of *a*-textured films is due primarily to the fact that 180° switching produces a much smaller maximum polarization in *a*-textured films ($P_r/P_s \cong 0.29$) than it does in films with *c* texture ($P_r/P_s \cong 0.8$).

The results obtained for *a*-type films may need refinement, however, because they describe an ensemble of single-domain crystallites whereas, for the grain whose four-fold axis oriented parallel to the surface of an extending substrate crystallite, twinning is energetically preferable.[11,24,25] In connection with, this we have calculated material constants for a model polydomain *a* texture, where all crystallites have a layered 90°-domain structure. It was assumed that the transverse dimensions of all 90° domains are the same and small compared to grain size, and that the domain walls are fixed. We used as starting data the theoretical values of the effective material constants for polydomain crystallites, which characterize the response of a crystallite as a whole to external actions. These constants were calculated by the domain-structure averaging procedure[26] using experimental values[20] on single-domain tetragonal BT and PT crystals. The matrices obtained by this averaging procedure relate already to the rhombic rather than tetragonal crystal symmetry. Under these conditions it appears reasonable to describe the texture by prescribing the grain distribution in orientation of the twinning axis, which is perpendicular to the four-fold axes in domains of both types, and in orientation of the polar grain axis, along which its mean polarization vector is directed.

Obviously enough, in the course of domain-structure formation the twinning axis of a grain in a film fixed to an extended substrate will be the pseudocubic axis which is the least misoriented with respect to the substrate normal (in a

TABLE I. Effective dielectric permittivities $\varepsilon^*_{ii}/\varepsilon_0$, piezoelectric coefficients d^*_{ij} (in pm/V), and elastic compliances s^{*E}_{ij} (in 10^{-3} GPa^{-1}) of polycrystalline barium titanate films.

Film	ε^T_{11}	ε^T_{33}	ε^f_{33}	d_{15}	d_{31}	d_{33}	d^f_{33}	s^E_{11}	s^E_{12}	s^E_{13}	s^E_{33}	s^E_{44}	s^E_{66}
c-texture, $P_r=0$	1793	701	701	0	0	0	0	5.23	−1.93	−2.19	6.68	17.3	14.3
c-texture, $P_r=0.79P_s$	1933	829	694	252	−45.4	114	53.5	5.33	−1.87	−2.33	6.92	19.9	14.4
a-texture, $P_r=0$	1089	2032	2032	0	0	0	0	6.29	−2.31	−2.2	5.34	15.2	17.21
a-texture, $P_r=0.29P_s$	1082	2080	1995	38.6	−38.6	81.9	38.9	6.31	−2.3	−2.23	5.40	15.3	17.23
Twinned *a*-texture, $P_r=0$	894	1513	1513	0	0	0	0	6.25	−2.26	−2.11	5.32	16.6	17

TABLE II. Effective dielectric permittivities $\varepsilon_{ii}^*/\varepsilon_0$, piezoelectric coefficients d_{ij}^* (in pm/V), and elastic compliances s_{ij}^{*E} (in 10^{-3} GPa^{-1}) of polycrystalline lead titanate films.

Film	ε_{11}^T	ε_{33}^T	ε_{33}^f	d_{15}	d_{31}	d_{33}	d_{33}^f	s_{11}^E	s_{12}^E	s_{13}^E	s_{33}^E	s_{44}^E	s_{66}^E
c-texture, $P_r=0$	107	74	74	0	0	0	0	4.78	−1.45	−1.34	8.37	16.0	12.46
c-texture, $P_r=0.79P_s$	116	93	91	51.3	−4.8	50.2	46.2	4.80	−1.43	−1.40	9.10	16.8	12.45
a-texture, $P_r=0$	87	113	113	0	0	0	0	6.77	−1.30	−1.53	4.57	13.5	16.13
a-texture, $P_r=0.29P_s$	88	115	115	16.7	−0.56	12.8	12.5	6.78	−1.29	−1.54	4.63	13.6	16.14
Twinned *a* texture, $P_r=0$	82	101	101	0	0	0	0	7.14	−0.32	−1.10	4.83	14.6	14.9

structural transition, the lattice can undergo only compressive strain along the twinning axis). One may therefore assume that the crystallite twinning axes in an unpolarized film with polydomain *a* texture will be oriented uniformly within two solid angles given by the inequalities $0 \leqslant \theta < \theta^{**} = \arctan\sqrt{2}$ and $\pi - \theta^{**} < \theta \leqslant \pi$, where θ is now the angle between the twinning axis and the substrate normal. As for the polar axes of the crystallites, they should be uniformly distributed in all directions compatible with the given twinning-axis orientation.

We used the corresponding distribution function to calculate the effective constants of an unpolarized film with polydomain *a* texture. The results obtained (see Tables I and II) show that grain twinning practically does not affect the elastic compliances s_{ij}^{*E} of BT and PT films. At the same time this process may reduce substantially the transverse dielectric permittivity ε_{33}^{*T} of the film, as this is seen for a BT film (Table I).

In conclusion, let us analyze the effect of the substrate on the results of experimental measurements of the dielectric and piezoelectric constants of ferroelectric films. It is known[10] that 2D film clamping generates mixed boundary conditions, because dielectric measurements leave unchanged the strains S_{11}, S_{12}, and S_{22} and the stresses T_{13}, T_{23}, and T_{33}. Accordingly, the observed film dielectric permittivities ε_{ij}^{*f} should differ both from the ε_{ij}^{*T} constants at fixed stress and from the permittivities ε_{ij}^{*S} at constant strain. By writing piezoelectric equations relating the stresses and electric induction in a film to strains and electric field at macroscopic level, and using the appropriate boundary conditions, one can readily derive expressions connecting, for instance, ε_{ij}^{*f} with ε_{ij}^{*S}. The dielectric response along the substrate normal, which is usually measured experimentally, for heterostructures with the symmetry of macroscopic properties under study here can be written

$$\varepsilon_{33}^{*f} = \varepsilon_{33}^{*S} + \frac{e_{33}^{*2}}{c_{33}^{*E}}. \tag{12}$$

Equation (12) was used by us to calculate the dependence of ε_{33}^{*f} on residual polarization in textured BT and PT films. The results of the calculations, presented in Figs. 1 and 2 and Tables I and II, show that 2D clamping, as expected, reduces the observed film permittivity ε_{33}^{*f} compared to the permittivity ε_{33}^{*T} at constant stress. The difference between ε_{33}^{*f} and ε_{33}^{*T} increases with increasing piezoelectric constants of the film, and in BT films with a large residual polarization, ε_{33}^{*f} turns out to be even smaller than that in an unpolarized film (Fig. 1, Table I).

The observed piezoelectric response of a thin film should differ also from that of the corresponding bulk sample.[27] When studying the inverse piezoelectric effect, this is due to an electric-field-induced change in internal stresses in the film. One can readily show that the effective film piezoelectric coefficient d_{33}^{*f}, which has recently become a subject of intensive investigation,[27,28] can be calculated within our approach as $d_{33}^{*f} = e_{33}^*/c_{33}^{*E}$. Calculations of d_{33}^{*f} show that 2D clamping of a film brings about a decrease of its piezoelectric coefficient compared to the theoretical value of d_{33}^* (see Figs. 3 and 4 and Tables I and II), so that in BT films, for instance, d_{33}^{*f} may differ by more than two times from d_{33}^*.

Support of Volkswagen Stiftung (Grant I/71644) is gratefully acknowledged.

*E-mail: pertsev@domain.ioffe.rssi.ru

[1] R. Waser, Curr. Opin. Solid State Mater. Sci. **1**, 706 (1996).
[2] J. F. Scott and C. A. Paz de Arajuo, Science **246**, 1400 (1989).
[3] P. Muralt, M. Kohli, T. Maeder, A. Kholkin, K. Brooks, N. Setter, and R. Luthier, Sens. Actuators A **48**, 157 (1995).
[4] M. Marutake, J. Phys. Soc. Jpn. **11**, 807 (1956).
[5] V. I. Aleshin, Krystallografiya **32**, 422 (1987) [Sov. Phys. Crystallogr. **32**, 245 (1987)].
[6] V. I. Aleshin and É. M. Pikalev, Zh. Tekh. Fiz. **60**, No. 3, 129 (1990) [Sov. Phys. Tech. Phys. **35**, 350 (1990)].
[7] T. Olson and M. Avellaneda, J. Appl. Phys. **71**, 4455 (1992).
[8] M. L. Dunn, J. Appl. Phys. **78**, 1533 (1995).
[9] C.-W. Nan and D. R. Clarke, J. Am. Ceram. Soc. **79**, 2563 (1996).
[10] N. A. Pertsev, A. G. Zembilgotov, and A. K. Tagantsev, Phys. Rev. Lett. **80**, 1988 (1998).
[11] N. A. Pertsev and A. G. Zembilgotov, J. Appl. Phys. **78**, 6170 (1995).
[12] N. A. Pertsev and A. Yu. Emel'yanov, Fiz. Tverd. Tela (St. Petersburg) **39**, 127 (1997) [Phys. Solid State **39**, 109 (1997)].
[13] G. Arlt, J. Mater. Sci. **25**, 2655 (1990).
[14] B. Wang, Int. J. Solids Struct. **29**, 293 (1992).
[15] Y. Benveniste, J. Appl. Phys. **72**, 1086 (1992).
[16] J. D. Eshelby, in *Progr. Solid Mechanics*, edited by I. N. Sneddon and R. Hill (North-Holland, Amsterdam, 1961), Vol. 2, p. 89.
[17] M. L. Dunn, Int. J. Eng. Sci. **32**, 119 (1994).
[18] J. H. Huang and J. S. Yu, Composites Eng. **4**, 1169 (1994).
[19] D. M. Barnett and J. Lothe, Phys. Status Solidi B **67**, 105 (1975).
[20] E. G. Fesenko, V. G. Gavrilyachenko, and A. F. Semenchev, *Domain Structure of Many-Axial Ferroelectric Crystals* [in Russian] (Rostov-Don, 1990), 192 pp.
[21] J. F. Nye, *Physical Properties of Crystals* (Clarendon, Oxford, 1964; Mir, Moscow, 1960, 385 pp.).
[22] J. S. Speck, A. Seifert, W. Pompe, and R. Ramesh, J. Appl. Phys. **76**, 477 (1994).
[23] F. Jona and G. Shirane, *Ferroelectric Crystals* (Pergamon, Oxford, 1962; Mir, Moscow, 1965, 555 pp.).

[24] A. L. Roytburd, Mater. Res. Soc. Symp. Proc. **221**, 255 (1991).
[25] W. Pompe, X. Gong, Z. Suo, and J. S. Speck, J. Appl. Phys. **74**, 6012 (1993).
[26] A. V. Turik, Fiz. Tverd. Tela (Leningrad) **12**, 892 (1970) [Sov. Phys. Solid State **12**, 688 (1970)].
[27] K. Lefki and G. J. M. Dormans, J. Appl. Phys. **76**, 1764 (1994).
[28] A. L. Kholkin, E. L. Colla, A. K. Tagantsev, D. V. Taylor, and N. Setter, Appl. Phys. Lett. **68**, 2577 (1996).

Translated by G. Skrebtsov

LATTICE DYNAMICS. PHASE TRANSITIONS

Model of the lattice dynamics and study of the vibronic structure of intracenter transitions in ZnO:Ni^{+2} crystals

A. N. Kislov* and V. G. Mazurenko

Ural State Technical University, 620002 Ekaterinburg, Russia
(Submitted March 31, 1998; resubmitted June 4, 1998)
Fiz. Tverd. Tela (St. Petersburg) **40**, 2213–2216 (December 1998)

This paper presents a calculation of the defect vibrations induced in a ZnO:Ni crystal by the Ni^{+2} impurity. The computations are done by a recursive method in the shell model. Based on the model calculations, the vibronic structure in the absorption spectra of the intracenter $d-d$ transitions in the ZnO:Ni crystal is interpreted. © *1998 American Institute of Physics.* [S1063-7834(98)01612-8]

Crystals of zinc oxide ZnO doped with impurities of the $3d$ transition metals are widely used in various areas of technology because of the features of some of their chemical and physical properties. The study of the vibrational properties of these crystals is of special interest. Extensive experimental material has been accumulated on the vibrational spectra of ZnO crystals with impurities of the $3d$ elements.[1,2] However, the experimental data do not always make it possible to study in detail the change of the phonon spectrum when a defect is introduced into the crystal. Numerical methods that depend on definite theoretical models must be used. The most promising method for studying the vibrational properties of crystals with defects is the recursive method of Ref. 3. This has proven to be one of the few suitable methods for modelling the lattice dynamics of ionic crystals in which a substantial role is played by the long-range Coulomb interaction with charged defects. Calculations by this method of the vibrational spectrum of certain defect crystals with ionic bonding have been reported in a number of papers.[4,5]

The goals of this paper are to model the vibrational spectrum of the ionic–covalent crystal ZnO with a nickel impurity Ni^{+2} ($3d^8$) in a neutral state relative to the crystal lattice and to use this calculation as a basis for interpreting the vibronic structure of the zero-phonon line of the following intracenter $d-d$ transitions: $A_1-{}^3T_1(F)\rightarrow A_1-{}^3T_1(P)$, $A_1-{}^3T_1(F)\rightarrow E-{}^3T_1(P)$,[2,6] $A_1-{}^3T_1(F)\rightarrow A_1-{}^3T_2(F)$, and $A_1-{}^3T_1(F)\rightarrow E-{}^3T_2(F)$.[7]

1. TECHNIQUE AND RESULTS OF CALCULATIONS

The essential problem in modelling the structure and lattice dynamics of crystals with impurities is to correctly describe the interaction not only between the ions of the crystal matrix but also between the impurity and the other ions of the crystal. Because of the complexity of this problem, an approach is widely used in practical calculations for the oxides of many elements[8–10] in which it is assumed that the interaction between the ions is pairwise and central, while the polarizability of the ions is taken into account by using the shell model. In this phenomenological model, the ion–ion, ion–shell, and shell–shell interaction potential $U_{ij}(r)$ is represented by a sum of short-range $V_{ij}(r)$ and long-range Coulomb terms,

$$U_{ij}(r)=V_{ij}(r)+Z_iZ_j/r \tag{1}$$

in which, when writing the Coulomb part, it is assumed that the ions are points and that their charges are constant. The short-range part $V_{ij}(r)$ consists of the Born–Mayer term, which describes the repulsion of the ions because of overlap of their electron shells, and a term responsible for the dipole–dipole interaction of the ions:

$$V_{ij}(r)=A_{ij}\exp(-r/\rho_{ij})-C_{ij}/r^6, \tag{2}$$

where subscripts i and j number the ions and the shells, which lie at a distance r from each other, and A_{ij}, ρ_{ij}, and C_{ij} are constants of the interaction potential that depend on the type of ion.

For the ZnO crystal, the parameters A_{ij}, ρ_{ij}, and C_{ij}, as well as the charges of the shells and the coupling constants of the nucleus and the shell, are given in Ref. 9. The parameters of the short-range part of the interaction potential $V_{ij}(r)$ in that paper were fitted to the elastic constants and permittivity. In doing so, the stability of the ZnO crystal was determined for the case in which it has cubic structure. The results of our calculations of the dispersion curves for a number of highly symmetrical directions of the Brillouin zone on the basis of these parameters showed that it was impossible to use them in further theoretical calculations, since the behavior of the acoustic and optical branches qualitatively differs from the experimental data.[11] In this paper, we used an approach in which the parameters A_{ij}, ρ_{ij}, and C_{ij} in the ZnO crystal were determined on the basis of the known short-range potential for a pair of ions with a similar electron structure, namely nickel Ni^{2+} and oxygen O^{-2} ions. Starting from different sets of parameters of the short-range potential, presented in Refs. 8–10 for the NiO crystal, and fitting the results of the calculation to the experimental frequencies in high-symmetry directions of the Brillouin zone, we obtained

TABLE I. Parameters of the interionic interaction potentials in ZnO.

Interacting ions	A_{ij}, eV	ρ_{ij}, Å	C_{ij}, eV·Å^{-6}
Zn^{+2}–Zn^{+2}	890	0.3	0
Zn^{+2}–O^{-2}	1934	0.2792	0
O^{-2}–O^{-2}	88760	0.149	0

TABLE II. Parameters of the shell model for a ZnO crystal.

Ion	Charge of shell, $\|e\|$	Coupling constant, eV·Å^{-6}
Zn^{+2}	3.7492	116.40
O^{-2}	−2.9345	51.78

a set of parameters (Table I) that gives a good description of the dispersion curves for the ZnO crystal (Fig. 1). We should point out that, when the parameters A_{ij}, ρ_{ij}, and C_{ij} (Table I), the charges of the shells, and the coupling constants (Table II) were chosen, the stability of the crystal lattice relative to the lattice parameters $a = 3.25$ Å and $c = 5.21$ Å was taken into account in terms of the method of molecular statics.[12]

It is well known that zinc oxide crystallizes in the hexagonal wurtzite structure with four ions in the primitive cell and is characterized by a space group of symmetry C_{6v}^4. Its phonon spectrum consists of nine optical and three acoustic branches, which, when the wave vector **q** is zero, are classified in four types: A_1, B_1, E_1, and E_2, determined by the irreducible representations of space group C_{6v}^4. The vibrations of symmetry B_1 are inactive in the Raman spectrum and the IR absorption spectrum. The vibration of type E_2 is active only in the Raman spectrum. A vibration of type A_1, polarized along the hexagonal C axis, and a vibration of type E_1, polarized perpendicular to the C axis, are observed in the IR absorption and Raman spectra. The phonon branches of the optical dipole vibrations that transform as a polar vector under symmetry operations and are active in the IR absorption spectra split because of interaction with the electrostatic Coulomb field into longitudinal (LO) and transverse (TO). It can be seen from Fig. 1 that the calculated LO–TO splitting is somewhat different from the experimentally observed value.

When physical processes that occur with the participation of phonons are being interpreted, important information comes from local vibrations of definite symmetry, which are characterized by the symmetrized local densities of states (SLDS) of the phonons. In the recursive method, the diagonal elements of the Green's function, associated with the dynamic matrix of an ion cluster in real space, are used to calculate the SLDS of the phonons. The accuracy with which the SLDS of the phonons is calculated in the recursive method is determined by the size of the cluster under consideration. A study of the phonon spectrum by the recursive method in the rigid-ion model showed that, when the Coulomb long-range interaction is explicitly taken into account, the necessary accuracy of the calculations is achieved for a cluster made up of 1000–1500 ions. In the shell model, computer-time expenditures substantially increase when the computations involve a dynamic matrix. The technology of sparse matrices currently makes it possible to consider clusters of up to 1000 ions.

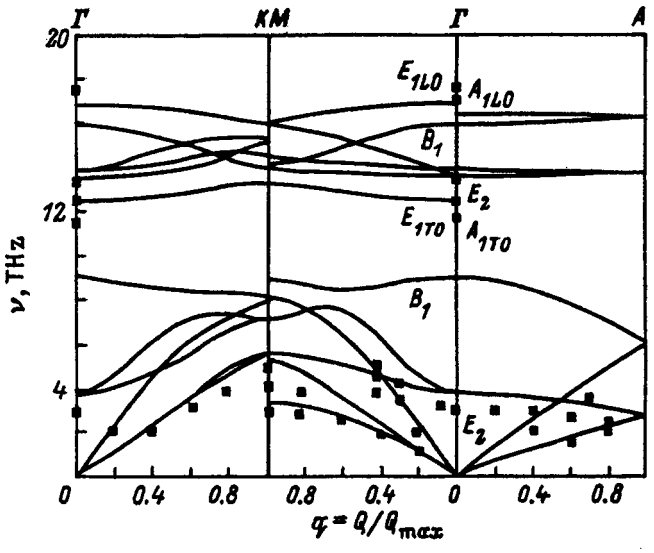

FIG. 1. Results of the calculation of the dispersion curves for a ZnO crystal. The squares show the experimental values.[10]

When a Ni^{+2} impurity is introduced into the ZnO crystal, the crystal vibrational states that show up in actual processes are distorted. The defect has a substantial influence on the motion of the nearest-neighbor ions. Because of this, the most significant information concerning the vibrations of a crystal with a defect comes from the SLDS of the phonons, projected onto the region made up of the first coordination sphere (CS). The Ni^{+2} impurity that replaces the Zn^{+2} ion in the ZnO crystal breaks the translational symmetry, and the point group of the positional symmetry of the impurity (group C_{3v}) must be taken into account when describing the vibrations. The 15-dimensional vibrational representation of the defect region that includes the first CS breaks up into irreducible representations of point group C_{3v}:

$$\Gamma(15) = 4A_1 + A_2 + 5E. \tag{3}$$

Choosing the basis vector of the irreducible representation, obtained by the standard methods of group theory, for the initial vector, we calculate by the recursive method the SLDS of the given symmetry Γ for an ideal crystal, $G_\Gamma^0(\nu)$, or for a defect crystal, $G_\Gamma(\nu)$. The maxima in the $G_\Gamma(\nu)$ spectrum that do not coincide with the features in $G_\Gamma^0(\nu)$ determine the vibrations of symmetry Γ induced by the Ni^{+2} impurity in ZnO.

The static distortion of the crystal field by the Ni^{+2} impurity was computed in the approximation of the method of molecular statics. The calculations showed that the shift of the equilibrium position of the nearest neighbors of the nickel is very insignificant and can be neglected. This is explained by the similarity in the behavior of the short-range part of the interaction potential for Zn^{+2} and Ni^{+2} ions in a ZnO crystal and consequently by the small difference of the matrices of the force constants for the given ions used in the method of molecular statics.

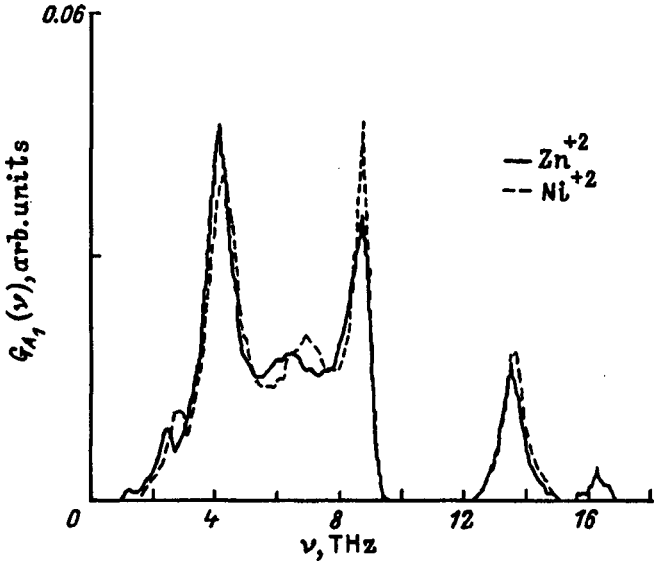

FIG. 2. SLDS of the vibrations projected onto a displacement of type-A_1 symmetry of a Zn^{+2} ion in a ZnO crystal (solid curve) and a Ni^{+2} ion in $ZnO:Ni^{+2}$ (dashed curve).

The technique described above was used to calculate the SLDS of phonons with symmetry A_1, A_2 and E. Figure 2, for example, shows the calculated SLDS of the vibrations projected onto the displacement of symmetry A_1 of the Zn^{+2} ion in a ZnO crystal and of the Ni^{+2} ion in $ZnO:Ni^{+2}$. It can be seen that two resonance vibrations appear at frequencies $\nu_{Ni}(A_1)=2.8$ and 6.8 THz in which the impurity itself participates. The calculations do not predict the existence of defect vibrations of type A_1 in which the impurity is at rest.

2. DISCUSSION OF THE RESULTS

When a nickel impurity is introduced into the ZnO lattice, a perturbation responsible for the distortion of the crystal lattice appears. This perturbation can be represented by a set of phonons with which the electronic ground state of the impurity interacts. The symmetry of these vibrations is determined by the irreducible representations present in the decomposition of the symmetrized product of the irreducible representation $[\Gamma_a^2]$ according to which the wave function of the electronic ground state (a) transforms under symmetry operations. For Ni^{+2} in a ZnO crystal, the ground state of the d^8 configuration is A_1. Therefore, the change of the equilibrium positions of the ions when a Ni^{+2} impurity in the ground state is present in the ZnO crystal is associated with vibrations of symmetry A_1.

The study of optical transitions in which phonons participate provides an understanding of the actual picture of the internal interaction processes of radiation with matter. Intracenter transitions between the impurity levels are possible in a $ZnO:Ni^{+2}$ crystal. The zero-phonon line of such a transition is accompanied by vibrational satellites caused by the emission of a phonon due to electron–phonon interaction. The intensity of these satellites depends on the square of the matrix element of the perturbation operator f that translates the system from one electron state (a) to another (b), on the value of the electron–phonon coupling of the transition, and on the density of the phonon states of a crystal with an impurity. Moreover, limitations determined from well-known selection rules are imposed on an intracenter transition.

For $ZnO:Ni^{+2}$ crystals, the low-temperature absorption spectra for intracenter d–d transitions of type $A_1-{}^3T_1(F)\rightarrow A_1-{}^3T_1(P)$ and $A_1-{}^3T_1(F)\rightarrow E-{}^3T_1(P)$ are shown in Refs. 2 and 6, and those for transitions of type $A_1-{}^3T_1(F)\rightarrow A_1-{}^3T_2(F)$ and $A_1-{}^3T_1(F)\rightarrow E-{}^3T_2(F)$ are given in Ref. 7. The presence of such transitions is caused by splitting of the ^3F and ^3P states of the free Ni^{+2} ion by a tetrahedral crystal field of symmetry Td. The resulting states are divided by spin–orbit coupling into a series of energy levels that in turn, under the action of the actual trigonal field C_{3v}, are again split into sublevels of definite symmetry. The ground state from which transitions occur for a Ni^{+2} ion in a ZnO crystal is the $A_1-{}^3T_1(F)$ state; at liquid-helium temperatures, only the zeroth vibrational level is occupied in it.

If the radiation that interacts with the vibronic state and produces the vibronic transition has π polarization, i.e., if it is polarized in the orientation $\mathbf{E}\|C$ (where $\mathbf{E}$ is the electric vector of the radiation), the electric dipole moment operator transforms according to irreducible representation A_1. For radiation with σ polarization ($\mathbf{E}\perp C$), the electric dipole moment operator that determines the transition probability transforms according to an irreducible representation of type E. In this case, according to the selection rule, states of symmetry A_1 and E can be dipole-active. An $A_1\rightarrow A_1$ transition is then allowed for π-polarized radiation, while $A_1\rightarrow E$ is allowed for σ-polarized radiation. Moreover, for an intracenter transition of type $A_1\rightarrow A_1$, the zero-phonon line is accompanied by a phonon sideband consisting of vibrations of A_1 symmetry. With a transition of type $A_1\rightarrow E$, a vibration of E symmetry contributes to the creation of the vibrational satellite.

Reference 7 shows the absorption spectra of a ZnO crystal doped with Ni^{+2} for the transitions $A_1-{}^3T_1(F)\rightarrow A_1-{}^3T_2(F)$ and $A_1-{}^3T_1(F)\rightarrow E-{}^3T_2(F)$. The intensity of the vibrational background is insignificant in these spectra. Strengthening of the structure of the spectrum associated with vibrations of type A_1 is observed in the region of frequencies 3.1, 7.4, and 16.4 THz, while that associated with type-E vibrations is observed around 4.8, 14.4, 16.4 THz. A rigorous analysis of the vibronic satellites is difficult in this case. However, it can be noted that maxima close to these frequencies are present in the calculated $G_\Gamma(\nu)$ spectra for the corresponding symmetries A_1 (Fig. 3) and E.

A more detailed interpretation can be carried out for absorption spectra involving the transitions $A_1-{}^3T_1(F)\rightarrow A_1-{}^3T_1(P)$ and $A_1-{}^3T_1(F)\rightarrow E-{}^3T_1(P)$.[6] The vibrational background of the spectra possesses a rich structure. Table III shows the frequencies corresponding to the positions of the most intense peaks. This table also gives the frequencies of the positions of the features in the calculated $G_\Gamma(\nu)$ spectra of the SLDS for vibrations of symmetry A_1 and E. Good correlation is observed between the frequencies. It can be asserted that the two lines in the vibronic structure determined by vibrations of symmetry A_1, at frequencies 3.2 and 7.0 THz, are caused by the interaction of

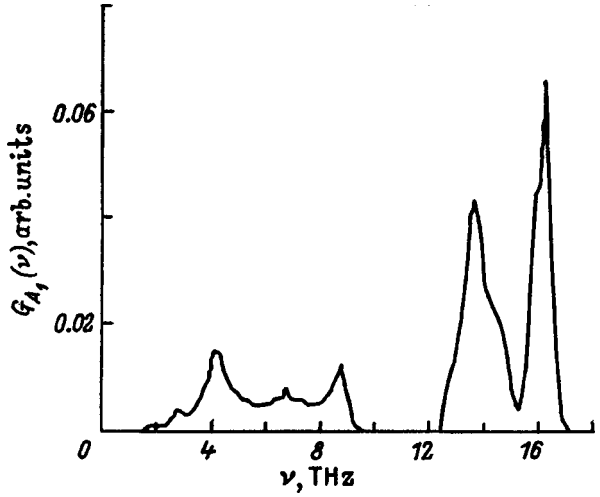

FIG. 3. Calculated SLDS of vibrations of symmetry A_1 projected onto the defect region bounded by the first CS for a $ZnO:Ni^{+2}$ crystal.

resonance vibrations of the Ni^{+2} impurity with the electronic transition. The interpretation of the other lines is analogous to the interpretation of those in Ref. 6, where the position of the lines was compared with the position of the critical points of the dispersion curves at the frequency of which a Van Hove singularity is observed in the total density of phonon states of an ideal ZnO crystal. The analysis of the vibrational background of the zero-phonon line makes it possible to assert that its structure qualitatively reflects the form of the SLDS of the phonons, obtained in numerical calculations for a crystal with a defect.

TABLE III. Frequencies of the maxima in the absorption spectra and SLDS in a $ZnO:Ni^{+2}$ crystal (in THz).

Vibrations of symmetry A_1		Vibrations of symmetry E	
Calculation	Experiment[6]	Calculation	Experiment[6]
2.8	3.2	2.2	3.0
4.0	4.0	4.0	4.0
⋯	4.9	6.0	5.8
⋯	5.3	8.8	8.6
6.8	7.0	13.6	13.1
8.6	8.1	14.2	15.5
13.6	13.0	16.2	17.3
16.2	16.4		

The calculations carried out here for defect vibrations of various symmetries for zinc oxide ZnO doped with nickel Ni^{+2} have thus made it possible to connect the observed vibronic peaks in the spectrum of the intracenter transitions with the vibrational spectrum of $ZnO:Ni^{+2}$. In analyzing the vibronic peaks, such an approach is more correct than an approach in which the analysis of the experimental data is based on information concerning the vibrational spectrum of an ideal crystal and neglects the appearance of defect vibrations induced by the impurity.

The authors express their gratitude to A. N. Varaksin for checking the stability of the ZnO crystals with the parameters of the potentials of the interionic interaction used in the calculations.

This work was supported by the Russian Fund for Fundamental Research (Project No. 96-02-16278-a).

*E-mail: ank@dpt.ustu.ru

[1] I. P. Kuz'mina and V. A. Nikitenko, *Zinc Oxide. Production and Optical Properties* (Nauka, Moscow, 1984), 166 pp.
[2] H. A. Weakliem, J. Chem. Phys. **36**, 2117 (1962).
[3] R. Haydock, V. Heine, and M. J. Kelly, J. Phys. C **5**, 2845 (1972).
[4] V. G. Mazurenko and A. N. Kislov, Fiz. Tverd. Tela (Leningrad) **33**, 3433 (1991) [*sic*].
[5] A. N. Kislov, V. G. Mazurenko, V. I. Sokolov, and A. N. Varaksin, Fiz. Tverd. Tela (St. Petersburgh) **39**, 2147 (1997) [Phys. Solid State **39**, 1921 (1997)].
[6] U. G. Kaufmann and P. Koidl, J. Phys. C **7**, 791 (1974).
[7] U. G. Kaufmann, P. Koidl, and O. F. Schirmer, J. Phys. C **6**, 310 (1973).
[8] M. J. L. Sangster and A. M. Stoneham, Philos. Mag. B **43**, 597 (1981).
[9] G. V. Lewis and C. R. A. Catlow, J. Phys. C **18**, 1149 (1985).
[10] A. M. Stoneham and M. J. L. Sangster, Philos. Mag. B **52**, 597 (1985).
[11] A. W. Hewat, Solid State Commun. **8**, 187 (1970).
[12] Yu. N. Kolmogorov and A. N. Varaksin, Deposited at the All-Union Institute of Scientific and Technical Information, Reg. No. 2395 (1989).

Translated by W. J. Manthey

The initiating action of continuous heating on structural remodeling in Ag_3AsS_3 crystals

I. M. Shmyt'ko,*) N. S. Afonikova, and N. A. Dorokhova

Institute of Solid-State Physics, Russian Academy of Sciences, 142432 Chernogolovka, Moscow Region, Russia

(Submitted April 28, 1998)
Fiz. Tverd. Tela (St. Petersburg) **40**, 2217–2220 (December 1998)

The effect of continuous heating on the characteristics of phase transformations in proustite (Ag_3AsS_3) is established. It is shown that continuous heating, like continuous cooling, stimulates structural remodeling, in this case reducing the temperature of the known phase transitions.
 [S1063-7834(98)01712-2]

Phase transformations in crystals are usually studied with the experimental conditions as close as possible to equilibrium. Special attention in this case is paid to thermally stabilizing the sample and eliminating temperature gradients, since the latter produce macroscopic mechanical strains in the crystals and consequently change the temperature or blur the phase transitions. However, structural effects are frequently observed that appear as the temperature changes and that cannot always be explained by the action of macroscopic strains or relaxation processes during the transition to a new equilibrium state. In this respect, it is interesting to study structural processes during continuous cooling and heating.

Incommensurately modulated phases are especially sensitive to temperature changes. They show changes in the behavior of the wave vector, the refractive index, the permittivity, the global hysteresis characteristics, etc., depending on the history of the sample and the path over which the temperature is varied in the region of the phase transitions.[1–3] The resulting anomalies have been associated with the incompleteness of the relaxation processes in the defect subsystem of the crystal and with manifestations of the pinning of modulations on these defects.

The effect of a continuous temperature variation on the structural characteristics of crystals containing incommensurately modulated phases was first systematically studied on proustite crystals in our papers.[4–6] It was established that, when the samples are continuously cooled, the temperatures of all three phase transitions known for this material increase, the more so, the higher the cooling rate. The initiating action of continuous cooling was later confirmed on crystals of thiourea $(SC(NH_2))_2$, Rb_2ZnCl_4, and $TMA-ZnCl_4$ (the A_2BX_4 family), which also contain incommensurately modulated phases.[7,8] It was also shown that the initiating action of cooling is associated neither with mechanical stresses caused by a temperature gradient in the sample during cooling, nor with changes in the electron subsystem, nor with a change of the dielectric (pyroelectric) characteristics, nor with any other known factors. However, these results are still insufficient for the detected effect of the induction of structural transformations by continuous temperature variation to be regarded as a new physical phenomenon. To round out the picture of the physical phenomenon, studies of the influence of continuous heating on the structural characteristics of these and other compounds are also necessary. The anomalous influence of continuous heating on phase transitions was noted in crystals of gadolinium molybdate and lead orthophosphate,[9,10] for which a significant reduction of T_c was observed when the temperature was rapidly increased. In this case, the interpretation of the reduction of T_c was based on the assumption that the experiment was carried out under nonequilibrium conditions. The authors explained the reduction of the transformation temperature in the gadolinium molybdate, which is ferroelastic, as the result of the appearance of tensile stresses in the sample because of inhomogeneous heating.

Since, in the case of modulated systems, the anomalies of the physical properties involved incompleteness of the relaxation processes in the defect subsystem of the crystal and manifestations of the pinning of modulations on these defects, the setup of the experiments becomes the determining factor, with the heating being carried out from a low-temperature phase in which the heterophase fluctuations of the modulated phases are temperature-suppressed. Such a setup prevents the pinning of fluctuations of the incommensurate phase at the defects, and the initiating effect, if there is such a thing, must appear in pure form.

The influence of continuous heating on the characteristics of phase transitions in crystals with incommensurate phases was studied for this paper, using as an example proustite, which has three phase transitions: normal phase $\leftrightarrow$ incommensurate phase at 60 K, incommensurately modulated $\leftrightarrow$ commensurately modulated at 48–50 K, commensurately modulated $\leftrightarrow$ ferroelectric phase at 28–30 K. The phase transition at 60 K is a second-order phase transition, while the phase transitions at 48–50 K and 28–38 K are first-order phase transitions. The same samples on which experiments were done on the influence of continuous cooling were used here. The heating from the low-temperature phase was carried out from liquid-helium temperatures, at which fluctuations of the modulated phases are energetically of low probability.

1. EXPERIMENTAL TECHNIQUE

Thin chips of proustite $1\times1\times0.02$ mm, with the surface of the chip parallel to the (10.1) plane, were studied. The

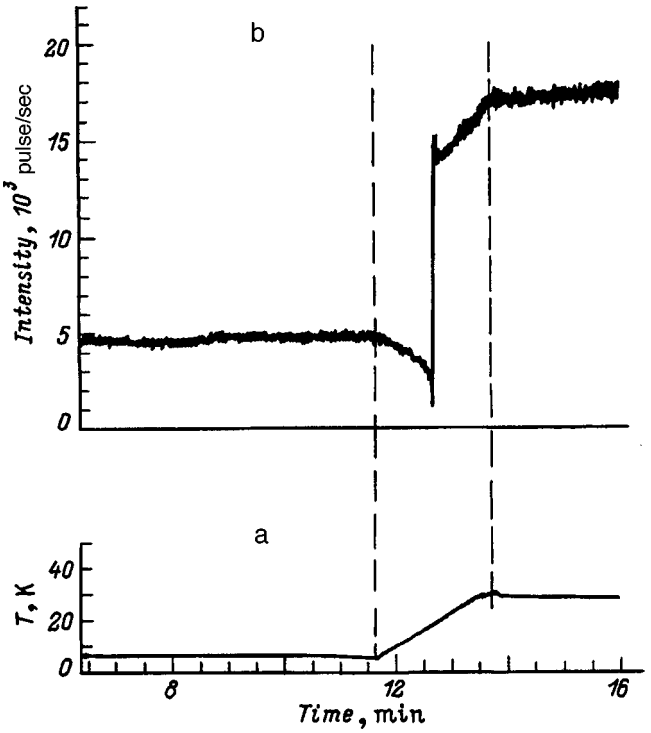

FIG. 1. Temperature variation (a) and the corresponding intensity variation of the (-60.6) Bragg reflection (b) for one of the experiments.

experiments were run on a DRON-4 x-ray diffractometer, which we automated to allow the temperature and the diffracted-beam intensity to be simultaneously recorded while the temperature was continuously varied. The crystals were placed in the well of a liquid-helium cryostat that made it possible to continuously heat the sample at an adjustable rate. The heating rate was varied by varying the current on the helium-vapor heater in the well of the cryostat. The temperature was measured with a thermocouple whose cold end was placed next to the sample, while the second end was at 0 °C. The diameter of the welded ball was 0.5–0.7 mm.

The structural state of the crystal was analyzed from the temperature dependence of the peak intensity of the (-60.6) Bragg reflection. To do this, the detector of the diffractometer was adjusted to the position of the reflection close to the phase transition in the high-temperature (or low-temperature) phase and remained fixed during the heating. When the phase-transition temperature T_c $(\sim 30\,\mathrm{K})$ is reached, because of the sharp change of the cell parameters,[11] a misadjustment of the sample from the exact Bragg position occurs, and consequently there is an abrupt change of the intensity of the Bragg reflection. This jump served as a reference point for measuring T_c in experiments with continuous heating. As an example, Fig. 1 shows how the temperature and the intensity of the Bragg reflection varied in one of the experiments. The jump in the intensity of the Bragg reflection corresponds to the phase-transition temperature T_c.

With rapid heating (cooling), it was not always possible to keep the rate of temperature variation (dT/dt) constant. In this case, the method of least squares was used to make an estimate of the mean heating rate, which was then used in constructing the main characteristics of the process. When the interval of the temperature variation was large (for 4.2 to 120–140 K, for example), the estimated heating rate was taken as the temperature difference of the beginning and end of the heating, divided by the heating time. However, the estimated rates of temperature variation were not used to construct the dependences of the transformation characteristics, but were used only to qualitatively confirm the processes as they occurred.

It should be especially pointed out that, before beginning each temperature experiment, the sample was held at the beginning temperature of the heating (cooling) for a long time, in order to ensure relaxation of possible diffusion processes with characteristic times comparable with the time for one heating (cooling) cycle.

2. EXPERIMENTAL RESULTS AND DISCUSSION

Before carrying out experiments with continuous heating, we made certain, as before,[4] that continuous cooling increases T_c above the equilibrium value. For example, when the crystal is cooled from a temperature of 35 K from the commensurately modulated phase $R3_c$ to the ferroelectric phase Cc at a rate of 20.9 K/min, T_c increases by 3.8 degrees. It should be pointed out that no pinning of the modulation can explain the increase of T_c in this case, since it would reduce and not increase T_c, just as in the case of the ''instrumental effect,'' in which the temperature of the sample does not go beyond the temperature of the coolant vapor.

With continuous heating, a decrease of the transition temperature $T_{c\,\mathrm{heat}}$ by comparison with the equilibrium value $T_{c\,\mathrm{equ}}$ is observed; i.e., like continuous cooling, continuous heating stimulates in proustite crystals phase transformations that result in an earlier transformation from the low temperature Cc phase to the modulated $R3c$ phase. The dependence of $(T_{c\,\mathrm{heat}}-T_{c\,\mathrm{equ}})$ on the heating rate is shown in Fig. 2a. It can be seen from this figure that, as the heating rate increases, the reduction of T_c first increases and then, beginning with a rate of 8–10 K/min, decreases.

The decrease of the inducing action of heating at high heating rates has, in our opinion, the following explanation. To make a transition into a new phase state, nucleation centers must be formed. In the case of ordering-type phase transitions, which we are dealing with here,[12] their formation requires a definite time. If the heating (cooling) rate is large, while the temperature-variation interval from the beginning of the heating to T_c, as in our case, is small, a number of nucleation centers of the new phase state sufficient for the phase transition either simply cannot form in the time of the temperature variation (and the structural remodeling occurs at the usual temperature) or forms close to the equilibrium T_c (and then the effect of the stimulating action of continuous heating is less pronounced). This conclusion is supported by the observed dependence of the effect on the initial temperature for a constant heating rate (Fig. 2b). It can be seen that the closer the temperature of the beginning of the heating is to $T_{c\,\mathrm{equ}}$, the smaller is the decrease of $T_{c\,\mathrm{heat}}$. This result of a decrease of the effect at high rates also repudiates the non-

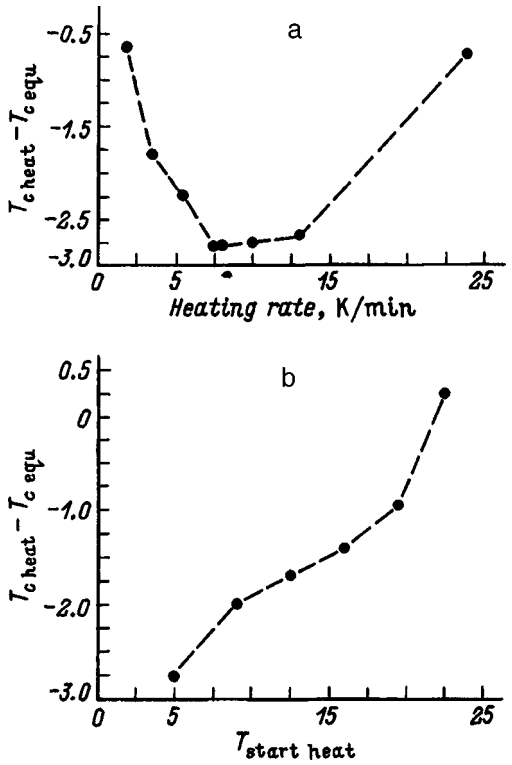

FIG. 2. Shift of T_c ($T_{c\,heat} - T_{c\,equ}$) vs heating rate (a) and vs the starting temperature of heating with a constant sample-heating rate equal to 9.3 K/min (b).

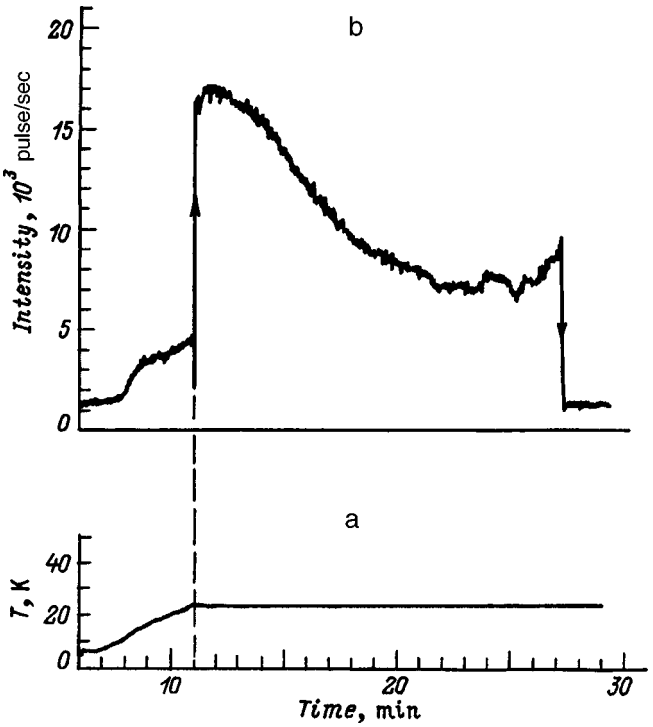

FIG. 3. Temperature variation (a) and the behavior of the intensity of the (−60.6) Bragg reflection (b) in experiments to determine the characteristic decay time of heat-stimulated metastable states.

equilibrium heating mechanism, as we mentioned above. The opposite phenomenon would be observed in that case: The higher the heating rate, the larger the effect would be.

Heat-stimulated structural states are unstable and return to the initial low-temperature C_c phase after some characteristic time (several minutes). As an example, Fig. 3 shows the temperature and structural path of an experiment in which, immediately after a heating-initiated phase transition, the sample was temperature-stabilized (the horizontal section on the dependence of the thermocouple readings). It can be seen from this figure that the crystal returns to the original low-temperature phase in 16 min.[1)]

Continuous heating, like continuous cooling, not only stimulates the Cc–$R3c$ transition, but also reduces temperature $T_{\text{lock-in}}$ (the lock-in transition) and the temperature T_i of the transition from the incommensurately modulated phase to the paraphase (the IC transition). Figure 4 shows the time dependences of the Bragg reflection (−60.0) in the region of the lock-in and IC transformations for different rates and initial temperatures of cooling. The steps in the dependences of the intensity correspond to the lock-in and IC transitions. For these transitions, as for the $Cc \leftrightarrow R3c$ transition, the actual temperature reduction depends on the heating rate and has a form analogous to that shown in Fig. 2.

The results concerning the stimulating action of continuous heating on phase transitions in proustite obtained in this paper, combined with our earlier results concerning the stimulating action of continuous cooling in various crystals, thus give a basis for asserting that continuous temperature variation is a new, previously unknown factor that acts on phase transitions. These results do not provide an explanation of the nature of this action. Since all the preceding experiments were done on crystals containing modulated commensurate and incommensurate phases in definite temperature regions, it is hoped that the nature of the stimulating action of continuous temperature variation on the characteristics of phase transitions can be explained by carrying out similar studies on crystals that do not contain modulated phases but that undergo phase transformations of the ordering and shift type.

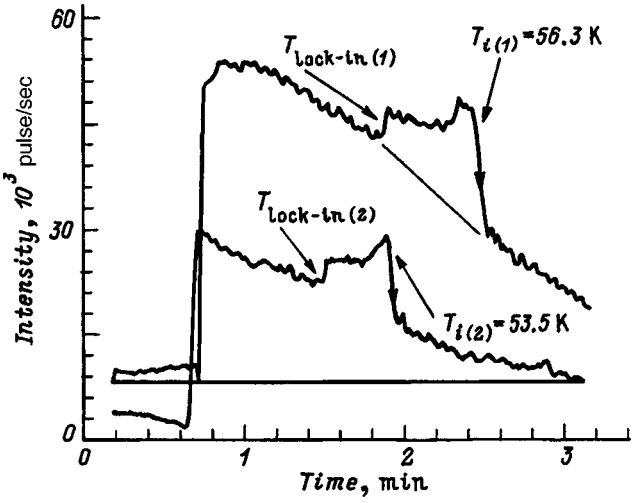

FIG. 4. Characteristic behavior of the intensity of the (−60.6) Bragg reflection in the region of the lock-in and IC phase transitions. The heating rate is 16.8 (*1*) and 22.9 K/min (*2*). $T_{i\,equ} = 60$ K and $T_{\text{lock-in equ}} = 50$ K.

The authors are grateful to G. A. Ryazankin for help in automating the experiment.

This work was supported by INTAS Grant N 93-3230-ext.

*)E-mail: shim@issp.ac.ru

1)The intensity increase before the $C_c \rightarrow R3c$ transition and the reverse $R3c \rightarrow Cc$ transition is caused by the diffraction-extinction effect produced by microscopic strains of the lattice when heterophase precipitates form.

[1] B. A. Strukov, Izv. Akad. Nauk SSSR, Ser. Fiz. **51**, 1717 (1987).
[2] F. Mogeon, G. Dolino, and M. Vallade, Phys. Rev. Lett. **62**, 179 (1989).
[3] O. G. Vlokh, V. S. Zhmurko, I. I. Polovinko, V. N. Mokryĭ, and S. A. Sveleba, Kristallografiya **36**, 769 (1991) [Sov. Phys. Crystallogr. **36**, 430 (1991)].
[4] N. S. Afonikova, S. S. Khasanov, and I. M. Shmyt'ko, JETP Lett. **41**, 314 (1985).
[5] I. M. Shmyt'ko, V. Sh. Shekhtman, B. Sh. Bagautdinov, and N. S. Afonikova, Fiz. Tverd. Tela (Leningrad) **32**, 2441 (1990) [Sov. Phys. Solid State **32**, 1416 (1990)].
[6] I. M. Shmyt'ko, B. Sh. Bagautdinov, and N. S. Afonikova, Izv. Akad. Nauk SSSR, Ser. Fiz. **56**, 10, 69 (1992).
[7] B. Sh. Bagautdinov and I. M. Shmyt'ko, JETP Lett. **59**, 182 (1994).
[8] B. Sh. Bagautdinov, V. V. Gladkiĭ, S. N. Kallaev, V. A. Kirikov, and I. M. Shmyt'ko, JETP Lett. **59**, 119 (1994).
[9] N. N. Bol'shakova, I. I. Sorokina, and V. M. Rudyak, Fiz. Tverd. Tela (Leningrad) **25**, 296 (1983) [Sov. Phys. Solid State **25**, 168 (1983)].
[10] V. M. Rudyak and N. N. Bol'shakova, Kristallografiya **39**, 93 (1994) [Crystallogr. Rep. **39**, 82 (1994)].
[11] S. S. Khasanov and V. Sh. Shekhtman, Ferroelectrics **67**, 55 (1986).
[12] T. D. Krushel'nitskaya, Fiz. Tverd. Tela (Leningrad) **22**, 1046 (1980) [Sov. Phys. Solid State **22**, 610 (1980)].

Translated by W. J. Manthey

The effect of a magnetic field on Jahn–Teller ordering in the monoclinic crystal $RbDy(WO_4)_2$

V. P. D'yakonov, V. I. Markovich,* V. L. Kovarskiĭ, and A. V. Markovich

Donetsk Physicotechnical Institute, Ukrainian Academy of Sciences, 340114 Donetsk, Ukraine

M. Borowiec, A. Endzheĭchak, and G. Szymczak

Physics Institute, Polish Academy of Sciences, 02-668 Warsaw, Poland

(Submitted May 12, 1998)
Fiz. Tverd. Tela (St. Petersburg) **40**, 2221–2225 (December 1998)

This paper presents the results of a study of the thermal properties of monoclinic single-crystal $RbDy(WO_4)_2$ at temperatures of 2–15 K and in magnetic fields up to 6 T. From the results of measurements of the heat capacity and thermograms, two structural phase transitions are detected, at $T_{c1}=4.9$ K and $T_{c2}=9.0$ K. The transformation from the high-temperature phase to the low-temperature phase occurs via an intermediate phase. The field dependences of the critical temperatures are found for various magnetic-field orientations. $H-T$ phase diagrams are constructed for $H\|a$ and $H\|c$. An anomalous increase (by almost an order of magnitude) of the relaxation time of the system, associated with structural instability of the crystal lattice, is detected in the region of the structural phase transitions. A symmetry analysis is carried out, and possible crystal structures of the low-temperature phase are indicated.
 [S1063-7834(98)01812-7]

Structural phase transitions caused by the cooperative Jahn–Teller effect can occur in crystals that have a sublattice of ions in which the electronic ground state is degenerate or pseudo-degenerate.[1] For a dysprosium-ion sublattice, such transitions actually occur in a number of compounds: molybdates, vanadates, and arsenates.[1–4] A lowering of the symmetry and a reconstruction of the energy spectrum of the Dy^{3+} ion usually occurs in such a transition.

A test that characterizes the Jahn–Teller nature of structural phase transitions is the magnetic-field dependence of the transition temperatures. There is special interest in the case of antiferrodistortion ordering of the distortions in low-symmetry dysprosium compounds. Thus, in potassium–dysprosium tungstate $KDy(WO_4)_2$, which has a monoclinic structure in the high-temperature phase, a structural phase transition of Jahn–Teller type, with $T_c=6.38$ K, shows antiferrodistortion behavior and is characterized by strong anisotropy in the magnetic-field dependence of the transition temperature.[5] Moreover, when single-crystal $KDy(WO_4)_2$ was studied calorimetrically, an anomalous increase was detected in the relaxation time of the system after a thermal pulse in the temperature region above T_c; this showed that the crystal lattice is unstable and was an argument in favor of the existence of an incommensurate phase for $T>T_c$.

The theoretical treatment of Ref. 3 shows that, when the antiferrodistortion structure is disturbed by a magnetic field, the transition temperature in the low-field region decreases proportionally to the fourth power of the magnetic field, but, as it approaches the critical value of H_{cr}, it rapidly decreases to zero.

The goal of this paper is to carry out calorimetric studies of monoclinic single-crystal $RbDy(WO_4)_2$ in the low-temperature region of 2–15 K and at magnetic fields up to 6 T in order to detect and study the features and nature of the structural phase transitions.

1. SAMPLES AND EXPERIMENTAL TECHNIQUE

Rubidium dysprosium tungstate $RbDy(WO_4)_2$ belongs to the class of tungstates of the alkali and rare-earth elements.[6,7] The structure of $RbDy(WO_4)_2$ at low temperatures has not yet been studied (only the data for room temperature are known). The low-temperature phase of rubidium dysprosium tungstate undergoes a polymorphic transition to a high-temperature phase at 1098 K. Therefore, single crystals of $RbDy(WO_4)_2$ were grown using a modified Czochralski method on an oriented [110] seed crystal. The growth rate was about 0.05 mm/h.[8]

Rubidium dysprosium tungstate crystallizes into the monoclinic α-$KY(WO_4)_2$ structure (C_{2h}^6-C2/c) typical of a number of double rare-earth tungstates at room temperature. The lattice parameters are $a=10.66$ Å, $b=10.45$ Å, and $c=7.569$ Å. The monoclinic angle equals $\beta=94.5°$. The unit cell of $RbDy(WO_4)_2$ contains four formula units. The Dy^{3+} ion is surrounded by eight oxygen atoms and has local symmetry C_2. The Dy^{3+} cations are located on twofold axes of ($L2$) symmetry (coinciding with the [010] crystallographic directions) inside a distorted eight-pointed figure made up of oxygen atoms, in which two of the Dy–O distances exceed the other six, which are similar to each other. The density of single-crystal $RbDy(WO_4)_2$ is about 7.79 g/cm^3. The ground state of the dysprosium ion is $^6H_{15/2}$. In the crystal field of monoclinic symmetry, the multiplet is split into eight Kramers doublets.

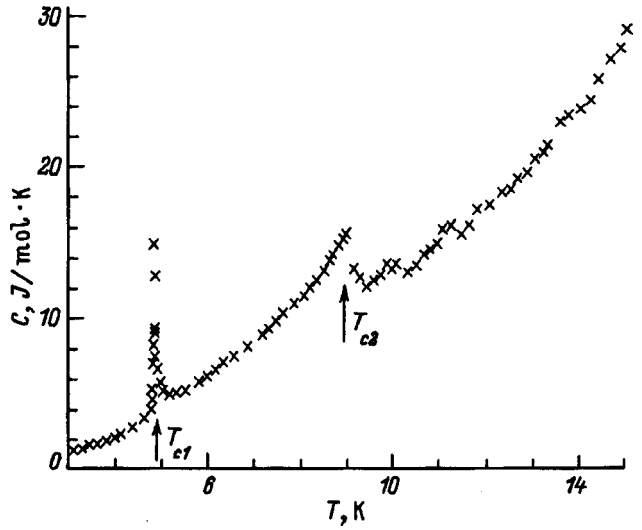

FIG. 1. Temperature dependence of the heat capacity of single-crystal $RbDy(WO_4)_2$. The arrows show the positions of the phase-transition temperatures.

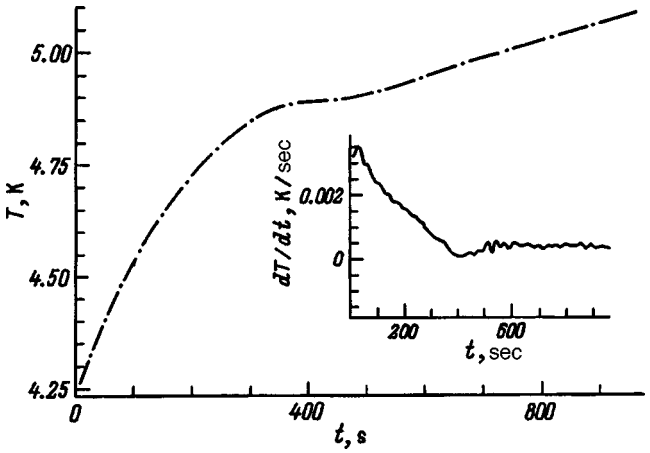

FIG. 2. Thermogram of $RbDy(WO_4)_2$ in the region of a first-order phase transition. The inset shows the time derivative of the temperature, dT/dt.

The details of the experimental apparatus for measuring the heat capacity and the methodological features of the measurement were described in detail earlier.[8,9] Besides the heat-capacity measurements, quasi-static thermograms were measured on the same apparatus; the temperature-scanning rate was varied over a wide range (0.1–1 K/min) as the temperature was increased but was not adjusted as the temperature was decreased, when it equalled about 0.2 K/min.

The measurements were made on a $RbDy(WO_4)_2$ sample with dimensions of about $4\times3\times0.5$ mm and a mass of 0.0493 g. The sample was mounted on a sapphire substrate 20 mm in diameter and 0.3 mm thick, using 0.2 mg of Apiezon N vacuum grease. The measurements were made with the magnetic field oriented along the *a* and *c* axes of a single crystal of $RbDy(WO_4)_2$.

2. RESULTS AND DISCUSSION

As can be seen from Fig. 1, the temperature dependence of the heat capacity $C(T)$ has singularities in the neighborhoods of 4.9 and 9.0 K. The $C(T)$ anomalies are apparently associated with structural transitions, since the rare-earth sublattice becomes magnetically ordered at lower temperatures ($T_N=0.818$ K).[9] They have different characters: The first is a delta function at $T_{c1}=4.9$ K and is typical of first-order phase transitions; the second is a wide lambda anomaly with a peak at $T_{c2}=9.0$ K and is typical of second-order phase transitions. The features of the transitions can be made more precise by using quasi-static thermograms. Actually, the thermogram shows the presence of an area associated with a hidden thermal transition in the region of T_{c1} (Fig. 2) and the absence of such in the neighborhood of T_{c2}. Figure 2 also shows the dependence of the time derivative of the temperature, dT/dt, from which the transition temperature was determined more accurately than from a thermogram, especially when measured in magnetic fields. In the region of T_{c2}, the derivative dT/dt also made it possible to reliably record the transition temperature from the inflection point. The thermodynamic characteristics of the first-order phase transition were determined by the thermogram method: The interval of the transition is ≈1 K, the temperature hysteresis is ≈0.4 K, the change of the enthalpy is $\Delta H\approx0.15$ J/mol, and the corresponding entropy change is $\Delta S/R\approx0.02$.

In an earlier investigation of the heat capacity of $KDy(WO_4)_2$, we detected a sharp increase (by almost an order of magnitude) in the relaxation time of the temperature of the sample after applying a heat pulse at $T>T_c=6.38$ K. The relaxation time τ in this case was about 20–30 sec for $T<T_c$, whereas it was about 150–200 sec for $T>T_c$. The situation is similar in $RbDy(WO_4)_2$. In the region of T_{c1}, τ sharply increases from 10–20 sec to 250–300 sec and then only increases very weakly with increasing temperature.

The existence of two phase transitions, of first and second order, as well as the anomalous increase of τ for $T>T_c$ suggests that it is possible that a modulated structure exists in this temperature region. As follows from an investigation of the thermal[10,11] and optical properties,[4] such a phase with modulated order not commensurate with the lattice parameter actually exists in the compositionally similar compounds $MDy(MoO_4)_2$ (M=Cs,K). There is also a first-order phase transition [$T_{c1}=42$ K for $CsDy(MoO_4)_2$ and $T_{c1}=11.5$ K for $KDy(MoO_4)_2$] and a second-order phase transition [$T_{c2}=59.4$ K for $CsDy(MoO_4)_2$ and $T_{c1}=14.3$ K for $KDy(MoO_4)_2$] in these compounds, while the intermediate phase is an incommensurate superstructure. When the incommensurate phase is formed, additional phonon scattering occurs at spatial structural inhomogeneities. The size of these inhomogeneities is comparable with the free path length of the phonons. Estimates of the effective mean free path of the phonons in $CsDy(MoO_4)_2$ in the region of existence of the incommensurate phase gives a value of about 80 Å.[11] The appearance of the incommensurate phase in $CsDy(MoO_4)_2$ is accompanied by an abrupt decrease (by about a factor of 2.5) of the thermal conductivity in the region of T_{c1}. The sharp increase of τ in the region of T_{c1} in $RbDy(WO_4)_2$ and $KDy(WO_4)_2$ is probably also associated with the jump in the thermal conductivity caused by the formation of the incommensurate phase.

One more feature of the $C(T)$ dependence in

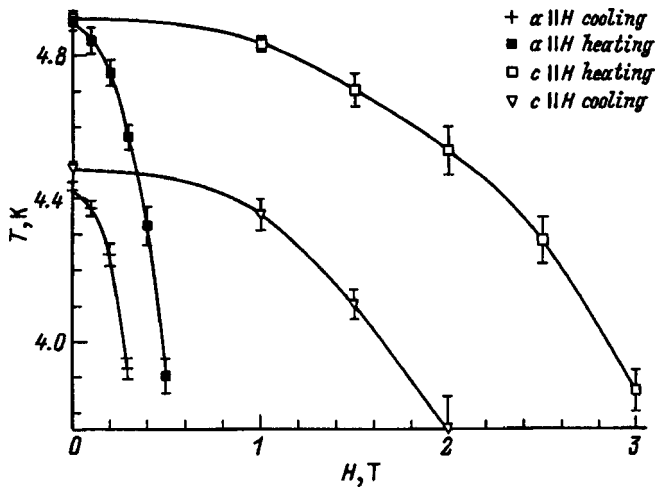

FIG. 3. Transition temperature T_{c1} vs magnetic field during heating and cooling along two crystallographic directions.

$RbDy(WO_4)_2$ is the following: A comparison of the heat capacity of $RbDy(WO_4)_2$ (Fig. 1) and $KDy(WO_4)_2$ (Ref. 8) shows that, at $T=15$ K, the heat capacity of the former compound is about a factor of 5 greater than that of the latter. Since these compounds have similar composition and structure (at least in the high-temperature phase), this difference, in our opinion, can be caused by the presence in $RbDy(WO_4)_2$ of additional singularities on the $C(T)$ curve, associated with the structural transitions for $T>15$ K.

The effect of a magnetic field on the temperature of the structural transitions was also studied for this paper. The magnetic field vector was parallel to the *a* and *c* crystallographic axes. The results for the field dependences of T_{c1} and T_{c2} are shown in Figs. 3 and 4. The very existence of structural phase transitions in a magnetic field is evidence of the antiferrodistortion ordering of the distortions. Measurements in the direction of the *c* axis were made in fields up to 3.5 T. This is associated with the fact that applying large fields $H\|c$ damages the sample. This phenomenon is apparently associated with the occurrence of the metamagnetoelastic effect in $RbDy(WO_4)_2$, in which the strain in the crystal increases sharply when critical magnetic fields are reached in a definite orientation relative to the crystallographic axes.[3,12] When this occurs, the magnetic field can induce strain with the same symmetry as the strains of the sublattice. Therefore, in this effect, the magnetic field, when it reaches a value comparable with the intersublattice interaction parameters, can transport the crystal into a ferrodistortion phase. It was predicted earlier that the metamagnetoelastic effect can occur in crystals of double rare-earth tungstates and molybdates, and estimates were obtained for the critical magnetic field that causes metamagnetoelastic behavior.[12] These estimates gave values of $H\sim 3-10$ T, and this agrees well with our experimental results.

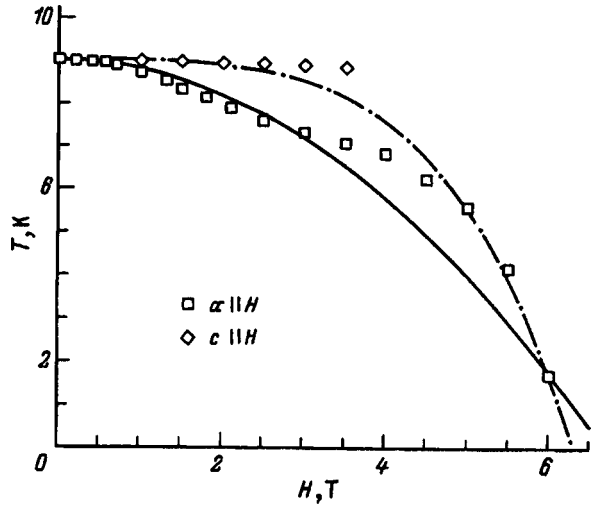

FIG. 4. Transition temperature T_{c2} vs magnetic field along two crystallographic directions. Fitted to Eq. (1) with $n=2$ (solid curve) and $n=4$ (dashed curve).

We should point out that strong anisotropy of the magnetic-field dependences of T_{c1} and T_{c2} is observed in $RbDy(WO_4)_2$, as well as in $KDy(WO_4)_2$. It should be pointed out that the area on the thermogram for the low-temperature first-order structural transition decreases with increasing magnetic field, while the value of the hysteresis increases. In magnetic fields greater than 3 T, it is impossible to determine transition temperature T_{c1} from dT/dt. The points on Fig. 4 for the cooling and heating thermograms coincide, which is evidence that the second-order transition at $T_{c2}(H)$ is maintained in a magnetic field.

It is of interest to study the character of the variation of the critical temperature with magnetic field. The experimental dependences of $T_{c1,2}(H)$ were compared with calculated curves of the form

$$T_c(H)=T_c(O)-\alpha H^n, \tag{1}$$

where $n=2,4$. The best agreement with the experimental points is observed for $T_{c1}(H)$ and $T_{C2}(H)$ curves with $n=2$. Figure 4 shows the calculated dependences for $n=2$ (solid curve) and $n=4$ (dashed curve). As can be seen from this figure, when the magnetic field is along the *a* axis in the low-field region (up to 3 T), the experimental points are best described by the curve with $n=2$. With $H\|c$ in fields up to 3.5 T, the transition temperature T_{c2} is virtually constant, and therefore such a comparison was not carried out in this case. The field dependence of $T_{c1}(H)$ in the low-field region is also best described by Eq. (1) with $n=2$. It should be pointed out that, in the $KDy(WO_4)_2$ crystal, the field dependence of the transition temperature with $H\|a$ is also best described by a dependence of the form of Eq. (1) with $n=2$. Note that, for the curve on the phase diagram corresponding to the breakdown of the antiferroelastic structure by a magnetic field, an analytical expression of the form of Eq. (1) with $n=4$ is obtained in the region of relatively weak fields.[3] Such a dependence is actually confirmed in the case of the $KDy(MoO_4)_2$ crystal,[4] in which magnetically inequivalent Dy^{3+} centers arise during the transition to the antiferrodistortion state. As follows from the results of EPR measurements, magnetically inequivalent Dy^{3+} centers do not appear in $RbDy(WO_4)_2$,[13] and this is possibly the reason for the different behavior of the $T_c(H)$ dependences in crystals of rare-earth tungstates and molybdates. The behavior of

TABLE I. Wave vector stars corresponding to a phase transition with a doubled unit cell.

Symmetry point	Number of wave-vector star	Rays of wave-vector star
V	4	(1/2;0;1/2); (1/2;0;−1/2)
L	5	(1/2;1/2;1/2); (1/2;1/2;−1/2)
A	7	(0;1/2;0)
Y	8	(1;0;0)
M	9	(1;1/2;0)

$T_{c1,2}(H)$ can also be affected by the lower symmetry of the crystal lattice of the tungstates relative to the molybdates.

As already indicated, there are currently no low-temperature structural measurements for single-crystal Rb $Dy(WO_4)_2$, and this paper therefore provides a symmetry analysis in order to determine the possible types of the low-temperature phase and the symmetry properties of the order parameter.

We shall start from the fact that the high-temperature phase has a monoclinic, base-centered lattice and is described by the space group of symmetry C_{2h}^6.[6,7] There are five irreducible representations for which a phase transition is possible in which the volume of a primitive cell doubles, i.e., the lattice breaks up into two equivalent sublattices. These representations are shown in Table I. For two-ray stars 4 and 5, a two-sublattice structure results when a phase transition occurs over a one-ray channel. Stars 7 and 9 assume Lifshitz invariants of the form

$$\eta_1 \frac{\partial \eta_2}{\partial x} - \eta_2 \frac{\partial \eta_1}{\partial x},$$

$$\eta_1 \frac{\partial \eta_2}{\partial y} - \eta_2 \frac{\partial \eta_1}{\partial y}, \qquad (2)$$

where x and y are the Cartesian coordinates in a plane perpendicular to the C_2 symmetry axis. Therefore, in the case of stars 7 and 9, the phase transition necessarily goes through an incommensurate phase. When a phase transition occurs over stars 4, 5, and 8, a transition through an incommensurate phase is possible only in a certain region of values of the parameters, where the coefficient of the terms quadratic in the gradient in the Landau functional becomes negative. Moreover, when a transition occurs over the two-ray stars 4 and 5, there is a possibility that four-sublattice structures will also be formed. As follows from the experimental results of the magnetic-field dependences of $T_{c1,2}$ (Figs. 3 and 4), the boundaries of the incommensurate phase do not display tendencies to converge in both directions studied here. This suggests that the phase transition most likely goes along star 3 or 7, with the incommensurate structure being modulated in a plane perpendicular to the C_2 axis.

The calorimetric studies of $RbDy(WO_4)_2$ have thus shown that the transition from the high-temperature to the low-temperature phase results from at least two structural phase transitions: at $T_{c1}=4.9$ K and at $T_{c2}=9.0$ K. This transition is apparently caused by antiferrodistortion ordering of the distortions and occurs via an intermediate incommensurate phase. It is found that the low-temperature phase transition is a first-order phase transition, whereas the absence of hysteresis and flat spots on the thermograms makes it possible to assume that the second transition is a second-order phase transition. The results of a study of how a magnetic field applied along the *a* and *c* crystallographic axes affects the temperatures of the structural phase transitions show a strong anisotropy in the $T_{c1,2}(H)$ dependences and also confirm the antiferrodistortion character of the ordering of the distortions. As a result of these studies, $H-T$ phase diagrams have been constructed. A symmetry analysis has been carried out, and all the wave-vector stars along which a transition is possible into a two-sublattice structure have been indicated. The wave-vector stars for which a Lifshiftz invariant exists have been indicated. Possible structures of the low-temperature phase have been determined.

*E-mail: markov@host.dipt.donetsk.ua

[1] G. A. Gehring and K. A. Gehring, Rep. Prog. Phys. **38**, 5 (1975).
[2] M. D. Kaplan and B. G. Vekhter, *Cooperative Phenomena in Jahn–Teller Crystals* (Plenum Press, New York, 1995).
[3] M. D. Kaplan, Fiz. Tverd. Tela (Leningrad) **26**, 89 (1984) [Sov. Phys. Solid State **26**, 51 (1984)].
[4] Yu. N. Kharchenko, Fiz. Nizk. Temp. **22**, 394 (1996) [J. Low Temp. Phys. **22**, 306 (1996)].
[5] V. P. D'yakonov, V. I. Markovich, V. L. Kovarskiĭ, A. V. Markovich, M. Borovets, A. Endzheĭchak, and G. Shimchak, Fiz. Tverd. Tela (St. Petersburgh) **40**, 750 (1998) [Phys. Solid State **40**, 691 (1998)].
[6] S. V. Borisov and R. F. Klevtsova, Kristallografiya **13**, 517 (1968) [Sov. Phys. Crystallogr. **13**, 264 (1968)].
[7] P. V. Klevtsov and L. P. Kozeeva, Dok. Akad. Nauk SSSR **185**, 571 (1969) [Sov. Phys. Dokl. **14**, 185 (1969)].
[8] M. Borovets, V. P. D'yakonov, A. Endzheĭchak, V. I. Markovich, A. A. Pavlyuk, and G. Shimchak, Fiz. Tverd. Tela (St. Petersburgh) **38**, 2232 (1996) [Phys. Solid State **38**, 1229 (1996)].
[9] M. Borowiec, V. P. Dyakonov, A. Jedrzejczak, V. I. Markovich, and H. Szymczak, J. Low Temp. Phys. **111**, 5/6 (1998).
[10] É. E. Anders and S. V. Startsev, Fiz. Tverd. Tela (Leningrad) **34**, 812 (1992) [Sov. Phys. Solid State **34**, 434 (1992)].
[11] E. E. Anders, I. V. Volchok, A. I. Zvyagin, V. B. Kokshenev, and S. V. Startsev, Izv. Akad. Nauk SSSR, Ser. Fiz. **50**, 369 (1986).
[12] M. D. Kaplan, JETP Lett. **35**, 105 (1982).
[13] M. Borowiec, V. P. D'yakonov, A. Pavlyuk, A. Prokhorov, H. Szymczak, J. Magn. Magn. Mater. (1998) [in press].

Translated by W. J. Manthey

LOW-DIMENSIONAL SYSTEMS AND SURFACE PHYSICS

Excitation spectra of a system of two coupled quantum wells

Yu. E. Lozovik, O. L. Berman, and A. A. Panfilov

Institute of Spectroscopy, Russian Academy of Sciences, 142092 Troitsk, Moscow Region, Russia
(Submitted May 19, 1998)
Fiz. Tverd. Tela (St. Petersburg) **40**, 2226–2228 (December 1998)

Quasi-particle spectra, reconstructed by e-h pairing, have been calculated for a system of spatially separated electrons (e) and holes (h) in ground state. The regions of strong pairing interaction and significant correlation effects are reached by abandoning the BCS approximation and using instead interpolation expressions for correlation energies, which depend functionally on the coefficients of the $u-v$ transformation, with subsequent minimization of the total energy of the reconstructed state with respect to the parameters of the $u-v$ transformation. The dependence of the spectra on quantum-well separation and particle concentration in a system of two coupled quantum wells is discussed. © *1998 American Institute of Physics.* [S1063-7834(98)01912-1]

Systems with spatially separated electrons (e) and holes (h) in a system of coupled double quantum wells are presently attracting considerable interest of experimenters,[1–4] in particular, in connection with the prediction of the existence of superfluidity in this system,[5] quasi-Josephson phenomena,[5,6] and unusual properties in strong magnetic fields[7–9]. Phase transitions occurring in systems with spatially separated electrons and holes were studied.[10,11] One considered, in particular, the formation of a superfluid liquid and the metal-insulator transition in these systems.

It is of interest to find excitation spectra of spatially separated electrons and holes in a system of coupled double quantum wells within a broad range of carrier concentrations n and quantum-well separations D, including the regions with sufficiently strong interactions, where correlation effects are essential and the BCS approximation fails. In particular, one can obtain spectra in the liquid exciton phase as well. Observation of these spectra would permit one to follow the rearrangement in the system associated with spontaneous symmetry breaking. It is calculation of spectra for this system within a broad range of D and n that is the objective of this work.

The Hamiltonian of a system of spatially separated e and h can be written in the secondary quantization representation

$$\hat{H}=\sum_{p=0}^{\infty}\left[\left(\frac{p^2}{2m_e}-\mu_e\right)a_p^+a_p+\left(\frac{p^2}{2m_h}-\mu_h\right)b_p^+b_p\right]$$
$$+\frac{1}{2}\sum_{pp'k}\{V(k)[a_p^+a_{p'}^+,a_{p'+k}a_{p-k}+b_p^+b_{p'}^+,b_{p'+k}b_{p-k}]$$
$$-2\tilde{V}(k)a_p^+b_{p'}^+,b_{p'+k}a_{p-k}\},\qquad(1)$$

where

a_p^+ and b_p^+ are the electron and hole creation operators;

$m_e=m_h$ are the effective electron and hole masses;

$V(k)=2\pi e^2/\epsilon k$ is the Coulomb interaction in a layer;

$\tilde{V}(k)=(2\pi e^2/\epsilon k)\,e^{-kD}$ is the interaction between an electron and a hole located in different layers;

D is the distance between the e and h layers;

ϵ is the static dielectric permittivity;

μ_e and μ_h are the chemical potentials determined by the normalization conditions (we assume the e and h concentrations equal, $N_e=N_h=N$);

$$\sum_p\langle a_p^+a_p\rangle=\sum_p\langle b_p^+b_p\rangle=\frac{1}{2}\,n,$$

where $n=N/S$ is the surface particle concentration in the system, and S is the system area.

Introduce the units $e^2/\epsilon=m=\hbar=1$, where $m=(m_em_h)/(m_e+m_h)$ is the reduced particle mass.

The pairing of electrons and holes makes the ground state of the system unstable.[12,13] Spontaneous breaking of symmetry in a system results in a rearrangement of the excitation spectrum, which is associated with the formation of a nonzero gap in the spectrum caused by electron and hole pairing.

The reconstructed quasi-particle spectrum in the Hartree-Fock approximation, renormalized with inclusion of pairing, can be written[10,11]

$$E(p)=\frac{1}{z_p^2+1}\left[(z_p^2-1)(p^2-r_s^2\mu p_0^2)-\frac{\sqrt{2}p_0 r_s}{\pi}\int_0^\infty p'dp'\int_0^{2\pi}d\phi\frac{(z_p^2-1-2z_pz_{p'}\exp[-D\tilde{p}_f\sqrt{p^2-2pp'\cos\psi+p'^2}])}{(z_{p'}^2+1)\sqrt{p^2-2pp'\cos\phi+p'^2}}\right]\frac{\tilde{p}_f^2}{2}, \tag{2}$$

where $E^e(p)=E^h(p)=\frac{1}{2}E(p)$, and $z_p=u_p/v_p$ is a function related to the Bogolyubov transformation coefficients u_p and v_p, which will be determined by variational techniques. The momenta in Eq. (2) are measured in units of $\tilde{p}_F=p_F/p_0$, where $p_F=(2\pi n)^{1/2}$, and $p_0=[2\int_0^\infty qdq/(1+z_q^2)]^{1/2}$.

To determine the zero-temperature excitation spectrum for a liquid consisting of spatially separated electron-hole pairs one has to calculate the dependence of ground-state energy on concentration.

The total energy of the system E_t can be written

$$E_t=E_{H-F}+E_{\rm corr}, \tag{3}$$

where $E_{\rm corr}$ is the correlation energy, and E_{H-F} is the energy of the system in the Hartree-Fock approximation renormalized with inclusion of pairing:[10,11]

$$2\frac{E_{H-F}}{n}=\frac{4}{r_s^2p_0^4}\int_0^\infty\frac{p^3dp}{1+z_p^2}-\frac{\sqrt{2}}{\pi^2r_s^2p_0^3}\times\int_0^\infty pqdpdq\int_0^{2\pi}d\phi\frac{V(p-q)+V(p-q)z_pz_q}{(1+z_p^2)(1+z_q^2)}, \tag{4}$$

where $r_s=\sqrt{1/\pi n}$ is the mean distance between particles.

We minimized the total energy of the system, which is a sum of the Hartree-Fock and correlation energies, on a class of trial functions for u for v.

For small momentum transfers, the correlation energy E_1^c is calculated with the use of RPA diagrams constructed based on Green's functions with inclusion of the *e-h* pairing.[11] Introducing the notation

$$V_{ee}^{\rm eff}(p,p',q)=V_{hh}^{\rm eff}(p,p',q)=V(q)(u_pu_{p'}u_{p'+q}u_{p-q}+v_pv_{p'}v_{p'+q}v_{p-q}-2e^{-qD}u_pu_{p-q}v_{p'+q}v_{p-q}), \tag{5}$$

and

$$V_{eh}^{\rm eff}(p,p',q)=V(q)(u_pv_{p'}u_{p'+q}v_{p-q}+v_pu_{p'}v_{p'+q}u_{p-q}-2e^{-qD}u_pu_{p-q}v_{p'+q}v_{p-q}), \tag{6}$$

we obtain

$$E_1^c=\int qdqI_1,$$

$$I_1=-\frac{2}{p_0^2r_s^2}\left[\int_0^\infty\frac{d\omega}{2\pi}\ln\left(1+\frac{8p_0r_s}{\sqrt{2}\pi}\int_0^{p_0}pdpV^{\rm eff}(p,p,q)\times\frac{\tilde{E}(p)}{\omega^2+(2\tilde{E}(p))^2}\right)+\frac{p_0r_s}{\sqrt{2}}\int_0^{p_0}pdpV^{\rm eff}(p,p,q)\right]. \tag{7}$$

For large momentum transfers, the Green's function should be constructed in second-order perturbation theory.[11] In this case the quasi-particle energy can be written

$$E_2^c=\int qdqI_2,$$

$$I_2=-\frac{1}{4\pi^3r_sp_0^2}\int_0^{p_0}pdpkdk\frac{V^{\rm eff}(p,k,q)}{E(q)}, \tag{8}$$

where

$$V^{\rm eff}(p,p',q)=2V_{ee}^{\rm eff}(p,p',q)+V_{eh}^{\rm eff}(p,p',q),$$

The correlation energy $E_{\rm corr}$ for all momentum transfers can be constructed by harmonic joining, an interpolation used by Brinkman and Rice[14] (see also Refs. 10,12) to calculate the metallic electron-hole liquid:

$$I=\frac{I_1I_2}{I_1+I_2}. \tag{9}$$

Taking into account the correlation effects yields the following contribution to the energy per pair of particles

$$E_{\rm corr}=\int_0^\infty qdqI(q),$$

and the chemical potential in Eq. (2) can be presented in the form

$$\mu=E_t+n\frac{dE_t}{dn},$$

where the total energy of quasi-particles E_t (a functional of z_p) is given by Eq. (3).

In contrast to a one-component electron gas, the vertices in these diagrams for calculation of the total ground-state energy E_t of the system are renormalized because of electron-hole pairing, and depend on the transformation coefficients u_p and v_p.

The variational calculation of the total energy E_t [Eq. (3)] was performed numerically. All expressions were preliminarily made dimensionless using for the units of length and energy the radius and energy of a two-dimensional exciton, respectively: $a_2^*=\varepsilon_0\hbar^2/2me^2$ and $\mathrm{Ry}_2^*=me^4/2\varepsilon^2\hbar^2$, where $m=(m_em_h)/(m_e+m_h)$ is the reduced mass.

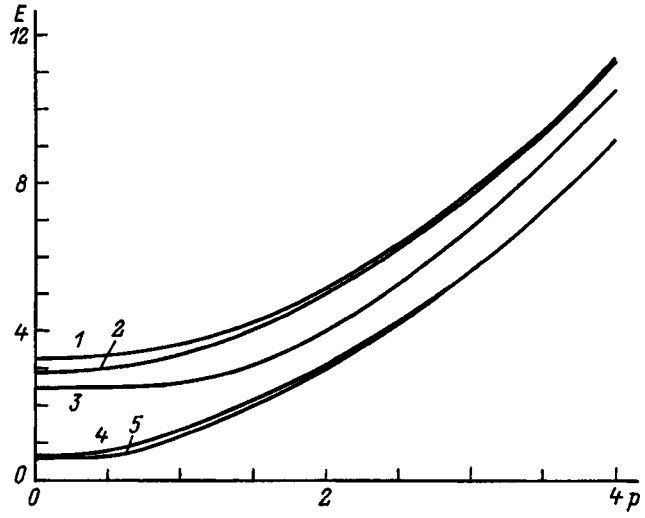

FIG. 1. Reconstructed quasi-particle spectrum $E(p)$ (in units of Ry_2^*, p is the momentum in units of p_F). r_s and D: *1* — 2.2, 0; *2* — 1.6, 0; *3* — 1.0, 0; *4* — 2.2, 0.5; *5* — 1.6, 0.5.

The total ground-state energy E_t of the system, which is a sum of the Hartree-Fock and correlation energies, was minimized using a trial function z_p

$$z_p = A\left(1+\frac{p^2}{4}\right)^{3/2} + B, \tag{10}$$

where A and B are variational parameters[10]. The trial function (10) was chosen so that, for $B=0$, function z_p^{-1} coincides with the Fourier transform of the wave function of the two-dimensional Wannier–Mott exciton (for the semimetallic state, $v_p=0$, i.e., $z_p \to \infty$).

Minimization with respect to the variational parameters A and B was done by the Monte Carlo technique. The values of A and B were chosen at random to calculate the energy of the system. Next the increments ΔA and ΔB of parameters A and B were prescribed. At the next step, parameters A and B were assigned the values $A+k\Delta A$ and $B+k\Delta B$, where the random number $k=0, 1,$ or -1. The new values of parameters A and B were accepted if the corresponding energy was less than the one obtained with the previous values of the parameters, otherwise the new values of A or B were rejected. ΔA and ΔB (the lattice periods on which random walk takes place) were chosen equal to $10^{-3}-10^{-2}$ of the values of the corresponding parameters A and B.

This variational procedure was used to calculate the total ground-state energy of the system E_t for different values of parameter r_s and different distances D between the e and h layers. The value of z_p corresponding to the minimum value of the ground-state energy functional was substituted into the expression for the quasi-particle spectrum (2) to obtain finally excitation spectra for this system with inclusion of electron-hole pairing and electron and hole correlations (see Fig. 1).

For $D=0$ and $r_s \to \infty$ (i.e., for concentration $n \to 0$), the ground-state energy (per one e-h pair) approaches the two-dimensional exciton energy. An earlier publication[15] calculated the dependence of the energy of one exciton in a system of a spatially separated electron and hole on interplanar distance. The results obtained in the present work for quasiparticle spectra (Fig. 1) demonstrate in the limit of large r_s a good agreement with the energy of an exciton with a spatially separated electron and hole (in the limit of small r_s, the BCS approximation[5] holds). An analysis of the calculations shows that the influence of correlation effects on quasiparticle spectra falls off rapidly with increasing interlayer distance to become negligible already for $D \gtrsim a_0^*$. The values of A and B obtained variationally indicate that the exciton phase is stable in the above e-h system for all D (in an anisotropic e-h system, a Mott transition occurs[11]).

The spectrum of new quasi-particles has a gap at $T=0$ for all n and D; this gap decreases with increasing density n and increasing interlayer distance, which is associated with a weakening of the e-h attraction responsible for e-h pairing with increasing D, and with the screening of the e-h attraction which increases with increasing density n. For $n \to 0$, this gap becomes equal to the binding energy of the two-dimensional exciton. This means that the isotropic e-h system under study behaves as an insulator for all n and D. Note that, for large momenta, the spectrum approaches the free-particle spectrum $E(p)=p^2/2m$ for all n and D.

Support of the Russian Fund for Fundamental Research, an INTAS grant, and of the ''Solid-State Nanostructures'' Program is gratefully acknowledged. O. L. B. acknowledges the assistance of the ISSEP Foundation and ICFPM Program.

[1] U. Sivan, P. M. Solomon, and H. Shtrikman, Phys. Rev. Lett. **68**, 1196 (1992).
[2] L. V. Butov, A. Zrenner, G. Abstreiter, G. Böhm, and G. Weimann, Phys. Rev. Lett. **73**, 304 (1994).
[3] T. Fukuzawa, E. E. Mendez, and J. M. Hong, Phys. Rev. Lett. **64**, 3066 (1990); J. A. Kash, M. Zachau, E. E. Mendez, J. M. Hong, and T. Fukuzawa, *ibid.* **66**, 2247 (1991).
[4] M. Bayer, V. B. Timofeev, F. Faller, T. Gutbrod, and A. Forcel, Phys. Rev. B **54**, 8799 (1996).
[5] Yu. E. Lozovik and V. I. Yudson, JETP Lett. **22**, 274 (1975); Zh. Éksp. Teor. Fiz. **71**, 738 (1976) [Sov. Phys. JETP **44**, 389 (1976)]; Yu. E. Lozovik and V. I. Yudson, Solid State Commun. **19**, 391 (1976).
[6] A. V. Klyuchnik and Yu. E. Lozovik, Zh. Éksp. Teor. Fiz. **76**, 670 (1979) [Sov. Phys. JETP **49**, 335 (1979)].
[7] I. V. Lerner and Yu. E. Lozovik, Zh. Éksp. Teor. Fiz. **78**, 1167 (1980) [Sov. Phys. JETP **51**, 588 (1980)]; *ibid.* **80**, 1488 (1981) [**53**, 763 (1981)]; *ibid.* **82**, 1188 (1982) [**55**, 691 (1982)].
[8] A. B. Dzyubenko and Yu. E. Lozovik, Fiz. Tverd. Tela (Leningrad) **25**, 1519 (1983) [Sov. Phys. Solid State **25**, 874 (1983)]; *ibid.* **26**, 1540 (1984) [**26**, 938 (1984)].
[9] Yu. E. Lozovik, O. L. Berman, and V. G. Tsvetus, JETP Lett. **66**, 355 (1997); Phys. Rev. B (to be published).
[10] A. V. Klyuchnik and Yu. E. Lozovik, Fiz. Tverd. Tela (Leningrad) **20**, 625 (1978) [Sov. Phys. Solid State **20**, 364 (1978)].
[11] Yu. E. Lozovik and O. L. Berman, JETP Lett. **64** 573 (1996); Zh. Éksp. Teor. Fiz. **111**, 1879 (1997) [JETP **84**, 1027 (1997)]; Fiz. Tverd. Tela (St. Petersburg) **39**, 1654 (1997) [Phys. Solid State **39**, 1476 (1997)].
[12] L. V. Keldysh and Yu. V. Kopaev, Fiz. Tverd. Tela (Leningrad) **6**, 2791 (1964) [Sov. Phys. Solid State **6**, 2219 (1964)].
[13] L. V. Keldysh and A. P. Silin, Kr. Soobshch. FIAN No. 8, 33 (1975).
[14] W. F. Brinkman and T. M. Rice, Phys. Rev. B **7**, 1508 (1973).
[15] Yu. E. Lozovik and V. N. Nishanov, Fiz. Tverd. Tela (Leningrad) **18**, 3267 (1976) [Sov. Phys. Solid State **18**, 1905 (1976)].

Translated by G. Skrebtsov

Resonant optical orientation and alignment of excitons in superlattices

V. P. Kochereshko, E. L. Ivchenko, and D. R. Yakovlev

A. F. Ioffe Physicotechnical Institute, Russian Academy of Sciences, 194021 St. Petersburg, Russia

F. Lavallard

Groupe de Physique des Solides, URA 17 du CNRS, Universités Paris 6 et 7, 75251 Paris cedex 05, France
(Submitted April 7, 1998; resubmitted May 25, 1998)
Fiz. Tverd. Tela (St. Petersburg) **40**, 2229–2235 (December 1998)

Exciton states in short-period GaAs/AlGaAs superlattices have been studied by optical orientation and optical dipole-moment alignment methods. The effect of magnetic field in the Faraday and Voigt geometries on the degree of linear and circular polarization of photoluminescence have been studied under resonant and nonresonant excitation. The constants of electron-hole exchange interaction in the exciton have been determined. © *1998 American Institute of Physics.* [S1063-7834(98)02012-7]

Applying optical carrier-orientation methods to studies of such quasi-two-dimensional semiconductor objects as heterojunctions, quantum-well (QW) structures, and superlattices (SL) permits one to determine a number of important parameters characterizing the carrier spectrum in such structures. The optical orientation method was used successfully to measure g factors, lifetimes, and spin relaxation times of electrons,[1] electron-momentum relaxation times;[2,3] and, in short-period SLs, carrier localization processes were investigated[4] and the cross section of exciton formation was determined[5]. The exciton optical orientation and alignment methods were used to advantage in combination with time-resolved spectroscopy.[6–8]

Optical orientation of carriers by circularly polarized pump light produces electron-hole pairs with a given angular-momentum projection. The electron and the hole created under nonresonant photoexcitation with photon energy in excess of the gap width relax independently of one another. The degree of circular polarization of the secondary luminescence is determined by the sum of the degrees of orientation of electrons, ρ_e, and holes, ρ_h:

$$P_{\rm cir}=\frac{\rho_e+\rho_h}{1+\rho_e\rho_h},$$

where $\rho_e=\tau_s^e/\tau^e+\tau^e(\rho_e^0)$, $\rho_h=\tau_s^h/\tau_s^h+\tau^h(\rho_h^0)$, τ^e and τ^h are the electron and hole lifetimes, τ_s^e and τ_s^h are the electron and hole spin relaxation times, and ρ_h^0 and ρ_e^0 are the initial hole and electron orientations, respectively.

Information on the exciton states can be obtained by studying the degree of circular (linear) photoluminescence (PL) polarization under resonant circularly (linearly) polarized photoexcitation, as this was demonstrated on bulk semiconductors.[9,10]

Resonant photoexcitation with an energy close to that of the exciton resonance results in direct creation of the exciton. In the case of circularly polarized excitation, the degree of polarization of the secondary luminescence is dominated by the spin relaxation of the exciton as a whole. The difference between the degrees of the exciton PL polarization under resonant and nonresonant photoexcitation is determined by the difference between the mechanisms by which the excitons and carriers undergo spin relaxation.

Resonant excitation of excitons by linearly polarized light results in population of a linear combination of excitonic states with an angular-momentum projection of $+1$ and -1,

$$|1/2,-3/2\rangle \pm |-1/2,3/2\rangle,$$

i.e. of states with a given dipole moment.

The degree of linear polarization of the secondary luminescence is determined by the processes involving relaxation of the exciton dipole moment. This phenomenon is called optical alignment of exciton dipole moments. Optical alignment is possible only under resonant, linearly polarized photoexcitation.

Investigation of the effect of magnetic field on PL polarization under exciton optical alignment conditions is the most promising tool to probe the structure of excitonic states. In this way one can determine such exciton parameters as the g factor, the exciton lifetime τ, and the electron-hole exchange interaction Δ in the exciton.

This work uses the methods of resonant optical orientation and optical alignment of exciton dipole moments in magnetic fields oriented in the Faraday and Voigt geometries to probe free and localized excitons in short-period GaAs/AlGaAs SLs and to determine the exciton parameters.

1. THEORY

We are using here the density matrix formalism to describe the optical orientation and alignment of excitons. Under continuous photoexcitation, the components $\rho_{mm'}$ of the exciton density matrix satisfy the equation[11]

$$-\left(\frac{\partial\rho}{\partial t}\right)_{\rm rec}-\left(\frac{\partial\rho}{\partial t}\right)_{\rm sr}+\frac{i}{\hbar}[H_{\rm exch}\rho]+\frac{i}{\hbar}[H_{\mathbf{B}}\rho]=G. \qquad (1)$$

The terms on the left-hand side describe the exciton recombination, spin relaxation, exchange interaction, and Zeeman effect in the presence of an external magnetic field **B**, and G is the generation matrix. The electron and hole spins of the $e1-hh1$ heavy-hole exciton state $|s,j\rangle$ are $|s=\pm 1/2\rangle$ and $j=\pm 3/2$, respectively. Electron-hole exchange coupling in systems with symmetry D_{2d} results in a splitting of the fourfold-degenerate ground state of the exciton ($n=1$) into three states, A_1+A_2+E. The doubly-degenerate state E with angular-momentum projections $|1/2,-3/2\rangle$ and $|-1/2,3/2\rangle$ is dipole active. The A_1 and A_2 states with momenta $|-1/2, -3/2\rangle$ and $|1/2, 3/2\rangle$ are dipole forbidden. Recalling that the heavy-hole transverse g factor is small enough to be neglected, the Hamiltonian linear in magnetic field can be written

$$H_{\mathbf{B}}=\frac{1}{2}\mu_0(g_e^{\parallel}\sigma_{ez}B_z+g_e^{\perp}\sigma_{\perp}\mathbf{B}_{\perp}+g_h^{\parallel}\sigma_{hz}B_z), \tag{2}$$

where $\sigma_{l\alpha}$ are the Pauli matrices for electrons ($l=e$) and holes ($l=h$). In a general case, the electron g factor in a GaAs/Al_xGa_{1-x}As SL is anisotropic, $g_e^{\parallel}\neq g_e^{\perp}$.[12] The recombination term $(\partial\rho/\partial t)_{\mathrm{rec}}$ is diagonal in the basis of the A_1,A_2, and E states,

$$\left(\frac{\partial\rho_{n,n'}}{\partial t}\right)_{\mathrm{rec}}=-\frac{1}{2}\left(\frac{1}{\tau_n}+\frac{1}{\tau_{n'}}\right)\rho_{n,n'}, \tag{3}$$

where τ_n is the lifetime of state n. Obviously enough, the lifetime τ of the dipole-active state E is shorter than the lifetime τ_0 of the dipole-forbidden states A_1 and A_2. If the relaxation of the electron and hole spins in the exciton proceeds independently, and the exchange splitting is small compared to temperature k_BT, the term describing spin relaxation in the s,j basis takes on the form

$$\left(\frac{\partial\rho_{sj,s'j'}}{\partial t}\right)_{\mathrm{sr}}=-\frac{1}{\tau_s^e}\left(\rho_{sj,s'j'}-\frac{1}{2}\delta_{ss'}\sum_{s''}\rho_{s''j,s''j'}\right)-\frac{1}{\tau_s^h}\left(\rho_{sj,s'j'}-\frac{1}{2}\delta_{jj'}\sum_{j''}\rho_{sj'',s'j''}\right). \tag{4}$$

The actual form of the generation matrix $G_{mm'}$ depends essentially on the excitation conditions, namely, whether the excitation is resonant, i.e. the incident-photon energy is close to the excitonic resonance energy, or nonresonant, where excitons form through binding of photoexcited electrons and holes.

Using Eqs. (1)–(4), one can readily calculate the components $\rho_{mm'}$, as well as the luminescence intensity I, circular polarization of the luminescence

$$P_{\mathrm{cir}}=\frac{I_{\sigma^+}-I_{\sigma^-}}{I_{\sigma^+}+I_{\sigma^-}} \tag{5a}$$

and linear polarization

$$P_{\mathrm{lin}}=\frac{I_1-I_2}{I_1+I_2},\quad P'_{\mathrm{lin}}=\frac{I_{1'}-I_{2'}}{I_{1'}+I_{2'}} \tag{5b}$$

with respect to the orthogonal axes *1*, *2* and *1'*, *2'*, with the *1'* axis turned through 45° relative to axis *1*. For the secondary luminescence emitted along the normal to the interface one can write the following relations

$$I\propto\rho_{1,1}+\rho_{-1,-1},\quad P_{\mathrm{cir}}=\frac{\rho_{1,1}-\rho_{-1,-1}}{\rho_{1,1}+\rho_{-1,-1}},$$

$$P_{\mathrm{lin}}=\frac{2\mathrm{Re}\{\rho_{1,-1}\}}{\rho_{1,1}+\rho_{-1,-1}},\quad P'_{\mathrm{lin}}=\frac{2\mathrm{Im}\{\rho_{1,-1}\}}{\rho_{1,1}+\rho_{-1,-1}}. \tag{5c}$$

Section 2 presents experimental data obtained on a type-I SL and compares them with theory. We are going to use the following simplifying assumptions: we neglect the term describing the spin relaxation of excitons in Eq. (1) and take into account only that of free carriers before they combine to form the exciton (under nonresonant optical excitation).

2. EXPERIMENT

We studied type-I GaAs/$Al_{0.3}Ga_{0.7}$As SLs grown by MBE on (100)GaAs. The structures were not doped intentionally, and the background impurity concentration was 10^{15} cm^{-3}. The SL period varied from 35 to 50 Å, and the number of periods in all samples was 50. To reduce to a minimum the effect of the surface, the SLs were coated by a 2000-Å thick Al_xGa_{1-x}As cap layer. Low-temperature ($T=1.6$ K) PL, PL excitation, optical orientation, and reflectance spectra in Faraday and Voigt geometries were studied in magnetic fields up to 7 T. The degree of circular and linear polarization was measured by means of a quartz modulator operating as a $\lambda/4$ plate. Time-resolved PL spectra were obtained under excitation with 2-ps long pulses generated by a mode-locked Ar laser. The PL was measured with a streak camera with 25-ps resolution.

A. Optical alignment of excitons

PL spectra of the studied structures under continuous unpolarized excitation by a HeNe laser at a power level of 100 mW/cm^2 exhibit a strong $e1-hh1$ PL line associated with heavy-hole exciton recombination. We measured reflectance spectra of these structures and determined the resonant frequencies of the excitonic transitions. It was established that the Stokes shift between the PL line maximum and the resonant frequency $\hbar\omega_0$ of the excitonic transition in our samples does not exceed 1 meV (Fig. 1a).

No optical alignment effects are observed under nonresonant PL excitation by linearly polarized light with photon energy in excess of the SL gap width ($\hbar\omega>E_g$). The degree of optical orientation under circularly polarized photoexcitation is also small and does not exceed 5%.

Resonant excitation with photons of energy $\hbar\omega_{ex}<E_g$, where photon absorption results in direct creation of an exciton, produces optical alignment of excitons if the light is linearly polarized (Fig. 1b).The observed linear polarization of the excitonic PL exhibits a strong spectral dependence originating from exciton localization processes. The linear PL polarization disappears when $\hbar\omega_{ex}$ is increased above E_g of the SL.

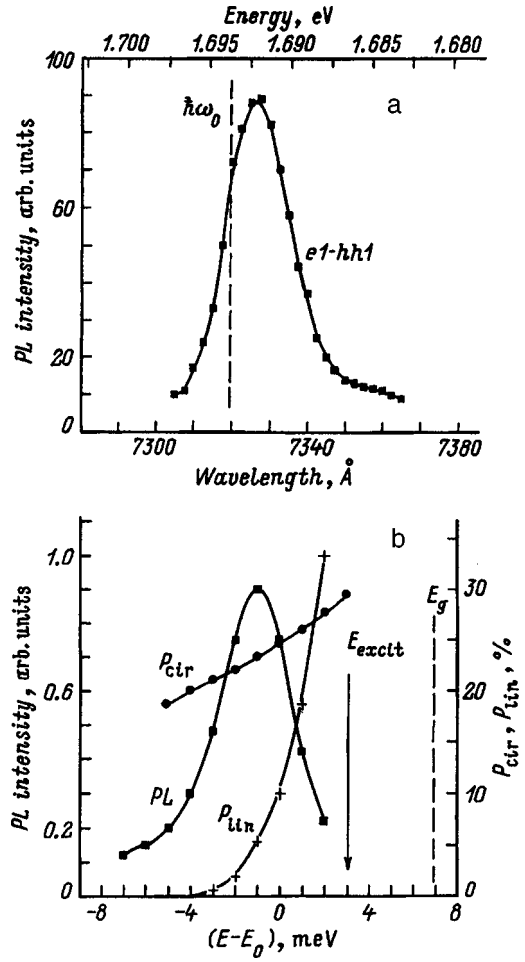

FIG. 1. (a) Spectrum of a GaAs/$Al_{0.3}Ga_{0.7}As$, (20/20 Å)×50 superlattice in the heavy-hole exciton region obtained under He-Ne laser excitation at 1.6 K at a power level of 100 mW/cm^2. Dashed line shows the position of the exciton resonance derived from reflectance spectra. (b) Spectral behavior of the degree of linear polarization of the luminescence, $P_{\rm lin}$, obtained under linearly polarized quasi-resonant excitation, and of the degree of circular polarization $P_{\rm cir}$, under circularly polarized excitation, plotted in units of detuning (E_0-E), where E is the detected energy, and E_0 is the position of the exciton resonance. Dashed line identifies the position of E_g. The arrow refers to the excitation energy.

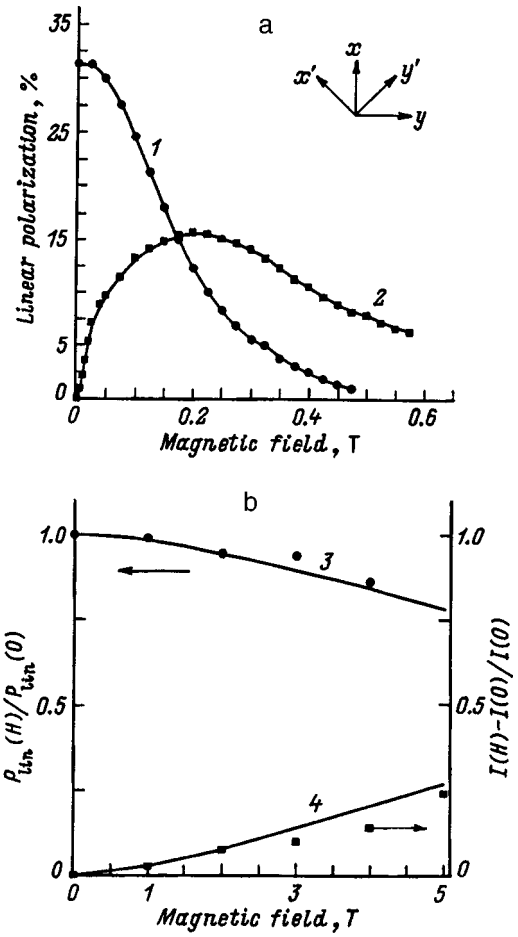

FIG. 2. (a) Magnetic-field dependence of the degree of linear polarization of the photoluminescence under linearly polarized excitation, $P_{\rm lin}(H_\parallel)$, obtained in Faraday geometry. Curve *1* was taken in the (x,y) axes coinciding with the pump polarization, and curve *2*, in the (x',y') axes, turned through 45° with respect to the (x,y) frame. (b) Magnetic-field dependence of the degree of linear polarization of the photoluminescence under linearly polarized excitation, $P_{\rm lin}(H_\perp)$, obtained in Voigt geometry (curve *3*); magnetic-field dependence of the total luminescence intensity (curve *4*).

Resonant excitation also brings about a noticeable increase of the degree of exciton optical orientation as a result of suppression of the spin relaxation of the carriers forming the exciton. The maximum degree of observed linear and circular polarization is ~30% in place of the expected 100% (Fig. 1b). This value varies from one sample to another but does not exceed 40% in our structures. We believe this decrease in the degree of PL polarization to be caused by depolarization in scattering from surface roughness, as the light enters or leaves the sample. This effect can be taken into account by multiplying the true degree of polarization by a depolarization factor $f_d<1$.

Figure 2a plots the degree of linear polarization of excitonic PL obtained in Faraday geometry under quasi-resonant, linearly polarized photoexcitation *vs* longitudinal magnetic field. Curve *1* was taken in the (x,y) axes coinciding with the pump-light polarization direction, and curve *2*, in the (x',y') axes, turned through 45° relative to the pump polarization. Magnetic field applied in Faraday geometry splits the exciton states with the angular momentum projection $|m\rangle = \pm 1$ and effective exciton g factor $g^{\parallel}_{\rm exc}=|g^{\parallel}_e+g^{\parallel}_{hh}|$. This results in both a turn of the polarization plane of the linearly polarized light and in its depolarization. The density matrix formalism (see Sec. 1) permits one to derive expressions for the degree of linear $P_{\rm lin}$ (circular $P_{\rm cir}$) polarization of luminescence under linearly (circularly) polarized resonant excitation in a longitudinal magnetic field:

$$P_{\rm cir}(B_z)=P_{\rm cir}(0), \tag{6}$$

$$P_{\rm lin}(B_z)=\frac{P_{\rm lin}(0)}{1+(\Omega_\parallel\tau)^2}, \quad P'_{\rm lin}(B_z)=\frac{P_{\rm lin}(0)\Omega_\parallel\tau}{1+(\Omega_\parallel\tau)^2}, \tag{7}$$

where $\hbar\Omega_\parallel=g^{\parallel}_{\rm exc}\mu_0 B_z$, τ is the exciton lifetime, B_z is the z component of the magnetic field, and $P'_{\rm lin}$ is the degree of linear polarization measured in the (x',y') frame. For simplicity we have neglected in Eq. (7) the spin relaxation of the exciton. Relations (7) describe the magnetic-field-induced

rotation of the plane of light polarization and its partial depolarization (the Hanle effect). The width of the $P_{\rm lin}(B_z)$ curve can be written

$$B_{1/2}=(|g^{\parallel}_{\rm exc}|\mu_0\tau)^{-1}.$$

Knowing the exciton g factor, one can thus determine the exciton lifetime τ, and conversely, by measuring independently the lifetime, one can derive the g factor. The halfwidth of the depolarization curve determined from Fig. 2a is 0.2 T. Taking for an estimate $|g^{\parallel}_{\rm exc}|\approx 1$ yields $\tau=350$ ps, which appears reasonable and can be reconciled with direct measurements of the kinetics. The sign of $g^{\parallel}_{\rm exc}$ can be readily established knowing that of the $P'_{\rm lin}(B_z)/P_{\rm lin}(0)$ ratio. The maximum degree of polarization in the (x',y') axes reaches as high as 0.5 of that in the (x,y) frame, which implies the absence of noticeable in-plane anisotropy.

In Voigt-geometry experiments ($B\perp z$), the magnetic field mixes the dipole-active exciton states $|-1/2,3/2\rangle$ (or $|1/2,-3/2\rangle$) with angular momentum ± 1 with the dipole-forbidden states $|1/2,3/2\rangle$ (or $|-1/2,-3/2\rangle$) with momentum ± 2. The amount of this mixing is determined by the relative magnitude of the Zeeman splitting $g^{\perp}_{\rm exc}\mu_0 B_{\perp}$ of the E and A_1,A_2 states in a transverse magnetic field and the exciton exchange-interaction constant Δ. Because of the large splitting of the light- and heavy-hole states, only the electronic g factor contributes to $g^{\perp}_{\rm exc}$.

Figure 2b displays the depolarization of optical exciton alignment in a transverse magnetic field (curve *3*). Besides the depolarizing influence of transverse magnetic field, one observes also an increase in the luminescence intensity (curve *4* in Fig. 2b). This effect directly demonstrates the mixing of dipole-active and dipole-forbidden excitonic states by transverse magnetic field and implies a large difference between the lifetimes in these states. The total PL intensity and the degree of linear polarization of the PL in a transverse magnetic field are given by

$$I(B_{\perp})=I(0)\frac{1+\dfrac{\tau}{\tau_0}+(1+\eta)u}{\left(1+\dfrac{\tau}{\tau_0}\right)(1+u)}, \tag{8a}$$

$$P_{\rm lin}(B_{\perp})=P_{\rm lin}(0)\frac{1+\dfrac{\tau}{\tau_0}+u}{1+\dfrac{\tau}{\tau_0}+(1+\eta)u}, \tag{8b}$$

where

$$u=\frac{\Omega_{\perp}^2\tau\tau_0}{1+(\Delta\overline{\tau}/\hbar)^2}\cong\frac{1}{4}\left(\frac{\hbar\Omega_{\perp}}{\Delta}\right)\frac{(\tau+\tau_0)}{\tau\tau_0}, \tag{9}$$

$\overline{\tau}=2\tau\tau_0/(\tau+\tau_0)$, $\hbar\Omega_{\perp}=|g^{\perp}_{e}|\mu_0 B_{\perp}$, and it is assumed that $\hbar/\overline{\tau}\ll\Delta$. For simplicity, we have neglected in Eq. (8) the exchange splitting $\Delta_{1,2}$ between the A_1 and A_2 states ($\Delta_{1,2}=0$ corresponds to cylindrical symmetry, and $\Delta_{1,2}\neq 0$, to tetragonal symmetry). In order to obtain the variation of $P_{\rm lin}$ in a transverse magnetic field, we assumed that even under resonant excitation some excitons are created in the optically inactive state $|\pm 2\rangle$, so that $G_{2,2}, G_{-2,-2}$, and the ratio

$$\eta=\frac{G_{2,2}+G_{-2,-2}}{G_{1,1}+G_{-1,-1}} \tag{10}$$

are nonzero. As follows from (8), $I(B_{\perp})/I(0)<(1+\eta)$ and $P_{\rm lin}(B_{\perp})/P_{\rm lin}(0)\geqslant(1+\eta)^{-1}$. Besides, because τ_0 is much greater than τ, the product $P_{\rm lin}(B_{\perp})\,I(B_{\perp})$ does not depend on magnetic field B.

The fitting of the relations $P_{\rm lin}(B_{\perp})$ and $I(B_{\perp})$ to Eqs. (8a) and (8b) is shown in Fig. 2b with a solid line. The fit yielded the following exciton parameters:

$$\Delta=0.05\ \text{meV},\quad g^{\perp}_{\rm ex}=0.05,\quad g^{\parallel}_{\rm ex}=1,\quad \tau=3.5\times 10^{-10}\text{s}.$$

Thus the exciton optical-alignment method permits one to isolate states within the comparatively broad exciton luminescence band that are responsible for free-exciton recombination, and to determine the exciton parameters, namely, the lifetime, g factor, and electron-hole exchange-coupling constant.

B. Optical orientation of excitons and carriers

In contrast to optical alignment, optical orientation can be observed both on excitons and free electron-hole pairs, i.e., under both resonant excitation involving direct exciton creation and nonresonant optical pumping, where the exciton forms by binding ''nongeminate'' electrons and holes. In these conditions, the degree of PL polarization is determined by the spin relaxation of excitons and carriers and can differ strongly, depending on the actual photoexcitation conditions. The circular PL polarization observed under resonant excitation with photons of energy 2 meV above the exciton resonance was 30%, whereas that measured under nonresonant excitation above E_g of the SL, only 5%. The small degree of circular polarization in this case is accounted for by the strong spin relaxation of electrons and holes [note that the spin relaxation rate of holes is an order of magnitude higher than that of electrons (see Ref. 13)] due to the linear-in-K terms in the SL electron miniband.

Figure 3a shows the dependence of the degree of PL circular polarization, $P_{\rm cir}=[P_{\rm cir}(\sigma^+,B_z)-P_{\rm cir}(\sigma^-,B_z)]/2$, on longitudinal magnetic field B_z for two different regimes of photoexcitation by circularly polarized light.

In the case of nonresonant excitation of an SL with $\hbar\omega>E_g$ (curve *1* in Fig. 3a) one observes a substantial growth of the degree of circular PL polarization, $P_{\rm cir}$, in a longitudinal magnetic field. The degree of polarization increases from 5 to 30%, the value observed under resonant excitation with $\hbar\omega\approx E_g$. We associate the small value of $P_{\rm cir}$ with the efficient operation of the precession mechanism of spin relaxation by Dyakonov–Perel'. The growth of $P_{\rm cir}$ in a weak longitudinal magnetic field is due to suppression of this mechanism and is described by the expression[14]

$$\frac{1}{\tau_s(B)}=\left(\frac{\beta}{\hbar}\right)\left\langle\frac{K_{\perp}^2\tau_p}{1+(\Omega_c\tau_p)^2}\right\rangle.$$

Here τ_s is the spin relaxation time, τ_p is the electron-momentum relaxation time, $\Omega_c=eB_z/m_{\perp}c$ is the cyclotron

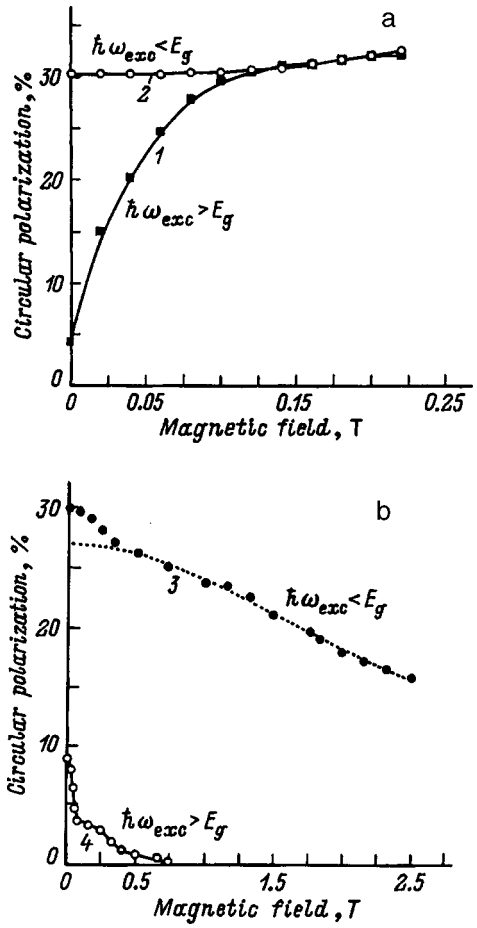

FIG. 3. Magnetic-field dependence of the degree of circular polarization of the photoluminescence under circularly polarized excitation obtained in (a) Faraday and (b) Voigt geometries under nonresonant (*1*,*4*) and resonant (*2*,*3*) exciton excitation.

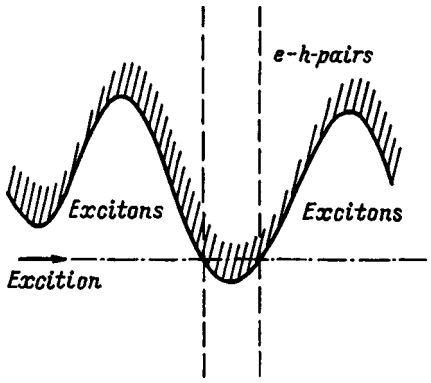

FIG. 4. Diagram of the exciton excitation process in the presence of gap width fluctuations.

frequency, $m_\perp$ is the effective electron mass in the lowest miniband, $m_\perp = m_{xx} = m_{yy}$, and $\beta K_\perp$ is the electron miniband splitting, which is linear in K. The angular brackets denote averaging over the stationary photoelectron distribution function. The halfwidth of the $P_{\rm cir}(B_z)$ curve can be used to determine the electron momentum relaxation time τ_p. For our structure $\tau_p \approx 10$ ps.

The degree of circular PL polarization under resonant exciton creation directly by photons is maximal and is independent of the longitudinal-magnetic-field B_z (curve *2* in Fig. 3a). The explanation for the absence of a longitudinal-magnetic-field effect on the exciton luminescence polarization lies in that the Dyakonov–Perel' mechanism of carrier spin relaxation by precession is no longer effective for localized excitons and is suppressed by free-exciton exchange interaction. The coincidence of the maximum degrees of polarization in curves *1* and *2* of Fig. 3a supports the conclusion that the difference of the maximum degree of polarization from 100% is due to some extraneous reasons (for instance, surface roughness).

In a transverse magnetic field, one observes the Hanle effect on excitons and carriers in Voigt geometry. Figure 3b plots the degree of circular PL polarization, $P_{\rm cir}$, *vs* transverse magnetic field for two regimes of optical excitation by circularly polarized light, namely, at 1 meV above the exciton resonance (curve *3*) and under nonresonant excitation above E_g of the SL (curve *4*). Curve *3* clearly exhibits two Hanle profiles. One profile is broad, with a halfwidth $B_{1/2} \approx 5$ T and a relatively high polarization. The second profile has a halfwidth $B_{1/2} \approx 0.5$ T. The broad Hanle profile disappears as one crosses over to nonresonant photoexcitation, and it can be assigned to the exciton contribution. The narrow profile, associated with the electronic Hanle effect, persists under nonresonant excitation as well (curve *4* in Fig. 3b). The ratio of the exciton and carrier contributions to the degree of PL polarization varies over the exciton luminescence ($e-hh1$) band profile. The broad depolarization profile, representing the exciton contribution, can be expressed as

$$P_{\rm cir}(B_\perp) = \frac{P_{\rm cir}(0)}{1+(B_\perp/B_{1/2})^4}, \tag{11}$$

$$B_{1/2}^{-1} = |g_e^\perp|\mu_0\left(\frac{|\Delta_{12}|\tau}{2\hbar\Delta_1\Delta_2}\right)^{1/2}. \tag{12}$$

We have taken here into account the exchange splitting of the terms A_1 and A_2: Δ_i ($i=1,2$) is the splitting of the E and A_i levels, $\Delta_{12} = \Delta_1 - \Delta_2$. The assumption $\Delta_1 \neq \Delta_2$ results in a quadratic-in-$B_\perp$ splitting of the exciton doublet E and suppression of optical orientation in a transverse magnetic field, while not affecting the linear polarization $P_{\rm lin}$ for $\eta = 0$ and $B \| 1$ or $B \| 2$.

Thus resonant optical orientation of excitons reveals two contributions, viz., 1) due to excitons which were created, relaxed in energy and momentum, and annihilated as a whole (the broad Hanle profile), and 2) due to excitons which existed at some stage as unbound carriers, combined to form excitons, and annihilated thereafter (the narrow Hanle profile). The coexistence of these two contributions implies the presence of SL gap-width fluctuations (Fig. 4). In these conditions, if photoexcitation is done at energies less than the average SL gap width, there will be regions where E_g is still smaller. In these regions the pump light creates electron-hole pairs which, while not being bound in an exciton, can still contribute to exciton luminescence. These fluctuations are comparable in dimensions to the carrier mean free path.

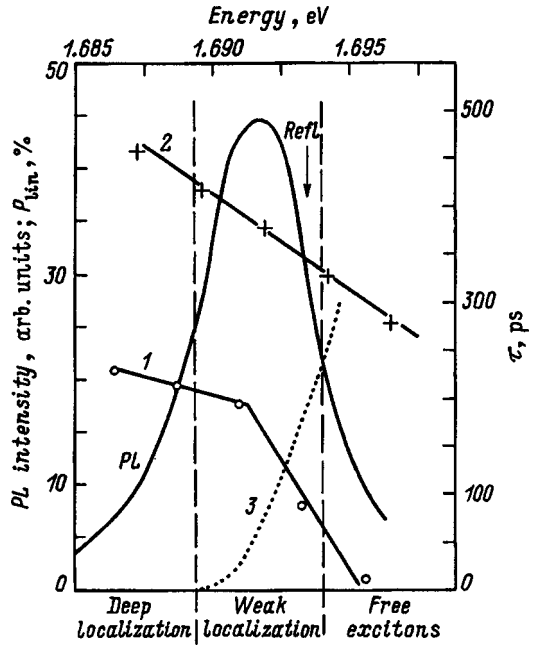

FIG. 5. Luminescence spectrum of a $GaAs/Al_{0.3}Ga_{0.7}As$ (20/20 Å)×50 superlattice in the heavy-hole exciton resonance region. *1* — spectral dependence of the luminescence rise time τ_r, *2* — spectral dependence of the luminescence decay time τ_d, *3* — spectral dependence of the degree of exciton optical alignment $P_{\rm lin}$. The three characteristic regions of variation of $P_{\rm lin}, \tau_r$, and τ_d associated with different exciton-localization processes are identified.

3. DISCUSSION OF RESULTS

The part played by carrier and exciton localization at E_g fluctuations is seen from the ps-scale luminescence kinetics as well (Fig. 5). One sees in this figure the spectra of the rise time τ_r and decay time τ_d of the exciton PL. Also shown is the spectral behavior of the degree of exciton optical alignment $P_{\rm lin}$.

One can isolate in the exciton PL profile three characteristic regions:

1) The short-wavelength edge of the exciton PL band. This region is characterized by a short PL rise time, a large degree of PL linear polarization, and a comparatively short PL decay time. The fraction of the broad (exciton) Hanle profile is the largest at this edge. This implies that it is primarily free excitons that contribute to the short-wavelength wing of the exciton PL line;

2) The central part of the band, the region of the maximum in exciton PL. This region exhibits a strong increase in τ_r, a small degree of linear polarization, and a rise in τ_d. This suggests that the PL maximum, which lies $\sim$1 meV below the exciton resonant frequency determined from reflectance spectra, is due to luminescence of localized excitons, where the exciton is localized as a whole, and localization does not affect the internal structure of the exciton, and this is manifest in the weak PL linear polarization;

3) The long-wavelength wing of the luminescence line is characterized by zero linear PL polarization, and large τ_r and τ_d. This region originates from luminescence of deeply localized excitons, where localization and subsequent energy relaxation change the exciton inner structure, a process which results in a complete loss of the initial exciton dipole-moment alignment.

Thus optical dipole-moment alignment and resonant optical orientation of excitons can serve as powerful tools to probe exciton states. By using these methods, we have succeeded in determining the magnitude of electron-hole exchange coupling in the exciton and estimating the exciton g factor. These methods have permitted us to isolate the contributions due to free and localized excitons within the relatively broad structureless exciton-luminescence band.

The results obtained can be summed up as follows.

Measurements in a longitudinal magnetic field performed in Faraday geometry revealed both suppression of the optical alignment signal and rotation of the average exciton dipole moment.

Experiments performed in Voigt geometry in a transverse magnetic field revealed partial suppression of exciton optical alignment, which is associated with mixing of exciton states with the total angular momenta ± 1 and ± 2.

It was found that the homogeneous structureless excitonic PL band can be divided into parts with essentially different exciton relaxation characteristics, namely, the short-wavelength wing is due to free-exciton luminescence; the region near the maximum in the luminescence band originates from annihilation of localized excitons, where localization does not bring about a change in the exciton inner structure becoming manifest in spin relaxation; and the long-wavelength wing on the PL line is caused by recombination of deeply localized excitons, and in their relaxation and localization the information on the initial state of the exciton is completely lost.

This work was started with active participation of I. N. Ural'tsev, whose premature death prevented his assistance in the final stage of preparing the paper.

Support of the Russian Fund for Fundamental Research (Grant 98-02-18219), INTAS (93-3657 Ext), Volkswagen Stiftung, and ''Nanostructures'' Program is gratefully acknowledged.

[1] *Optical Orientation*, Eds., F. Meier and B. Zakharchenya, Modern Problems in Condensed Matter Sciences, Vol. 8 (North-Holland, Amsterdam, 1984; Nauka, Leningrad, 1989).
[2] I. N. Ural'tsev, E. L. Ivchenko, P. S. Kopev, V. P. Kochereshko, and D. R. Yakovlev, Phys. Status Solidi B **150**, 673 (1988).
[3] I. N. Ural'tsev, V. P. Kochereshko, P. S. Kop'ev, A. M. Vasiliev, and D. R. Yakovlev, Surf. Sci. **229**, 459 (1990).
[4] P. S. Kopev, V. P. Kochereshko, I. N. Ural'tsev, and D. R. Yakovlev, in *Laser Optics of Condensed Matter*, Eds. J. L. Birman, H. Z. Cummins, and A. A. Kaplyanskii (Plenum Press, New York, 1988), p. 87.
[5] P. S. Kop'ev, V. P. Kochereshko, I. N. Ural'tsev, and D. R. Yakovlev, JETP Lett. **46**, 89 (1987).
[6] H. Stolz, D. Schwarze, W. von der Osten, and G. Weimann, Superlattices Microstruct. **6**, 271 (1989).
[7] T. Amand, B. Dareys, B. Baylac, X. Marie, J. Barrau, M. Brousseau, D. J. Dunstan, and R. Planel, Phys. Rev. B **50**, 11624 (1994).
[8] A. Frommer, E. Cohen, A. Ron, J. A. Kash, and L. N. Pfeiffer, J. Phys. IV **3**, 179 (1993).
[9] E. M. Gamarts, E. L. Ivchenko, M. I. Karaman, V. P. Mushinskiĭ, G. E. Pikus, B. S. Razbirin, and A. N. Starukhin, Zh. Éksp. Teor. Fiz. **73**, 1113 (1977) [Sov. Phys. JETP **46**, 590 (1977)].
[10] E.L. Ivchenko, G. E. Pikus, B. S. Razbirin, and A. N. Starukhin, Zh. Éksp. Teor. Fiz. **72**, 2230 (1977) [Sov. Phys. JETP **45**, 1172 (1977)].
[11] G. E. Pikus and E. L. Ivchenko, in *Excitons*, Modern Problems in Condensed Matter Sciences (North-Holland, Amsterdam, 1982), Vol. 2, edited

by E. I. Rashba and M. D. Sturge (Nauka, Moscow, 1985).
[12] E. L. Ivchenko, V. P. Kochereshko, I. N. Ural'tsev, and D. R. Yakovlev, in *High Magnetic Fields in Semiconductor Physics III: Quantum Hall Effect and Magneto-Optics*, edited by G. Landwehr, Springer Series on Solid State Sciences (Berlin, 1992), p. 533.
[13] R. Ferreira and G. Bastard, Phys. Rev. B **43**, 9687 (1991); T. C. Damen, L. Vina, J. Cunningham, J. Shah, and L. J. Sham, Phys. Rev. Lett. **67**, 3432 (1991).
[14] E. L. Ivchenko, P. S. Kop'ev, V. P. Kochereshko, I. N. Ural'tsev, and D. R. Yakovlev, JETP Lett. **47**, 486 (1988).

Translated by G. Skrebtsov

FULLERENESS AND ATOMIC CLUSTERS

Study of cluster materials obtained by selective laser photochemistry

D. V. Kolmykov, A. B. Krynetskiĭ, and S. S. Fadeeva

General Physics Institute, Russian Academy of Sciences, 117924 Moscow, Russia
(Submitted April 21, 1998)
Fiz. Tverd. Tela (St. Petersburg) **40**, 2236–2238 (December 1998)

This paper presents experimental results from the study of the characteristics of cluster materials obtained by resonance laser photochemistry. The effect of the redox reagents used in the photoprocessing on the size and shape of cluster structures of gold has been studied. The minimum size of the structures, measured by electron microscopy, is 30–50 nm. When organic acids are used as redox reagents, fractal structures formed from flat scales are synthesized. Redox reagents based on alcohols form cluster structures of fractal type consisting of spherical clusters. © *1998 American Institute of Physics.* [S1063-7834(98)02112-1]

The modern development of nanotechnologies and various aspects of their applied use have required new methods to be created for obtaining nanoparticles of given shapes and sizes.

Interest in the study of such systems is caused in a fundamental respect by the features of the cluster state of matter and in an applied respect by the possibility of synthesizing promising materials for new technology and engineering.[1]

Cluster materials are based on the groupings of metal atoms surrounded by ligands and lying at distances that allow direct metal–metal interaction and determine the structural type of the material. The possibility of varying the distance in the metal–metal system in such structures while maintaining the collective electronic behavior makes it possible to consider the problem of creating materials with various types of interactions, depending on such parameters as the nature and number of the ligands, the degree of oxidation of the metals, etc.

One of the approaches to the creation of metallic ultradisperse particles is to use various forms of radiations.[2]

Laser radiation sources have significantly expanded the possibilities of finding new approaches to the solution of this problem. The main advantage of laser technology is that it makes it possible to flexibly control the photoprocess of cluster synthesis. Putting it into practice involves using the methods of laser photochemistry.

Selective laser action on metal ions in solution, with resonance excitation of the electron states of the ions, is capable of reducing them to the neutral state in the presence of redox reagents. The fixed product of the photochemical reactions in this case will be neutral metals in a stable cluster form.[3]

The goal of this paper was to study methods of obtaining cluster materials by using selective photochemical processes stimulated by laser radiation in a solution containing gold ions.

1. EXPERIMENTAL APPARATUS

A XeCl laser with the following characteristics was used in the experiments on obtaining cluster materials by the selective laser photochemistry of ions: wavelength $\lambda = 308$ nm, lasing pulsewidth $\tau = 22$ ns, repetition rate $F = 10$ Hz, and laser power $P = 50$ MW.

A 1.00069 N solution of $HAuCl_4$ in 1 M HCl was taken as the starting solution. A standard solution of 0.5 M HCl and doubly distilled water were used to prepare working solutions of $HAuCl_4$ and the redox reagents. Ethanol (absolute), doubly distilled isopropanol (analytical grade), formic acid (99%), and glacial acetic acid distilled over Cr_2O_3 were taken as reducers $[R_A]$.

The test samples were prepared by the following technique: to 2 ml of a 2 mM solution of $HAuCl_4$ in 0.5 M HCl were added 2 ml of a solution of the redox reagent in 0.5 M HCl.

The relationship $[R_A] \gg [M^{+Z}]$, where $[M^{+Z}]$ is the concentration of gold ions in solution, was maintained in all the experiments.

The solution was carefully mixed until air bubbles were completely eliminated and was irradiated in a quartz cell with laser radiation for 3 min, with equal exposure intervals ($t = 30$ sec). No anticoagulation stabilizers were used in the experiments.

The radiation of the excimer laser was transformed by a UV optical system having a 22×10-mm exit aperture and an aperture size of 45×10 mm, ensuring uniform irradiation of the solution.

After each irradiation session, cluster structures consisting of reduced metallic gold were precipitated onto a substrate made from glassy graphite to study their shapes and sizes. The sizes and shapes of the particles were measured on a ''CamScan-4'' scanning electron microscope in the secondary-electron emission regime and in the reflected-electron regime. The microscope is equipped with a LaB_6

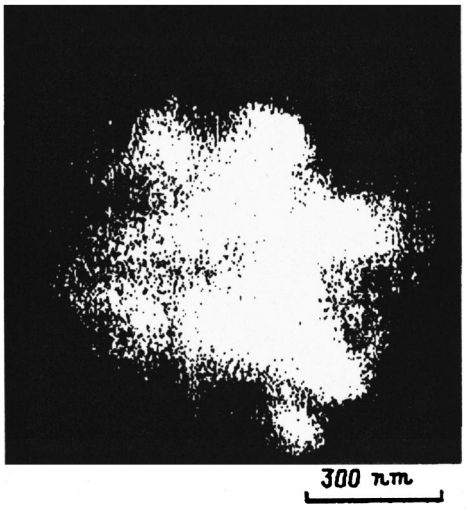

FIG. 1. Cluster structure of $Au(0)_n$, formed by the reduction of Au(+3) under resonance laser irradiation (R_A-C_2H_5OH)

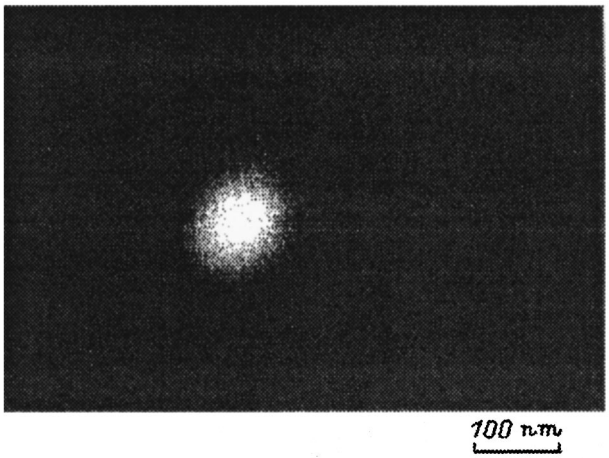

FIG. 2. Base element of a cluster structure of $Au(0)_n$ (R_A-C_2H_5OH).

electrode. The resolution of the device was no less than 4.5 nm on the test samples.

The composition of the test samples was qualitatively determined using a *WDX*–3PC x-ray spectrometer with dispersion over wavelengths and a resolution over heavy elements no worse than 12 ppm.

The material was qualitatively analyzed both by recording the entire spectrum and by tracking the SNR for a line of the element being studied. The material of the sample was analyzed with a beam current of 100 nA and an accelerating voltage of 30 kV in the spot-focusing regime.

A preliminary scan of the substrate was carried out in the reflected electron regime in order to display the regions where the gold cluster structures were localized. Subsequent measurements of the size and shape of the cluster structures were made in the secondary-electron-emission regime with a beam current of 30 nA and an accelerating voltage of 25 kV.

The size on the image was measured with the standard microscope attachments. The image was processed further by means of an IBM-486 computer.

2. EXPERIMENTAL RESULTS

A. Effect of the nature of the redox reagent on the size and shape of the cluster

The influence of the nature of the redox reagents on the size and shape of the resulting hydrosols was studied in the experiments on the laser synthesis of gold cluster structures. The redox reagents included not only compounds that became incorporated in the ligand neighborhood of the complex and produce intramolecular electron transfer: formic acid (HCOOH) and oxalic acid ($C_2H_2O_4$), but also compounds typical of the process of intermolecular electron transfer during the reduction of a molecular ion: ethyl alcohol (C_2H_5OH) and isopropyl alcohol ($CH_3CHOHCH_3$).

Compounds obtained with the participation of redox agents that produce intermolecular electron transfer are characterized by spherical cluster formations with a mean size of 300 nm (Fig. 1). The smallest cluster complex of spherical shape recorded with the electron microscope was 30–40 nm across (Fig. 2).

Cluster complexes of regular shape in the form of triangles and parallelepipeds were recorded on substrates containing gold cluster structures obtained by laser photoreduction with the participation of ethyl alcohol. It can be inferred from the signal intensity of the image that the cluster structure has high density (close packing). The unusual shape, not observed previously, can be explained by the interaction of the cluster complex during its formation with the material of the substrate (glassy graphite) (Fig. 3).

Cluster complexes obtained using isopropyl alcohol as a redox reagent have the conventional shape for gold clusters—dense spherical formations of fractal type with a size of 300 nm. The minimum recorded size of individual spherical gold complexes was 50–100 nm.

The cluster complexes obtained by laser photochemical synthesis with the participation of HCOOH and $C_2H_2O_4$ are amorphous systems consisting of separate scales with a mean size of 100–300 nm (Fig. 4).

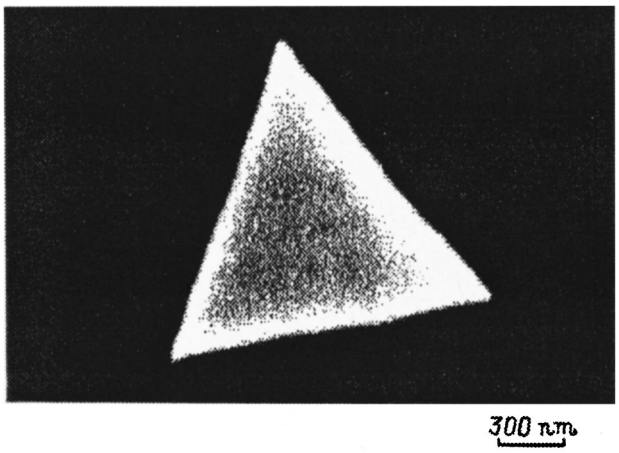

FIG. 3. Cluster complex of $Au(0)_n$ obtained by precipitation on glassy graphite.

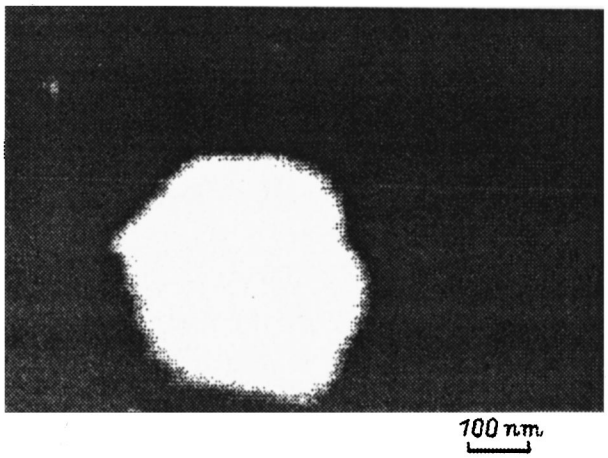

FIG. 4. Cluster structure of $Au(0)_n$ formed by the reduction of Au(+3) by resonance laser irradiation (R_A-HCOOH).

B. Effect of the redox-reagent concentration $[R_A]$ on the size and shape of the gold hydrosols

The efficiency of the photochemical synthesis of gold cluster compounds during a redox process stimulated by resonance laser radiation depends on the concentration of the reducing agent.

The effect of the concentration of the redox reagent on the size and shape of the cluster formations was studied. The redox-reagent concentration $[R_A]$ in the experiments varied from 0.1 to 1 M/l. For all the redox reagents used in synthesizing cluster structures by resonance laser photochemistry, it was established that, when $[R_A]$ is increased by a factor of 10, the minimum size of the gold clusters increases: from 50–100 to 1000–3000 nm.

C. Effect of the laser power on the size and shape of the cluster structures

The optical properties of the gold clusters and cluster complexes are being actively studied, because fractal properties have been detected in the structure of the colloidal aggregates. It was shown in Ref. 4 that a fractal nature of clusters formed from metallic particles results in unique optical properties. One of the consequences of these systems is to increase the surface activity of the cluster complexes.

Accordingly, increasing the time during which the laser acts must cause the total number of cluster structures to vary. A study of photographs obtained on a scanning microscope showed that the size of the individual structures grows to stable values (300 nm) and that the total number of cluster complexes increases.

Summarizing the results on the synthesis of gold cluster structures by resonance laser photochemistry, the following conclusions can be drawn: 1) gold cluster structures synthesized by resonance laser photochemistry have basically fractal structures; 2) the shape of the gold cluster structures obtained by laser photochemistry is determined by the nature of the redox reagents; 3) increasing the exposure time of the laser irradiation stimulates an increase in the geometrical size of the cluster structure and makes its configuration more complex.

[1] J. De May and M. Moeremans, *Advanced Techniques in Biological Electron Microscopy*, edited by J. K. Kohler (Berlin, 1986), Vol. 3, p. 229.
[2] A. Henglein, J. Phys. Chem. **97**, 5457 (1993).
[3] A. D. Pomogaĭlo, Usp. Khim. **66**, 750 (1997).
[4] V. M. Shalaev and M. I. Shtokman, Zh. Éksp. Teor. Fiz. **92**, 509 (1987) [Sov. Phys. JETP **65**, 287 (1987)].

Translated by W. J. Manthey

ERRATA

Erratum: Long-time relaxation of an ordered magnetic structure [Phys. Solid State 40, 467–470 (March 1998)]

S. K. Godovikov, Yu. D. Perfil'ev, Yu. F. Popov, and A. I. Firov
Fiz. Tverd. Tela (St. Petersburg) **40**, 2239 (December 1998)

[S1063-7834(98)02212-6]

Figure 2 in this article should read as follows:

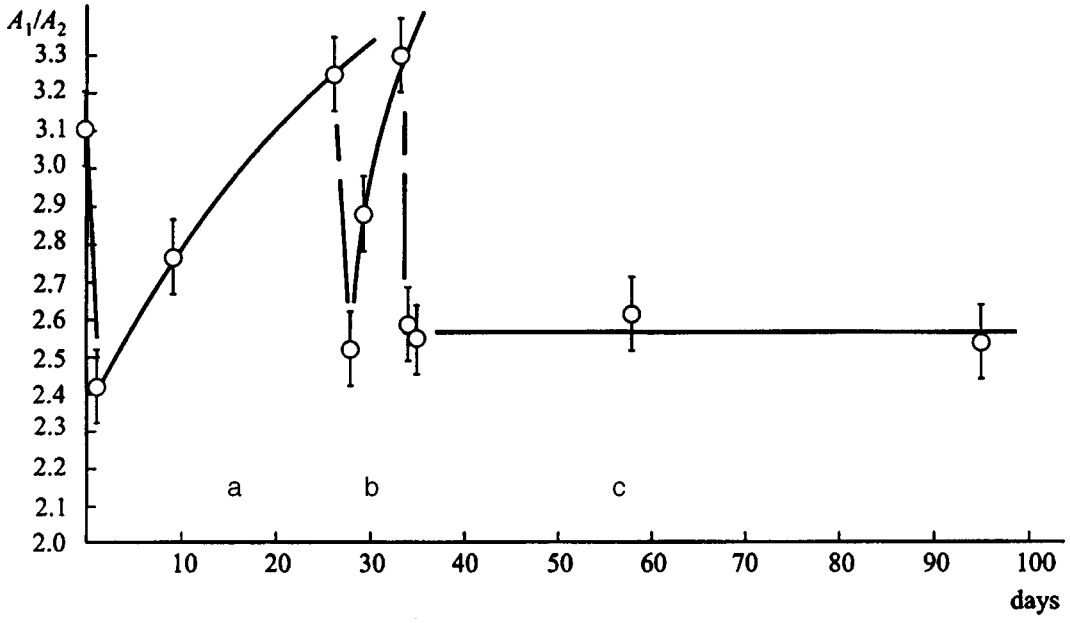

FIG. 2. Long-time relaxation in $Tb_{0.8}Y_{0.2}Fe_2$. a—After the application of a 125 kOe field, b—after repeated application of a 125 kOe field, c—after the application of a 150 kOe field.

